Evolution of depth dependent structure and magnetic properties of multilayers on annealing

By

Mulla Ahmad Basha

Enrollment number: PHYS01201604027

Solid State Physics Division
Bhabha Atomic Research Center, Mumbai-400085.

A thesis submitted to the
Board of Studies in Physical Sciences

In partial fulfillment of requirements
For the Degree of

DOCTOR OF PHILOSOPHY

Of

HOMI BHABHA NATIONAL INSTITUTE

May, 2020

Homi Bhabha National Institute

Evaluation Report of Ph.D. Viva-Voce
Board of Studies in Physical Sciences

A. General Details

1. **Name of the Constituent Institution:** Bhabha Atomic Research Centre, Mumbai

2. **Name of the Student:** Mr. MULLA AHMAD BASHA
3. **Enrolment Number:** PHYS01201604027
4. **Date of Enrolment in HBNI:** 06/01/2016
5. **Date of Submission of Thesis:** 26/05/2020
6. **Title of the Thesis:** Evolution of depth dependent structure and magnetic properties of multilayers on annealing

7. **Number of Doctoral Committee Meetings held with respective dates:**

Review Period	Date	Review Period	Date
1. 06/01/2016-31/01/2018	12/02/2018	2. 01/02/2018-07/01/2019	07/01/2019
3. 08/01/2019-27/02/2020	28/02/2020		

8. **Name and Affiliation of the Examiner 1: Prof. B. N. Dev, Indian Institute of Technology Kharagpur, WB, India**

Recommendations of the Examiner 1 (Thesis Evaluation) (i) accepted, (ii) accepted after revisions, or (iii) rejected: Accepted

9. **Name and Affiliation of the Examiner 2: Dr. Michael Fitzsimmons, Distinguished R&D staff member, ORNL, USA**

Recommendations of the Examiner 2 (Thesis Evaluation) (i) accepted, (ii) accepted after revisions, or (iii) rejected: Accepted

B. Record of the Viva-Voce Examination

1. **Date of Viva Voce Examination: 12/09/2020**

2. **Name and affiliation of External Examiner: Prof. B. N. Dev, Indian Institute of Technology Kharagpur, WB, India**

3. **Whether there were other experts / faculty/students present? Please enclose a soft copy of attendance sheet indicating participation in person/over video as per proforma given below at (5)**

4. **Recommendations for the award of the Ph.D. degree: Recommended / ~~Not Recommended~~**

The thesis identifies the influence of thermal annealing on the structural and magnetic properties of ferromagnetic multilayered films. The two ferromagnetic systems, (i) Gd/Co multilayers and (ii) Fe, Pt and Cu based multilayers, which have relevance to magnetic information technology, have been studied in this thesis with an emphasis on evolution of interface magnetic structure on annealing. Annealing of these multilayered films modified the interfaces and resulted in different structure and magnetic properties of these systems. The thesis contributes to the realization of a helical magnetic structure with a 2π Domain wall in Gd/Co multilayered films near compensation temperature. The annealing driven interdiffusion of atoms at interfaces forms a ternary alloy in the Fe, Pt and Cu based multilayers and showed improved magnetic properties for possible technological application. The results of this work have been published in peer reviewed international journals and the work presented in the thesis is of high standard.

5. **Attendance at Viva Voce (Doctoral Committee, External Examiner, others):**

S. N.	Composition	Name	Signature
1.	**Chairman**	**Dr. S. L. Chaplot**	S. L. Chaplot. 15-09-2020
2.	**Convener** (Guide)	**Dr. Surendra Singh**	Surendra Singh
3.	**External Examiner**	**Prof. B. N. Dev**	Bdev
4.	**Member**	**Prof. M. Senthil Kumar**	M Senthil
5.	**Member**	**Dr. V. K. Aswal**	VKA 15/9/20
6.	**Member**	**Dr. D. Bhattacharyya**	D Bhattacharyya

Others, who were present during the viva voce through online

7.	Harsh Bhatt, BARC	14.	Pramod Bhatt, BARC	21.	Ananyaa Mitra, BARC
8.	Yogesh Kumar, BARC	15.	S. Agarwalla, BARC	22.	Deepak Garg, BARC
9.	C. L. Prajapat, BARC	16.	Yasmeen Jafri, AMITY	23.	Madhu Ghanathe, BARC
10.	C. Gholap, BARC	17.	P. K. Jharapla, Univ. of Hyderabad	24.	Swayam Kesari, BARC
11.	Saibal Basu, BARC	18.	Sher Singh Meena, BARC	25.	Pulkit Prakash, BARC
12.	P. R. Sandeep, BARC	19.	M. Mukadam, BARC		
13.	Pralay Paul, BARC	20.	Bikash Saha, BARC		

15/9/2020

Surendra Singh

(Convener, Viva Voce Board)

डॉ. दिनेश वी. उडुपा / Dinesh V. Udupa
(Dean-Academic)
शैक्षणिक / Dean - Academic
भौतिक एवं गणितीय विज्ञान / Physical & Mathematical Science
होमी भाभा राष्ट्रीय संस्थान / Homi Bhabha National Institute
अणुशक्ती नगर / Anushakti Nagar
मुंबई / Mumbai - 400 094.

Contents

Summary

The focus of the research work presented in the thesis was the investigation of interface dependent structure and magnetic properties of ferromagnetic (magnetic/magnetic and magnetic/non-magnetic) multilayers using non-destructive techniques. The interface properties of the multilayers were controlled and varied by growing these multilayers under different deposition conditions and annealing at different temperatures. The interface dependent structure and magnetic properties have been studied using both macroscopic (XRD, SQUID) and depth dependent (SIMS, XRR, and PNR) characterization techniques. We have mainly studied two systems, 1) Gd/Co multilayers, and 2) Fe-Pt-Cu heterostructures and FePt/Cu multilayers, which have been grown by the sputter deposition technique. The Gd/Co system as a RE/TM multilayer has shown many interesting interface-driven magnetic properties, especially near compensation temperature and is being considered an important artificial ferrimagnet for all spin-based technological applications. Whereas the FePt alloy currently is one of the favorite materials for storage applications though requires a high-temperature treatment for the chemical ordering, which induces unfavorable properties for the application. We have studied the effect of the addition of Cu with different atomic % in FePt alloy by annealing of Fe-Cu-Pt heterostructures and FePt/Cu multilayers and observed interesting magnetic properties at different annealing temperatures.

Gd/Co multilayers grown on different substrates (glass and Si) with varying deposition conditions showed improved layer structures with different interface morphology (interface roughness, etc.). The Gd layers showed a polycrystalline growth with a face-centered cubic (*fcc*) structure, as compared to previous studies where the Gd was grown either in the amorphous phase or in hexagonal-closed packed (*hcp*) phase, which may be the reason for obtaining high-quality multilayer structure without alloy formation. Gd/Co multilayers grown

on glass substrates showed higher interface roughness as compared to that grown on Si substrate at identical deposition conditions. Gd/Co multilayers grown on glass substrates were also used to study the annealing dependent magnetic properties, whereas multilayers deposited on Si substrates were used to investigate the temperature and field dependent magnetic properties. We have shown that the compensation temperature (T_{comp}), which is a signature of the antiferromagnetic exchange interaction between Co and Gd at interfaces, is strongly correlated to the interface morphology and increases with an increase in interface roughness. Annealing of Gd/Co multilayers resulted in an increase in roughness as well as the formation of an alloy layer at interfaces, leading to modification in magnetic properties with additional magnetically complex phases at low temperatures.

We have further explored the interface-driven exchange coupling in Gd/Co multilayers as a function of temperature and field. The magnetic measurements revealed that multilayer having lower intermixing at interfaces are strongly coupled and showed negative exchange bias at temperatures < T_{comp}. Multilayers having lower interface roughness also showed a planar 2π domain wall (DW), within both the Co and Gd layers at $T_{comp.}$ In addition growth of the magnetic domain with magnetization perpendicular (in-plane) to the applied field in the central part of each Gd layer at T_{comp} was observed for the multilayer with lower interface roughness. These magnetic inhomogeneities in the central part of each Gd layer are highly correlated and contributed to the antisymmetric magnetoresistance (MR) observed in these multilayers at T_{comp}. The formation of magnetic helical structure around T_{comp} showed additional irreversibility in MR as a function of field. Like other studies on RE/TM multilayers, the Gd/Co multilayers also showed temperature-dependent magnetic phases with AFM coupling at Gd/Co interfaces at all the temperatures. Field dependent measurement suggested an increase in the compensation temperature with an increase in the applied field and the alignment of the Gd (Co) moment along the applied field is highly dependent on the field.

Other systems with magnetic (FePt) and nonmagnetic (Cu) layer studied here deals with evolution of structure and magnetic properties of a FePtCu ternary alloy formed upon annealing of a Fe-Cu-Pt trilayers and FePt/Cu multilayers. The trilayers and multilayers showed drastically different magnetic properties on annealing isochronally (300 to 600 ^{o}C) for 0.5 hr under similar conditions, suggesting interface dependent interdiffusion kinetics in these systems. We observed a rapid and long-range interdiffusion of atoms at interfaces with the formation of an alloy layer on annealing the trilayer heterostructures at temperature > 400 ^{o}C. The trilayers exhibited different exchange bias at room temperature on annealing at different temperatures. It showed a positive exchange bias (~ +120 Oe) on annealing at 400 ^{o}C, which on further annealing at higher temperature (≥ 500 ^{o}C) showed a negative exchange bias (~ -100 Oe). The study suggested the coexistence of hard-soft magnetic phases along the thickness of the systems on annealing above 400 ^{o}C, which contributes to the observed exchange bias. Whereas annealing of FePt/Cu multilayers under similar conditions up to a temperature of 600 ^{o}C suggest a small interdiffusion of atoms at different interfaces, which resulted in a marginal suppression in magnetic properties. Upon isothermal annealing (at 600 °C) for longer times (1.5-6.5 hr), multilayers showed large interdiffusion at interfaces and formation of ternary alloy and iron silicide (at substrate-film interface) phases. The study also suggested that evolution of ternary alloy is highly dependent of iron silicide phase formed in the multilayers system. Using reflectivity measurements, we also estimated the composition of ternary alloys formed in these systems, which is close to theoretical calculation of the compositions. In the FePtCu ternary alloy film, the increased Cu content (higher Cu content sample) leads to phase coexistence with larger fraction of face-centered tetragonal (*fct*) phase, which is responsible for its low saturation magnetization with a high coercivity at room temperature. These results demonstrate a mechanism of producing a ternary alloy phase of designed compositions on annealing the multilayers of different thickness, which showed distinctly different magnetic properties. The

tuning of magnetic properties of ternary alloy by adding different Cu content may be desirable for future magnetic devices.

The results have shown a strong influence of the film growth and thereby interface structure and morphology on the magnetic properties. As a future prospectus the correlation of interface driven magnetic properties in RE/TM system can be strengthened by the macromagnetic simulations, which will further help in designing the system for technological application. Annealing of the RE/TM multilayer also suggested modification in magnetic properties at low temperatures therefore a study of temperature and field dependent magnetic structure in RE/TM multilayer annealed at different temperature will be interesting for both application and fundamental research point of view. In addition, finding a RE/TM multilayer system with a compensation temperature near room temperature will be very promising system for technological application, especially for helicity dependent magnetic properties. In the case of FePt based system we observed interesting low temperature magnetic behaviour in SQUID measurements therefore it will be interesting to see detail depth dependent magnetic temperature at low temperatures using PNR. In addition, the study can be pursued by search for more suitable nonmagnetic material, e.g. Ag or Au, which is miscible with FePt alloy and provides improved magnetic properties of the alloy for technological application.

Chapter 1

Introduction

1.1 Surfaces, interfaces, and thin film magnetism

The interface phenomenon plays an important role in the development of advanced materials for various technological applications in the area of interface science and engineering. The science and technologies attached to magnetic recording and other magnetic devices have acknowledged an explosive growth in recent decades and their attractive properties have lead to an information revolution with constantly improving storage densities and processing rates of information [1-5]. Especially central to this pursuit is the material science of magnetism as it applies to surfaces, interfaces, and thin films [6-8]. It is very important to understand the physical and chemical processes that occur at the interfaces when two materials are brought in contact with each other and its impact on the overall magnetic properties of the system. Broken coordination and symmetries at the surfaces and often show properties that are different from the bulk. In thin films, different crystalline structures, defects, and strains at the interfaces can also modify the overall properties of the systems [9,10]. Therefore the preparation of controlled surfaces and interfaces, especially in magnetic heterostructures, provides a new area in the science of magnetism: highly interdisciplinary subjects involving physics, chemistry, and materials sciences [6-11].

Thin films are generally considered as quasi-two-dimensional (2D) structures, where the thickness is much smaller compared to the other two dimensions. Thin film heterostructure systems can be tuned for various technological applications and also show a wide interest in

the basic understanding of interface growth. One can deposit multilayer thin films by alternate deposition of dissimilar elements. These tailored structures have a larger surface to volume ratio than bulk and possess different structural, magnetic, and electronic properties. Diffusion at the interfaces of dissimilar elements by solid state reaction has grabbed attention in recent years as this process can produce new materials in the form an alloy as well as provide a technique to alter interface morphology in heterostructure and multilayers [12-14]. Multilayers of magnetic-non magnetic systems show various applications in different fields a few worth mentioning here are magnetic thin films as magnetic storage elements, magnetic sensors, metal-semiconductor systems in microelectronics, spintronics, etc. The different phenomena associated with the above application of magnetic/non-magnetic heterostructures and multilayers, which have been widely studied in recent years, are giant magnetoresistance, exchange bias (EB), perpendicular magnetic anisotropy, magnetization reversal, etc.

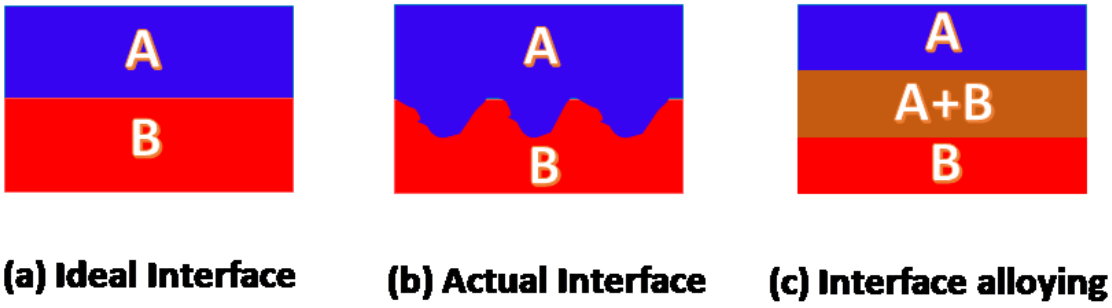

Fig. 1.1: Schematic of different types of interfaces (a) an ideal interface between layers of elements A and B, (b) interface with roughness, and (c) interface alloy formation of A and B elements in a binary system.

A solid interface consists of a small number of atomic layers that separate two dissimilar solids (A and B) in intimate contact with one another. Figure 1.1 shows a schematic of ideal and actual interfaces formed between two layers of materials A and B. An ideal interface with a sharp boundary between two materials is shown in Fig. 1.1 (a). In reality,

there is the penetration of materials across the boundary due to the inter-mixing/roughness of the components [Fig. 1.1 (b)], which is a measure of jaggedness at the interface. Hence the real interface is the combination of both these effects (intermixing and actual height fluctuation), which makes broader interfaces compared to the ideal flat interface. Figure 1.1 (c) shows an alloy layer at the interface which constituents with A and B. These are the interface structures, which controls and modify the magnetic interaction across the interface and thus show different magnetic properties for technological application.

Interfacial coupling and structures between different layers in magnetic heterostructures play a crucial role in determining overall properties. Thus, it is important to characterize and understand the interfacial coupling and interfacial magnetization configuration, which are essential in guiding material design. In this thesis, we have studied the structure and magnetic properties of primarily two systems, Rare earth (RE) / transition metal (TM), Gd/Co, and FePt/Cu multilayers, especially targeting the interface-driven properties. The interface structures of the multilayers were varied both by changing the growth conditions and by annealing the multilayers, which changes the interfaces in all aspect as described above (interdiffusion, intermixing, alloy formations, etc.) and showed modified magnetic properties. In this chapter, we will briefly discuss the basic magnetic properties of a thin film system with attention to the systems (Gd/Co and FePt/Cu) studied here.

1.2 Magnetic properties of thin films

This thesis focuses on the investigation of interface magnetism of ferromagnetic (FM) multilayers consisting of magnetic/nonmagnetic and magnetic/magnetic heterostructures of different interface morphology, which is achieved either by changing the growth parameters or annealing the multilayers as a function of temperature and time. In this section, we briefly discussed the basics of magnetism.

1.2.1 Basic of magnetism

The macroscopically measurable quantity for the material is electron magnetic moment which is given by the electronic structure of the solid. There are two ways one can define the origin of the magnetic moment of an electron: a) the precession of the electron at the particular orbital around the nucleus gives a magnetic moment, which is connected to the orbital momentum, b), every single electron has an intrinsic magnetic moment due to spinning of the electron, the electron spin. The electron's spin magnetic moment expressed as the so called Bohr magneton

$$\mu_B = \frac{eh}{4\pi m_e} \qquad (1.1)$$

where *e*, *h*, and m_e are electronic charge, Planck's constant, and the mass of the free electron, respectively. All the materials react to the applied magnetic field (*H*) because of this intrinsic magnetic moment through an internal magnetization (*M*), where both are connected by the magnetic susceptibility (χ):

$$\chi = M/H \qquad (1.2)$$

In addition, the magnetization of material also contributes to the externally measurable magnetic field, the magnetic induction (*B*) via

$$B = \mu_0 (H+M) \qquad (1.3)$$

where μ_0 is the permeability of the medium and *M* is the magnetic moment per unit volume. Materials can be distinguished by χ and classified into diamagnetic, paramagnetic, antiferromagnetic (AFM), and ferromagnetic materials. Diamagnetic and paramagnetic materials are those that exhibit no collective magnetic interactions and are not magnetically ordered, whereas AFM and FM materials exhibit long-range magnetic order below a certain critical temperature.

The non-cooperative behavior of the orbital electrons under the application of an external magnetic field is the main origin of diamagnetism. For diamagnetic materials when an external magnetic field is applied, they are magnetized opposite to the field direction, and thus the materials with $\chi < 0$ are described as diamagnetic. In paramagnetic materials, the atoms or ions have unpaired electrons in the partially filled orbitals. When the applied field is zero, the magnetization becomes zero. By applying the external magnetic field there will be a partial alignment of these atomic magnetic moments in the direction of the applied magnetic field resulting in a net positive magnetization and also a positive susceptibility ($\chi > 0$). Magnetic susceptibility of these materials shows slightly positive and lies in the range 10^{-5} to 10^{-2}. Some materials (FM and AFM) show magnetic order below a characteristic temperature, for which strong interaction of neighboring elements with spins S_i and S_j are necessary and described by Heisenberg Hamiltonian:

$$\mathcal{H} = -2\mathcal{J}S_i.S_j \qquad (1.4)$$

Where $\mathcal{J}$ is the exchange constant and it is positive for parallel alignment of magnetic moments of the adjacent atoms, called ferromagnet.FM materials show a large value of χ and spontaneous magnetization without any applied magnetic field. For the negative value of $\mathcal{J}$, the magnetic moment of the adjacent atoms is antiparallelly aligned, leading to no net magnetization and the system is called an AFM. Examples of ferromagnetic materials are Fe, Co, Ni, Gd, etc., and they possess a magnetic susceptibility of as high as 10^6. The exchange constant shows temperature dependence as it is closely related to the interatomic distance and thus both magnetic order phenomena occur below a critical temperature. This temperature is called *Curie temperature* (T_c) and *Neel temperature* (T_N) for FM and AFM materials, respectively. In general, the variation of $1/\chi$ with temperature for different magnetic materials is represented as a schematic in Figure 1.2.

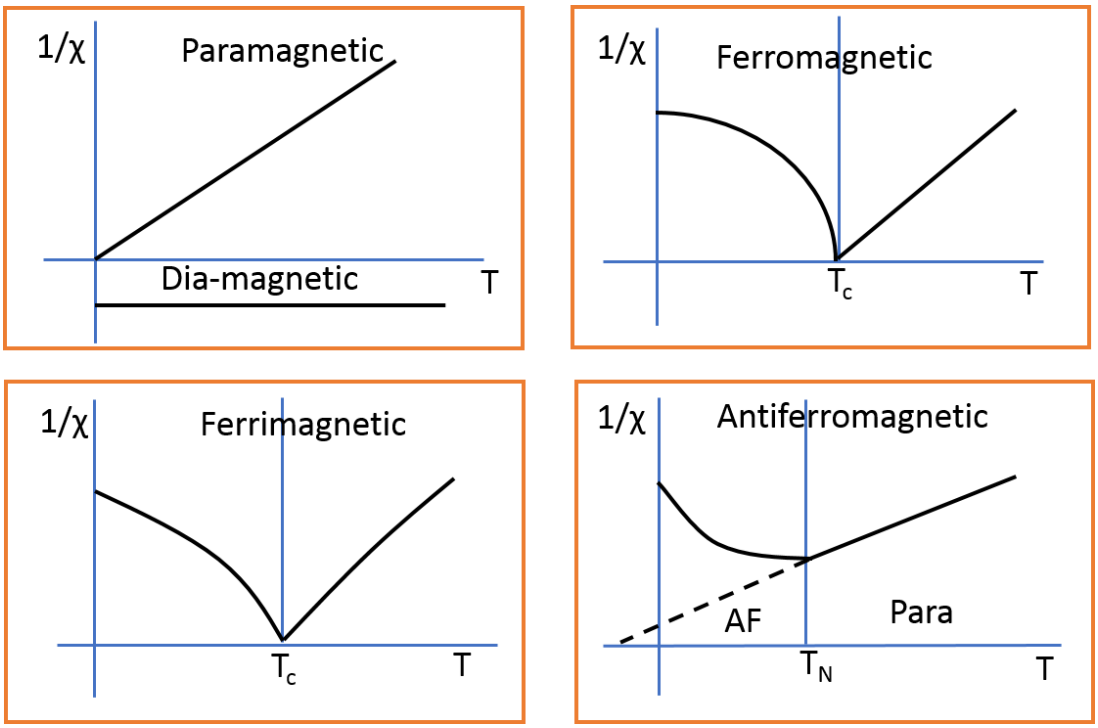

Fig. 1.2: Schematic diagram of a variation of susceptibility with temperature for different magnetic materials.

There is another kind of magnetism called ferrimagnetism, which results due to an antiparallel alignment of magnetic moments of the different elements. In contrast to antiferromagnets, the magnetizations of two sublattices of ferrimagnets have different values, and hence like ferromagnets, the spontaneous magnetization is non-zero. The magnetic moment also shows temperature dependence. Ferrimagnetism is generally shown by alloy and RE/TM heterostructures.

Thin film heterostructures and multilayers with interface defects also show two different kinds of magnetic properties which are termed as *superparamagnetism*(SP) and *spin glass* magnetic behaviors. SP is a size effect of ferromagnetism and ferrimagnetism materials. When FM or ferri-magnetic particle size becomes very small (few nm), magnetism in such materials appears as paramagnetic in nature even below Curie temperature. The SP phenomenon imposes condition or limitation on the size of the particles in the magnetic

recording media, where SP behavior causes to lose their memory from thermal influences. The SP particles do not retain the magnetic remanence, which is very useful in biomedical applications. On the other hand, spin glasses are defined as frozen spins or disorder orientations of spins at low temperatures. Usually, spin glasses are in a magnetic frustration state where spins compete with each other and orient in a random direction, which has no specific configuration. In contrary to magnetic order (FM, AFM, ferrimagnetism) behavior, which is long-range in order, magnetism in spin glasses is a short-range in order.

1.2.2 Ferromagnetism and magnetic anisotropy

We have already discussed the ferromagnetism in the previous section in brief and detail can be found in various textbooks [15,16]. In this section, we will focus on the main properties of the ferromagnetic elements Fe, Co, Gd, and several alloys containing these materials with an introduction to magnetic anisotropy, which can greatly influence the magnetic properties of thin film and multilayers. Ferromagnetism was generally known in crystalline materials for a long time, later ferromagnetism was observed in amorphous material such as RE-TM alloy (e.g. TbFe, etc.), which suggested that long-range magnetic order can be found without any structural long-range order [17]. In general, ferromagnetism appears to be anisotropic because of different contributions such as magnetocrystalline, shape, surface, or interface as well as unidirectional magnetic anisotropy [15]. The dipolar and spin-orbit interactions are mainly responsible for magnetic anisotropy. The dipolar interaction, usually long-range order, depends on shape (geometry) of the sample and contributes largely for the in-plane magnetization, especially for thin films. The Gd, Co, and Gd/Co, Fe/Pt layered films investigated in this thesis all show an in-plane magnetization due to shape anisotropy. The spins and crystal lattice are coupled through spin-orbit interactions and the orientation of the magnetization relative to the crystal axis depends on the symmetry of the

crystal and thus contributes to magnetocrystalline anisotropy. In addition, the spin-orbit interaction is responsible for the magneto-elastic or magnetostrictive anisotropy induced in a strained system especially observed in multilayer systems due to lattice mismatch between adjacent layers. Surface anisotropy is important for the ultra-thin film, which originates due to broken symmetry of electron orbital at the surface or interface.

In general, the presence of magnetic anisotropy in a ferromagnet leads to preferred directions of the magnetization (magnetic moment density) with respect to the crystal lattice or macroscopic dimensions. The preferred directions of magnetization are called magnetic easy axes (or plane) and the other direction is called a magnetic hard axis. For FM materials, other than spontaneous magnetization, the hysteresis is an important characteristic property and is defined as the energy required for a magnetization reversal. The magnetic easy axis is associated with a sharp magnetization reversal. Whereas the magnetic hard axis is associated with a gradual and reversible magnetization change with increasing applied magnetic field until the saturation magnetization (M_s) is reached at the anisotropy field (H_a). Thus, the hysteresis curve [$M(H)$] associated with a ferromagnetic materials shows the coercive field and determines whether a ferromagnet is considered as magnetically hard (large H_c) or soft (small H_c).

Figure 1.3 shows an example for both reversal mechanisms, where M (H) hysteresis loops have been measured for as-deposited FePt/Cu multilayer deposited on a Si (001) single crystalline substrate. This multilayer shows a soft ferromagnet with a full remanence ($M_r = M_s = 1$), an easy axis coercivity of H_c~35 Oe, and a hard axis saturation field of H_a ~40 kOe. Using H_a and M_s one can also estimate the magnetocrystalline anisotropy constant (K) by: $H_a = 2K/M_s$.

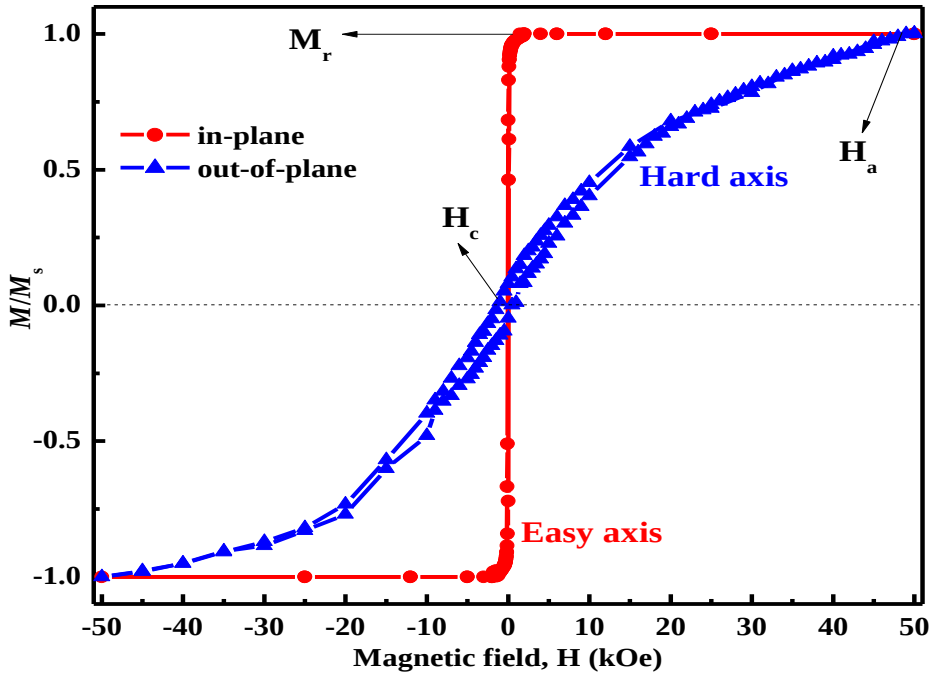

Fig. 1.3: Room temperature hysteresis loop of as-deposited FePt/Cu multilayer measured by SQUID along the in-plane and out-of-plane direction of the multilayer.

1.2.3 Magnetization reversal and domain walls

In general, magnetization reversal is a process of magnetization inversion from positive saturation magnetization to negative saturation magnetization or vice versa, which is achieved by sweeping an external applied field with sufficient strength to align the magnetization uniformly along the field direction[18]. Sweeping the external applied field along the field axis the projection of the magnetization will show a hysteretic behavior, suggesting multiple local free energy minima for the system. The *M*(*H*) hysteresis loops and magnetization reversal have been some of the most important features of ferromagnetic materials, which are related to the rather complex landscape of free energy. In the ferromagnetic sample, during the magnetization reversal, the competition between exchange energy, anisotropy energy, the magnetostatic energy, and Zeeman energy results in the formation of magnetic domains.

Domains are the region of alignment in the sample with uniform magnetization and different domains are separated by domain walls, a region in which magnetic moments rotate coherently. Since the total energy depends on the sample shape, size, and relation to the easy axis, the domain formation will nucleate at the characteristic nucleation field, which is closely related to the internal structure of the system. For thin films, the uniaxial anisotropy, higher interface roughness, pinning center due to defects at interfaces play an important role in deciding the nucleation field for the formation of domains.

There are two types of domain walls: the Neel wall and the Bloch wall. In the Neel wall, the moments rotate within the plane covered by the magnetization directions of the initial and the nucleated domain. In the case of the Bloch wall, the moments rotate out of this plane. The width of the domain wall depends on the anisotropy constant and exchange stiffness. Therefore the magnetization reversal of thin film systems consisting of two or more ferromagnetic layers strongly depends on the exchange coupling strength. The exchange coupling strength in magnetic heterostructure can be varied by the material as well as the thickness of the layers. Figure 1.4 represents the schematic of two types of wall formation in magnetic materials.

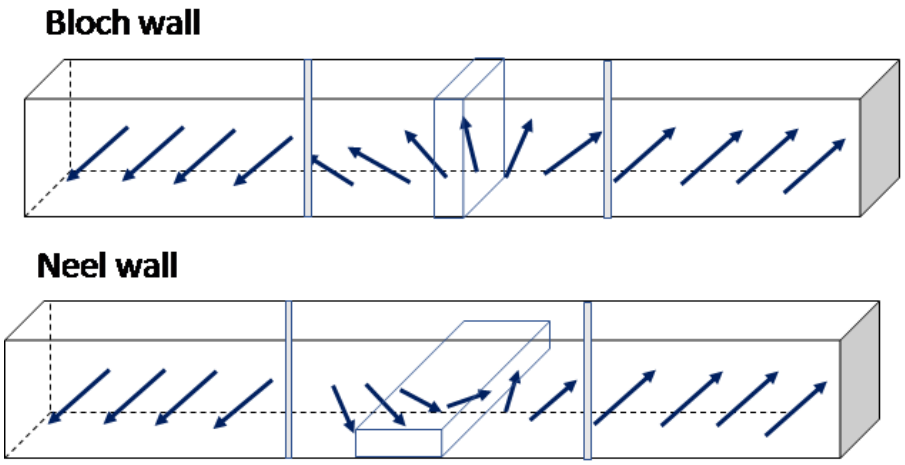

Fig. 1.4: Schematic view of Bloch wall (moments are rotating in the perpendicular plane) and Neel wall (moments are rotating in the same plane).

Recently the existence of 2π-planar domain walls (DWs) has been reported for RE/TM heterostructures [19-22], where the magnetization process of such systems in the form of 2π-DWs is attributed to topologically stable helices. The planer 2π-DWsformation within the layers is believed to be stabilized by the in-plane magnetocrystalline anisotropy and exchange coupling at the interfaces.PNR with polarization analysis measurements showed that antiferromagnetic-coupling at the RE/TM (e.g., Tb/Fe, Gd/Co) interface felicitates the formation of π or 2π planar DWs[20-22].

1.2.4 Exchange Bias effect

In general, exchange bias is a phenomenon induced at the interfaces of the FM and the AFM materials due to unidirectional magnetic anisotropy when a FM/AFM system is cooled through Neels temperature of AFM [23]. The characteristic feature of the EB effect is the shift of the hysteresis loop from $H = 0$ after field cooling in a high positive saturation field (Fig. 1.5). This bias (E_B) is usually negative (shift of hysteresis loop towards negative field axis on cooling the sample in the positive applied field), but can also be positive (shift of hysteresis loop towards positive field axis on cooling the sample in the negative applied field). Meiklejohn and Bean have first discovered this exchange Bias in 1956 while studying Co particles embedded in their native antiferromagnetic oxide (CoO) [23]. Since then it has been discovered in different systems like nanomaterials [24], thin films [25], FM film on AFM single crystal [26], and soft/ hard magnetic interfaces [27], etc. Hemstead et al.,[28] later showed that this novel phenomenon could be used to bias the sensors to store the information in the computer hard disk drives.

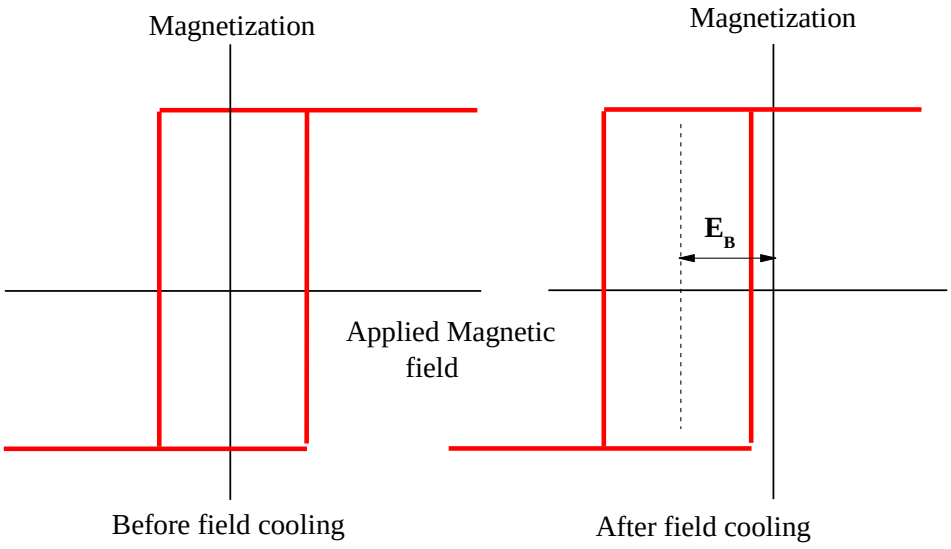

Fig. 1.5: Schematic of hysteresis loop shift after the field cooling.

The EB effect in the thin film systems has been studied in the *M*(*H*) measurements in different forms e.g. shift of the field-cooled (FC) hysteresis loop along the magnetic field axis, an enhancement of the coercivity of magnetization measurements in FC condition as compared to that measured under zero field-cooled (ZFC) condition [29], asymmetrical hysteresis [30] modified magnetization reversal mechanisms [31] and the training effect[32]. The training effect is a measure of the shift in the hysteresis curve in acyclic hysteresis loop measurement and a decrease in the exchange bias field is observed on an increase in the number of cycles. The EB is an interface phenomenon and microscopically it depends on system based details such as structural and magnetic interface roughness/defects, interface magnetization, anisotropy, film thickness, intermixing, alloy formation at the interface, etc., which are a few competing factors to influence the EB of the system. To understand the origin of the EB effect, a large number of theoretical models are proposed, however almost all the theories put forward some assumptions especially for interface magnetization.

Since we also observed the EB effect in both the systems (Gd/Co multilayer and Fe-Cu-Pt heterostructures) studied in this thesis, we will give a brief introduction of the exchange

bias effect observed in these types of systems. The EB effect in Gd/Co system resulted due to a helical magnetic structure with AFM exchange interaction at interfaces, whereas the annealing-driven EB effect in the Fe-Pt-Cu systems occurred as a result of exchange interaction in hard/soft magnetic phases.

Exchange bias in soft/hard ferromagnetic phases

Recently, hard/soft magnetic phases [33-38] have attracted much interest in the field of exchange bias due to their resemblance to a conventional AFM/FM layered EB systems. In general, the soft/hard magnetic phase systems show a room temperature exchange bias effect as compared to conventional EB where a field cooling is essentially required. The room temperature exchange bias effect shown by soft/hard magnetic phase systems is primarily due to the competition between exchange coupling at the interface and dipolar energies because of the magnetic state of the hard phase. Under the applied external field, the magnetization of the soft phase reverses first and due to strong interface coupling to hard layer, which induces effective additional field, called as exchange field. Magnetically hard phase provides thermal stability, while the soft phase reduces the reversal field [27]. The exchange bias effects, a measure of the shift in the hysteresis loop at room temperature has been observed for ferrimagnetic-ferrimagnetic [39], FM-FM [40,41], antiferromagnetically coupled FM bilayers [42] and the [Co/Pt] multilayer grown on the soft NiFe film [43]. The shift in the hysteresis loop of a NiFe thin film deposited on top of a Pt/Co multilayer with perpendicular anisotropy was observed without any heating or cooling procedure [43]. Exchange bias is also observed for hard and soft ferromagnetic phase formed on annealing of FePt film [44] and Fe-Pt-Cu trilayer systems [38], where anisotropy of hard phase couple with the magnetization of soft phase to give the EB.

Exchange bias effect in helical magnetic structures

Usually, when FM and AFM bilayer cooled under an external magnetic field, an exchange bias is induced due to strong interface exchange anisotropy. These types of FM-AFM systems can also be manufactured by using RE and TM interfaces. Where strong antiferromagnetic coupling between the RE and TM interfaces induced helical magnetic structure in the form of a planer DW across the interfaces [45, 46]. These domains freeze when cooled under the external field and result in an exchange bias effect. The RE-TM alloys as well as RE/TM ferrimagnetic multilayers e.g. CoNi/Gd [47], Co/$CoGd_2$ [48], and GdFe/TbFe[49] exhibit exchange bias. The existence of π or 2π planer DW with a helical magnetic structure leading to exchange bias effect and double hysteresis loop (DHL) have been reported in Fe/Tb, Fe/Dy based multilayers [50]. The exchange bias field is believed to depend on the energy required to form the π or 2π DWs in the soft magnetic layer (TM) and anisotropy of the RE layer. In these RE/TM heterostructures, it is also proposed that the layer having larger magnetization decides the bias direction, which strongly depends on interface interaction and thus the EB (positive or negative) effect can be selectively modified by choosing a different combination of RE/TM heterostructures.

1.3 Annealing driven interdiffusion and alloying at interfaces in thin films

Interdiffusion plays a crucial role in thin films and in many engineering phenomena. It decides the kinetics of microstructural changes in thin film systems and controls the properties of thin film heterostructures at higher temperatures. In addition, interdiffusion is a driving force for nucleation of new phases, recrystallization, grain growth, segregation, and phase transformations at interfaces which can have a wide range of usage in technology. The

problem of interdiffusion and reactions at interfaces in thin films received great attention when researchers found new alloy phases, not seen in bulk, at the interface of thin films used for integrated circuits [51, 52]. Annealing-induced interdiffusion and formation of crystalline alloy phases in crystalline thin films and multilayers have been studied in a large number of systems [53-56]. Annealing of heterostructures, especially metal-metal heterostructures, also provides an excellent route to produce alloy phases at interfaces, at much lower temperatures compared to their melting temperatures. Diffusion in the solid state was first analyzed quantitatively by Fick [57]

1.3.1 Fick's laws of diffusion

Consider the flux of diffusing particles in one dimension (x-direction) as shown in Fig. 1.6. Diffusion of atoms (*M*) through a solid (*N*) can be described by Fick's law, in which the diffusion flux (*J*) of the atoms is dependent on the gradient of the concentration of the atoms (*C*). This can be written as Fick's first law:

$$J = -D\nabla C \qquad (1.5)$$

where *D* is the diffusion coefficient. The *D* is dependent on material properties of element *M* and *N* as well as on the temperature and the concentration gradients of the elements.

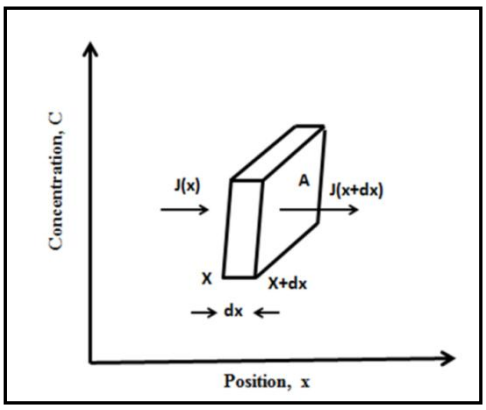

Fig. 1.6: Flux across area 'A' due to particle flux J(x)

In addition diffusion coefficient in Fick's law is temperature dependent, as the mobility of atoms (elements) is higher at higher temperatures. For thin film geometry the solution will be:

$$C(x,t) = \frac{N}{\sqrt{\pi Dt}} e^{-x^2/4Dt} \qquad (1.6)$$

The quantity $2\sqrt{Dt}$ is a characteristic *diffusion length* in two-dimensional and can be termed as L_d. The temperature dependence of the diffusion coefficient (constant)is usually described by the Arrhenius equation, which is given by:

$$D = D_0 \exp(-\frac{E_a}{k_B T}) \qquad (1.7)$$

where D_0 is the pre-exponential factor, E_a is the activation energy for diffusion, k_B is the Boltzmann constant, and T is the temperature in Kelvin. By using the Arrhenius equation, we can calculate the activation energy, *'E_a'* for diffusion constants with temperature.

1.3.2 Estimation of diffusion constant and activation energy

Specular x-ray reflectivity (XRR) and polarized neutron reflectivity (PNR) [13, 14, 53-55, 58] for a compositionally modulated multilayer have been used extensively for accurate measurement of interdiffusion in nm length scale at the interfaces [59-63]. The technique consists of monitoring the intensity (reflectivity) of the Bragg peaks of a multilayer system, due to the repetition of the bilayer periodicity in the multilayer, as a function of annealing temperature and time. On annealing, the multilayer at an elevated temperature, diffusion of atoms takes place across the interfaces, which may lead to the formation of alloy layers at the interfaces. This modification at interfaces reduces the intensity of the Bragg peaks in the reflectivity pattern as a result of a reduction in contrast at interfaces.

The specular XRR pattern for a multilayer system, where there is bilayer periodicity, is shown in the inset of Fig 1.7 (a). Reflectivity pattern shows the Bragg peak due to bilayer periodicity and on annealing, the multilayer with a bilayer period of '*d'* [= d_1+d_2, the thickness of two layers] at different temperatures and for different times results in a decay of the reflectivity of Bragg peaks. This decay is related to the diffusion coefficient (*D*) and the intensities of reflected beams [*R* (*Q*)] and *D* at the Bragg peak positions before and after annealing the multilayer are related by following expression [64]:

$$R_n(Q,t) = R_n(Q,0)\exp\left(-\frac{8n^2\pi^2 D(T)}{d^2}t\right) \qquad (1.8)$$

where *n* is the order of Bragg peak and $R_n(Q, 0)$ and $R_n(Q, t)$ are the corresponding reflected intensity before and after annealing the ML at a temperature of *T* for a time *t*. The variation of the Bragg-peak reflectivity $R_n(T)$ and the period $d(T)$ allows one to obtain the diffusion constant *D* for an annealing temperature of *T*. The diffusivity estimated using this technique is a very low diffusivity in a short temperature range and over a short spatial length (nm length in multilayers). The average diffusion length L_d is related to the diffusivity *D(T)* in the direction normal to the multilayer (two-dimensional diffusion) through the relation: $L_d = \sqrt{2D(T)t}$.

The above equation is equivalent to the 1D solution of Fick's law in Q-space. From the temperature dependence of the diffusivity, activation energy E_a can be extracted assuming Arrhenius's behavior as given in equation (1.7). The ln(*D*) vs 1/*T* plots are in general a linear function in the entire temperature interval as shown in Fig. 1.7 (b) for the FePt/Cu system. The linearity implies that there is only one activation energy. The slope of the curve gives the value of E_a ~1.1 eV.

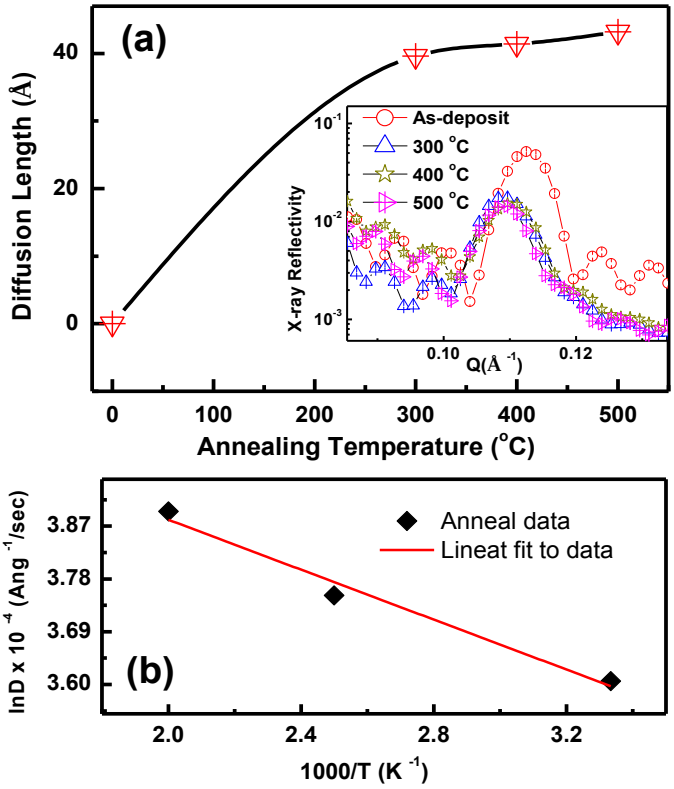

Fig. 1.7: (a) variation of diffusion lengths with the annealing temperature in a FePt/Cu multilayer. Annealing temperature 0^{o} in (a) belongs to as-deposited state. (b) Arrhenius plot for activation energy calculation.

1.3.3 Estimation of the composition of alloy layer using reflectivity techniques

The specular XRR and PNR [14,58] provide the electron scattering length density (ESLD, ρ_x) and nuclear scattering length density (NSLD, ρ_n), respectively for each layer in the multilayer consisting of layers of elements *A* and *B*. Upon annealing the multilayer if an alloy (A_xB_{1-x}) is formed at the interfaces, we can precisely estimate the stoichiometry of the alloy using these reflectivity measurements even if the alloy is in the amorphous phase. The ESLD and NSLD value obtained from XRR and PNR for an alloy layer at the interface formed due to interdiffusion is given by:

$$\rho_x = N_A r_0 Z_A + N_B r_0 Z_B \quad (1.9)$$

$$\rho_n = N_A b_{coh}^A + N_B b_{coh}^B \quad (1.10)$$

where *'N_A'* and *'N_B'* are the number density of the components in the alloy layer, *'b'* and *'Z'* are the coherent nuclear scattering lengths and atomic numbers of the components (A and B) respectively. *'r_0'* is the classical electron radius [14, 58]. On the left-hand side of above Eqns. are ρ_x and ρ_n as obtained from the fits to XRR and PNR data. Using these values one can solve these equations for 'N_A' and 'N_B', which provide the atomic ratio, and hence composition of alloy can be estimated.

1.4 Ferromagnetic multilayers

The interface-driven phenomenon at the magnetic/magnetic and magnetic/non-magnetic heterostructures, especially RE/TM (Gd/Co) and Fe-Pt-Cu heterostructures, which show strong interface dependent magnetic properties, have been studied in this thesis. These systems exhibit technologically oriented properties like EB, planer domain wall, AFM interaction, and antisymmetric magnetoresistance that are highly dependent on interface structure. In this section, we will discuss the detailed interface dependent properties of these two systems and related literature.

1.4.1 Gd/Co multilayers

Gadolinium (Gd) is the only room temperature ferromagnet among the RE materials with a Curie temperature of 293 K. Its permanent magnetic moment amounts to 7.98 μB, which exceeds the value of Co by a factor of ~4.5. The magnetic moment of Gd is completely governed by the spin moment μ_s of the 4f-shell. Whereas Co is a TM ferromagnet with a T_c of ~ 1400 K. In RE/TM (RE like Gd, Tb, Dy, etc. and TM like Fe, Co, Ni, etc.) hybrid systems,

the magnetic behavior is ruled by the underlying strong AF interaction at the interfaces. The AF coupling has accepted considerable interest in RE/TM heterostructures, where a wide variety of magnetic ground states are observed as a result of the competition between exchange and Zeeman energies. Hence these systems behave like a giant or artificial ferrimagnetic system that exhibits compensation at a particular temperature at which total moments of RE-TM heterostructures tend to zero [65-68]. RE-TM alloy multilayer systems with exchange coupling at interfaces have also been studied as an exchange spring magnets, especially for exhibiting the interfacial domain walls (iDWs) in the magnetization reversal process [69].

Theoretical studies on Fe/Gd multilayers performed by Camley *et al*., [66-67] have predicted the existence of different magnetic phases e.g. low-temperature Gd-aligned (Gd moment aligned along the applied field and opposite to Fe moment), high-temperature Fe-aligned (Fe moment aligned along the applied field but Gd moment opposite to Fe moment), and twisted phase (in-plane canting of Fe and Gd moment) around compensating temperature. A comparison of the temperature dependence of the magnetization of samples with the theoretical calculations was first reported by Motokawa et al.,[70]. Later the magnetic behaviour of these systems was successfully studied by the mean-field approach [71-73]. The proximity effect at the interfaces of Gd and TM layers have also shown an enhancement of Gd magnetization at room temperature were observed.

A typical temperature dependent magnetization curve for RE/TM (Gd/Co multilayer) multilayer showing a compensation temperature as well as representation of different magnetic phases (e.g. Gd-aligned, Co-aligned, etc.,) is depicted in Fig. 1.8. The $M(T)$ data are measured for the Gd/Co multilayer in an applied field of +500 Oe under field cooled (FC) condition. The alignment of moments of the Gd and Co layer with respect to the applied field

(*H*) is shown in the figure. The multilayer show minimum magnetization near a temperature of ~ 125 K, suggesting a compensation temperature (T_{comp}) of 125 K.

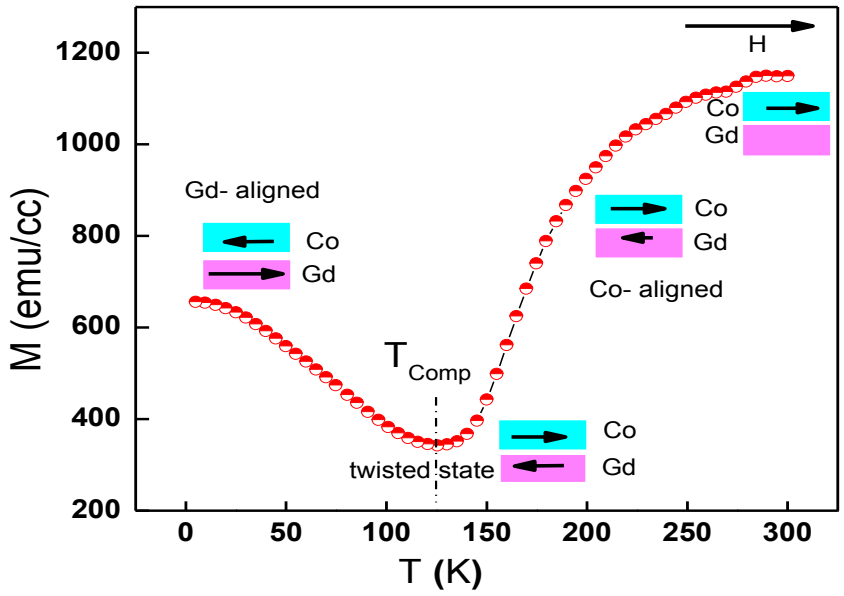

Fig. 1.8: Temperature dependent magnetization in Gd/Co multilayer.

Recently, the studies of the magnetization dynamics in RE/TM multilayers have attracted great attention as these materials are considered possible for the realization of ultrafast magnetic switching [74]. These materials have also been considered a potential candidate for realizing devices with higher speed and density. Magnetic helices, which are manifested as 2π planar DWs, are also believed to be important for realization in magnetic device application. To explore these interface-driven properties of RE/TM systems it is difficult to measure the exact magnetic structures of the individual layers using macroscopic measurement techniques such as SQUID magnetometry or magnetoresistance measurements. Recently Paul et. al,[20, 21, 50], using the PNR technique, have shown that an AF-coupling at RE/TM interfaces assists in the formation of planar DWs which remain frozen upon cooling. The study also suggested that planner DWs in RE-TM multilayers lead to the EB effect and

double hysteresis loop (DHL), which are highly dependent on the temperature and magnetic field.

Gd/Co multilayers and alloys as an artificial ferrimagnet have been studied earlier [65, 73]. However, a high interface reaction was observed in these systems which produce a significant Co alloying throughout the Gd layer. Magnetization and magnetoresistance measurements from Gd/Co multilayers suggested antiferromagnetic interface coupling and a thickness-dependent compensation temperature for Gd/Co multilayers [65]. In this thesis, we have investigated high-quality Gd/Co multilayers with different interface properties, where the temperature and the magnetic field dependent PNR measurements from these multilayers suggested the existence of magnetic helices with π and 2π planer DWs. A correlation between the depth-dependent magnetic configurations, macroscopic magnetization, and magneto-transport properties of Gd/Co multilayers grown under different conditions are discussed in chapters 3 and 4.

1.4.2 Fe-Pt-Cu heterostructures

The FePt alloy thin films have been studied extensively for its technological application; however, this alloy shows many ferromagnetic phases. The disordered face-centered cubic (*fcc*) (or A1-phase) phase, which is also ferromagnetic is the most common phase observed for a room temperature deposited FePt thin film. The $L1_0$ chemically ordered phase of FePt alloy with face-centered tetragonal (*fct*) crystal structure is the equilibrium phase under ambient conditions that show the wide application in magnetic storage recording devices due to high magnetic anisotropy. However, a high temperature (ordering temperature) treatment (either growing the alloy film at a higher temperature or a post-annealing)is required to produce the *fct* ordered phase from the *fcc* disorder phase of FePt alloy film because of the higher energy barrier for atomic diffusion for ordered phase. Annealing of as-

grown disordered *fcc* FePt films as well as growing FePt films at higher substrate temperature changes the properties of the alloy film. Several investigations were performed to decrease the ordering temperature by adding a third element (Ag, Au, Cu, N etc.) to the FePt system. The study shows that the addition of Cu in FePt is completely miscible and it is expected that Cu replaces Fe in the FePt alloy[75].

The Cu addition in FePt alloy results in the formation of a ternary alloy of $FePt_{(1-x)}Cu_x$ (FePtCu) and influences the overall magnetic properties of the alloy. The addition of Cu in the FePt alloy layer can be achieved by introducing (a) a Cu buffer layer, (b) a capping Cu layer, and (c) an intermediate layer. Thus a systematic depth-dependent study is required to study the evolution of structure and magnetic properties of the alloy layer formed on annealing. We have studied the kinetic growth of the FePtCu ternary alloy on annealing of (i) Fe-Cu-Pt trilayers with Cu as a capping layer (Fe/Pt/Cu heterostructure) and intermediate layer (Fe/Cu/Pt heterostructure) and (ii) FePt/Cu multilayers with different Cu thicknesses grown on Si substrates. The evolution of the structure and magnetic properties of these systems on annealing at different temperatures and times are discussed in chapter 5 (trilayer systems) and chapter 6 (multilayer systems).

Cu layer thickness decides the atomic % of Cu in the composition of the ternary alloy and different thickness of Cu layers are grown to study the structure and magnetic properties of ternary alloy with varying Cu contents. Therefore an understanding of interdiffusion of Cu, Fe and Pt elements across interfaces in FePt/Cu systems through solid-state reaction on annealing the FePt/Cu system and its dependent on the formation of different phases of a ternary alloy is very important, as annealing at different temperatures will change the exchange interactions between different possible configuration at interfaces viz Fe-Cu-Fe, Fe-Pt-Fe, Cu-Pt, Fe-Pt, which results into different magnetic properties.

Brombacher et al.,[76] have studied the formation of ternary $[Fe_{51}Pt_{49}]_{100-x}Cu_x$ alloy phases with a Cu content of 0-21% on rapid annealing of $Fe_{51}Pt_{49}$/Cu bilayers of different thicknesses and observed modification in magnetic properties as a function of both annealing temperature (500 to 800 ^oC) and Cu content. The study suggested that the addition of Cu systematically reduced the perpendicular magnetic anisotropy and enhancement of both the *A*1-$L1_0$ phase transformation and the development of the (001) texture was also observed. The addition of a large amount of Cu (60% concentration) into FePt film on annealing the FePt/Cu multilayer has shown a room temperature SP behavior [77] for a ternary compound, which may be useful in biomedical applications.

Chapter 2

Experimental techniques

2.1 Introduction

In this chapter, we have described the experimental techniques employed for the preparation of thin film and multilayer systems as well as the techniques used for structural and magnetic characterization. We have used the DC magnetron sputtering technique for growing all the thin film/multilayer samples (Gd/Co multilayers, Fe-Cu-Pt heterostructures, and FePt/Cu multilayers) studied here. These films have been prepared at UGC-DAE-CSR, Indore, India, in collaboration with Dr. M. Gupta. The sputtering technique has specific advantages over other deposition techniques and this will also be addressed briefly in this chapter. The structural properties of the thin film systems have been probed using grazing incidence x-ray diffraction (GIXRD), and XRD in the Bragg-Brentano θ-2θ geometry. The depth dependent layer structures were investigated using x-ray reflectivity (XRR) and secondary ion mass spectrometry (SIMS) techniques. The macroscopic magnetic and magnetotransport characterizations were performed using the superconducting quantum interference device (SQUID) and four-probe techniques. The depth dependent magnetization and magnetic structure studies were performed using polarized neutron reflectivity (PNR) technique in both specular and off-specular mode. The magnetization depth profiles of the thin film systems were investigated by PNR without spins polarization analysis technique using the PNR instrument at Dhruva, BARC [78]. The depth dependent magnetic structure and in-plane magnetic inhomogeneities as a function of temperature and magnetic field for Gd/Co multilayers (discussed in chapter 4) were investigated using PNR with spin

polarization analysis measurements using OFFSPEC reflectometer at the ISIS neutron and muon source, RAL, UK [79].

2.2 Sample preparation

Different methods can be employed for the deposition of thin films and multilayers, which depend on the availability and advantages of one technique over another [80, 81]. Often several parameters, which strongly influence the growth of the thin films such as, type of deposition method, deposition rates, partial pressure variation, substrate temperature, etc., are optimized before deposition of thin films. Optimization of these parameters can provide the control over the properties of the thin films, essential for modern technological applications i.e., thermally stability, adhesion, stoichiometry controllable, low porosity, etc., [82]. Hence choosing the right deposition technique for thin film growth is crucial for controlling the properties of the system.

2.2.1 DC magnetron sputtering

In general, sputtering is an ejection of atoms by bombarding a solid target using highly energetic ions via energy transfer [80,81]. When positive ions (inert gaseous) are accelerated with a high velocity and bombarded on a target material, the ejection of surface atoms occurs due to the momentum transfer, which is usually known as sputtering (cathode sputtering). The total yield of the sputtering process is defined by the ratio of the number of ejected atoms and incident projectiles (ions). The sputtering yield depends on various parameters e.g., incident ion energy, surface binding energy of target atom, material composition, the distance between target material & substrate, and variation of the sputtering power, etc., thus it is widely varied. Among the inert gases, Ar is widely used as sputtering gas because of its low

ionization value and availability. The deposition technique requires a low-pressure atmosphere.

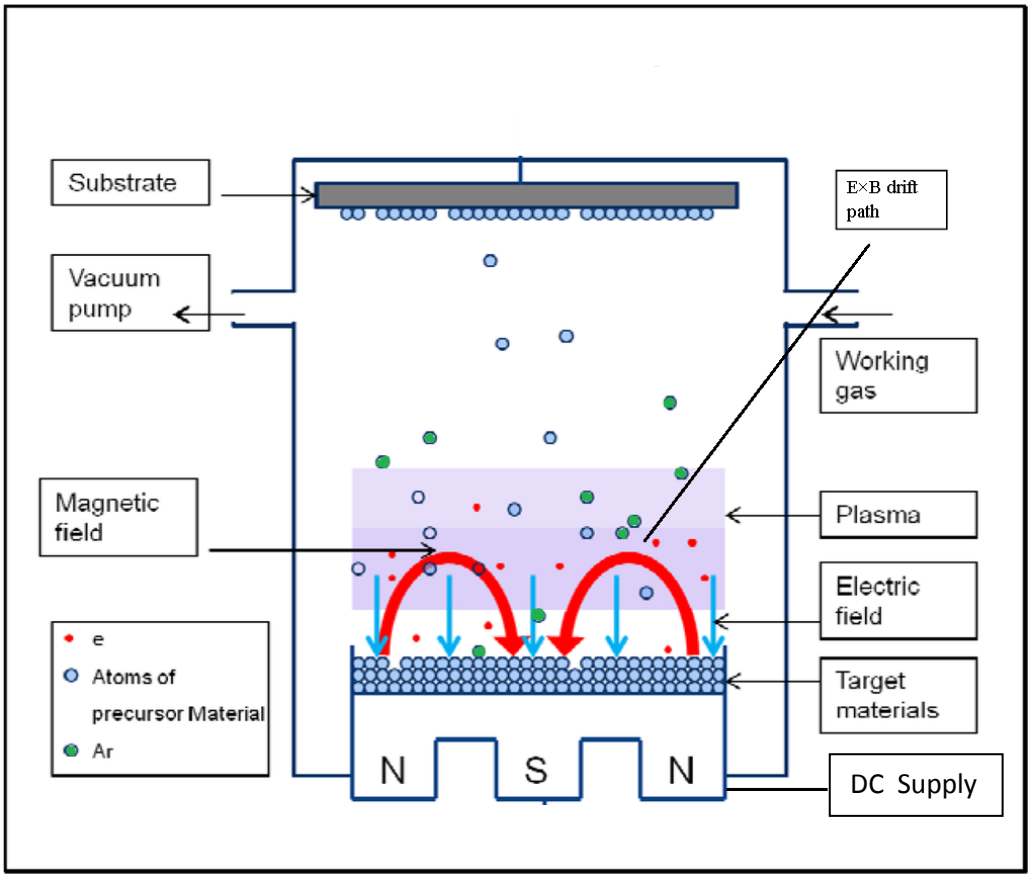

Fig. 2.1: Schematic and process of magnetron sputtering.

Figure 2.1 shows the schematic of a conventional sputtering process. Usually, the target is connected to a negative voltage (cathode) and the substrate is connected with the positive voltage (anode), which is maintained at ground potential with respect to the target during the sputtering. The inert gas plasma is generated by sufficient breakdown of gas with the voltage U given as:

$$U = \frac{A.P.L}{ln(PL)+B} \qquad (2.1)$$

where P is the sputtering gas pressure and L is the distance between substrate and target and A and B are constants, which are characteristic of the target material. In the sputtering process, the ejected atoms have the energy of a few tens of eV. Figure 2.2 shows the photograph of the DC magnetron sputtering system, used for growing the thin film samples. The DC magnetron sputtering system is supplied by AJA international and is equipped with a fully automated control system using software commanding. This system is equipped with six magnetron targets assembly which can use targets of different sizes (1 to 3-inch diameters). For the deposition of the Gd-Co and the Fe-Pt-Cu based systems, we have fixed the distance between the substrate and target ~ 12 cm, and the substrate was rotated at a speed of 60 rpm. We have grown all these thin films at room temperature. The sputtering parameters for the sputtering system are given in Table 2.1.

Fig. 2.2: Photograph of DC magnetron sputtering

Table 2.1: Salient features of the DC magnetron sputtering system

Parameter	**Range**
Base vacuum	1×10^{-5} Pa
No. of targets	6 (3-3", 2-2", 1-1")
Co-sputtering & reactive sputtering	Yes
Substrate heating	800 ºC
Background gas	Ar, N_2, O_2 with automated control

Compared to the other evaporation techniques, sputtering gives (a) better adhesion of atoms on the substrate, (b) high uniformity and density of deposited film, (c) deposition can be done over large surface area (with optimization of substrate rotation). In addition, by proper target cooling process during sputtering, one can deposit the high melting point elements. Using sputtering one can deposit alloy layers (like FePt alloy from FePt target) from a composite material target. Hence with a better understanding of different parameters and getting control over the quality of the deposited films, sputtering becomes one of the versatile techniques for preparing high-quality thin films and multilayers.

2.2.2 Interface modification

As described in chapter1, interfaces play an important role in deciding the properties of thin film systems. Interface morphology can be modified by varying different deposition conditions during the growth of thin films. We have also used this method to vary the interface structure of the thin films studied in this thesis and investigated the interface dependent properties. We varied the sputtering gas pressure to modify the deposition rate and

obtained different interface properties by growing multilayers of the same bilayer thickness. The detail of the parameters will be discussed in the chapter where we will discuss the system.

Annealing of the multilayers as a function of time and temperature can also modify interface structure. We have employed different annealing process 1) isochronal annealing: multilayers were annealed as a function of temperature for a fixed time, and 2) isothermal annealing: multilayers were annealed at a fixed temperature for different times. The evolution of the structure and magnetic properties of thin films induced by annealing have been investigated in this thesis.

2.3 Structural characterization techniques

2.3.1 X-ray diffraction (XRD) and grazing incidence XRD (GIXRD)

X-ray diffraction (XRD) is one of the powerful non-destructive techniques used for the determination of the crystalline structure of materials. The wavelength of the x-ray is typically closer to interatomic spacing in a material, which allows determining the exact crystal structure. Fig. 2.3 shows the schematic for the XRD. The periodic arrangement of atoms inside a crystalline material elastically scattered the incident x-ray.

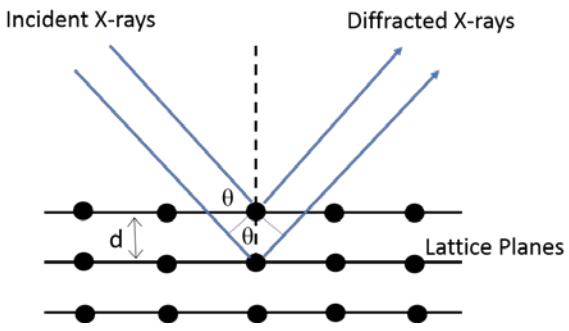

Fig. 2.3: Schematic of XRD.

The reflected x-rays interfere constructively when the Bragg's condition [83]: $2\,d\,sin\theta = n\lambda$, is satisfied, where λ, is the wavelength of the incident beam, d is the distance between adjacent atomic planes, and n is an integer giving the order of interference. XRD pattern is measured by the intensity of the reflected x-rays as a function of the angle (2θ) between the reflected and the incident beam.

On the other hand, for surface and interface crystal structure determination, GIXRD is widely used, which uses small incidence angles (α_i in Fig. 2.4) for highly collimated an x-ray beam. It is a surface selective technique and depth dependent crystal structure can be obtained by varying angle of incidence. Also one can eliminate the substrate intensity contribution by choosing the proper angle of incidence in GIXRD geometry. Due to the depth selectivity of this technique, only surface structure contributes to the Bragg reflections and therefore for thin film systems, GIXRD can be done for a very low scattering volume.

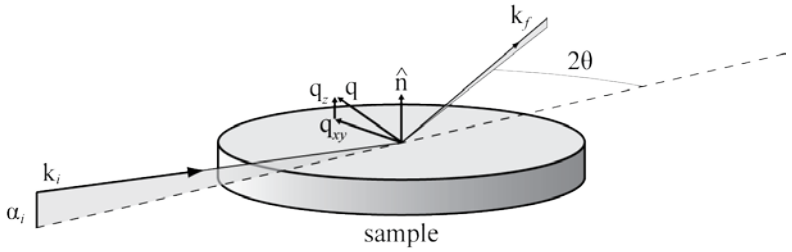

Fig. 2.4: Schematic of the GIXRD geometry with the angle of incidence near-critical angle.

Using XRD and GIXRD data for thin films, we have also estimated the crystallite size of elements (Gd, Co, etc.) in different layers using the Scherrer formula [83, 84]:

$$t = \frac{0.9\,\lambda}{B\,cos\theta} \qquad (2.2)$$

This formula relates the crystallite size t to the angular broadening B (in radians) at the Bragg reflection θ and x-ray wavelength λ.

2.3.2 Secondary ion mass spectrometry (SIMS)

SIMS [85] involves bombarding the surface of a sample with a beam of primary ions, thus emitting secondary ions and these ions are measured with a mass spectrometer to determine either the elemental or isotopic composition of the sample. SIMS can be operated in different modes depending upon the properties that one is looking for. The static SIMS mode is used for surface atomic monolayer profiling, which uses the very low primary beam ion intensity in pulse mode [Fig. 2.5(a)]. In contrast to static mode, the dynamic SIMS mode provides depth profiling using a high-intensity primary ion beam in a continuous mode [Fig. 2.5(b)]. By collecting the spectra during the sputtering in-depth distribution of elements and small clusters (e.g. oxides) can be monitored. We have used such depth profiling for our study. A primary ion beam of O^-, O^{2+}, Ar+, Cs^+, and Ga^+, are often used with energies between 1 and 30 keV. These primary ions are implanted or mixed with sample atoms to the depths of 1 to 10 nm. The time scale of collision cascade order of ~ 10^{-12}-10^{-13} sec.

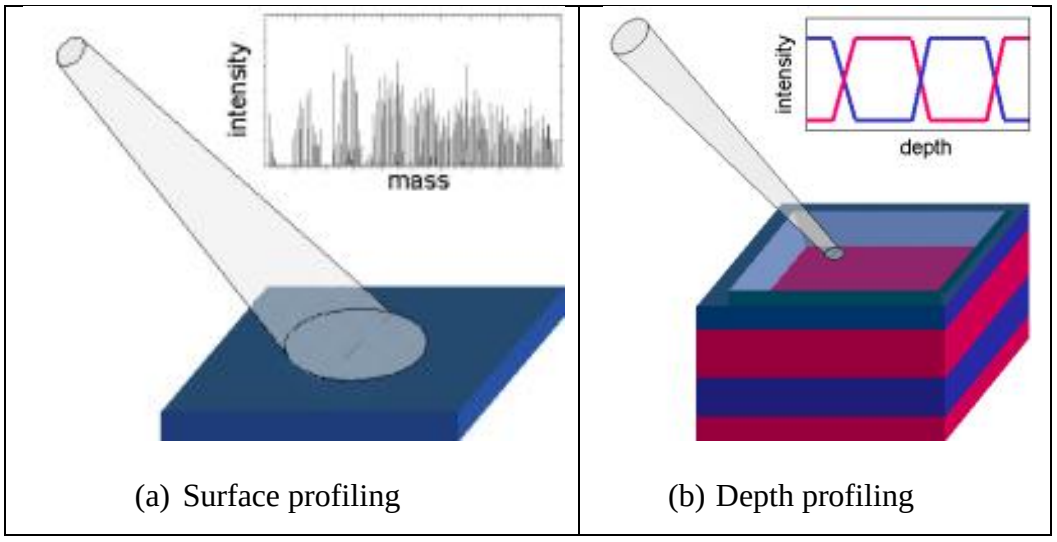

(a) Surface profiling (b) Depth profiling

Fig. 2.5: Schematic view of (a) surface profiling (b) depth profiling of materials using SIMS.

Elemental depth distribution analysis was carried out using Cameca IMS-7f SIMS instrument equipped with both oxygen duoplasmatron and cesium thermal ion source. Cs^+ primary ion beam with a beam current of 10±1 nA and impact energy of 5keV was raster scanned over an area of 250 µm × 250 µm on the sample surface. Pressure in the analysis chamber was maintained ~5×10^{-7} Pa and mass resolution (m/dm) of 400 was selected in all the analyses. All the depth profile analysis was carried out using Cs^+ secondary ion detection mode for minimizing the matrix effects that arise due to the presence of different composite layers of elements in the multilayer samples. Figure 2.6 shows the photograph of the Cameca IMS 7f SIMS measurements setup.

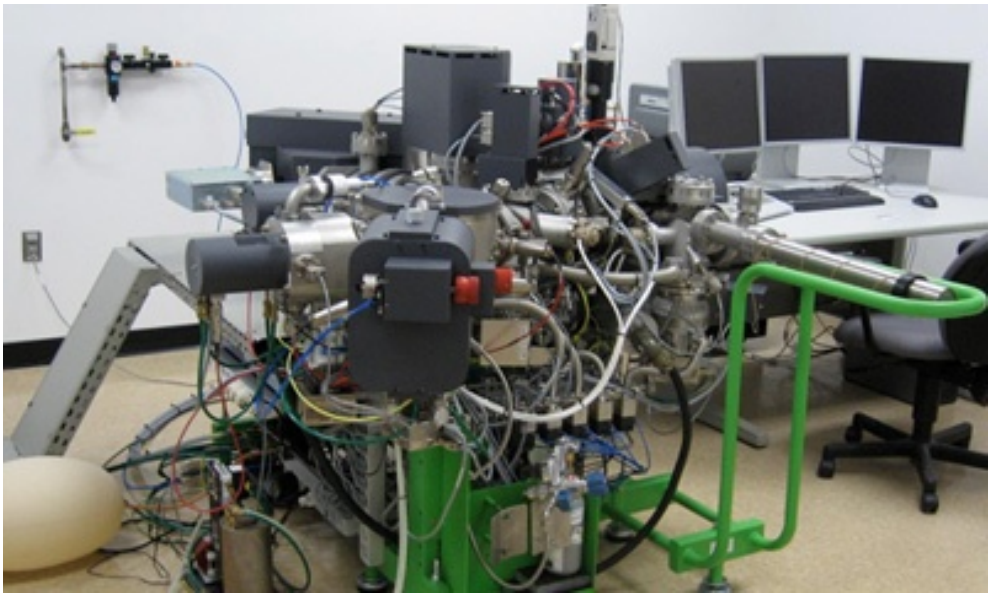

Fig. 2.6: Photograph of SIMS Cameca IMS 7f

2.3.3 X-ray reflectivity (XRR)

The intensity of the x-ray beam reflected at a glancing angle from a flat material surface depends upon the nature of the surface as well as the composition of the underlying matter.

Figure 2.7 shows the two types of possible reflections from a rough surface: (a) Specular reflection, when the angle of reflection (θ_i) is equal to the angle of incidence (θ_f) [($\theta_i = \theta_f$)], and (b) Off-specular reflection, where the above equality is not maintained ($\theta_i \neq \theta_f$). Specifically, specular reflectivity can be analyzed to reconstruct laterally averaged compositional depth profile along the normal to the surface. Specular x-ray reflectivity (XRR) determines the structural parameters of thin films viz. individual layer thickness, interface roughness, and the electron scattering length density (a measure to the density of the material) of the layers.

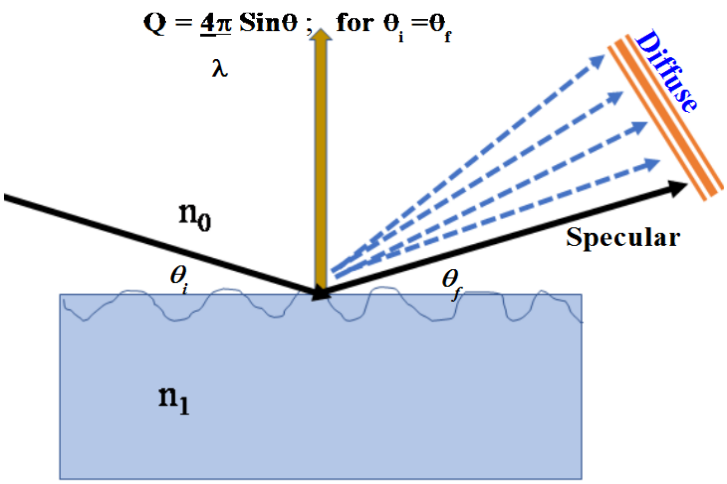

Fig. 2.7: Geometry of specular and off-specular (diffuse) reflectivity.

Specular reflectivity from a sample is measured as a function of the wave vector transfer Q [$Q = (4\pi/\lambda)\sin\theta$], where θ is the incident angle on the film and λ is the wavelength of the probe]. The reflectivity depends on the contrast in the refractive index between layers of a film. A generic expression for the refractive index for x-rays [86] can be given by

$$n = 1 - (\alpha - i\beta) \qquad (2.3)$$

with $\alpha = \frac{\lambda^2 r_0}{2\pi}\Sigma N_i(Z_i + f_i^{'})$ and $\beta = \frac{\lambda^2 r_0}{2\pi}\Sigma N_i f_i^{''}$ (2.4)

where Z_i is the atomic number of the i^{th} species, r_0 is the classical electron radius (= 2.818 fm), $f_i^{'}$ is the real anomalous dispersion factor, and $f_i^{''}$ is the absorption coefficient of the species for x rays. The electron scattering length density (ESLD), ρ_x for x-rays is given by [86]:

$$\rho_x = \Sigma N_i(Z_i + f_i^{'})r_0 \qquad (2.5)$$

. And thus for non-absorbing medium, the refractive index for x-ray is defined as:

$$n = 1 - \frac{\lambda^2 r_0}{2\pi}\sum_i N_i(Z_i + f_i) \qquad (2.6)$$

The critical angle of incidence below which the XRR is unity and for x-ray it can be given as:

$$\theta_c = \lambda\sqrt{\frac{r_0}{\pi}N_i(Z_i + f_i)} \qquad (2.7)$$

For most of the materials, this critical angle is a few arc minutes per Å wavelength. Like in optics one can evaluate the reflectivity for two mediums by *Fresnel* relationships, which gives the amplitude of specular reflection and the transmission coefficient of the beam. Thus *Fresnel* reflectivity (R_f) for an ideally flat surface of refractive index *n*, for a glancing angle θ, is, defined as [86,87]:

$$R_f = \left|\frac{sin\theta - \sqrt{n^2 - cos^2\theta}}{sin\theta + \sqrt{n^2 - cos^2\theta}}\right|^2 \qquad (2.8)$$

From Eqn. 2.8**,** for $cos\theta > n$, the *Fresnel* reflectivity is unity, i.e. for $\theta < \theta_c$ there will be a total external reflection of x-rays. Above the critical angle when $\theta >> \theta_c$ the reflectivity drops off as θ^{-4}. This rapid drop in intensity beyond critical angle makes reflectivity experiment intensity limited at larger angles. Roughness has the effect of reducing the specular reflectivity and this effect is incorporated in reflectivity by introducing a multiplicative exponential factor, as proposed by Nevot and Croce [87] and effective reflectivity is given by

$$R = R_f e^{-4Q^2\sigma^2} \qquad (2.9)$$

where σ and Q are the root-mean-square (*rms*) roughness amplitude and the perpendicular wave vector. This multiplicative "Debye-Waller-like" factor is due to the uncertainty in the location of the interface due to (a) jaggedness at the interface and (b) continuous change in density across the interface. The roughness amplitude σ is a convolution of both these effects.

To generate an x-ray reflectivity pattern theoretically for multilayer samples Parratt's formalism [88] is used extensively, which can also be applied for neutron reflectivity. Fig. 2.8 shows the XRR pattern generated using Parratt's formalism [88] for Co/Cu multilayer of 10 bilayers with a bilayer period of 10 nm (thickness of 5 nm each for Co and Cu, grown on Si substrate). The inset (bottom) depicts the ESLD profile of the multilayer representing periodic ESLD variation in 10 bilayers. Thus using XRR we can get a detailed layer structure of the designed multilayer.

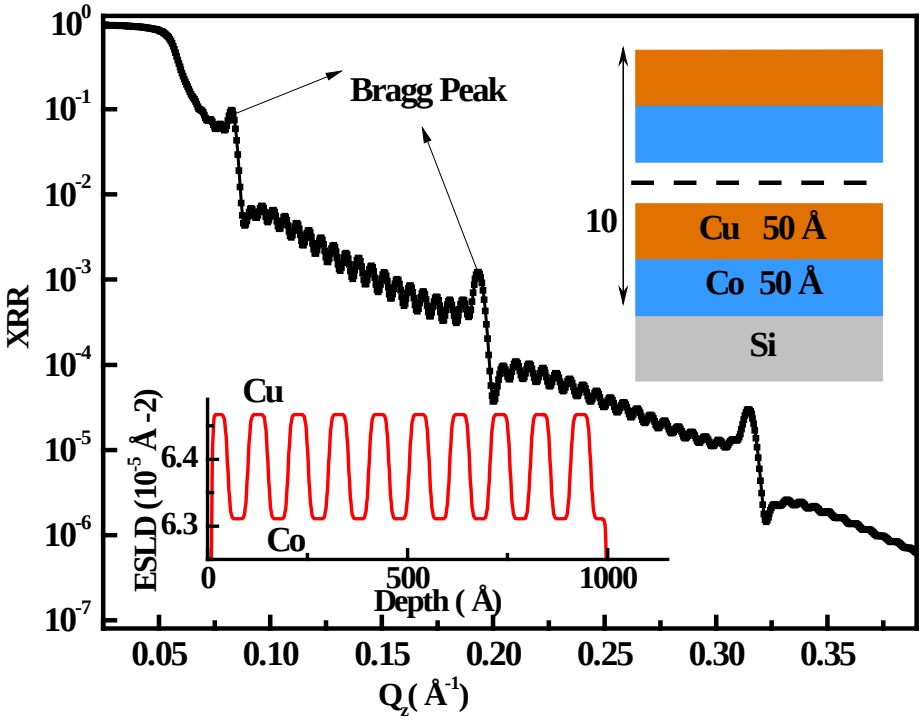

Fig. 2.8: Simulated X-ray reflectivity pattern from Co/Cu multilayer. Inset (bottom) shows the electron scattering length density (ESLD) depth profile for multilayer. The number 10 in the upper inset indicates the number of the bilayer in the Co/Cu multilayer.

2.4 Macroscopic magnetic characterizations

2.4.1 Superconducting quantum interference device (SQUID)

The macroscopic magnetization measurements of thin film samples were carried out using the Quantum designed superconducting quantum interference device (SQUID) magnetometer [89]. SQUID is made of two superconductors separated by a thin insulating layer to form two parallel Josephson junctions [90]. SQUID is a highly sensitive instrument in detecting the lower magnetization (10^{-6} emu) of the material and is widely used for the magnetic characterization of thin film materials. SQUID magnetometer consists of mainly five parts namely 1) a superconducting magnet (NbTi), 2) SQUID detector, 3) sample holding system, 4) temperature control module, and 5) liquid helium (2.25 K). Thus it can go up to low temperatures of 2.25 K. A magnetic field of up to 5 T can be generated by NbTi magnet. The stability of the temperature can be controlled by the cold gas and heating the wire around the sample chamber. The schematic sectional view of a SQUID magnetometer is shown in Fig. 2.9. The ideal SQUID voltage response due to a single dipole moment is given by

$$V(z) = c\,\varphi(z) \qquad (2.10)$$

where c is the instrument calibration factor. By inclusion of constants a and b, representing offset and linear drift, respectively, the SQUID response can be modified as:

$$V^{modified}(z) = a + b\,z + mV(z-z_0) \qquad (2.11)$$

Where z_0 represents the off-centering of the sample. Eqn. 2.11 is fitted to raw data measured by the SQUID magnetometer to the extraction of the magnetic moment. The heater in the isolation transformer is used (switch on) to destroy the prior history information using software that brings superconducting primary and secondary coil to the normal state. During

the measurements, this heater is usually switched off and it is only switched on for charging superconducting magnet to eliminate the induced current in the circuit. A typical voltage response in SQUID measurements is also shown in Fig. 2.9.

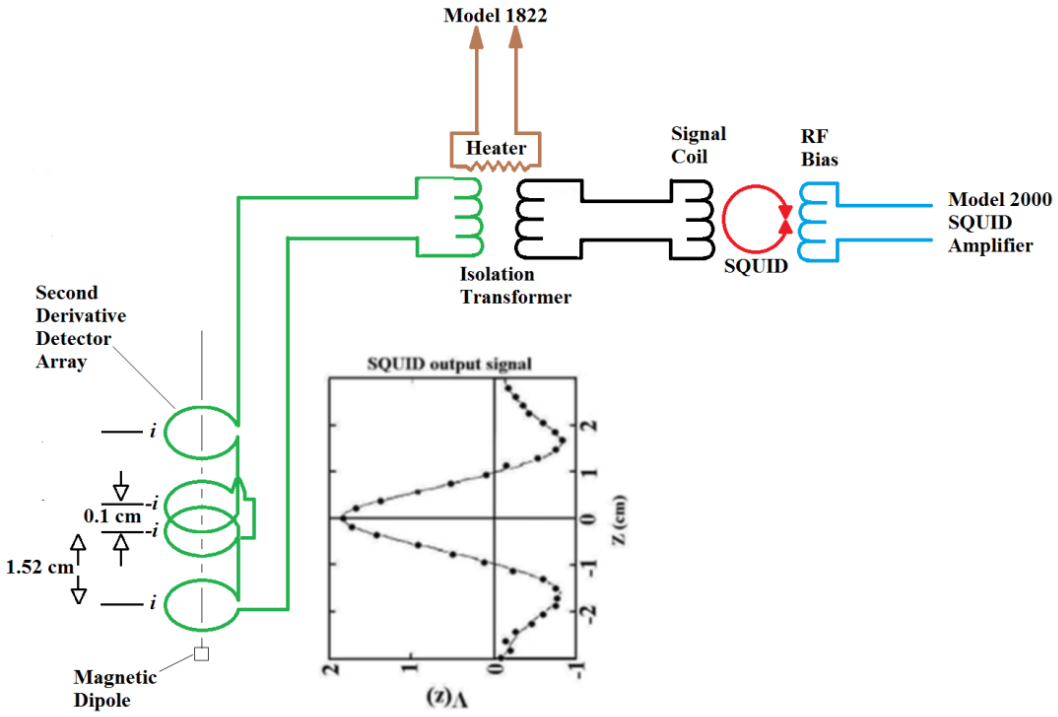

Fig. 2.9: Schematic of SQUID magnetometer measurements.

For all the thin film systems studied in this thesis, we have carried out magnetization measurement as a function of temperature [M (T)] and magnetic field [M (H)]. M (T) data are collected in both zero field cooled (ZFC) and field cooled (FC) mode.

2.4.2 Four probe resistivity measurements

Resistivity is an intrinsic property of the materials and understanding the charge transport mechanism of material is very important in case a magnetic thin film, especially for an application like giant magnetoresistance etc. The resistivity of the thin film systems in the

presence of the magnetic field shows dramatic changes and therefore magnetotransport measurements attracted a lot of interest in recent years for a device application. The two-probe resistivity measurement (Fig. 2.10 (A)) is a conventionally used technique, where the same contacts are used for current and voltage probes. However it imposes an annoying problem of contact resistance, especially for thin film systems. On the other hand, using different contacts for current and voltage, like in the four-probe resistivity measurements, a true resistivity of the film can be measured. We have used the four-probe method to measure magneto-transport data in a classic (linear) configuration as shown in Fig. 2.10 (B).

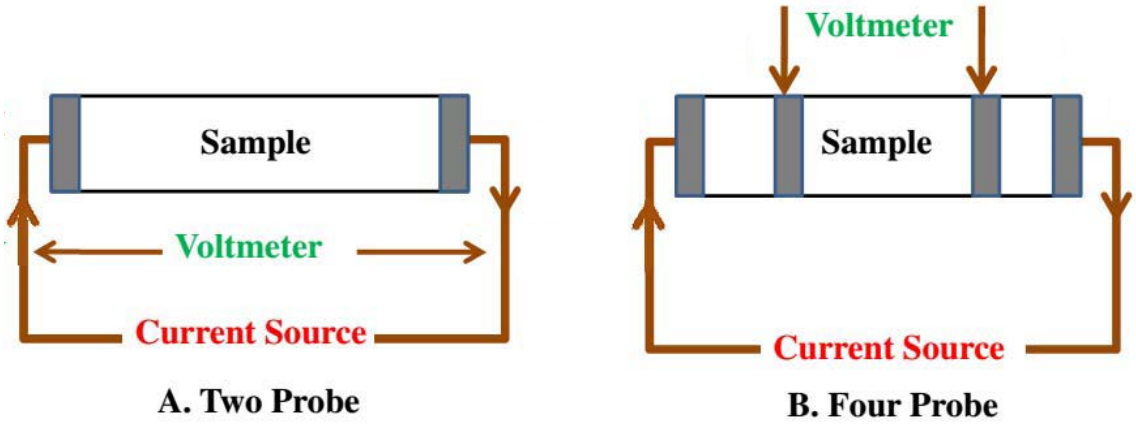

Fig. 2.10: Schematic of a two probe (A) and a four-probe (B) measurement setup.

The outer two probes are used for current flow and the inner two probes are used for voltage measurements from a thin film sample. A magnetic field can be applied in both in-plane and out of the plane direction using an electromagnet. The thermal effect can be eliminated by reversing the current and averaging the measured voltages since the thermal electromotive force does not depend on the current direction. Therefore the resistivity is given by,

$$\rho = \frac{a}{l}\left[\frac{V(+)-V(-)}{2}\right] \qquad (2.12)$$

where a is the area of cross-section perpendicular to the current, l is the voltage contacts separation, and V is the voltage measured. Magnetoresistance (MR) is usually defined as a percentage variation of resistance when a magnetic field is applied and is given by:

$$\%MR = \frac{R(H) - R(0)}{R(0)} \times 100 \quad . \qquad (2.13)$$

2.5 Depth dependent magnetic characterization: polarized neutron reflectivity (PNR)

The general principle of a polarized neutron reflectivity (PNR) experiment is illustrated in Fig. 2.11, in which a polarized neutron beam with polarization ***P*** collinear to the applied field (H) fall onto the magnetic thin film surface at an angle of incidence θ_i. The in-plane magnetization (M) of the film is rotated by an angle α from the applied field. The spin dependent PNR [91-95] is defined by four reflectivities depending on polarization channel, R^{++}, R^{--}, R^{+-}, and R^{-+}, where the first and second superscript denotes the direction of the incoming and reflected neutron polarization as parallel (+) or antiparallel (−) with respect to the external guide field direction. The PNR with no change in the polarization upon reflection is termed as non-spin-flip (NSF) reflectivities (i.e. R^{++}, R^{--}). The two non-spin-flip reflectivities, R^{++} and R^{--}, are related to the magnetization components parallel ($M_{\|}$) to the applied (in-plane magnetization of the sample) field. Whereas PNR with the change in the polarization of reflected beam is termed as spin-flip (SF) reflectivities (i.e. R^{+-}, and R^{-+}) and are related to the magnetization components perpendicular ($M\perp$) to the applied field. Thus employing all spin dependent neutron reflectivity with polarization analysis provides the direction of in-plane magnetization (magnitude of M and angle of rotation α of magnetization with respect to the applied field) along the depth of the heterostructures. For depth dependent

magnetic structure, one measure specular reflectivities ($\theta_i = \theta_f = \theta$). Therefore the resultant momentum transfer (Q) is equivalent to momentum transfer component Q_z normal to the sample surface and is given as $Q = Q_z = \frac{2\pi}{\lambda}\left[\sin(\theta_f) + \sin(\theta_i)\right] = \frac{4\pi}{\lambda}\sin(\theta)$, where λ is the wavelength of the neutron. Off-specular reflectivity ($\theta_i \neq \theta_f$) originates from lateral structures, such as interfacial roughness and magnetic domains, which break the in-plane translational symmetry of the sample and lead to an in-plane momentum transfer $Q_x = \frac{2\pi}{\lambda}\left[\cos(\theta_f) - \cos(\theta_i)\right]$.

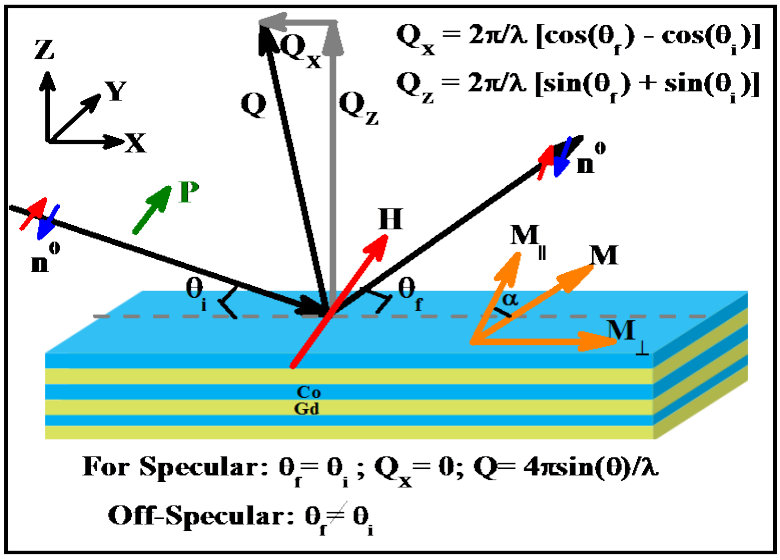

Fig. 2.11: Schematic of PNR experiment with a polarized neutron beam. Neutron beam incident (wave vector k_i) at the surface of the film with an angle of incidence of θ_i and reelected (wave vector k_f) at an angle of reflection of θ_f. The difference between the incoming and outgoing wave vector is defined as momentum transfer vector Q (i.e. $Q = k_i - k_f$). The polarization of neutron, P, is shown in the plane of the sample parallel to the applied field (H). The magnetization M (at an angle α with H) of the thin film is shown with the two in-plane component $M_{\|}$, parallel to the H, and $M_{\perp}$, perpendicular to H.

In this thesis, we discuss the PNR measurements in two cases: (i) when the angle (α = 0) of rotation of magnetization is zero, this case arises when the applied field is sufficient to align the magnetization of the film along the applied field and this measurement will be termed as PNR without polarization analysis. In general, we measure spin up (R^+) and spin down (R^-) reflectivities in this case and the PNR measurement provides the depth dependent magnetization information of the thin film systems. (ii) The α is finite, in this case all four reflectivities (R^{++}, R^{--}, R^{+-}, and R^{-+}) contribute and it will be discussed as PNR with polarization analysis.

2.5.1 Specular PNR without polarization analysis

Propagation of neutrons in any medium can be represented by the Schrödinger equation for the neutron wave function ψ(r) in the medium.

$$-\frac{\hbar^2}{2m_n}\nabla^2\psi(\vec{r})+V(\vec{r})\psi(\vec{r})=E_k\psi(\vec{r}) \qquad (2.14)$$

Where $\hbar$ is Planck's constant divided by 2π, V is the potential seen by the neutron, m_n is the mass of the neutron, $\vec{r}$ is the position vector of the neutron with wave function $\psi(\vec{r})$ and E_k ($= \frac{\hbar^2 k_0^2}{2m_n}$, where, $k_0 = 2\pi/\lambda$, is wave vector of the neutron) its energy. V represents the net effect of the interactions between the neutron and the scatterers in the medium through which it moves. For a good approximation, V is given by [96]

$$V=\frac{2\pi\hbar^2}{m_n}Nb;\;\; N=\frac{dN_A}{M} \qquad (2.15)$$

Where, N, d, N_A, M, b are the atomic number density, atomic density, Avogadro's number, atomic (molecular) weight, and the coherent neutron scattering length respectively. The scattering length b, change not only from one atomic species to another but also for the different isotopes of the same species because the interaction of a neutron with a nucleus

depends not only on the atomic number of the nucleus but also on the total spin state of the nucleus-neutron system. In general, the value of *b* is a complex quantity and the imaginary part of *b* ($=\sqrt{\sigma_a / 4\pi}$, where σ_a is absorption cross-section for thermal neutron) accounts for the absorption of the neutron in the medium. The absorption cross-section for neutrons is negligible for most of the elements, except for some elements e.g. Gd, Sm, B, and Cd.

Considering one-dimensional approximation and for planner sample, the potential *V* depends only on one spatial variable *z* (along the depth of the sample) the Schrödinger equation becomes:

$$\frac{d^2\varphi}{dz^2} + q^2\varphi = 0; \quad q^2 = \frac{2m_n}{\hbar^2}[E_k - V] - K^2 \qquad (2.16)$$

Where *q* and *K* are *z* and *x* component of the wave vector *k* respectively. The reflection amplitude (*r*) and the transmission amplitude (*t*) can be obtained in terms of the limiting forms of the solution of Eqn. (2.16).

$$e^{iq_1 z} + re^{-iq_1 z} \leftarrow \varphi(z) \rightarrow te^{iq_2 z} \qquad (2.17)$$

Where q_1 and q_2 are defined in Eqn. (2.16) for two mediums, says, 1 and 2, which consist of an interface. With proper boundary conditions at the interface, one obtained the reflectance (reflection amplitude, *r*) and the reflectivity: $R = r\,r^*$, where r^* is the complex conjugate of *r*. Similar formalism can be applied for XRR using Maxwell equations. Like XRR the refractive index of the medium for neutron is defined as $n = 1 - (\alpha - i\beta)$ where

$$\alpha = \frac{\lambda^2}{2\pi}\Sigma N_i b_i^{coh} \qquad \text{and} \qquad \beta = \frac{\lambda^2}{2\pi}\Sigma N_i b_i^{'} \qquad (2.18)$$

Where λ is the wavelength of neutron and b_i^{coh} is the coherent scattering length of the neutron (the neutron-nucleus interaction) for species *i* and $b_i^{'}$ is the absorption length of neutrons for the species *i*. For most of the samples, the neutron absorption coefficient is negligibly small.

$$\rho_{nuc} = \Sigma N_i b_i^{coh} \qquad (2.19)$$

The quantity ρ_{nuc} is called nuclear scattering length density (NSLD).

For magnetic samples the neutron sees additional potential due to its magnetic moment (μ_n = -1.913 β_N, where β_N the nuclear magnetron). Because of the magnetic moment, corresponding to the spin, the potential energy of a neutron contains a nuclear and a magnetic term:

$$V = V_n + V_m \qquad (2.20)$$

The nuclear part of *V* is defined in Eqn. (2.15). The magnetic part of the potential may be written as [97]:

$$V_m = \pm \mu_n B \qquad (2.21)$$

Where, *B* is the magnitude of magnetic induction and the +(-) applies for the spin component parallel (antiparallel) [i.e. spin up (spin down)] to the induction. In this case, the magnetization *M* is collinear to the polarization of the neutron (along the applied field, i.e. y-axis) i.e. α = 0 in Fig. 2.11. Analogous to the nuclear scattering length *b*, a magnetic scattering length *p* can be defined. This magnetic scattering length is related to μ_S the magnetic moment per atom expressed in units of Bohr magnetrons, according to:

$$p = \frac{m_n \mu_n \mu_0}{2\pi\hbar^2} \mu_S \qquad (2.22)$$

So the magnitude of magnetic potential can now be written in terms of *p*, the magnetic scattering length:

$$V_m = \frac{2\pi\hbar^2}{m_n} Np \qquad (2.23)$$

Where *N* is the same as defined in Eqn. (2.15) and *Np* is defined as magnetic scattering length density (MSLD). So, the total interaction potential for neutron in a magnetic medium can be written in the form

$$V = V_n + V_m = \frac{2\pi\hbar^2}{m_n} N(b \pm p) = \frac{2\pi\hbar^2}{m_n} (\rho_{nuc} \pm \rho_{mag}) \qquad (2.24)$$

Where (+) and (-) signs correspond to the spin up and spin down neutrons with respect to sample magnetization. The refractive index and critical angle for a neutron in the magnetic medium can be written as:

$$n = 1 - \frac{\lambda^2}{2\pi} N(b \pm p); \quad \theta_c = \lambda \sqrt{\frac{N(b \pm p)}{\pi}} \qquad (2.25)$$

For calculating the PNR profile from a magnetic multilayer, there is formalism developed by C.F. Majkrazk [98] and G. P. Felcher [99], which describes the specific case of the neutron polarization axis being parallel to the sample surface. Using Parratt [88] formalism and the matrix formalism given by Blundell and Bland [100] are also used to generate the theoretical PNR profile and both give identical profiles.

Therefore specular PNR without polarization analysis provides the depth profile of both a nuclear component ρ_{nuc} and a magnetic component ρ_{mag} of scattering length density (SLD) [14, 101]. The sign of the magnetic part depends on the polarization of the sample with respect to the polarization direction of the neutron beam. Thus the scattering length density (SLD) depth (along the film thickness, z-direction) profile $\rho_n(z)$ used to generate PNR profile is given below [14, 101]

$$\rho_n(z) = \rho_{nuc}(z) \pm \rho_{mag}(\mathrm{z}) \qquad (2.25)$$

Where $\rho_{nuc}(z) = \Sigma N_i(z) b_i; \quad \rho_{mag}(z) = \Sigma N_i(z) p_i = \mathrm{C}\, \Sigma N_i(z) \mu_i$ (2.26)

Where the summation is over each type of atom in the system, N(z) is the depth-dependent number density, b^{coh} is the nuclear scattering length, and μ is the magnetic moment of the scatterer atom in Bohr magnetons. The constant C = 2.645 fm/μ_B or 2.9109×10^{-9} Å^{-2} cc/emu [101]. The sign before ρ_{mag} in Eqn. (2.25) depends on the orientation of the magnetization relative to the neutron polarization and correspondingly we get two reflectivity patterns for two spins of neutrons, i.e., spin up (+), parallel to sample magnetization, and spin-down

neutron (−), antiparallel to sample magnetization. Fig. 2.12 shows the simulated PNR profiles for Co/Cu multilayer using Parratt's formalism, where Co moments are aligned along the applied field, thus α = 0, in this case. Inset (bottom) of Fig. 2.12 shows the depth profile of NSLD and MSLD for the Co/Cu multilayer. Therefore by measuring spin up (R^+) and spin down (R^-), PNR one can estimate the depth profiling of structure (NSLD) and magnetization (MSLD).

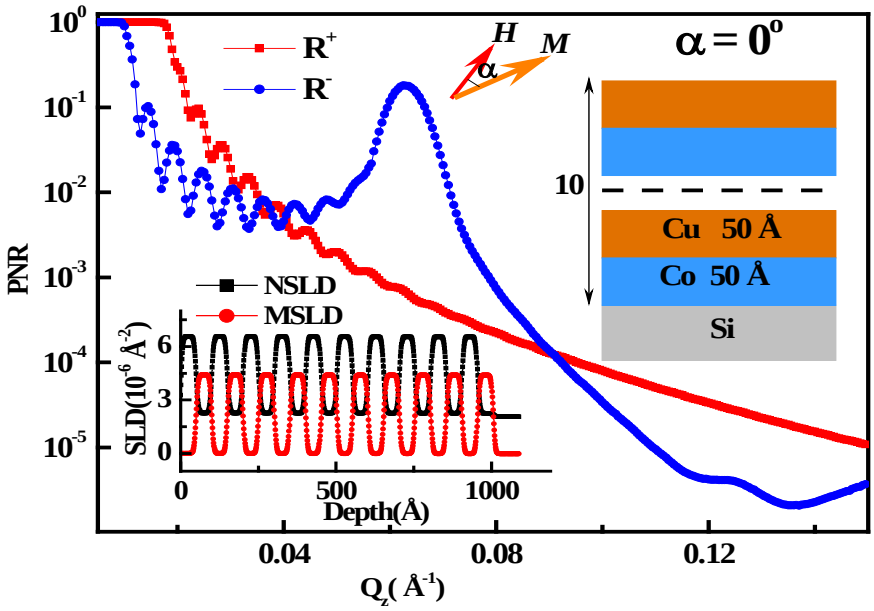

Fig. 2.12: Simulated PNR without spin polarization analysis for the Co/Cu multilayer. The magnetization of each Co layer in the multilayer is aligned along the polarization of neutron (applied field). Inset (bottom) shows the NSLD and MSLD depth profile of the multilayer.

2.5.2 Specular PNR with polarization analysis

Now we consider the case of finite angle α between the polarization and film magnetization (see Fig. 2.11). In this case, we have both the component of the magnetization and hence the matrix notation for the interaction potential is used to account for non diagonal elements of $V_{m.,}$

$$\begin{pmatrix} V_{++} & V_{+-} \\ V_{-+} & V_{--} \end{pmatrix} = \frac{2\pi\hbar^2}{m_n} N \left[\begin{pmatrix} b & 0 \\ 0 & b \end{pmatrix} + \begin{pmatrix} p_y & p_x \\ p_x & -p_y \end{pmatrix} \right] \qquad (2.27)$$

Using the above potential the Schrödinger equation becomes a set of two coupled equations,

$$\left[\frac{\partial^2}{\partial z^2} + \frac{Q_z^2}{4} - \frac{2m}{\hbar^2} V_{++}(z) \right] \psi_+(z) - \frac{2m}{\hbar^2} V_{+-} \psi_-(z) = 0$$

$$\left[\frac{\partial^2}{\partial z^2} + \frac{Q_z^2}{4} - \frac{2m}{\hbar^2} V_{--}(z) \right] \psi_-(z) - \frac{2m}{\hbar^2} V_{-+} \psi_+(z) = 0 \qquad (2.28)$$

The wave functions $\psi_+(z)$ and $\psi_-(z)$ gives the probability amplitude to find a neutron polarization either parallel (+) or antiparallel (-) to the applied field direction (i.e. y-axis). Therefore if the magnetization *M* of the film has a finite component $M_\perp$ (i.e. $\alpha \neq 0$) and non-diagonal elements $V_{\pm\mp}$ exist, the neutron spins start to precess and SF reflectivity occurs. Thus the non-zero non-diagonal potentials, which is responsible for SF reflection are pure of magnetic origin and NSF potentials $V_{\pm\pm}$ contains both nuclear and magnetic information on the $M_\parallel$. Therefore by measuring all four spin dependent reflectivities (NSF, R^{++}, R^{--}, and SF, R^{+-}, R^{-+}), one can get the detailed magnetic structure (both *M* and α).

Solving Eqn. (2.28) for polarization dependent wave function the amplitude of reflected and transmitted waves can be obtained by using boundary conditions and a matrix method [98, 99, 101-104] which gives a reflectance matrix [102]:

$$\begin{pmatrix} r_{++} & r_{+-} \\ r_{-+} & r_{--} \end{pmatrix} = \begin{pmatrix} R_+ cos^2\left(\frac{\alpha}{2}\right) + R_- sin^2\left(\frac{\alpha}{2}\right) & (R_+ + R_-) cos\left(\frac{\alpha}{2}\right) \sin\left(\frac{\alpha}{2}\right) \\ (R_+ - R_-) \cos\left(\frac{\alpha}{2}\right) sin\left(\frac{\alpha}{2}\right) & R_+ sin^2\left(\frac{\alpha}{2}\right) + R_- cos^2\left(\frac{\alpha}{2}\right) \end{pmatrix} \qquad (2.29)$$

Where the $R_\pm$ are the *Fresnel* reflection amplitudes for neutron polarization parallel or antiparallel to the magnetization of the film,

$$R_\pm = \frac{\frac{Q_z}{2} - \sqrt{\frac{Q_z^2}{4} - Q_{z,c\pm}^2}}{\frac{Q_z}{2} + \sqrt{\frac{Q_z^2}{4} - Q_{z,c\pm}^2}}; \text{ with } Q_{Z,c\pm} = 2k sin\theta_{c\pm} = \sqrt{16\pi N(b \pm p)} \qquad (2.30)$$

The resulting spin dependent reflectivities for a single magnetic film on a substrate are given as

$$R^{++} = |r_{++}|^2 = \frac{1}{4}|R_+(1+cos\alpha) + R_-(1-cos\alpha)|^2$$

$$R^{--} = |r_{--}|^2 = \frac{1}{4}|R_+(1-cos\alpha) + R_-(1+cos\alpha)|^2, \text{ and} \qquad (2.31)$$

$$R^{+-} = R^{-+} = \left|r_{\pm\mp}\right|^2 = \frac{1}{4}|R_+ - R_-|^2 sin^2\alpha$$

The spin dependent reflectivities from a multilayer can be calculated by recursive application of the transfer matrix and this formalism is well reported in [98, 99, 101-104]. However, we have simulated the spin dependent reflectivities from a Co/Cu multilayer. Fig. 2.13 shows the spin dependent PNR profiles of Co/Cu multilayer of 10 bilayers with a bilayer thickness of 10 nm and co moments are making an angle of 30 degrees with respect to applied field (or polarization of neutron). Thus PNR data with polarization analysis can be used to investigate the depth dependent magnetic structure from a multilayer.

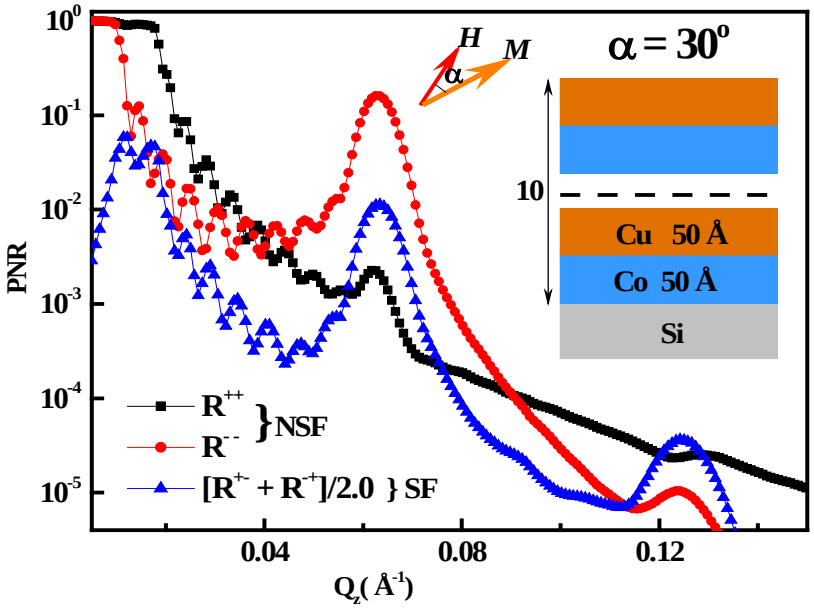

Fig. 2.13: Simulated spin dependent reflectivities from a Si/[Co(5 nm)/Cu(5 nm)]$_{10}$ multilayer assuming the angle between the Co magnetization and applied field is 30 deg in each Co layer.

2.5.3 Off-specular PNR with polarization analysis

In the case of thin film the in-plane inhomogeneities both structure and magnetic, like structural roughness, magnetic roughness, and distribution of in-plane magnetic domains, leads to off-specular scattering with a finite Q_x and accordingly $\theta_i \neq \theta_f$. The lateral wave vector transfer $Q_x = \frac{2\pi}{\lambda}[\cos(\theta_f) - \cos(\theta_i)]$, reveals the correlation of lateral magnetic inhomogeneities (roughness and domains) in the plane of the multilayer, via off-specular PNR. Like specular reflectivity, off-specular scattering is also a coherent phenomenon of constructive interference from neutron wave scattered from the different regions of the thin film within the coherence volume. Off-specular scattering from random in-plane interfaces has been described within the framework of the distorted-wave Born approximation (DWBA) [105]. The detail for polarized neutron off-specular scattering from in-plane domains has been given in [91, 92, 95, 102, 106]. In general, within DWBA the lateral fluctuations are considered by a small correction or perturbation $V_p(x,y)$ to the local and well-defined potential $V(z)$, which represents the depth dependence of the scattering potential averaged over the lateral coordinate and provide specular reflectivity. Thus the effective potential within DWBA is

$$V(r) = V(z) + V_p(x,y) \qquad (2.32)$$

Similarly, the neutron wave function ψ_d can be modified as

$$\psi_d(r) = \psi_l(r) + \psi_p(r) \qquad (2.33)$$

Where $\psi_l(r)$ is scattered wave function from the laterally average region and can be treated with potential V(z) for specular reflectivity. Scattered wave $\psi_p(r)$ correspond to residual perturbation potential$V_p(x,y)$. It is noted that both wave function and potential are neutron spin dependent. Thus using the above mentioned modified potential and wave function one

can calculate the scattering amplitude in DWBA as described in [92, 95, 102]. Using off-specular PNR with spin polarization we observed highly correlated magnetic roughness morphology (discussed in chapter 4) for Gd/Co multilayer system, which was treated under DWBA discussed in [95], which has been adopted in superfit routine [91], we have used to fit off-specular reflectivity data in chapter 4. The differential diffuse scattering cross-section is given by:

$$\frac{d\sigma}{d\Omega} = \left(\frac{Ak_0^4}{16\pi^2}\right) |\sum_{n=1}^{N} C_n|^2 S(q_{\parallel}) \qquad (2.34)$$

Where C_n are matrix elements defined in [95] and lateral roughness structure factor, $S(Q_x)$ for vertically correlated interfaces [38]

$$:S(Q_x) = \frac{\sigma_m^2 \xi}{\sqrt{2\pi}} \exp\left(-0.5 \frac{Q_x^2}{\xi^2}\right) \qquad (2.35)$$

Where σ_m and ξ are magnetic roughness and average lateral correlation length (magnetic domain size in the lateral direction) at the interface.

2.6 Polarized neutron reflectometer

2.6.1 PNR Instrument at DHRUVA reactor, BARC, India

PNR instrument at DHRUVA uses a monochromatic neutron beam with a wavelength of λ~2.5 Å [78], however, the wavelength of the neutron can be varied by rotating the monochromator. The reflectometer has been positioned on thermal neutron guide G2 in the Guide Tube Laboratory (GT Lab) of Dhruva Reactor. This instrument designed for vertical sample geometry which uses a linear position-sensitive detector (PSD), where only a sample is rotated to cover the desired *Q* range. Linear PSD also helps to collect both specular and off-specular reflectivity simultaneously at each angle of incidence. Figure 2.14 shows the photograph of the PNR instrument at DHRUVA, BARC [78]. This instrument does not have

a spin polarization analysis facility thus it is only being used to investigate the magnetization depth profiles of thin films. The specification of the instrument is given in Table 2.2.

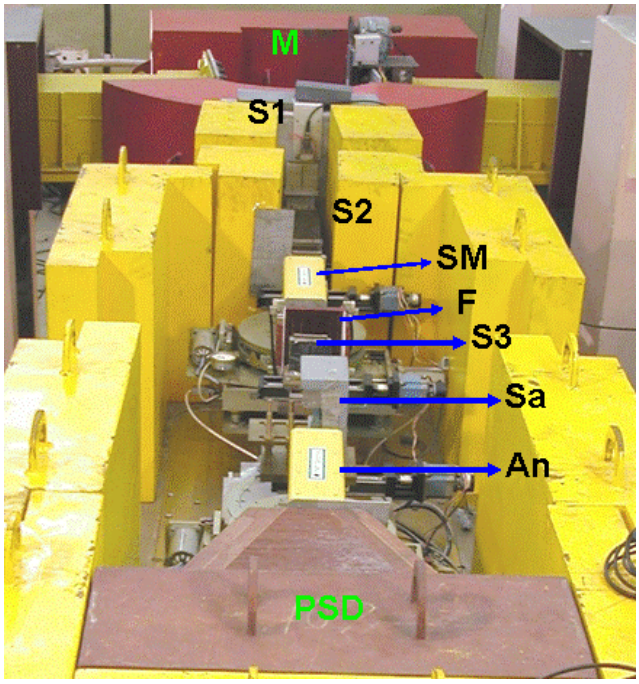

Fig. 2.14: Photograph of PNR at DHRUVA, BARC, India.

Table 2.2: Specification of polarized neutron reflectometer at Dhruva.

Scattering Plane	Horizontal (i.e. vertical sample orientation)
Monochromator	Cylindrical Si single crystal (113)
Incident Wavelength	2.5 -2.9 Å
Neutron flux at sample	~10^4 n/cm^2/sec
Polarizer/Analyzer and polarization	FeCo/TiZr based Supermirrors and >96%
The efficiency of D.C. Flipper	93%
Q-range	0.007$Å^{-1}$ to 0.09$Å^{-1}$
Minimum Reflectivity	10^{-4}

2.6.2 OFFSPEC reflectometer

OFFSPEC [79] is a time of flight polarised neutron reflectometer with low background and optimized for the measurement of off-specular reflection from a wide range of systems. It uses the neutrons of wavelength range 2.2-14 Å. Polarisation is achieved using a two-stage transmission and reflection supermirror polariser which provides at >95% polarised beam. A multi-channel polarising supermirror analyzer situated immediately before the detectors allow polarisation analysis of the off-specularly scattered beam.

For spin dependent PNR with polarization analysis measurements a reflectometer should equip with different components and a typical schematic for such an instrument is shown in Fig. 2.15. A supermirror Polarizer provides a neutron beam polarization along the applied field direction. The two spin flippers one before the sample and other after the sample are used to change the spin of the incoming and reflected neutrons. Typically a supermirror analyzer of similar specification as polarizer is used, to pass neutron of particular spin to the detector. The spin dependent reflectivity can be selected by using different flipper settings as given in Table 2.3.

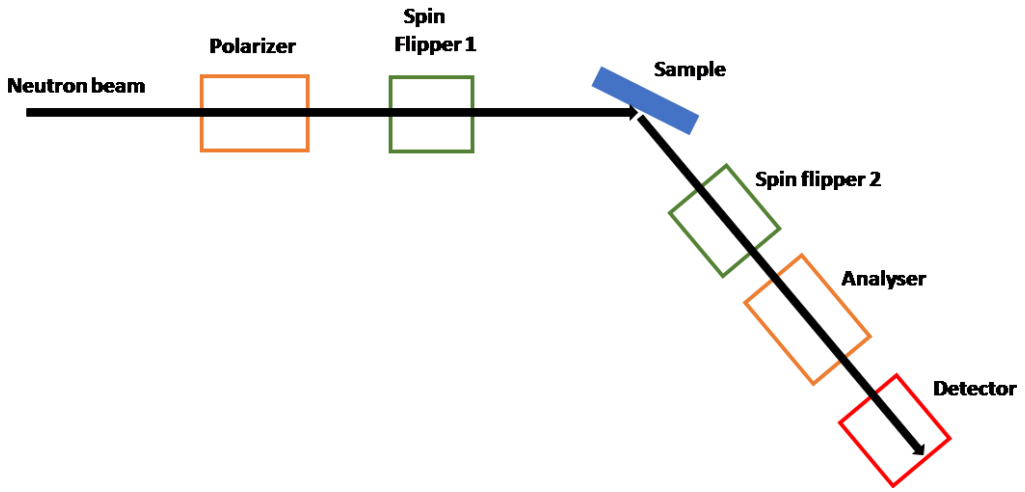

Fig. 2.15: Schematic of typical PNR instrument used for collecting spin dependent reflectivities with polarization analysis.

Table 2.3: Neutron spin states for different flipper settings for a reflectometer with a polarization analysis option.

Flipper 1	Flipper 2	Measured reflectivity
off	off	R^{++}
off	on	R^{+-}
on	on	R^{-+}
on	off	R^{--}

2.7 XRR and PNR Data analysis

In general, the analysis of reflectivity (XRR and PNR) data has two major obstacles. Firstly, the phase of the scattered wave can not be measured directly as it is required to reconstruct the scattering potential in a unique way. Secondly, once the phase is known, the scattering potential must be recovered from the complex reflection coefficient by solving the inverse problem for 1D quantum scattering. Since we usually measure the reflected intensity only over a limited range of scattering angles, an indirect method is required to get the information from measured data. Thus using the model, we generate the reflectivity profile and calculate the difference between experimental and simulated data using some error function E_r (e.g. χ^2 minimization) [107]. This model can accordingly be adjusted by some optimization method to get a closer agreement with the experimental data.

Specular XRR and PNR without polarization analysis data given in this thesis are fitted using a genetic algorithm-based optimization program [104], which uses Parratt formalism [88], as discussed in section 2.3 and 2.5 for XRR and PNR, respectively. For XRR a layer model consists of regions with SLD, $\rho(z)$. The parameters of a model include layer thickness, interface (or surface) roughness and ESLD. For PNR a layer model consists of regions of SLD $\rho(z)$, consists of NSLD and MSLD. Errors on parameters obtained from specular XRR

and PNR measurements represent the perturbation of a parameter that increased goodness of fit parameter corresponds to a 2σ error (95% confidence).

Spin dependent specular PNR with polarization analysis (R^{++}, R^{--}, R^{+-}, and R^{-+}) data as a function of temperature and magnetic field were analyzed with a genetic algorithm-based optimization program [104] which uses a matrix [100] and supermatrix method [91], as discussed in section 2.5. The layer model consists of NSLD, layer thickness, interface roughness, magnetization, and the angle of rotation of magnetization with respect to the applied field for each magnetic layer.

Off-specular PNR with polarization analysis data was analyzed using the superfit routine [91] which uses a supermatrix method [91, 92, 94, 95] within the framework of distorted wave Born approximation (DWBA) as discussed in section 2.5. Thus to fit PNR data in the off-specular mode we have used the formalism discussed in section 2.5, where we have considered the in-plane magnetic domain distribution at interfaces while keeping all the parameters obtained from specular PNR, fixed.

2.8 Optimization of thin films growth

The thin film systems studied in this manuscript were grown by DC sputtering technique and we have optimized the growth parameters of the deposition of an individual layer of the Gd and Co films. The FePt alloy was also deposited by co-sputtering of the Fe and Pt and growth parameters were also optimized. We have used X-ray scattering (both XRD and XRR) techniques for the characterization of these films, which provided detail atomic and layer structures of the films. Using the feedback from these measurements we finally grew the Gd/Co multilayers (studied in chapters 3 and 4), Fe-Cu-Pt heterostructures and FePt/Cu multilayers studied in this thesis.

2.8.1 Gd and Co thin films

Here we present XRR data and results obtained from XRR data from a few Co and Gd thin films [108] which prepared for optimization of parameters for growing the Gd/Co multilayers discussed in chapters 3 and 4. XRR data are analyzed using the formalism discussed in the previous section. The XRR data (solid circles) and corresponding fits (continuous lines) of Co films of different thickness are shown in Fig 2.16(a) and (b) shows the XRR measurements from Co, and Gd, Co/Gd bilayers, respectively. Different parameters (thickness, ESLD, and roughness) obtained from XRR measurements from these thin films are given in Table 2.4 along with the deposition conditions.

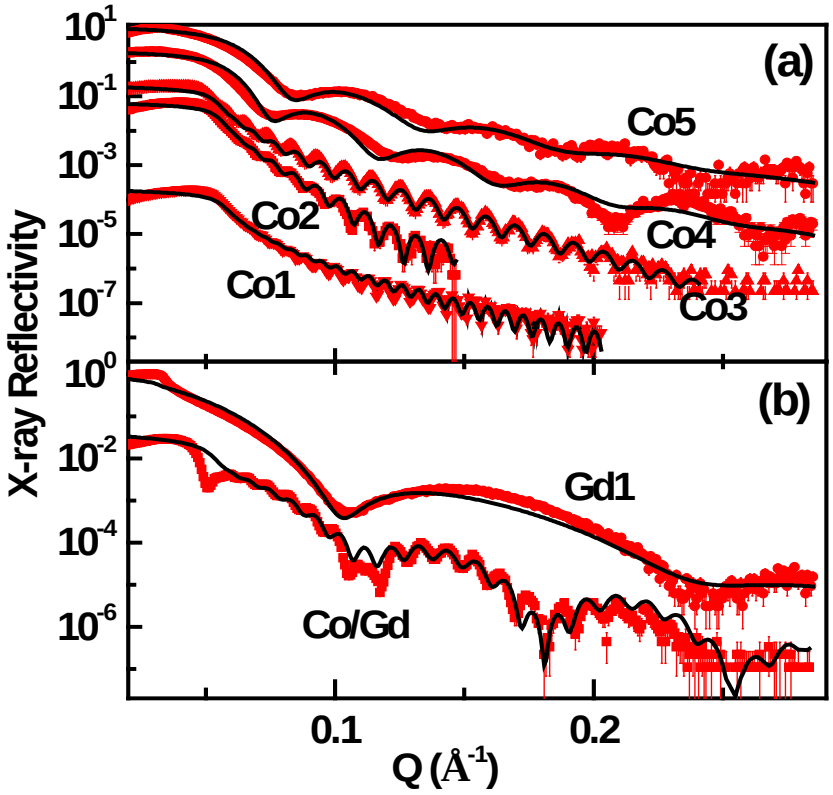

Fig. 2.16: XRR profiles of Co, Gd, and Co/Gd bilayer films

Table 2.4: Physical parameters for growth of Co and Gd films and parameters obtained from XRR fit. The error on parameters obtained from XRR are less than 5%.

Deposition Parameters				**Parameters obtained from XRR**		
Samples	**Argon Pressure (Pa)**	**Power (watts)**	**Rate of deposition (Å/min)**	**Thickness (Å)**	**ESLD (10^{-5} Å^{-2})**	**Roughness (Å)**
Co1	0.54	23	173	866	5.95	10
Co2	1.00	50	500	480	6.12	9
Co3	0.30	95	346	347	5.89	11
Co4	0.54	31	37	111	5.89	8
Co5	0.54	50	97	97	6.04	4
Gd1	0.54	36	56	56	5.27	5

2.8.2 Optimization of Co-sputtered FePt films

We have grown three FePt samples under different sputtering conditions and studied the structural properties of these films using XRR [109]. FePt thin films were grown on a Si (001) substrates by the co-sputtering method in a multi-target DC magnetron sputtering system, discussed earlier, using pure Fe (99.99%) and Pt (99.99%) targets. Three FePt films of different thicknesses (S1, S2 and S3) were co-sputtered at different sputtering powers of Pt target. The sputtering power for the Fe target was kept constant (~ 45 watts) for all the samples. Sputtering power of Pt target for S1, S2 and S3 were kept as 10 watts, 15 watts and 20 watts, respectively. The base pressure of ~1.3×10^{-5} Pa was maintained during the growth of all the samples. The XRR data (solid circles) and corresponding fits (solid lines) of FePt

samples are shown in Fig. 2.16. Inset shows the corresponding ESLD depth profile of the sample which best fitted the XRR data. Different parameters (thickness, ESLD and roughness) obtained from XRR measurements from these thin films are given in Table 2.5 along with different deposition parameters used during growth. XRR analysis suggested similar thickness for all the samples however film grown with the lowest sputtering power showed large surface roughness as compared to other samples.

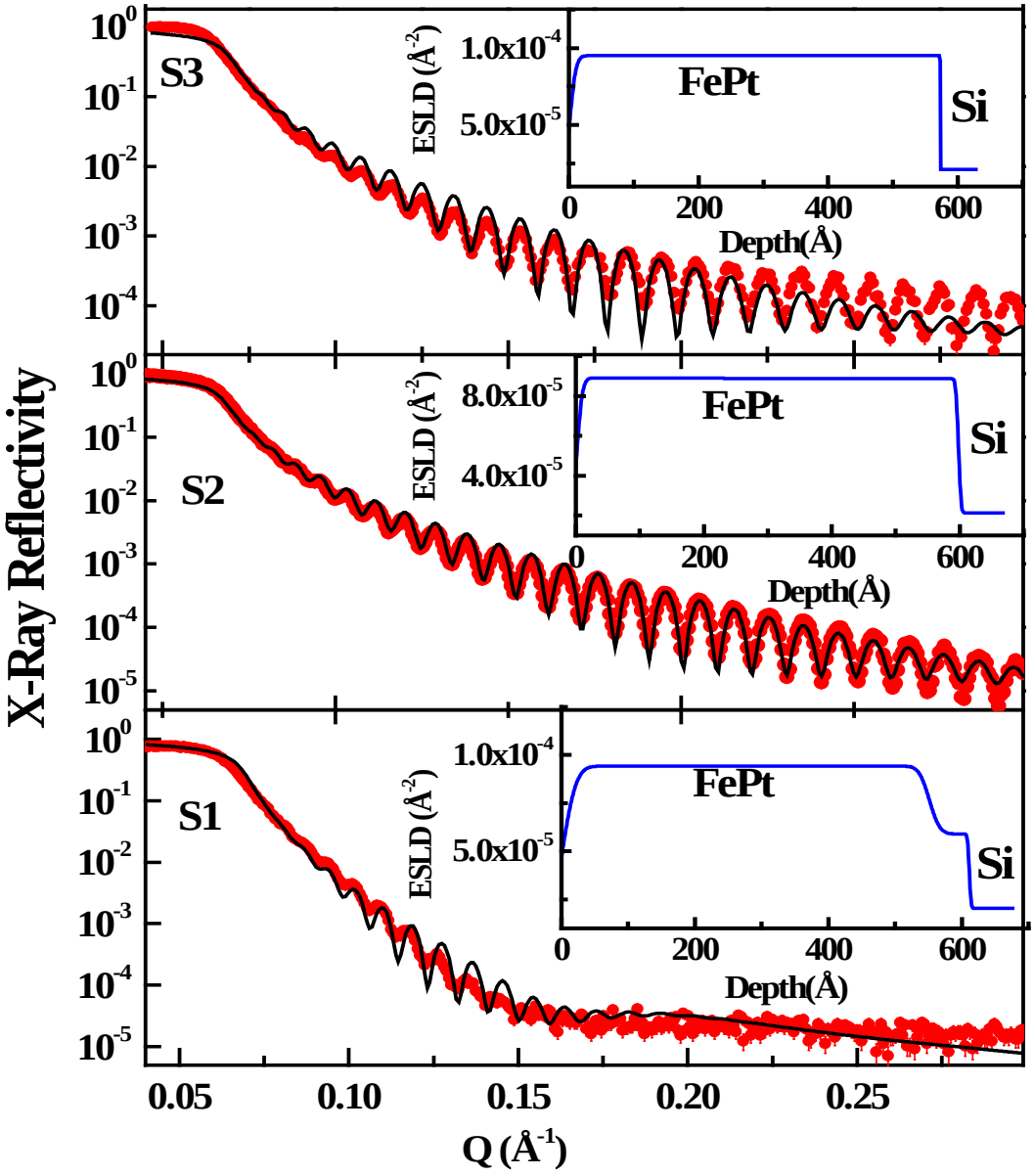

Fig. 2.17: XRR profiles of FePt thin films, S1, S2, and S3 grown on Si substrate. Inset shows the corresponding ESLD profile obtained from XRR for three films.

Table 2.5: Growth parameters of FePt films and parameters obtained from XRR data. The error on parameters obtained from XRR are less than 5%.

Deposition Parameters				**Parameters obtained from XRR**		
FePt Samples	**Ar Pressure (Pa)**	**Power (watts)**	**Deposition Time (min)**	**Thickness (Å)**	**ESLD (10^{-5} Å^{-2})**	**Roughness (Å)**
S1	0.2	Fe-45, Pt-10	27	610	9.51	16
S2	0.2	Fe-45, Pt-15	23	600	9.00	8
S3	0.2	Fe-45, Pt-20	20	575	9.51	8

Chapter 3

Effect of interface morphology on the structure and magnetic properties of Gd/Co multilayers

3.1 Introduction

Rare-earth (RE)/transition metal (TM) ferromagnetic multilayers are interesting model systems for studying the exchange interaction between RE and TM layers, where the magnetic state is determined by a competition between the Zeeman energy and interfacial exchange energy [20, 66, 68,74,110]. At low fields, the multilayer magnetization is governed by the antiferromagnetic (AF) interlayer coupling and represents a ‘‘giant’’ or artificial ferrimagnet of varying ground states. These ferrimagnetic (FM) alloys and multilayers are of great interest fundamentally as well as from a technological point of view. Multilayer systems of RE specially Gadolinium (Gd) and TM (like Fe, Co, and Ni) have attracted a lot of attention to study various phenomena, e.g. exchange interaction, complex magnetic behaviours and phases [74,111,112]. Among these systems, Fe/Gd multilayers have been extensively investigated [67,113-117], where Fe and Gd layers coupled antiferromagnetically. Different temperature dependence of Gd and Fe magnetization exhibits an in-plane cancellation of moments at the compensation temperature (T_{comp}), where Gd and Fe moments are equal and opposite to each other, so the net moment in the system tends to zero [67,74,114,118].

Theoretical studies on Fe/Gd multilayers performed by Camley *et al*., [67,114,115] have predicted the existence of different magnetic phases e.g. a low temperature phase in

which the Gd moment is aligned along the applied field and opposite to Fe moment (Gd-aligned), a high temperature phase where Fe moment is aligned along the applied field but Gd moment opposite to Fe moment (Fe-aligned), and twisted phase (in-plane canting of Fe and Gd moment) around compensation temperature. Earlier studies on Gd/Co multilayers suggested the formation of abrupt interfaces and alloying throughout the Gd layer due to asymmetric interdiffusion of atoms during the growth [74, 118]. Further, interfaces have been found to play a vital role in determining the magnetic configuration in Gd/TM multilayers. An enhanced magnetic moment at interfaces and reduced magnetic moment in the Gd layer was observed at low temperatures for such systems [33, 116, 119-121]. Despite active research in RE/TM systems, details of magnetic phases and interactions in Gd/Co multilayers are still unclear. Hence, a study of depth dependent structure, magnetic properties, and their correlation is necessary to understand the effect of interfaces on magnetic properties of Gd/Co heterostructures.

In this chapter, we study the evolution of depth dependent structure and magnetic properties of the Gd/Co multilayers grown on glass substrates with an emphasis on investigation of interface dependent properties. Interfacial dependence was achieved by varying the deposition conditions as well as by annealing the multilayers at different temperatures. Combination of several structural and magnetic characterization techniques viz. grazing incidence x-ray diffraction (GIXRD), secondary ion mass spectrometry (SIMS), superconducting quantum interference device (SQUID), x-ray reflectivity (XRR) and polarized neutron reflectivity (PNR), were used to study the structure-magnetic correlation of Gd/Co system as a function of temperature and field. The study reveals that the modifications in magnetization at low temperatures are directly correlated to roughness and alloy formation at interfaces on annealing.

3.2 Sample preparation and experimental details

Two Gd/Co multilayers were grown using dc magnetron sputtering of Gd and Co targets alternatively [122] on a glass substrate with a nominal structure: glass/[Gd(145 Å)/Co(85 Å)]$_{\times 8,}$ where 8 is the number of repeats. To obtain varied interfacial properties, two multilayers of similar thicknesses, henceforth known as S1 and S2, were deposited under different argon gas pressure of 0.2 Pa and 0.4 Pa, respectively. Before deposition, a base pressure of 1×10^{-5} Pa was achieved. The exact individual thickness of each layer was estimated using XRR measurements. Here we have grown thicker Gd and Co layer to reduce intermixing/interdiffusion at the interfaces. Also, the substrate was kept at room temperature during the growth of the multilayers. For greater uniformity, substrates were rotated along their own axis at 60 revolutions per minute (rpm). In order to correlate the dependence of structure and magnetic properties of interfaces these multilayers were annealed at 200 °C, 300 °C, and 400 °C under a vacuum ~ 10^{-4} Pa for a time period of 30 minutes at each annealing stage.

The crystalline structure of samples was investigated using GIXRD with Cu K_α radiations. Elemental depth distribution analysis of Gd and Co present in the as-deposited and annealed multilayer samples were carried out using Cameca IMS-7f SIMS instrument equipped with both oxygen duoplasmatron and cesium thermal ion source. Small pieces of the samples were used for magnetization measurements using a SQUID magnetometer. All the magnetization measurements reported in this paper, the magnetic field was along the plane of the film. The depth dependent structural and magnetic properties of the multilayers were characterized by XRR and PNR.PNR experiments were carried out using a polarized neutron reflectometer instrument (neutron wavelength ~ 2.5 Å) at DHRUVA, India[78]. An in-plane magnetic field of 1500 Oe was applied to the samples during PNR measurements.

The details about the non-destructive depth dependent characterization techniques (XRR and PNR) and data analysis formalism used here have been discussed in chapter 2.

3.3 Effect of interface morphology on magnetic properties

Interface morphology plays an important role in deciding the overall properties of the RE/TM multilayer system. Variation of interface structure (coordination, interface roughness, intermixing and alloying, etc.) assists the modification of interface exchange interactions and hence the magnetic properties of the system. The interface structure can be modified either by varying the growth conditions (e.g. sputtering pressure of Ar) during deposition or by annealing the multilayer systems. Adopting these, we have investigated the effect of interface modification and its correlation to the magnetic properties of Gd/Co multilayers in this section.

3.3.1 Interface modification by variation of sputtering pressure

GIXRD and SIMS measurements

Figure 3.1(a) shows the GIXRD patterns recorded for two as-deposited Gd/Co multilayers (S1 and S2). All the recorded data were taken at a fixed angle of incidence of 1º. We found that the Gd layer has grown with a polycrystalline face-centered cubic (*fcc*) structure [different reflections for *fcc* Gd are indexed [123] in Fig. 3.1 (a)] with a strong preferential growth along (111) direction in both the samples. This finding is in contrast to earlier studies on Gd/Co multilayer systems [74, 118], where a hexagonal closed packed (*hcp*) structure was observed for Gd. However, Co has grown with polycrystalline *hcp* structure, with a preferential growth along (101) direction. Fig. 3.1 also shows the crystalline

phase of single Co and Gd layer grown on glass substrates before growing these Gd/Co multilayers and single films were also grown as polycrystalline structures.

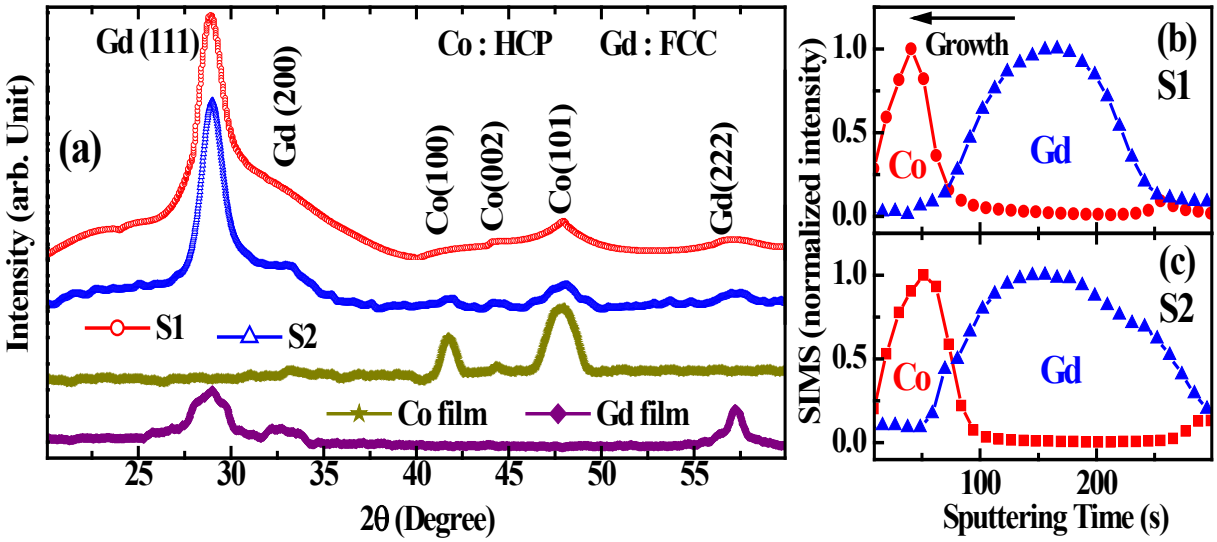

Fig. 3.1: (a) GIXRD data for the Gd/Co multilayers (S1 and S2) along with single Co and Gd films. SIMS depth profile for a bilayer of Gd/Co multilayers S1 (b) and S2 (c).

The different crystalline structures across interfaces (e. g. *fcc*/*hcp* or *hcp*/*hcp*), is also known to play a major role in interdiffusion of elements at the interfaces [124] and therefore different crystalline structure for Gd in the present study might be one of the reason that we found well-defined multilayer structure of Gd and Co, without forming an alloy layer during deposition, as described earlier [74, 118]. Since both the multilayers show similar GIXRD pattern we have compared the crystallite size of Gd and Co in these multilayers using the Scherrer formula. We have estimated the crystallite size of Gd and Co from their (111) and (101) Bragg's reflections, respectively. We obtained a crystallite size of 62 and 65 Å for the Gd in multilayers S1 and S2, respectively. Similarly, we estimated a crystallite size of 50 and 40 Å for Co in the multilayers S1 and S2, respectively.

SIMS data for a bilayer of multilayer samples S1 and S2 are shown in Fig. 3.1 (a) and (b), respectively. We found a well-defined bilayer of Gd and Co for both the multilayers, however, more diffusion at interfaces for the S2 can be seen as a broader ion yield (intensity) profiles for both Co and Gd in Fig. 3.1 (c).

XRR and PNR measurements

Figure 3.2(a) shows the XRR data for S1 (closed circles) and S2 (closed triangles). Detailed analysis of XRR data provided the individual layer thickness, electron scattering length density (ESLD), and roughness at different interfaces. Parameters obtained from XRR are given in Table 3.1. The thickness of Gd and Co layers in S1 (S2) multilayers, obtained from XRR was 140±5 Å (137±6 Å) and 84±4 Å (83±4 Å), respectively. We obtained larger roughness at interfaces of multilayer S2 as compared to that of S1 as it is evident from ESLD depth profile [Fig 3.2(b) & (c)].

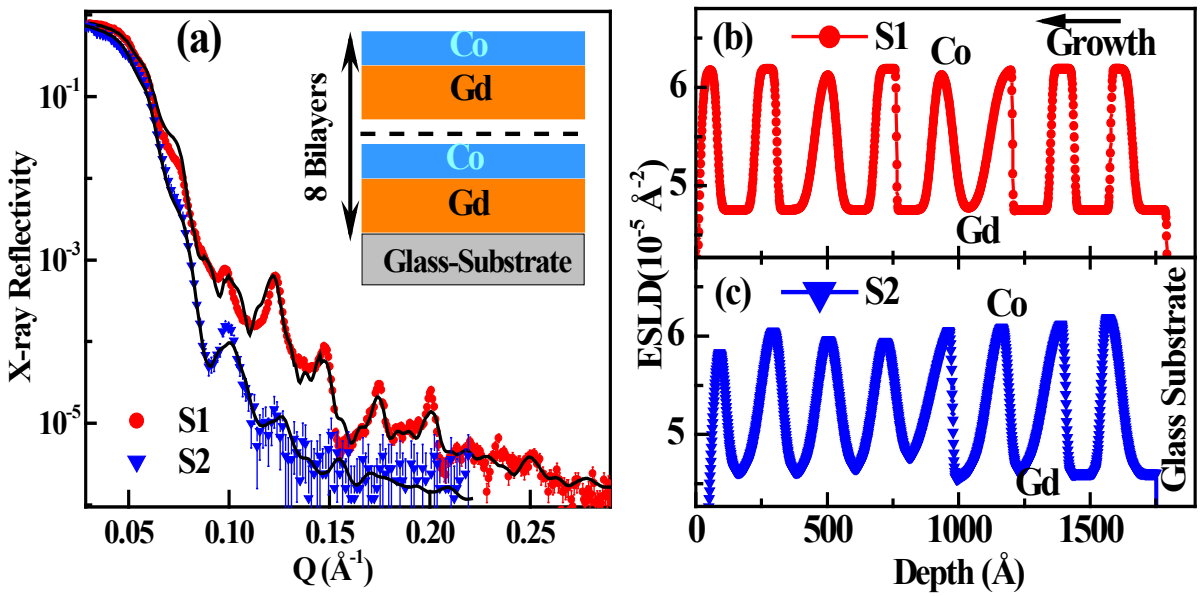

Fig. 3.2: (a) XRR data (symbols) along with fit (solid lines) for Gd/Co multilayers S1 and S2. Inset (a) shows the schematic of a multilayer film. Electron scattering length density (ESLD) depth profiles of Gd/Co multilayers S1 (b) and S2 (c).

Average interface roughness for two interfaces, Gd/Co (Co on Gd) and Co/Gd (Gd on Co), for S1 (S2), as obtained from XRR, are 10±1 Å (17± 2 Å) and 16 ±2 Å (27 ±3 Å) respectively. There are large asymmetries in the roughness which may be depending on the growth sequence as well as the surface energy of the atoms. Due to different deposition conditions, both the interfaces in the S2 have higher roughness compared to S1. It is noted that Co is the top layer in multilayer and we obtained a very thin layer (thickness ~ 15-20 Å) of cobalt oxide (CoO) at the film-air interface (shaded area in Fig. 3.2(b) and (c) at the surface).

Table 3.1: Parameters for deposited Gd/Co multilayers S1 and S2 obtained from XRR and PNR. Parameters shown in brackets are those obtained from PNR measurements.

Parameters	**Sample S1**		**Sample S2**	
	Co	Gd	Co	Gd
Thickness (Å)	84±4 [86±3]	140±5 [142±4]	83±4 [84±3]	137±6 [136±4]
Roughness (Å)	16±2 [12±2]	10±1 [7±2]	27±3 [20±3]	17±2 [15±2]
SLD (10^{-6} Å^{-2})	62.1±1.2 [2.24±0.10]	47.5±1.5 [1.96±0.07]	61.5±2.0 [2.22±0.07]	46.0±1.2 [1.96±0.08]

Figure 3.3(a) shows the PNR data recorded at room temperature (RT ~ 300 K) for S1 and S2, respectively. For S2, data has been shifted by a factor of 100 for better visualization. Fig. 3.3(b) and (c) show the nuclear scattering length density (NSLD) and magnetization depth profiles, respectively, for S1 and S2, which best fitted the PNR data from these samples. Structural parameters obtained from PNR data are given in Table 3.1. Inset of Fig. 3.3(a) shows the PNR data (as well as best fit) from S2 in a limited Q range around the

critical angle of incidence (indicated by an arrow). The open circle with a line and open triangle with a line in the inset of Fig. 3.3(a) are fit to R^+ and R^- (PNR data), respectively, assuming the same parameters, which best fitted (red and blue lines) the PNR data, except with negligible absorption for Gd layers. It suggests that large absorption of the Gd layer highly affects the PNR data near-critical angle of incidence (indicated by an arrow) and needed to be incorporated by fitting the absorption factor. We obtained a value of (2.7, 12) in fm for real and imaginary (absorption) part of coherent scattering length for Gd and this was kept fixed while analyzing PNR data in different cases of annealing.

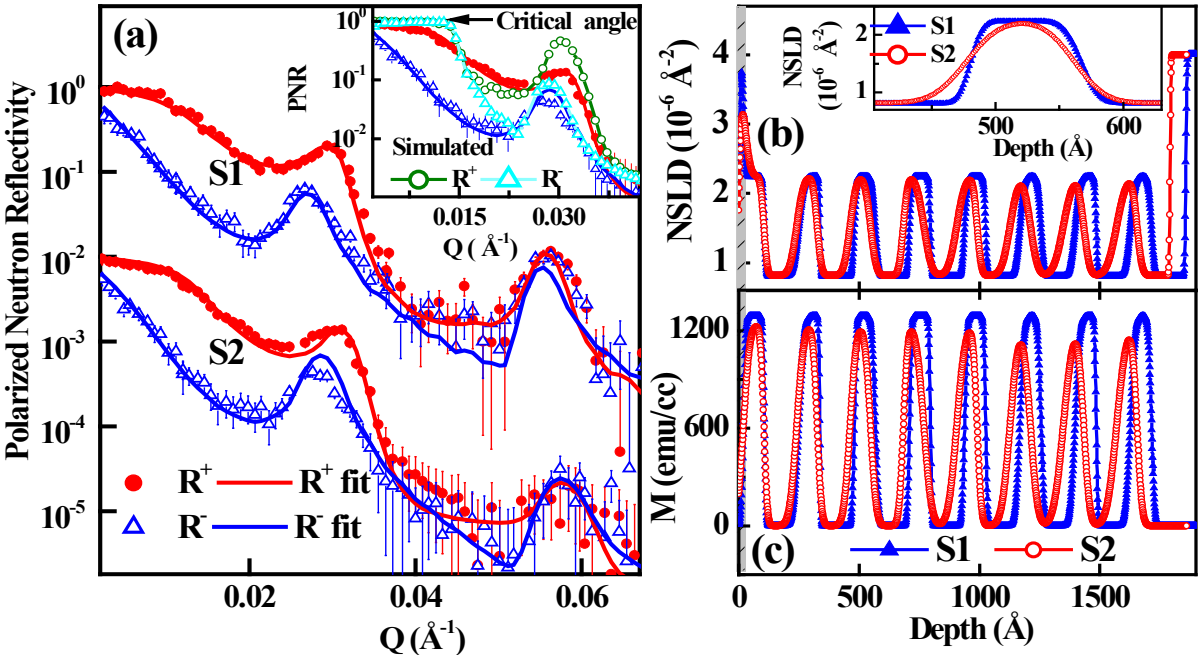

Fig. 3.3: (a) PNR data (symbols) along with fit (solid lines) for Gd/Co multilayers S1 and S2. Inset (a) shows the PNR data and fit for the Gd/Co multilayer S2 along with the simulated reflectivity profiles assuming low absorption cross-section of Gd. NSLD (b) and magnetization (c) depth profiles of Gd/Co multilayers S1 and S2 obtained from PNR. Inset (b) shows the NSLD variation of multilayers across two interfaces.

Inset of Fig. 3.3(b) shows NSLD profiles across two interfaces (Gd/Co and Co/Gd) of the S1 and S2. Higher interdiffusion (roughness) at the interfaces was observed for multilayer S2 and the magnetization profiles in S1 and S2 follow the structural roughness at the interfaces. Thus the XRR and PNR results revealed that both the samples have very close layer thickness with the only difference between them being the interface roughness.

SQUID measurements

Figure. 3.4(a) shows the RT magnetic hysteresis [M (H)] curves for the S1 and S2 multilayers. At 300 K, Gd is in a paramagnetic state, and Co is ferromagnetic. Both the samples exhibit ferromagnetic hysteresis loops at RT. Observation of a very small coercive field (H_c ~15 Oe) suggests a soft ferromagnetic nature for both the samples. The M(H) curves (in emu/cc) have been normalized with respect to the total thickness of Co layers as obtained from reflectivity data.

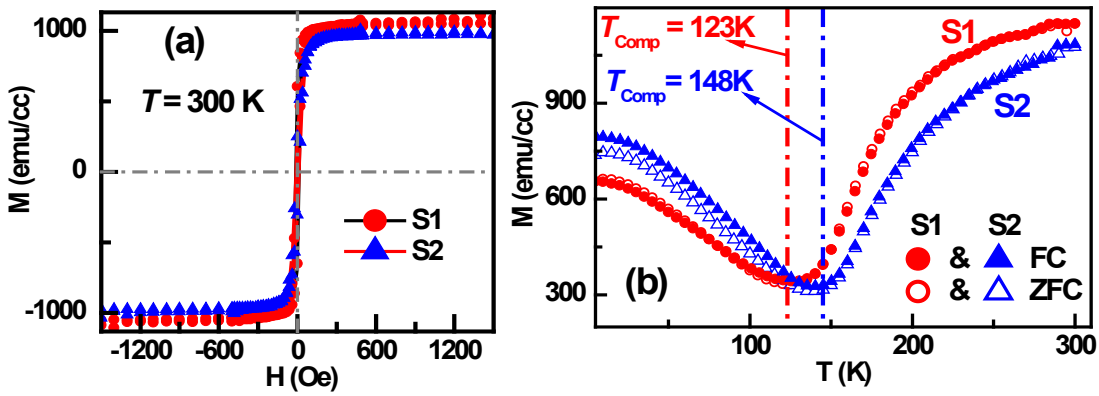

Fig. 3.4: (a) Room-temperature magnetic hystereses for Gd/Co multilayers S1 and S2. (b) temperature dependent magnetization in FC and ZFC modes for S1 and S2.

The saturation magnetization for both the samples is smaller than the bulk Co magnetization (~1400 emu/cc). The ratio of remnant magnetization (M_r) with saturation

magnetization (M_s), M_r/M_s, for S1 and S2 were found to be quite different, 0.6 and 0.3, respectively, suggesting a modification in magnetization due to the difference in the interface roughness and which may also be related to interface magnetism.

To study the effect of interfaces on the magnetization behavior of the Gd/Co system, we have performed temperature dependent measurements in both zero field cooled (ZFC) and field cooled (FC) conditions for the samples, as shown in Fig. 3.4 (b). For ZFC (FC) measurements, samples were cooled from RT (300 K) to 5 K in a field of 0 Oe (500 Oe) and the magnetization values were recorded while warming the samples in an applied field of 500 Oe. We observed a clear dip in magnetization for both the samples at a temperature, called T_{comp}. Comparison of temperature dependent $M(T)$ curves, for as-deposited samples, indicate drastic changes like, (i) different T_{comp}, (ii) splitting between FC and ZFC data. The shift in T_{comp} in Gd/Co multilayer was also found to be thickness dependent [74]. However, the samples studied here, have a similar thickness. We obtained lower T_{comp}(~ 123 K) for S1 than that of S2 (T_{comp} ~ 148 K). Moreover, the FC and ZFC data for S2 show a clear separation below T_{comp}, indicating possible different magnetic phases or uncompensated moments at the interfaces in this sample. A similar variation in T_{comp} has also been observed in Fe/Gd system, which was attributed to different surface termination in the system [125].

Due to the dominance of exchange energies over the Zeeman energy, either the Co or Gd is forced to align antiparallel to the applied field [67, 114]. In this study, we have used very smaller field (~ 500 Oe for SQUID measurements and 1.5 kOe for PNR measurements) and it is possible to assume the antiparallel alignment of Gd and Co moments since J_{AF}, exchange coupling (-2.1×10^{-15} erg [74]) between Co and Gd spins, is large enough in comparison with Zeeman energy ($\mu_B H = 9.2 \times 10^{-17}$ erg, with μ_B, the Bohr magneton, and H = 10 kOe) even at 10 kOe [70]. Thus, under the influence of the strong interfacial coupling, the Gd moments tend to align opposite to the Co moments and hence the system behaves like

a giant ferrimagnet. We believe that the changes in magnetization strongly depend on the modifications at the interfaces. XRR and PNR data suggested higher interface roughness for multilayer S2 as compared to that of S1. SIMS measurements also corroborate with the reflectivities data.

3.3.2 Interface modification upon annealing the multilayers

GIXRD and SIMS measurements

To elucidate the effect of interfaces in the Gd/Co system, we have carried out a comparative study by investigating the influence of heat treatment (annealing) on the structural and magnetic properties of these two multilayers. Both the samples were annealed in identical conditions, under vacuum in a temperature range of 200 ^{o}C – 400 ^{o}C, which tends to modify the interface structure in these samples. The attempt has been to trace the overall change in the magnetic properties on annealing and correlate that with the change at the interfaces due to alloying and intermixing. Fig 3.5 (a) and (b) shows the recorded GIXRD pattern for S1 and S2, respectively, at different annealing temperatures from 200-400 ºC.

We observed a similar crystalline structure of both S1 and S2 on annealing up to 400 ºC. We observed a change in the full-width half maxima (FWHM) of different Bragg peaks for both the multilayers upon annealing, suggesting variation in the crystallite size of atoms on annealing the multilayers. We estimated the Co and Gd crystallite (grains) size from the line widths in GIXRD data using Scherer formula as mentioned earlier. Fig. 3.5 (c) and (d) show the evolution of the crystallite size of Gd and Co in S1 and S2, respectively, on annealing the multilayers. In general, for both the samples, the crystallite size of the Co grains remained nearly constant when annealed at 200 ^{o}C and it drastically reduced on further annealing. Gd grain size also reduced on annealing, but it was less pronounced in both the samples. We observed that the reduction in grain size on annealing is directly correlated with

a reduction in the thickness of Co and Gd layers, as shown later using reflectivity measurements.

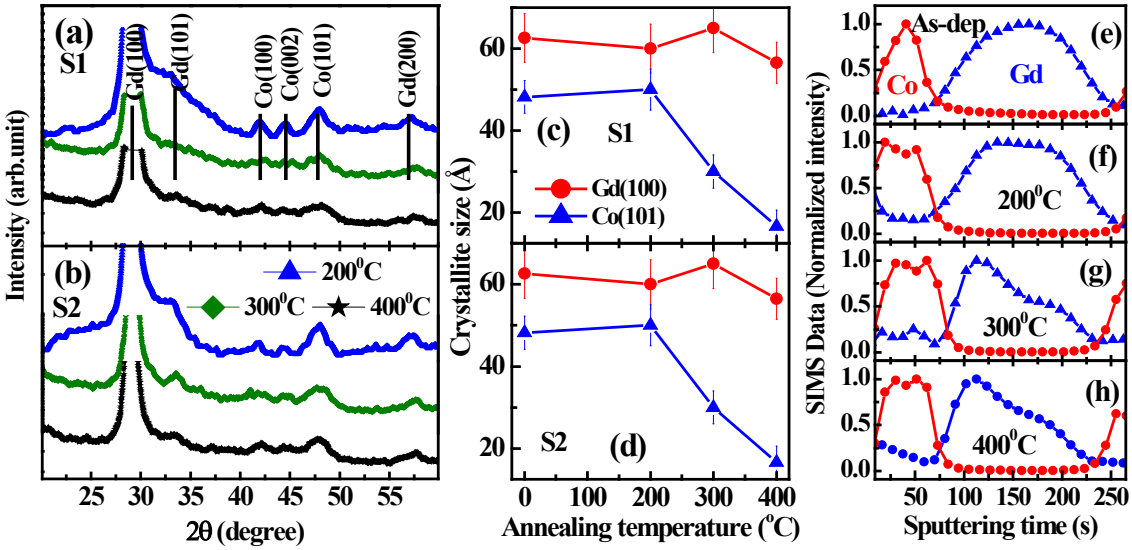

Fig 3.5: GIXRD pattern of multilayers S1 (a) and S2 (b), annealed at different temperatures.Variation of grain sizes of the Gd and Co in the S1 (c) and S2 (d) as a function of annealing temperature. (e-h) Comparison of SIMS data for a bilayer of the multilayer S1 for as-deposited state and annealed at different temperatures.

Fig. 3.5(e)-(h) show the SIMS data form Gd/Co multilayer (S1) as a function of annealing temperature. We have shown the SIMS data for the top bilayer (at air interface). Fig. 3.5(e)-(h) clearly suggests a change in SIMS data at different annealing temperatures, which are: (i) increase (decrease) in a width of peaks corresponding to Co (Gd); (ii) asymmetry in peak shape of Gd. The modifications in SIMS data, on increasing the annealing temperature, indicate higher interdiffusion. However due to poor resolution for SIMS as compared to reflectivity techniques it is difficult to quantify the formation of very thin alloy at the interfaces as observed by reflectivity measurements discussed later.

XRR and PNR measurements

Figure 3.6(a) and (b) show the XRR data for annealed multilayers S1 and S2, where data have been shifted by a factor of 100 for better visualization. Fig. 3.6(c) and (d) show the ESLD depth profile at different annealing temperatures for multilayers S1 and S2, respectively, which best fitted [solid lines in Fig. 3.6(a) and (b)] the XRR data at different annealing temperatures. Inset of Fig 3.6(a) and (b) show the ESLD profile across two interfaces of a bilayer of multilayers S1 and S2, respectively. Structural parameters obtained from XRR for multilayers annealed at different temperatures are given in Table 3.2.

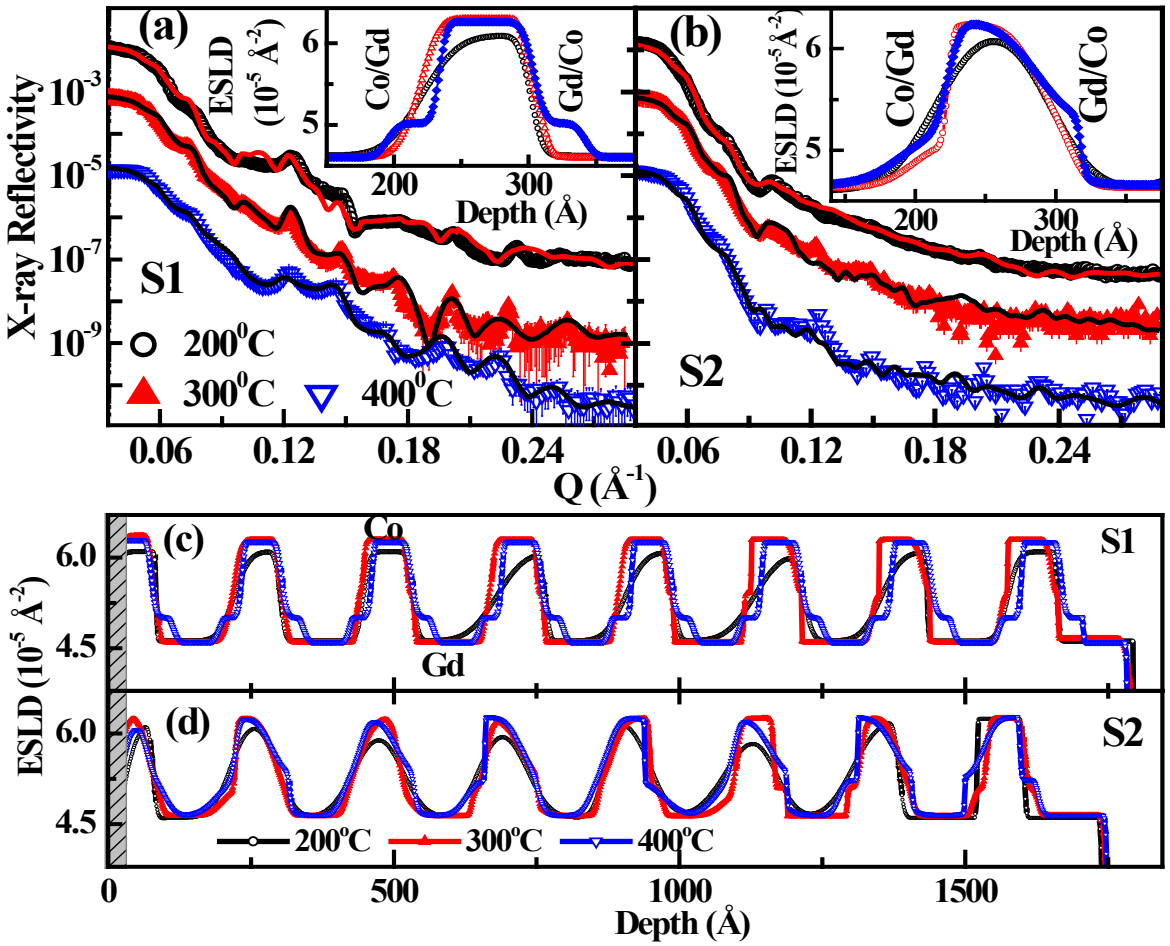

Fig 3.6: The x-ray reflectivity (XRR) data at different annealing temperatures from multilayer samples S1 (a) and S2 (b). The electron scattering length density (ESLD) depth profile for multilayers S1 (c) and S2 (d) at different annealing temperatures. Inset (a) and (b) show the ESLD profiles of S1 and S2, respectively, across the interfaces.

Upon annealing S1 and S2 at 200 ^{o}C, we observed an asymmetric increase in roughness at interfaces. The asymmetry is more in the case of S1, where roughness at the Co/Gd interface is higher than that at the Gd/Co interface. An increase of 4 Å in average roughness of the Gd/Co interface was observed, whereas the roughness of the Co/Gd interface has increased from 16 Å to 26 Å. A thin alloy layer (thickness ~ 15 Å) is formed at the interfaces on annealing the multilayers at 300 ^{o}C. The alloy layer at interfaces is treated as a new layer of definite ESLD (or NSLD) for analyzing reflectivity data. The alloy layers restrict further interdiffusion at interfaces and hence reduce average roughness at each interface (Gd/alloy, alloy/Co, Co/alloy, and alloy/Gd interfaces). The alloy layer may provide an extra coupling of interface interaction in the system.

Further annealing the multilayers at 400 ^{o}C, an increase in the thickness of the alloy layer was observed, which is accompanied by a reduction in the thickness of the Gd and Co layers. Due to the larger roughness of S2 as compared to S1, alloy at the two interfaces have marginally different ESLD. It is evident from Fig. 3.6(c) and (d) that the interface morphology of annealed multilayers (modification of roughness, alloy formation, etc.) highly depends on the morphology of the as-deposited state. Small variations in ESLDs were also observed on annealing the samples, especially on annealing samples above 300^{o}C, the ELSD increases for the Co layer whereas it decreases for the Gd layer.

Figure 3.7 (a) and (b) show the PNR data at room temperature from S1 and S2, respectively, at different annealing temperatures (shifted by a factor of 100). Modifications (small shift of Bragg peaks, variation in the difference (R^{+} - R^{-}) data, intensity reduction of Bragg peaks etc.) in reflectivity profiles at different annealing temperatures clearly indicate the variation in structure and magnetization depth profile on annealing the multilayers. Fig. 3.7 (c) and (d) show the NSLD depth profile and the corresponding magnetization depth

profile, respectively, of multilayers S1. Similarly, Fig.3.7 (d) and (f) show the NSLD and magnetization profile of the S2. Fig. 3.7 (g) – (j) show the NSLD and magnetization depth profile across two interfaces (Gd/Co and Co/Gd) of the multilayers. These NSLD and magnetization profiles were obtained from the best fit of corresponding PNR data at different annealing temperatures. The structural parameters obtained from PNR data are listed in Table 3.2, along with the parameters obtained from XRR data and both are found to be consistent with each other.

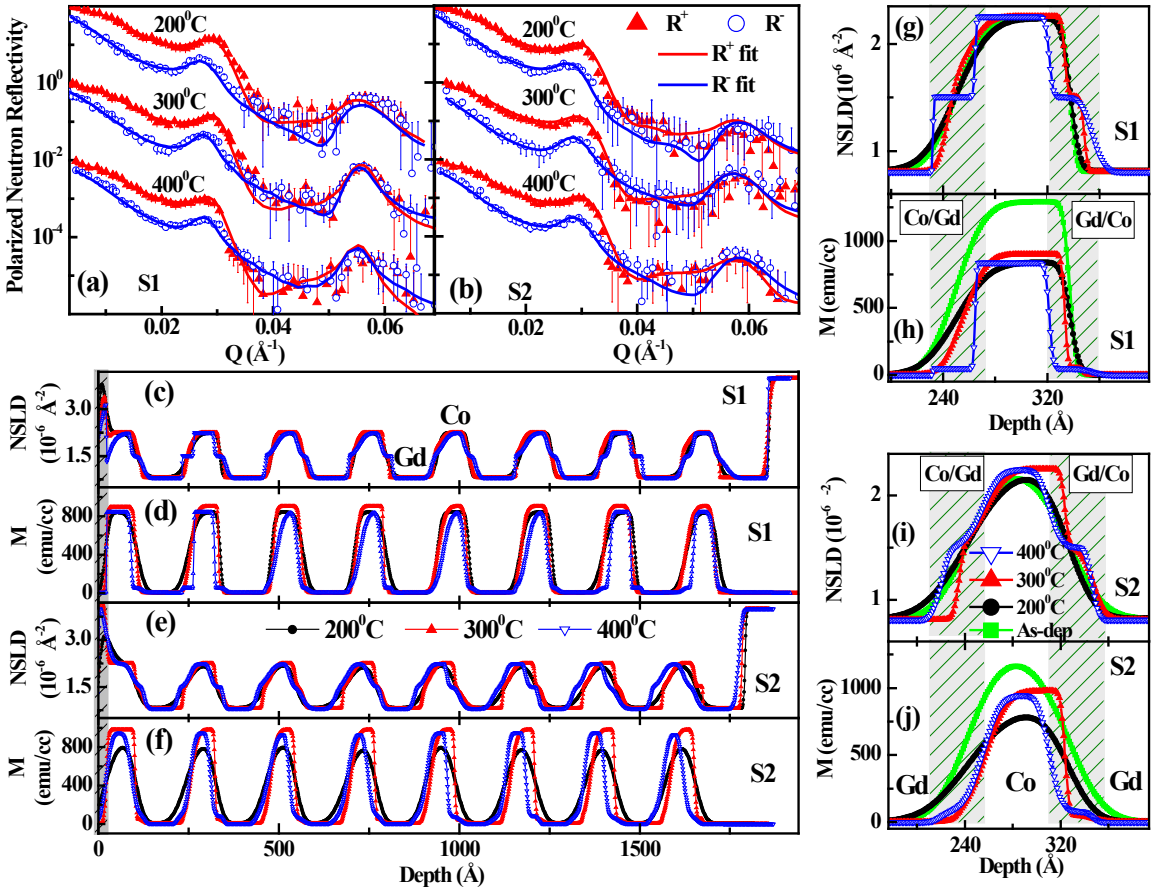

Fig. 3.7: Polarized neutron reflectivity (PNR) data at different annealing temperatures from multilayer samples S1 (a) and S2 (b). (c-f) Nuclear scattering length density (NSLD) and magnetization depth profile of multilayers S1and S2 at different annealing temperatures. (g)-(j) NSLD and magnetization depth profile across two interfaces of a bilayer of the multilayers S1 and S2.

Table 3.2: Parameters for annealed Gd/Co multilayers S1 and S2 at different temperatures, obtained from XRR and PNR. Parameters shown in parenthesis are those obtained from PNR measurements.

Parameters	**Multilayer S1**			**Multilayer S2**		
Annealed at 200^{0}C						
	Co	Alloy	Gd	Co	Alloy	Gd
Thickness (Å)	83±2 (85±3)		141±2 (136±4)	80±3 (82±2)		133±2 (136±3)
Roughness (Å)	26±3 (16±2)		14±2 (10±2)	31±4 (23±2)		22±2 (20±1)
SLD (10^{-6} Å^{-2})	62.1±2.0 (2.24±0.10)		46.7±1.0 (1.96±0.07)	61.5±2.0 (2.20±0.11)		46.0±1.2 (1.96±0.08)
Annealed at 300^{0}C						
	Co	Alloy	Gd	Co	Alloy	Gd
Thickness (Å)	74±3 (75±2)	14±2 (15±2)	120±2 (123±3)	67±2 (68±3)	24±2 (23±2)	107±4 (109±2)
Roughness (Å)	4.0±0.7 (3.5±0.8)	3±1 (4±0.8)	5.0±0.7 (6.0±0.6)	15±2 (12±1)	10±1 (8±1)	12±2 (8±1)
SLD (10^{-6} Å^{-2})	63.0±1.5 (2.26±0.11)	52.5±2.5 (2.13±0.10)	46.0±1.5 (1.94±0.10)	62.0±1.4 (2.20±0.11)	55.0±2.0 (2.12±0.10)	46.5±2.0 (1.96±0.08)
Annealed at 400^{0}C						
	Co	Alloy	Gd	Co	Alloy	Gd
Thickness (Å)	67±2 (60±4)	35±2 (33±4)	88±4 (95±5)	60±2 (57±3)	31±3 (35±2)	89±3 (92±3)
Roughness (Å)	5±1 (3±2)	4±1 (3±1)	5±1 (4±1)	16±2 (15±1)	12±1 (8±1)	12±2 (8±1)
SLD (10^{-6} Å^{-2})	60.0±3.0 (2.26±0.11)	50.0±3.0 (2.13±0.10)	46.0±1.5 (1.94±0.10)	62.0±1.4 (2.20±0.11)	55.0±2.0 (2.12±0.10)	46.5±2.0 (1.96±0.08)

Using NSLD and ESLD profiles of annealed (at 300 ^{o}C and 400 ^{o}C) multilayers, we have estimated the composition of binary alloy formed at interfaces by comparing the ESLD and NSLD value for alloy layer. The composition of the alloy phase has been obtained to be very close to the Co_2Gd phase for both the multilayers. This alloy layer formed on annealing the multilayers above 300 ^{o}C is different than the Gd_2Co alloy observed earlier by Andres *et.al.*[118] for thinner Gd/Co multilayers. An earlier study suggested that the Curie temperature for Co_2Gd alloy was ~ 400 K [126]. Also, the Co_2Gd/Gd interfaces studied earlier clearly suggest a reduction in interface exchange interaction [70] leading to modification in magnetic phases. PNR data also showed very small magnetization (~40-50 emu/cc) for Alloy (Co_2Gd) layers formed at the Gd/Co and Co/Gd interfaces on annealing multilayers at 300 ^{o}C and 400 ^{o}C (Fig. 3.7(h) and (j)). However, the magnetization of the alloy layer in the present study is very small as compared to that for similar alloy studied earlier [24] at a temperature of 295 K.

SQUID measurements

Figure 3.8 (a) and (b) show the room temperature $M(H)$ curves for multilayers S1 and S2, respectively, at different annealing temperatures. The in-plane M_s for two samples as a function of annealing temperature was estimated from SQUID and PNR data and shown in Fig. 3.8 (c). M_s estimated from PNR data at different annealing temperatures is a thickness averaged magnetization. There is an excellent match between the values obtained from macroscopic SQUID measurement with that obtained from the fits to PNR data. A drastic reduction in M_s can be observed on the annealing of both the samples at 200 ^{o}C. This is due to an increase in roughness extending the Co layer boundary. Once the distinct alloy layer emerges, an increase in M_s has been observed for both the samples on annealing at higher temperatures ($\geq$ 300 ^{o}C). This increase in M_s has resulted due to a reduction in interface

roughness and an increase in density (ESLD and NSLD) of Co layers in both the samples, as observed from XRR and PNR measurements.

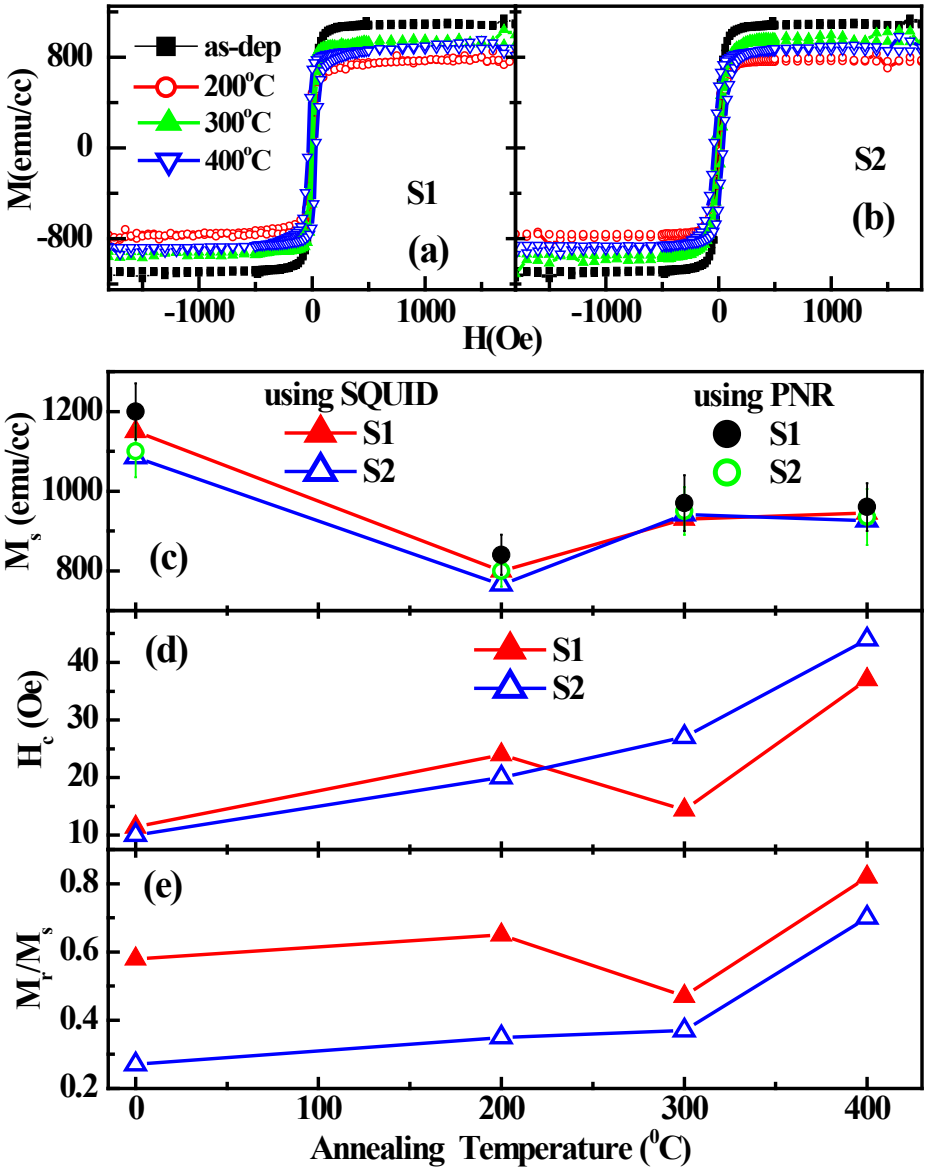

Fig. 3.8: Room temperature magnetic hysteresis curves for multilayers S1(a) and S2 (b), at different annealing temperatures.The variation of saturated magnetization (c), coercivity (d), and M_r/M_s (e) for S1 and S2 as a function of annealing temperatures. For comparison, we have also presented the thickness averaged (Co layers) magnetization of the samples measured by PNR. Zero annealing temperature corresponds to an as-deposited condition.

The other parameters, which clearly show the effect of annealing, are H_c and M_r/M_s, as shown in Fig. 3.8 (d) and (e), respectively. We observed an increase in H_c, on increasing the annealing temperature. A similar variation was also observed in M_r/M_s. An increase of ~2.5 - 3 times in H_c, on annealing of both the multilayers, at 400 ^oC has been observed. Upon annealing the multilayers at 400 ^oC, we observed a small increase in M_r/M_s for S1, while it was about ~ 2.5 times for S2.In general, an increase in both H_c and M_r/M_s was observed for both the samples on annealing from 200 ^oC to 400 ^oC, which is consistent with the previous study on Gd/Co multilayers [127] with much thinner Co and Gd individual layers. Interface alloying in the Gd/Co, due to annealing, causes pinning against domain wall motion [127] and increases in coercivity, which can further modify the magnetic phases in Gd/Co system.

Figure 3.9 shows the remarkable results of magnetization as a function of temperature, $M(T)$, in FC (closed triangle), and ZFC (open circle) mode for as-deposited and annealed multilayers. Upon annealing of both the samples at 200 ^oC, the T_{comp} has raised higher. The T_{comp} for S1 (S2) changes from ~125 °C (~150 °C) to ~198 °C (~175 °C), which may be purely related to the interface-driven phenomenon. The increase of roughness at the interfaces in both the samples modifies exchange interaction between Gd and Co layers and causes spin disorder/reorientation, which may change the T_{comp}. At T_{comp} the magnetic moment of Gd and Co are aligned opposite to each other and magnetization of the whole system reduces. We believe that increase in roughness in the present study may be modifying the spin reorientation/disorder in the system and hence increasing the T_{comp} (the Gd and Co magnetic moments are being aligned oppositely at a higher temperature). The spin disorder is also evident from the split in ZFC and FC data for higher annealing temperatures. On further annealing of the multilayers S1 and S2 at a higher temperature (~ 300 °C), T_{comp} decreases, while no compensating states are visible for both the samples on annealing at 400 °C. Moreover, we obtained higher separation in ZFC and FC magnetization on annealing, which

may be due to an increase in spin frustration at interfaces. Existence of many magnetic phases (e. g. Co-aligned, Gd-aligned, twisted phase) resulting from the heterogeneous mixture of FM and AF coupled interfaces because of intermixing and alloying of the Gd/Co on annealing, instead of individual FM or AF coupled layers, may increase the spin frustration in the system.

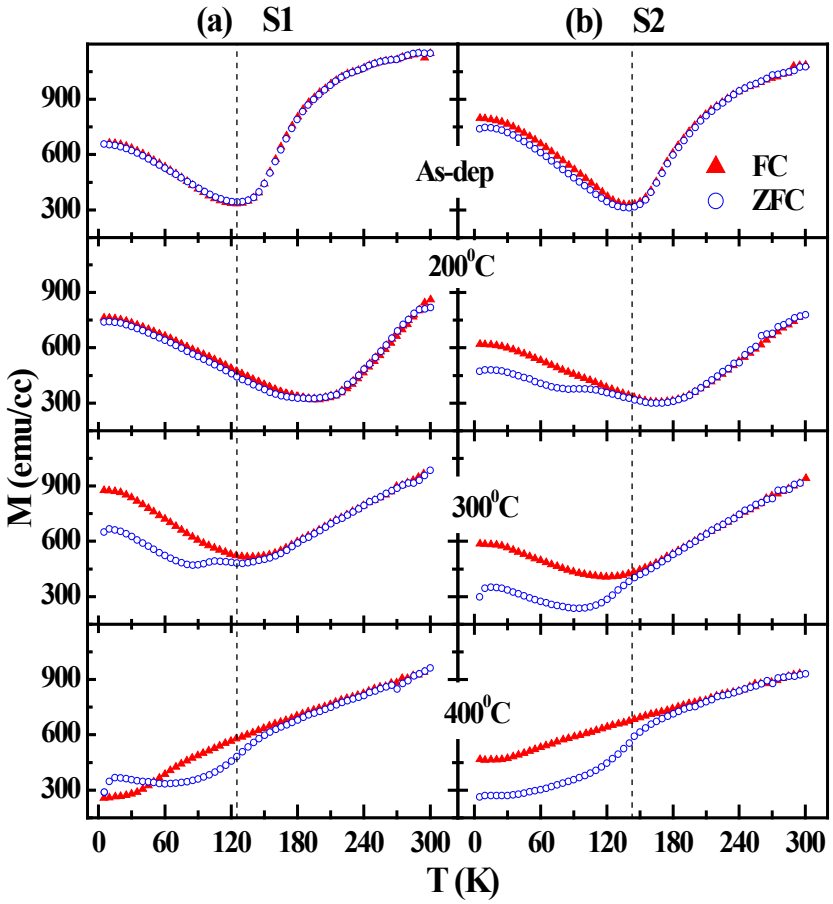

Fig. 3.9: The zero field cooled (ZFC) and field cooled (FC) magnetization data as a function of temperature from multilayers S1 (a) and S2 (b) annealed different temperatures.

We also observed the intersection of FC and ZFC data at ~45 K for the S1 on annealing at 400 °C, which is generally attributed to the isotropic, the antisymmetric, and the anisotropic–symmetric exchange interactions leading to different magnetic entities in these systems [128]. However, the formation of alloy layer at interfaces may provide extra

coupling of interface interaction, which may leads to the existence of different magnetic phases and increase in separation of FC and ZFC data and hence contribute significantly to additional modifications in FC and ZFC data from samples annealed at ≥ 300 ^{o}C.

.

3.4 Discussion

Using reflectometry techniques, we observed a reduction of Bragg peak intensity of multilayers on annealing at different temperatures. As discussed in chapter 1, reduction in the intensity of the Bragg peak of reflectivity profile on annealing provide an estimate of the diffusivity and hence activation energy of the constituent (Gd or Co) in the multilayer. Diffusivity (D) was calculated with the expression given in Eqn. (1.8). We used the first Bragg peak intensity of PNR data for multilayers S1 and S2 and calculated the diffusion length of the elements. Figure 3.10 (a) and (b) show the variation of diffusion length as a function of annealing temperature. Diffusion lengths of ~32.6 Å and ~34.4 Å were obtained for S1 and S2, respectively, on annealing at 200 °C, suggesting higher interface roughness favouring the diffusion of the constitute elements (Gd and Co) at interfaces. On further annealing of the multilayer at 300 ^{o}C and 400 ^{o}C we observed smaller changes in diffusivity, suggesting the formation of an alloy at the interface at these temperatures decreases the diffusion of the elements.

Using diffusivity one can estimate the activation energy (E_a) required for diffusion-controlled kinetics in Gd/Co multilayers. Temperature dependant diffusivity equation $D = D_0\exp(-E_a/KT)$, where D is the diffusivity at particular annealing temperature T, was used to estimate E_a. Figure 3.10 (c) and (d) show the Arrhenius plot ($\ln(D)$ vs $1/T$ plot) for two multilayers, S1 and S2, respectively. The straight line is the fit to data. Due to small variation in diffusivity for S2 the Arrhenius plot is not sufficient to extract the exact value of activation

energy. Using the Arrhenius plot we estimated the activation energy required for diffusion of elements in two multilayers, S1 and S2, and found that the activation energy for S1 (~ 1.1 eV) is much larger (~ 9 times) than that of S2 (~ 0.13 eV). This suggests that interdiffusion for the S2 is more than that of S1 and the as-deposited interface morphology may be contributing for the same.

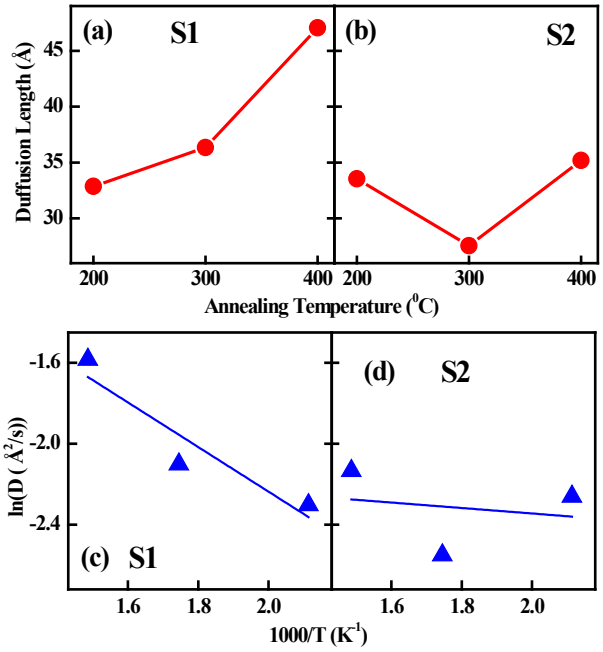

Fig. 3.10: Variation of diffusion lengths with the annealing temperatures of S1 (a) and S2 (b). Arrhenius plot ($ln(D)$ vs $1000/T$) plots for S1 (c) and S2 (d), used for estimation of activation energy.

A combination of XRR, SIMS, and PNR measurements confirmed the modifications at the interfaces. Figure 3.11 depicts the variation of interface morphology (roughness, alloy layer etc.) and corresponding magnetization properties as a function of annealing temperatures. An increase in roughness at the interfaces of both the samples on annealing at 200 ^{o}C resulted in an increase in the T_{comp}. Reflectivity measurements suggested a larger increase (~60 %) in roughness for S1 than that for S2 (~15%), on annealing at 200 ^{o}C.

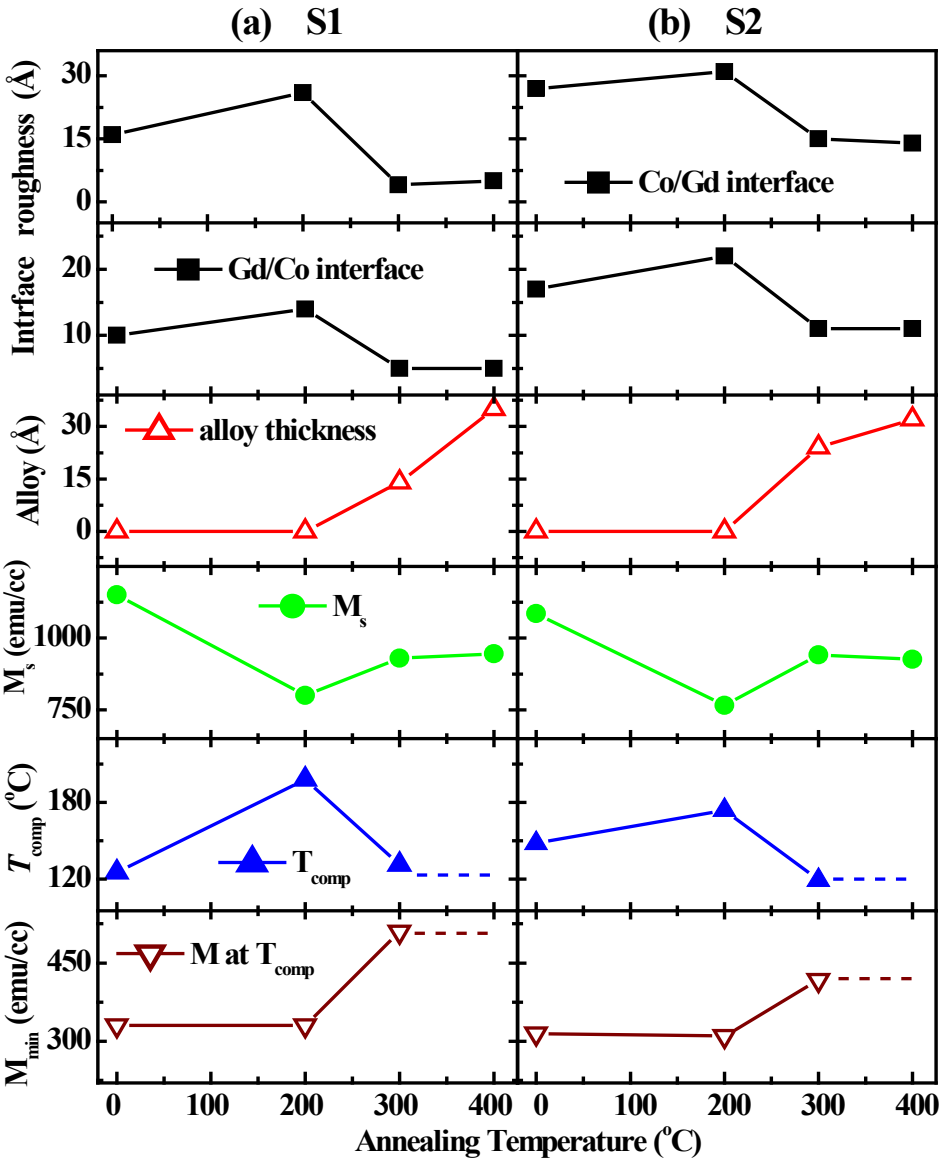

Fig. 3.11: Variation of different parameters (roughness, alloy layer thickness, magnetization compensation temperature, etc.) as a function of annealing temperature for multilayers S1 (a) and S2 (b). Annealing temperature 0°C corresponds to as-deposited multilayers.

Larger shifts (~75 K, about 60%) in T_{comp} to a higher temperature for S1, as compared to S2 (where a shift in T_{comp} is ~25 K, about 15%), on annealing at 200 °C, is directly correlated to the corresponding increase in roughness at interfaces for two samples. This affirms the dependence of T_{comp} on roughness morphology. However, separation of FC and

ZFC data for as-deposited sample S2 may be due to intermixing at interfaces, which is treated as roughness parameters in specular reflectivity [129]. On annealing, the samples at 200 ^{o}C, an increase in separation for both the samples was observed, which might be due to an increase in intermixing of these elements at the interfaces. However, we did not observe any alloy layer formation at interfaces on annealing the samples at 200 ^{o}C, which might provide an extra coupling for defining new magnetic phases in the system at low temperatures. Reduction in the roughness of different interfaces of samples annealed above 300^{o}C was correlated with an increase in density (ESLD and NSLD) of the Co layer, which resulted in an increase in saturation magnetization at RT of multilayers annealed at ≥ 300^{o}C.

Another interesting observation from low temperature magnetization is the variation of magnetization (M_{min}) at T_{comp} as a function of annealing temperature (Fig. 3.11). The M_{min} (for FC data) for as-deposited samples S1 and S2 have almost similar value (~ 300 emu/cc) and it remains the same on annealing the samples at 200 ^{o}C. However, an increase in M_{min} (~ 450-500 emu/cc) is observed for both the samples on annealing at 300 ^{o}C. Since alloy formation at interfaces initiates for annealed samples at 300 ^{o}C, we believe the magnetic structure of alloy phase at low temperature may modify the interaction between Co and Gd layers, which leads to a reduction in magnetization compensation and higher magnetization at T_{Comp}.

3.5 Summary

We have investigated the interface dependent magnetization of Gd/Co heterostructures using both macroscopic (GIXRD, SQUID) and depth dependent (XRR and PNR) characterizations. The interface properties of the heterostructures were controlled and varied by growing the films under different conditions and annealing the samples at different temperatures. In contrast to earlier studies, our results show that the Gd layers are grown with

polycrystalline *fcc* structure, which might have helped to grow the high quality of multilayer structure without alloy layer formation during deposition. The findings of depth dependent structures especially interface morphology are very well corroborated with the SIMS measurements. We have shown that the compensation temperature (T_{comp}), which is a signature of the antiferromagnetic exchange interaction between Co and Gd at interfaces, is strongly correlated to the interface morphology and increases with an increase in interface roughness. Correlation of structure-magnetic properties of multilayers annealed at 200 ^{o}C confirms the dependence of T_{comp} on interface roughness. Further annealing of the multilayers at 300 ^{o}C and 400 ^{o}C resulted in the formation of an alloy at interfaces, which provided an extra coupling for interface exchange interaction leading to additional magnetically complex phases at low temperatures. We have demonstrated that interface roughness, intermixing and alloy formation at the interface may affect magnetization behaviour in Co/Gd multilayers. These results offer valuable information to help us understand the mechanisms of interface induced magnetization in the RE/TM system. In addition, these results strongly suggest a need for a more complicated model which takes into account of interface roughness and roughness morphology in RE/TM systems for modelling the phenomena micromagnetically, generally used to explain the different magnetic phases in RE/TM systems. Hence these results will be helpful to understand the interface effect on magnetic properties of the RE/TM system for designing potential practical applications in high-performance magnetic RE/TM superlattices.

Chapter 4

Temperature and field dependent structure and magnetic properties of Gd/Co multilayers

4.1 Introduction

For the realization of magnetic memory and logic application devices with fast switching, the current-induced manipulation of magnetic order through a spin orbit torque has attracted great interest in recent times [130-132]. The Dzyaloshinskii-Moriya interaction [133], and the spin Hall effect via heavy-metal layers [134,135] were the major phenomena that attributed to large chiral spin torques. The artificial antiferromagnetic (AF) structures [136] that allow moving nanoscale magnetic domain walls (DWs) with the current at large velocities have shown considerable enhancement of the spin-torque efficiency for an exchange coupling torque (ECT) application. The compensated of rare earth (RE) and transition metal (TM) heterostructures, where the RE and TM moments are aligned antiparallel due to the strong AF interaction and the total net moment tends to zero at a particular temperature, termed as compensation temperature (T_{comp}), are potential candidate materials for realizing devices with higher speed and density [45,137,138]. Recent studies on a class of artificial ferrimagnets consisting of RE-TM alloys and heterostructures have also indicated the potential of these systems to exhibit DW motion via ECT [139, 140].

The use of nano-sized stable magnetic helices for magnetic energy storage application is predicated theoretically [19] and realized experimentally in RE/TM multilayer [50]. It has been recognized that properties like magnetization reversal and formation of helical

configurations (in the form of planer 2π DWs) in RE/TM heterostructures without application of magnetic field at the compensation temperature is the key to manipulating the magnetic devices [50]. Existence of the antiferromagnetic (AFM) exchange coupling between RE and TM layers, and a wide variety of magnetic configurations as a function of temperature and field, also lead to novel magnetic states and phase transitions between them [20, 66, 67, 73, 110]. The AFM coupling and various magnetic states in Gd/TM heterostructures have also been used for artificial ferrimagnets applications [141, 142]. A detailed magnetic structure determination across the interfaces of RE/TM heterostructure as a function of field and temperature is difficult to measure using macroscopic magnetometry techniques alone, due to the interface-driven nature of RE/TM systems [20, 66, 67, 73, 110]. The magnetic helix in heterostructures can be studied using depth-dependent magnetic characterization techniques e.g., nuclear resonant scattering [143], resonant magnetic x-ray reflectometry [144], or polarized-neutron reflectometry (PNR) [14,22,50,91,92,100,145] and they have their own advantages and disadvantages. However, using spin-dependent PNR with polarization analysis one can easily distinguish the helical structure of ferromagnetic alignment in heterostructures. In addition, PNR can be used to study the behaviour of interface DWs at the compensation, and evolution of domain size at the interfaces as a function of temperature and field.

In this chapter, we have studied the depth dependent magnetic structure, as a function of temperature and field, of Gd/Co multilayers grown on Si (100) substrates. We report the correlation of magnetic and magnetotransport properties across T_{comp} of Gd/Co multilayers grown with different interface morphology. The interface morphologies were modified by growing the multilayers under different argon pressures. Spin-dependent specular and off-specular PNR [14,22,50,91,92,100,145] in combination with x-ray reflectivity (XRR) [14] and x-ray diffraction (XRD) measurements were carried out to correlate the depth-dependent

structure and magnetic properties of these multilayers and understand their different macroscopic magnetization and magnetotransport properties across $T_{comp.}$

4.2 Sample preparation and experimental details

Three Gd/Co multilayers with a nominal structure of Si(100)/[Gd(140 Å)/Co(70 Å)]$_{\times 8}$, where 8 is the number of the bilayer (BL) repeats, were deposited using dc magnetron sputtering on a Si(100) substrates. In order to vary the interface properties, we have grown these multilayers of similar thicknesses under different Ar pressures. For first multilayer, henceforth known as S1, all the layers (8 BLs of the Gd and Co) were deposited at an argon pressure of 0.2 Pa, whereas in case of second multilayer, henceforth known as S2, all the layers were deposited at an argon pressure of 0.4 Pa (2 times the pressure compared to the S1). For the third multilayer, henceforth known as S3, the first four BLs on Si substrate were grown at the same argon pressure (0.4 Pa) as for S2, and the top four BLs were grown at an argon pressure of 0.8 Pa. The schematic representations of the multilayers are shown in Fig. 4.1.

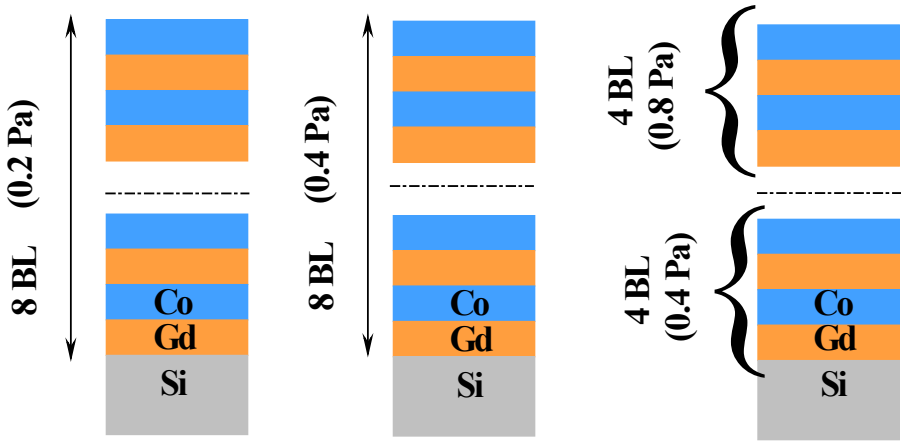

Fig. 4.1: Schematic representation of Gd/Co multilayers grown under different sputtering pressures, S1, S2, and S3.

The deposition was carried out under a high base vacuum pressure of 1×10^{-5} Pa before the deposition. All the multilayers were grown at room temperature. We have optimized different deposition parameters (deposition rate, time, deposition power) for growing Gd and Co layers of a similar thickness at different Ar pressure, before depositing the multilayers. We obtained a deposition rate of 23.5, 21 and 18 Å/min for the Gd layer and 70, 66 and 62 Å/min for the Co layer in an Ar pressure of 0.2, 0.4, and 0.8 Pa used for growing in multilayers S1, S2, and S3, respectively.

The crystalline structure of the multilayers was investigated using XRD with Cu K_α radiation. Macroscopic magnetization data along the plane of the film were obtained using a superconducting quantum interference device (SQUID) magnetometer. Magnetoresistance (MR) measurements were carried out by the four-probe method. For MR measurements the contacts were made by shouldering the indium shots on the sample surface. The depth-dependent structural and magnetic characterizations of the multilayers were carried out using XRR and PNR techniques. PNR measurements were carried out using the OFFSPEC reflectometer at the ISIS Neutron and Muon Source, RAL, UK. PNR data at different temperatures were taken in an in-plane applied field (H) of 500 Oe after cooling the multilayers from 300 to 5 K in the same field.

4.3 Results

4.3.1 Structural characterization

X-ray scattering measurements

Figure 4.2(a) shows the XRD patterns for multilayers S1, S2, and S3.In contrast to earlier studies on Gd/Co multilayer systems [119,146], where an *hcp* structure for the Gd

layer was observed, we found that the Gd layer has grown with a polycrystalline *fcc* structure in all the multilayers. However, Co has grown with polycrystalline *hcp* structures in all the multilayers. XRD data showed that (111) reflection for the Gd in all three multilayers gives the strongest intensity suggesting textured growth for Gd. We obtained a crystalline size of ~ 60 Å for the Gd in all the multilayers.

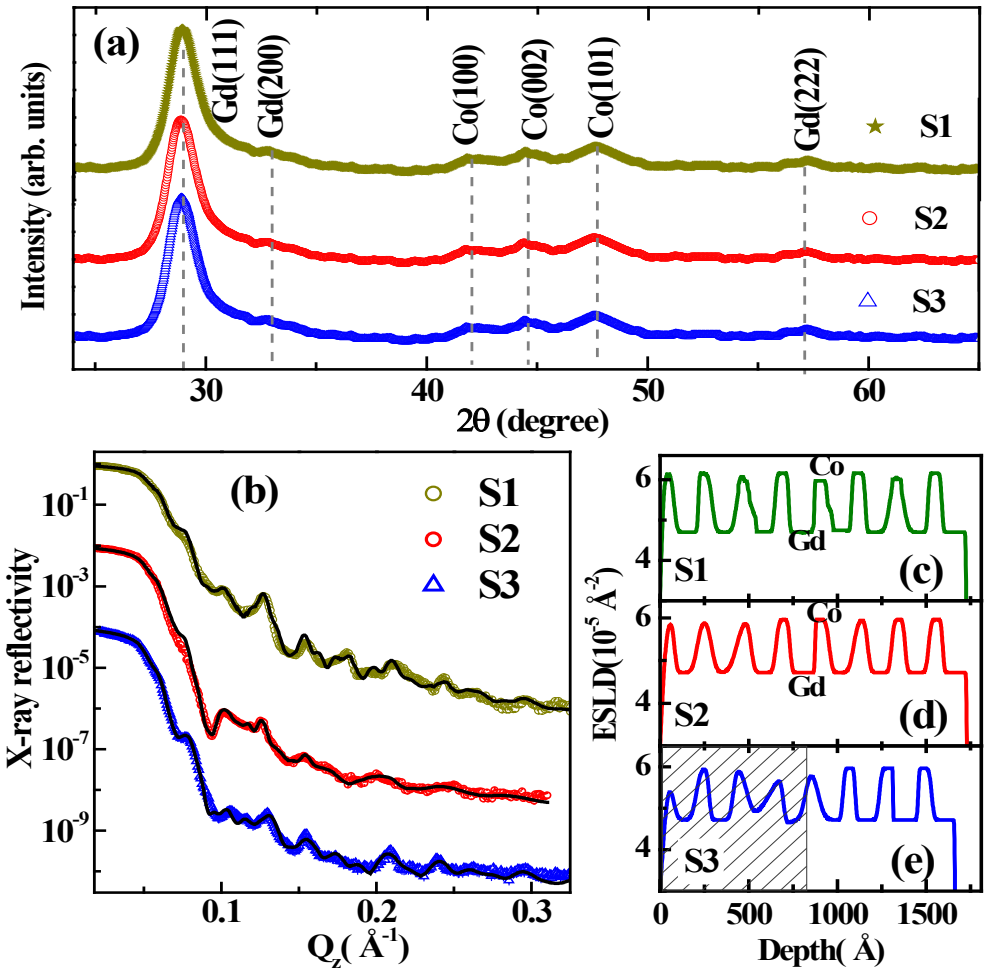

Fig 4.2: GIXRD (a) and XRR (b) data for Gd/Co multilayers, S1, S2, and S3. Solid lines in (b) show the fit to XRR data. (c)-(e) ESLD depth profiles for S1, S2, and S3, which best fitted the XRR data.

Figure 4.2 (b) shows the x-ray reflectivity data (symbols) for multilayers S1, S2, and S3 along with best fits (solid lines). XRR data for different multilayers are shifted vertically for

better visualization. Figure 4.2 (c)-(e) show the ESLD profiles of S1, S2, and S3, which best fitted the corresponding XRR data. XRR provides the individual layer thickness, ESLD profile, root mean square (*rms*) roughness at different interfaces of the multilayer. The parameters obtained from the XRR are given in Table 4.1. A small variation in the roughness is considered for best fit to data.

Table 4.1: Layer structural parameters [thickness (d), roughness (σ_s) and scattering length density (ρ)] obtained from specular X-ray and neutron reflectivity measurements.

Samples		layers	XRR			PNR		
			d (Å)	$\rho_x(10^{-5}$ Å$^{-2})$	σ_s(Å)	d (Å)	$\rho_n(10^{-6}$ Å$^{-2})$	σ_s(Å)
S1	All bilayers (0.2 Pa)	Gd	139±5	4.70±0.20	4±1	142±6	1.05±0.07	4±1
		Co	76±5	5.97±0.15	8±2	72±5	2.29±0.11	8±2
S2	All bilayers (0.4 Pa)	Gd	138±5	4.71±0.20	9±2	142±6	1.06±0.07	7±2
		Co	77±5	5.96±0.15	11±3	72±5	2.26±0.11	10±3
S3	Top 4 bilayers (0.8 Pa)	Gd	137±6	4.68±0.20	11±2	140±6	1.05±0.07	14±3
		Co	75±5	5.96±0.15	15±4	74±5	2.28±0.11	18±4

We obtained an average roughness of 4±1 Å and 8±2 Å for Gd/Co (Co on Gd) and Co/Gd (Gd on Co) interfaces, respectively, in the S1 and 8±2 Å and 12±3 Å for Gd/Co and Co/Gd interfaces, respectively, in the S2. In the case of S3, we observed a higher interface roughness for the top 4 BLs (grown in 0.8 Pa argon pressure), which is depicted in Fig. 4.2 (e) as a shaded region. We obtained an average roughness of ~11±2 Å and 15±4 Å for Gd/Co and Co/Gd interfaces, respectively, for the top 4 BLs of the S2, whereas bottom 4 BLs showed similar interface roughness as obtained for S2 (grown at same argon pressure). In Table 4.1 we have given parameters for the top 4 BLs of S3 and the parameters for the bottom 4 BLs are the same as obtained from S2. XRR measurements suggested an increase in

the interface roughness with the increase in sputtering (Ar) pressure. Moreover, specular XRR measurements clearly suggest a higher interface roughness at the Co/Gd interface for all the multilayers. Asymmetric interdiffusion at two interfaces in Co/Gd multilayers was also observed in an earlier study [124].

4.3.2 Macroscopic magnetization measurements

Magnetization (SQUID) and magneto-transport measurements

Figure 4.3(a)-(c) show the temperature dependent magnetization of S1, S2 and S3 multilayers in field cooled (FC) and zero field cooled (ZFC) modes. The FC data were recorded under the application of an in-plane magnetic field of 500 Oe. The dip in the *M(T)* data where it shows the minimum of magnetization (signature of antiferromagnetic coupling) is called compensation temperature (T_{comp}) and we obtained a T_{comp} of ~ 125 K, ~ 140 K and ~ 150 K for S1, S2 and S3, respectively. Similar *M(T)* behavior is also reported, earlier, for RE-TM systems [66, 67, 73, 119, 146], where Co moments dominate above the T_{comp} and Gd moment dominates below the T_{comp}. In addition, we observed a bifurcation between FC and ZFC below the T_{comp} for multilayers S2 and S3, which were grown at higher Ar pressure. Moreover, the bifurcation between FC and ZFC from S3 is more than that of S2. Such modifications in the macroscopic magnetization data may be due to different growth conditions affecting the interface morphology in these multilayers.

Figure 4.4 shows the macroscopic magnetization hysteresis loops *M(H)* at different temperatures for S1 (left panel), S2 (middle panel), and S3 (right panel) in a small field range (±500 Oe). Though we measured $M(H)$ curves up to a higher field of ±2000 Oe and to show a comparison of $M(H)$ data from three samples we have shown the data for smaller field range in Fig. 4.4. All the data were collected by applying in-plane magnetic field measurements. There is a decrease in the saturation magnetization with the increase in sputtering pressure

(increase in interface roughness) been observed at room temperature (300 K). For S3, we observed a lower saturation magnetization of ~900 emu/cc as compared to that of S1 (~1250 emu/cc) and S2 (~1130 emu/cc).

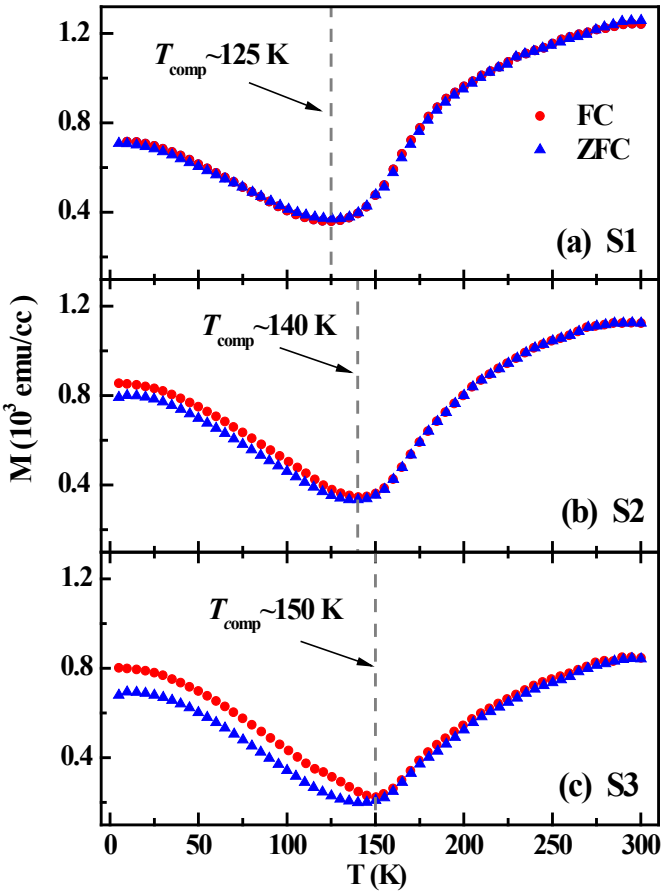

Fig.4.3: Magnetization data as a function of temperature [*M* (T)] under FC (in-plane applied field of 500 Oe) and ZFC conditions for multilayers S1 (a), S2 (b) and S3 (c).

Interestingly the temperature dependence of *M*(*H*) for S1, S2, and S3 showed distinctly different behaviors. Multilayers S1 and S2 showed a symmetric hysteresis loops with a small coercive field (H_c) of ≈ 15 Oe at 300 K, suggesting soft ferromagnetic nature, which increases on decreasing temperature near to the corresponding T_{comp} for S1 (~ 125K) and S2 (~ 140 K). Further decrease in the temperature below the $T_{comp,}$ both S1 and S2 showed a shift in hysteresis loops towards the negative magnetic axis, suggesting a negative exchange bias

effect for multilayers below T_{comp}. Moreover, S2 showed asymmetric hysteresis loops [147], which are shifted along the magnetization axis as well, suggesting additional pinning of moments possibly at interfaces. In contrast, S3 showed a symmetric double hysteresis loop (DHL) behavior [20] and symmetric hysteresis loops above and below T_{comp} (~ 150 K), respectively.

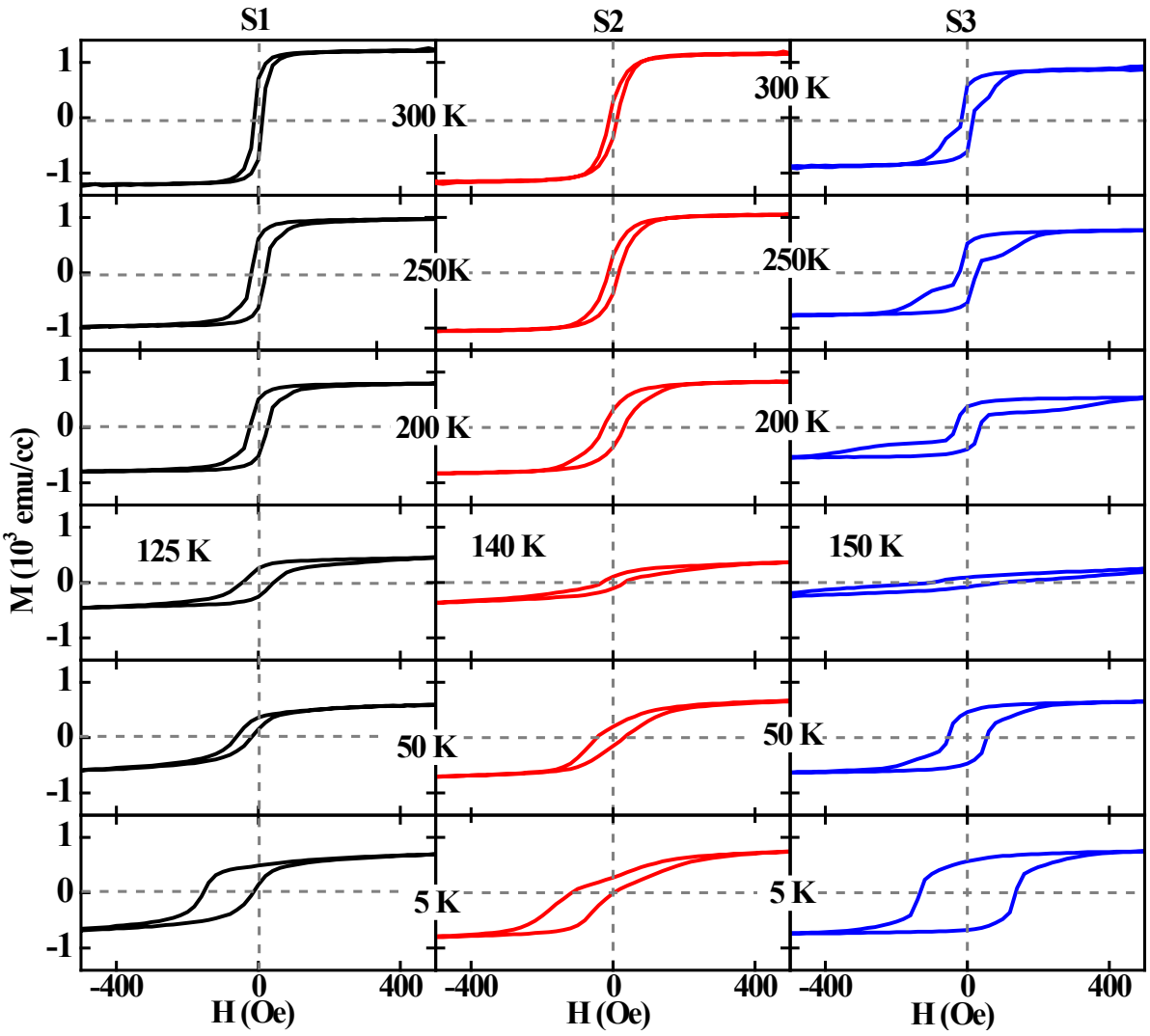

Fig. 4.4: DC magnetization [M (H)] curves at different temperatures for multilayers S1 (left panel), S2 (middle panel), and S3 (right panel).

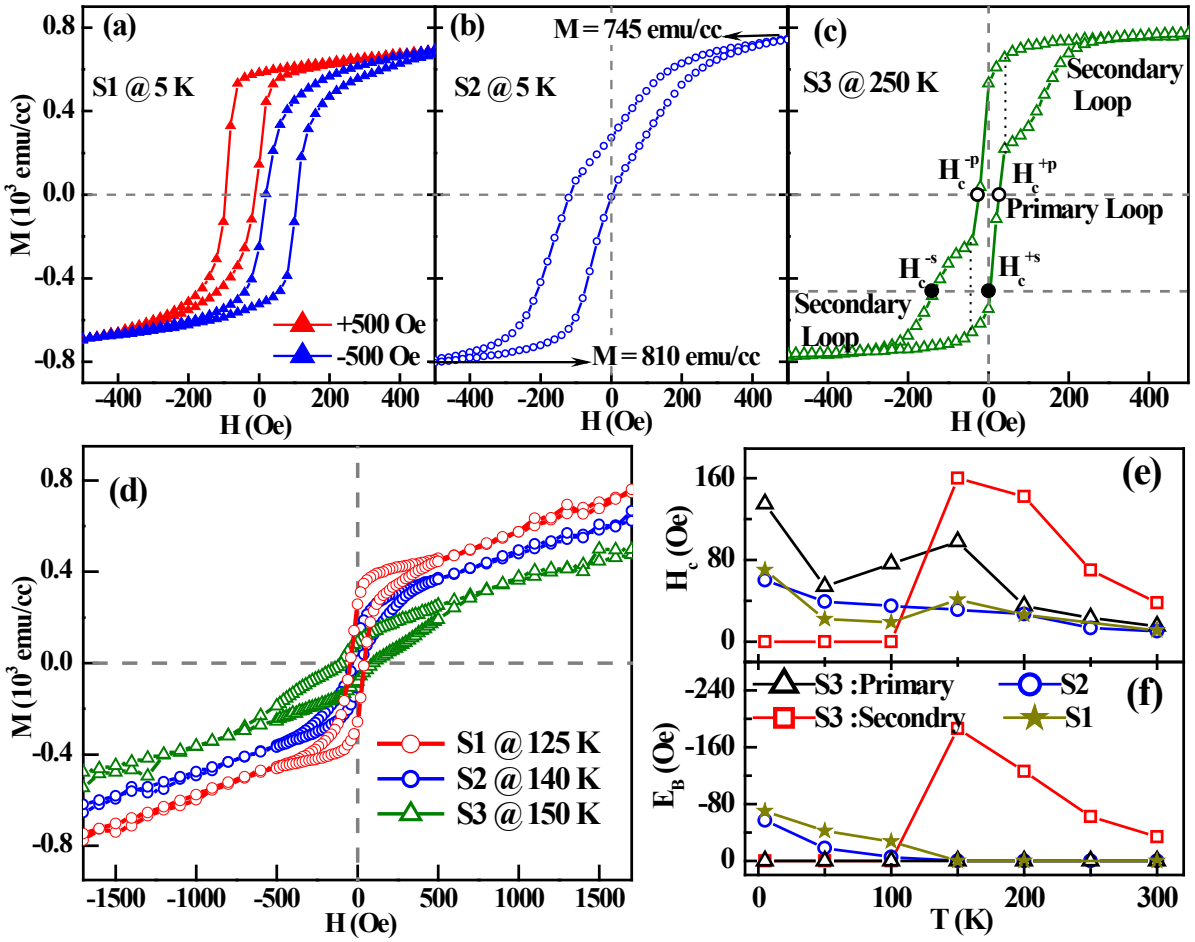

Fig. 4.5: *M* (*H*) curves for S1 (a) at 5 K in the cooling field of ± 500 Oe, (b) S2 at 5K data and S3 (c) at 250 K. Primary and secondary loops for DHL behavior for S3are also depicted in (c) (d) *M*(*H*) curves for S1, S2, and S3 at $T_{comp.}$ The variation of H_c (e) and E_B (f) with temperature.

To confirm the exchange bias at low temperature, we measured the in-plane magnetic hysteresis loops of S1 at 5 K after field cooling it from room temperature in an applied magnetic field of ± 500 Oe [Fig 4.5 (a)]. We observed a shift of hysteresis loop towards the negative (positive) field axis on cooling S1 in a field of +500 Oe (-500 Oe), confirming the negative exchange bias in the system. S2 also showed negative exchange bias at low temperatures however we found additional features like asymmetric nature of the hysteresis loop and small vertical shift of hysteresis loop (along the magnetization direction). Figure 4.5

(b) shows the hysteresis curve for S2 at 5 K. A significant vertical shift (~ 9% at 5 K) of the asymmetric hysteresis loop for S2 [Fig. 4.5(b)] below $T_{comp,}$ which increases on decreasing the temperature, suggests additional pinning of moments possibly at the interfaces. However, S3 did not show any exchange bias at low temperatures (below its T_{comp}). Figure 4.5 (c) depicts the DHL behavior of S3 at 250 K. Similar DHL behaviors as observed for S3 above T_{comp} were also observed in Fe/Tb multilayers[20], though at the low temperatures. The DHL is defined as a superimposition of two loops, a primary loop centered around H = 0.0 Oe and a secondary loop. We have also defined the primary and secondary loops for these DHL behaviors as shown in Fig. 4.5(c) where the $M(H)$ curve is symmetric with a secondary loop shifted along the applied field axis. Figure 4.5(d) shows the hysteresis loops of S1, S2, and S3 at T_{comp} up to the higher field range.

We have estimated the coercive field (H_c) and the exchange bias field (E_B) of all the multilayers at different temperatures. For S3, we have estimated the H_c and E_B of the primary and secondary loops of the DHL character of S2 [Fig. 4.5(c)] in a way similar to described by Paul et al.,[20] for Fe/Tb multilayers. The E_B and H_c are calculated by the average of the sum and difference of the coercive fields, respectively, for the positive and negative field axes and defined as: $E_B = (H_c^+ + H_c^-/2)$ and $H_c = (H_c^+ - H_c^-/2)$[18]. Figure 4.5(e) and (f) show the temperature dependence of H_c and $E_{B,}$ respectively, for S1, S2, and S3. We obtained a monotonic increase in H_c for S1 and S2 on decreasing the temperature from 300 to 5 K. S1 and S2 did not show any E_B above their respective T_{comp}, however, E_B increases below T_{comp} with a highest E_B of ~ -75Oe at 5 K in both the multilayers. For S3, the H_c of the primary loop increases with a decrease in temperature and we obtained the largest H_c of ~ 135 Oe at 5 K. The primary loop at different temperatures displayed no horizontal shift (E_B = 0.0 Oe). Both H_c and E_B of the secondary loops have a similar temperature dependence [Fig 4.5(e) and (f)] with the highest value of H_c (~ 160 Oe) and E_B (~ -185 Oe) occurring at $T_{comp,}$ and the value

of both parameters reduce to zero below $T_{comp.}$ Prieto et al., [148] observed DHL in permalloy (Py)/Gd/Py trilayer where two Py layers were AFM coupled, and it was shown that the DW in Py was controlled by the thickness of Gd layer resulting in a DW dependent magnetoresistance (MR).

Figure 4.6 shows the MR (%) data [$= \frac{(\mathcal{R}(\mathrm{H})-\mathcal{R}(0))}{\mathcal{R}(0)} \times 100$, where, $\mathcal{R}(H)$ and $\mathcal{R}(0)$ are the resistance in the applied field H and in zero field] at different temperatures in the longitudinal direction (applied field and current are in the same direction and along the plane of the film) as a function of the field for multilayers S1 (left panel), S2 (middle panel) and S3 (right panel). MR data measured on sweeping the field in the positive and negative direction are represented by red (line with closed squares) and blue (line with open triangles) curves, respectively. The magnetic field dependence of the MR data at 200 K, show almost reversible (saturated) regions beyond the resistance peaks at two magnetic fields (H_p), similar to other magnetic multilayers [149]. However, the magnetic field corresponding to resistance peaks are larger than the corresponding H_c. In general, H_p and H_c for metallic multilayer coincide with each other. While the coercive field characterizes the random magnetization direction in the entire sample, the peak of the magnetoresistance curves is also an indication of the disordered magnetization configuration. This is consistent with earlier reports on Fe/Gd and Co/Gd multilayers [65,150,151]. Larger H_p as compared to H_c. was also observed earlier for both thin-film and bulk samples [149,152,153] and was attributed to interface scattering. We believe the interface scattering also plays an important role in increasing the H_p beyond H_c in these systems. Furthermore, additional irreversibility in the MR at the field around H_p may be due to field-dependent magnetic structure across the interfaces in this system. The increase in MR at higher fields (> 1.5 kOe), below T_{comp}, suggests a competition between the Zeeman and AFM exchange energies resulting in an increase in the resistance with the increasing field in this region [151].

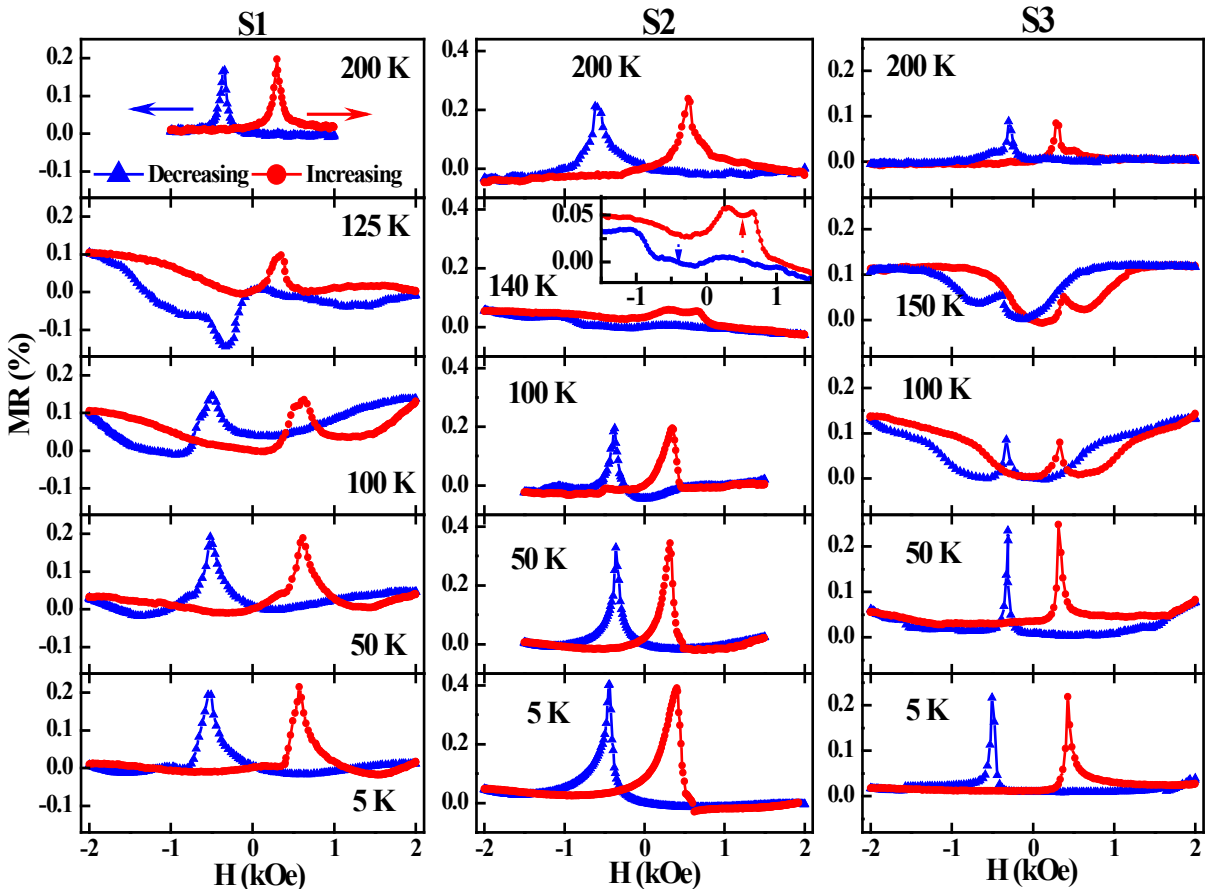

Fig. 4.6: MR (%) data in an applied in-plane magnetic field (longitudinal direction: Current and field are applied in the same direction) at different temperatures for the multilayers S1 (left panel), S2(middle panel) and S3 (right panel).

Interestingly we obtained a completely different MR behavior for these multilayers at and around their $T_{comp.}$ At compensation temperature (125 K and 140 K) for S1 and S2, an irreversible and antisymmetric MR (opposite variation of MR on sweeping the magnetic field in the two directions)was observed in both the multilayers; however it was more prominent in case of S1. The inset at 140 K for S2 highlights the opposite variation of the MR for the different field sweep directions. In the case of S3, we observed more irreversibility in MR at T_{comp} (150 K). We repeated measurements many times to ensure the repeatability of the data

and we observed the same behavior. The additional irreversibility in the field-dependent MR data for multilayers S1, S2, and S3 near T_{comp} may be due to the depth dependent magnetic structure within Co and Gd layers of these multilayers around $T_{comp.}$ To address this specific issue we have used the spin dependent PNR technique as described below.

4.3.3 Temperature dependent Magnetic structure

Depth dependent magnetization: Specular PNR measurements

Specular PNR with polarization analysis, i.e., non-spin-flip (NSF), R^{++} and R^{--}, and spin-flip (SF), R^{+-} and R^{-+}, reflectivities, are used to determine the magnitude and direction of the magnetization vector along the depth of the multilayer [22,91,92,95,100] as described in chapter 2. Figure 4.7 shows the specular PNR data as the NSF [R^{++} (red open circles), R^{--} (blue open triangles)] and SF [$(R^{+-} + R^{-+})/2.0$ (maroon star)] reflectivities and corresponding fits (solid lines) as a function of the wave-vector transfer $Q_{z,}$ normal to the sample surface, at different temperatures for S1 (left panel), S2 (middle panel) and S3 (right panel).

The specular reflectivity data are collected up to a Q_z of ~0.08 Å^{-1}, which includes two Bragg peaks due to the periodic repetition of BLs at Q_z ~ 0.03 Å^{-1} (1st order) and 0.06 Å^{-1} (2nd order) indicating a bilayer thickness of ~ 214 Å. It is noted that the scattering length of Gd varies with the wavelength of the neutron [154]. However, it does not show significant change for the wavelength range used in OFFSPEC and we obtained the NSLD of the Gd by fitting PNR data at 300 K [22]. Gd exhibits a large absorption for thermal neutrons [154], which has been incorporated for fitting PNR data. At 300 K, we did not observe any SF signal in all of the multilayers, suggesting the Co moments in the different layers are aligned along the applied field (the Gd layer has zero moments at 300 K, as T_c for the Gd is ~ 293 K). The nuclear scattering length density (NSLD) and magnetic scattering length density (MSLD) depth profiles at 300 K for S1, S2, and S3 are shown in the lower power of Fig. 4.7.

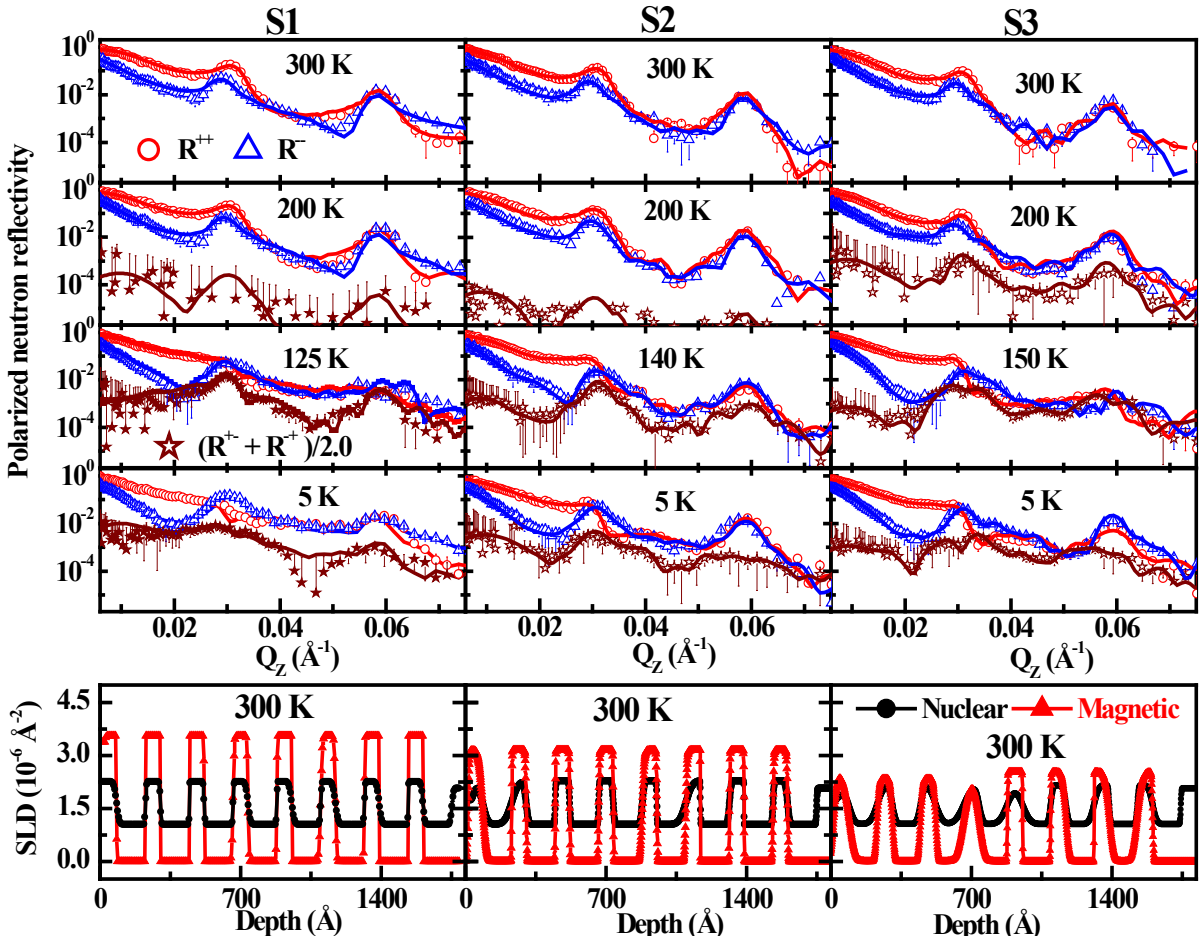

Fig. 4.7: Spin dependent specular PNR data [NSF: R^{++} (red open circles) and R^{--}(blue open triangles); SF: (R^{+-} + R^{-+})/2.0 (maroon star)] along with fit (solid lines) at different temperatures for the multilayers S1 (left panel), S2 (middle panel) and S3 (right panel). NSLD and MSLD depth profiles obtained from specular PNR data at 300 K for multilayers S1, S2, and S3 are shown in the corresponding lower panel.

The NSLD depth profiles of the multilayers obtained from PNR are consistent with the chemical structure obtained from XRR. The layer parameters obtained from PNR data at 300 K for all the multilayers are given in Table 4.1, along with the XRR results. We obtained a magnetic scattering length density (MSLD) of ~ 3.59±0.16×10^{-6} $Å^{-2}$ (1260±35 emu/cc), 3.15±0.15×10^{-6} $Å^{-2}$ (1085±25 emu/cc) for Co layers in the multilayers S1 and S2,

respectively, at 300 K. While for S3, we obtained a MSLD ~2.70±0.20 $\times 10^{-6}$ $Å^{-2}$ (~935±25 emu/cc) for Co layers in bottom 4 BLs and 2.37±0.14 $\times 10^{-6}$ $Å^{-2}$ (~820±20 emu/cc) for Co layers in the top 4 BLs. We obtained a smaller magnetization for Co as compared to its bulk value for all the multilayers. The magnetization values obtained from PNR are in good agreement with the magnetization obtained by SQUID data. The reduction in the average magnetization with an increase in sputtering pressure suggests this reduction is correlated to roughness/intermixing at interfaces.

Remarkably we obtained strong specular SF reflectivity for S3 at 200 K, whereas S1 and S2 show almost negligible specular SF signals, suggesting the existence of a perpendicular (in-plane) component of the magnetization for S3 at 200 K. Additional modification in both NSF and SF reflectivities (Fig. 4.7) are observed at low temperatures for both the multilayers, indicating a more complex magnetic structure at low temperatures, especially at T_{comp}. At 200 K, both S1 and S2 showed negligible specular SF reflectivity, suggesting the magnetization of multilayers is alignment parallel (along or opposite) to the applied field. Specular PNR from S1 and S2 at 200 K suggested an AF coupling between the Gd and Co layer, where Co (Gd) moments are aligned along (opposite to) the direction of the applied magnetic field. We obtained a MSLD of ~3.78±0.17 $\times 10^{-6}$ $Å^{-2}$(~ 1300±40 emu/cc) and ~3.25±0.13 $\times 10^{-6}$ $Å^{-2}$(1120±30 emu/cc) for the Co layer in the multilayer S1 and S2, respectively, at 200 K. In addition, we obtained a MSLD of ~ -0.85±0.05 $\times 10^{-6}$ $Å^{-2}$(~ -293±13 emu/cc) and ~ -0.70±0.06$\times 10^{-6}$ $Å^{-2}$(~ -245±15 emu/cc) for the Gd layer in the multilayer S1 and S2, respectively, at 200 K. The solid lines are the fit to SF data at 200 K for S1 and S2 assuming a small inclination of the moments from the applied field by a small angle (~1-1.5 degree) suggesting the moments are essentially parallel to the applied field at 200 K within error. Attempts to fit the PNR data for all multilayers, where we observed SF reflectivity (PNR data ≤ 125 K for S1; ≤ 140 K for S2; and ≤ 200 K for S3), with

homogeneous Gd and Co layers failed to reproduce the observed results and thus we considered a helical magnetic structure as depicted in Fig. 4.8(a).

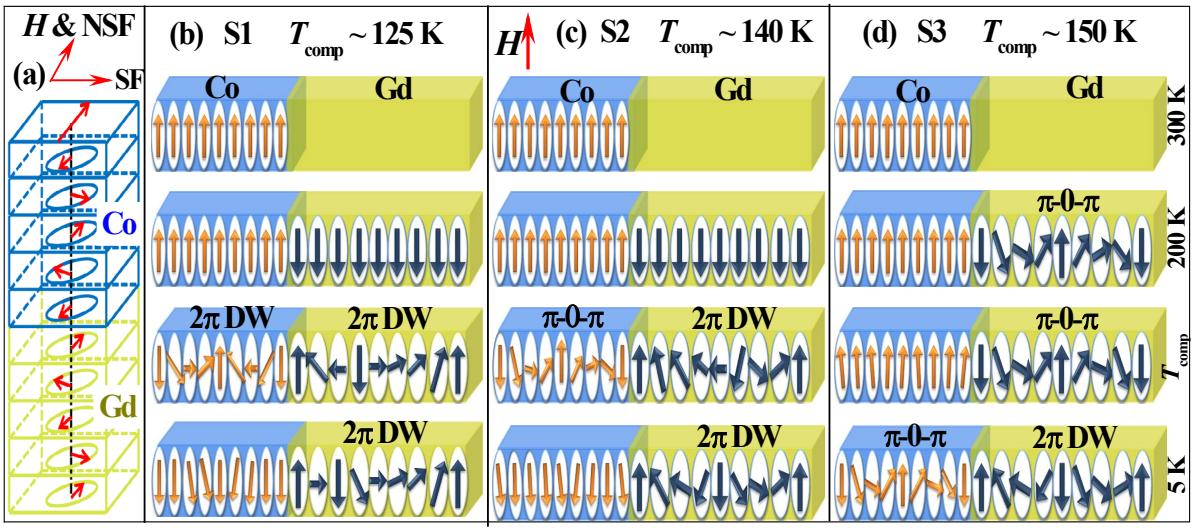

Fig. 4.8: (a) schematic of the magnetic helical structure. Representation of magnetic structures along the depth of a bilayer of Gd/Co in multilayers S1 (b), S2(c), and S3 (d) at different temperatures. For S3 the magnetic structures below 300 K in (d) represents for top 4 BLs.

We have split the individual Co and Gd layer into sub-layers with a constant magnetic moment within the Co and Gd layers but varying the angle of rotation of the magnetization with respect to the applied field i.e. a helical structure. For S3 the magnetic structure of bottom 4 BLs, which were grown at the same Ar pressure (0.4 Pa) as S2, exhibited identical magnetic structure as shown by S2 at all temperatures across $T_{comp.}$ The magnetic structure for a bilayer of the multilayers S1, S2, and S3 at different temperatures, obtained from PNR data, are shown in Fig. 4.8 (b),(c), and (d), respectively, and Fig. 4.8(d) shows the magnetic structure of a bilayer of the top 4 BLs of S3. PNR data at 200 K for S3 suggest a 2π planer DW with a π-0-π rotation in the Gd sub-layers of the top 4 BLs [Fig. 4.8 (d)], whereas Co moments in each layer of the top 4 BLs are aligned along the field direction.

PNR data at 125 K (~ T_{comp}) for S1 suggest a 2π rotation of moments for both the Gd and Co layers of a BL in both the multilayers with full 2π (0 to 2π) rotation of moments in the Gd layer and Co layer [see Fig. 4.8(b)] and form a planar 2π DW structure. In contrast, for S2 we obtained a 2π rotation of moments for both the Gd and Co layers of a BL with full 2π (0 to 2π) rotation of moments in the Gd layer and a π-0-π rotation of moments in the Co layer at 140 K (~ T_{comp}) [Fig. 4.8(c)]. The middle region (~25-35 Å) of each Gd layer in both S1 and S2, at their corresponding T_{comp} showed a magnetization perpendicular (in-plane) to the applied field. As mentioned earlier the magnetic structure of the bottom 4 BLs in S3 are identical to that of S2. However, we observed different magnetic structures of the top 4 BLs of S3. Specular PNR data for S3 at 150 K (~ T_{comp}) suggest the formation a 2π planer DW within each Gd layer with a π-0-π rotation of Gd moments and Co moments are aligned along the direction of the applied field with small deviation (~ ±10 degree).

Specular PNR measurements at 5 K for S1and S2 showed similar behavior and we observed that the Co magnetization is still aligned opposite to the applied field with a small variation in angle ($180^o \pm 10^o$) of rotation of moments for the Co sub-layers. The magnetization of the Gd sub-layers forms a 2π rotation within the Gd layer as shown in Fig. 4.8(b and c). Whereas the magnetization of the top 4 BLs of S3 at 5 K show 2π planar DW within both the Gd and Co layers with a 0-2π and π-0-π rotation of magnetization of Gd and Co sub-layers and shown in Fig. 4.8(d). Thus the temperature dependent magnetic structures in an applied field of 500 Oe for Gd/Co multilayers with different interface morphology show different magnetization structures across T_{comp} and these structures have been confirmed after considering different magnetization models. A comparison of the fits to PNR data of the multilayer S2 at 140 K assuming different magnetic structures are shown in Fig. 4.9.

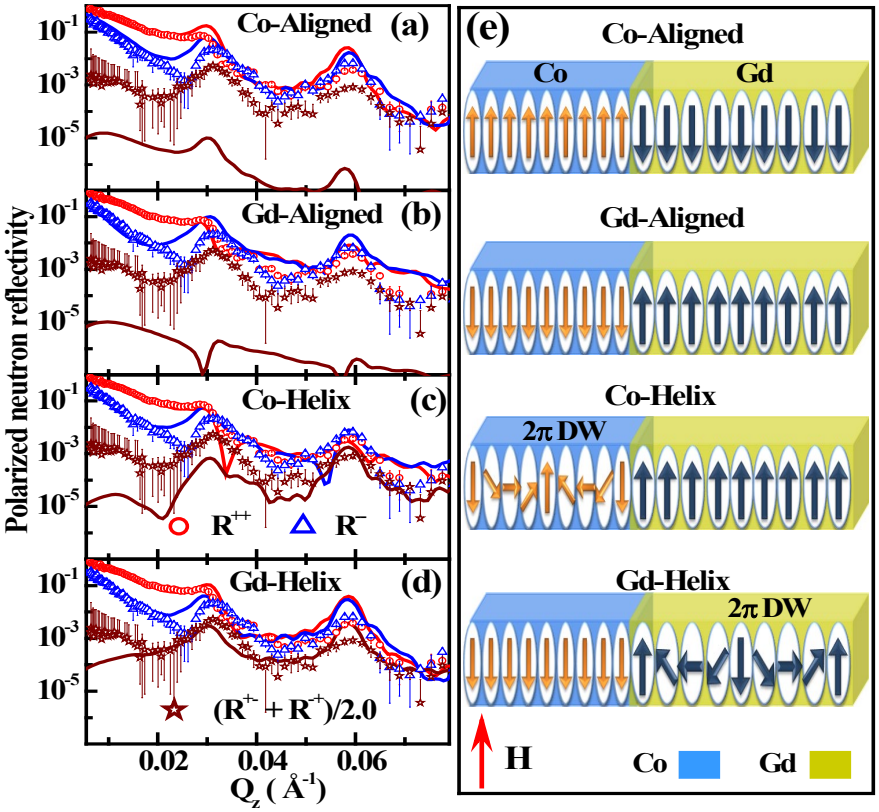

Fig. 4.9: (a-d) Specular PNR data [NSF: R^{++} (red open circles) and R^{--} (blue open triangles); SF: $(R^{+-} + R^{-+})/2.0$ (maroon star)] of S2 at 140 K. Solid lines are fits to data considering different magnetic models shown in (e).

We have considered different magnetic structures where Gd and Co moments are aligned antiferromagnetically at the interface and a few models of magnetic structure for a bilayer of Gd/Co as shown in Fig. 4.9 (e): (i) Co-aligned- where Co moments are aligned along the direction of the field and Gd moments are aligned opposite; (ii) Gd-aligned- Gd moments are aligned along the direction of the field and Co moments are aligned opposite; (iii) Co-helix- a 2π rotation of Co moment within Co layer and Gd moments are aligned parallel to the field; (iv) Gd-helix- a 2π rotation of Gd moment within Gd layer and Co moments are aligned antiparallel to the field. Figure 4.9 (a) to (d) shows PNR data (symbols) and fits (lines) for these magnetic structures. It is evident from Fig. 4.9 that none of the above

mentioned magnetic structure models for Gd/Co multilayer could represent well the experimental data and suggest the magnetization structures shown in Fig. 4.8 best describes PNR data at different temperatures.

In-plane magnetic inhomogeneities: Off-specular PNR measurements

While specular PNR as a function of Q_Z provides depth profiles of the nuclear and magnetic structures, the lateral wave vector transfer Q_X provides information on the correlation of lateral magnetic inhomogeneities (roughness and domains) in the sample plane, via off-specular scattering [91,92,95]. Figure 4.10 shows the NSF (R^{++}) and SF (R^{+-}) data (Q_x– Q_z intensity map) (upper panels) and corresponding simulated profiles (lower panels) from S1, S2, and S3, at different temperatures. The color pattern used to plot experimental and simulated $Q_x - Q_z$ intensity maps are shown in Fig. 4.10 (a) and (b), respectively, which shows a minor difference. We have not found any significant off-specular NSF signal at any temperature for all three multilayers and only a specular ridge around Q_x = 0.0Å^{-1} was observed. The $Q_x - Q_z$ intensity maps at different temperatures from S1 and S2 also suggest no significant off-specular SF signals at other temperatures except at their corresponding T_{comp}. The $Q_x - Q_z$ intensity maps from different multilayers showed off-specular SF (R^{+-}) signal along Q_x at a Bragg position with Q_z ~ 0.06 Å^{-1} for S1 and S2 at their respective $T_{comp.}$ The off-specular SF intensity as a function of Q_x at a Bragg position is termed as Bragg sheet. We observed a strong Bragg sheet for S1 (at 125 K) as compared to S2 (at 140 K) at their corresponding $T_{comp.}$ However, no significant off-specular SF signal was observed for multilayer S3 at any temperature across T_{comp}. The off-specular NSF (both R^{++} and R^{--}) signals for all the three multilayers at different temperatures only showed a specular ridge around Q_x = 0.0 Å^{-1}.

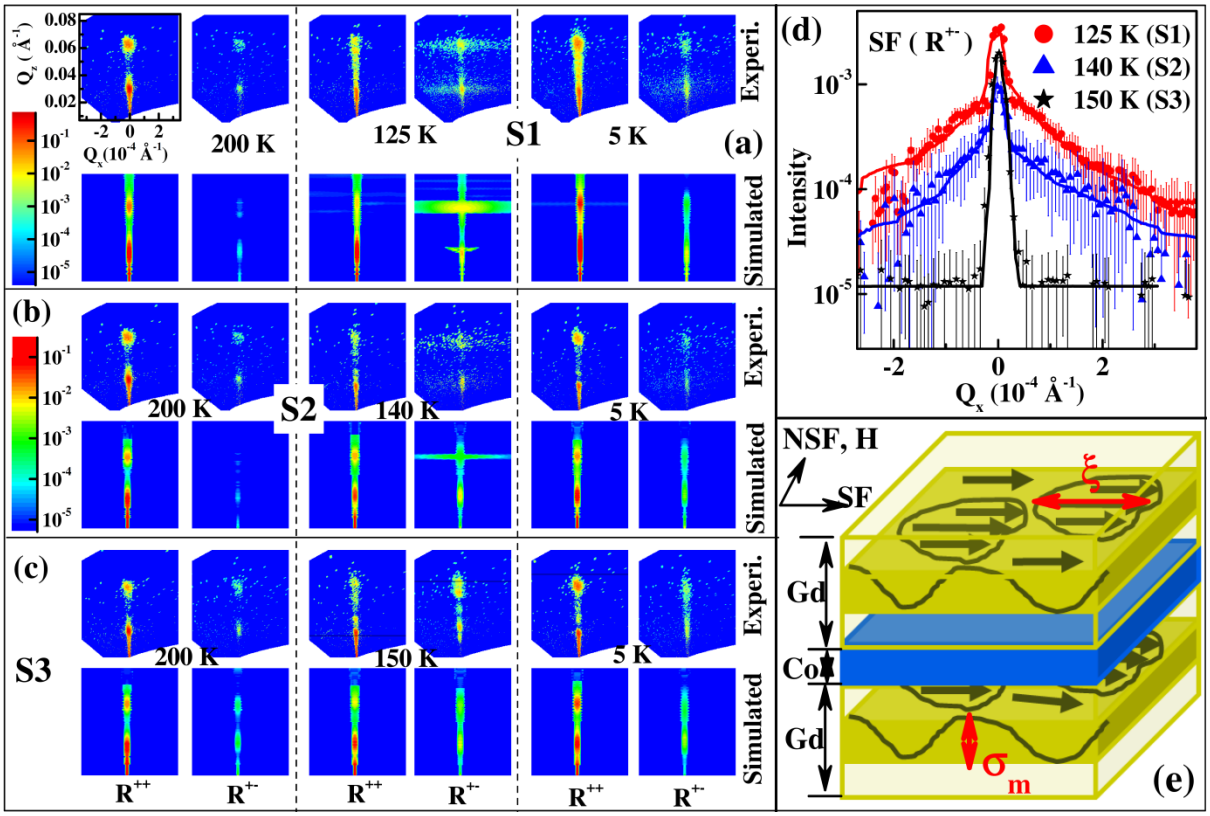

Fig. 4.10: Experimental PNR data (Q_x-Q_z map) (upper part) from the Gd/Co multilayers S1 (a), S2(b), and S3 (c), at different temperatures in NSF (R^{++}) and SF (R^{+-}) modes under an applied in-plane field (H) of 500 Oe. Simulated profiles at different temperatures are shown in a row below the experimental data. (d) Comparison of SF (R^{+-}) intensity (scattered) and fit (solid line) around the Q_z~ 0.06 Å^{-1} for three multilayers at their corresponding T_{comp}. (e) Schematic of spin alignment of the central Gd sub-layer in a bilayer, contributing to the Bragg sheet in R^{+-} intensity at 125 K and 140 K for S1 and S2, respectively.

Multilayers also showed identical SF signal in R^{-+} ($R^{+-} = R^{-+}$) mode. It is noted that SF signals result from the perpendicular (in-plane) component of the magnetization. The occurrence of Bragg sheet (off-specular intensity along Q_x at Bragg positions with Q_z ~ 0.06 Å^{-1}), only for off-specular SF mode for S1 and S2 at 125 and 140 K, respectively, suggests a magnetic origin and indicates the variation of magnetic inhomogeneities in the plane of the

multilayer. The distinct variation of off-specular SF intensity as a function of Q_x around the specular peak ($Q_x = 0$) for the three multilayers near T_{comp} clearly indicates the modification in the in-plane magnetic morphology of the multilayers and suggest its dependence on structural interface morphology.

Simulation of the off-specular reflectivity has been performed using the superfit routine [91]. The quality of the fit can also be compared by plotting the 1-dimensional (a line cut through Bragg sheet at Bragg peak) off-specular SF intensity as a function of $Q_{x.}$ A comparison of the 1-dimensional off-specular SF intensity (scattered) and corresponding fit (solid lines) as a function of Q_x around the $Q_z \sim 0.06$ Å^{-1}for two multilayers at T_{comp} is depicted in Fig. 4.10(d). A Bragg sheet in the SF off-specular signal of S1 at 125 K is well described by in-plane correlation length (magnetic domains) ($\sim\xi$) of 0.17±0.05μm at the central part [thickness ~25Å with *rms* magnetic roughness (σ_m) ~ 9±2 Å] of each Gd layer of S1.Whereas the SF off-specular signal for S2 at 140 K revealed a magnetic domain size of ~ 0.12±0.05μm and magnetic roughness of ~ 6±2Å for the central part (thickness ~ 35 Å) of each Gd layer. Moreover, the magnetic moment of these central regions of the Gd layer in S1 and S2 is aligned perpendicular (in-plane) to the applied field and $\sigma_m$for these intermediate Gd, layers are vertically correlated, which may be contributing to asymmetric MR in S1 and S2 at T_{comp}. We obtained an in-plane correlation length of ~ 0.08±0.04 μm and σ_m~ 4±1 Å for the intermediate Gd layers of S2 at 150 K, which are not correlated vertically. Figure 4.10(e) shows the schematic representation of a bilayer of Gd and Co depicting magnetization direction and magnetic domains in the central part of each Gd layer of the multilayers S1 and S2 at their T_{comp}. The growth of these vertically correlated magnetic inhomogeneities with magnetization perpendicular to the applied field is, therefore, contributing to SF reflectivity with a Bragg sheet at these temperatures. We obtained an in-plane correlation length of ~ 0.08±0.04 μm and σ_m~ 4±1 Å for the intermediate Gd layers of S3 at 150 K (T_{comp}), which

are not correlated vertically. Off-specular PNR at 5 K from all the multilayers also suggest a similar value of in-plane correlation length of ~ 0.08±0.04 μm and development of uncorrelated σ_m~ 7±1 Å for intermediate Gd layers.

4.3.4 Field dependent Magnetic structure

To study the field dependent magnetization we have performed macroscopic magnetization measurements for multilayer S1. Fig. 4.11 (a) shows the *M*(T) data from the multilayer S1 under FC and ZFC conditions in an in-plane field *H,* of 100, 500, and 2000 Oe after cooling the multilayer in the same fields for the FC condition. The *M*(*T*) data at all the fields show the same magnetization at 300 K. Below 300 K, we observed different *M*(*T*) behaviors at different applied fields, suggesting field-dependent interaction in this system, and similar field-dependent variation was also reported earlier for Fe/Gd multilayers [66,67]. At low field (~ 100 Oe) we observed splitting of ZFC and FC data at low temperatures (below ~ 150 K). Whereas *M*(*T*) data for both FC and ZFC conditions measured at higher fields (500 and 2000 Oe) almost follow each other throughout the temperature range.

The *M*(*T*) data show a minimum in magnetization at different temperatures for different applied fields. We obtained different T_{comp} [vertical dashed lines in Fig. 4.11(a)] in different fields. At 100 Oe we obtained a T_{comp} of 107 K for S1. At higher field (2000 Oe) the *M*(T) data show a flat region near T_{comp}, which is consistent with earlier measurements on thicker Gd/Fe multilayer at higher field [152,153], suggesting more distortion of moments near T_{comp} at higher field. The interesting observation from the *M*(*T*) data at the different applied fields is depicted in Fig. 4.11(b), where we have shown the field-dependent variation of T_{comp} and the value of the minimum magnetization (M_{min}) under FC. Both T_{comp} and M_{min} increases with the applied field. *M*(*T*) data showed the irreversibility in FC and ZFC curve at low temperature in an applied field of 100 Oe, similar irreversibility in FC and ZFC data was also

observed in Dy/Fe multilayer at low field, which was attributed to the magnetization changes in Dy layer [20].

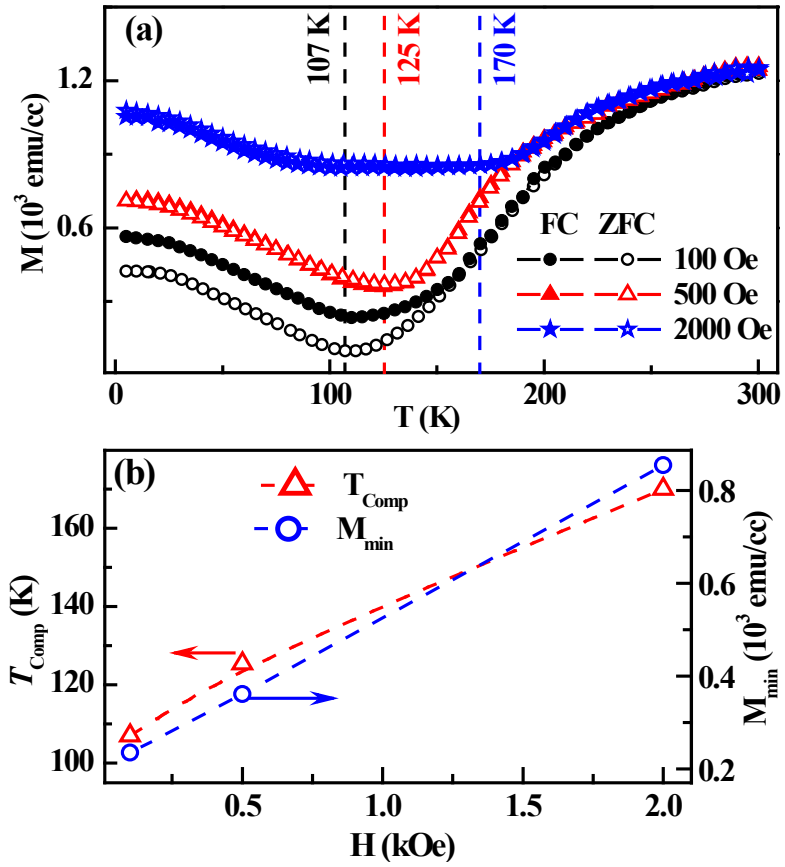

Fig. 4.11: (a) Magnetization data as a function of temperature from the Gd/Co multilayer S1 under ZFC and FC conditions at different applied magnetic fields. (b) Variation of the T_{comp} and minimum value of M(T) for FC conditions with applied magnetic fields.

In order to understand the correlation of the temperature-dependent macroscopic magnetization of the multilayer S1, we have studied the depth-dependent magnetization of the multilayer as a function of temperature in an applied in-plane field of 100 Oe using PNR. Figure 4.12(a) and (b) show the R^{++} (red circles), R^{--} (blue triangles) and $(R^{+-} + R^{-+})/2.0$ (maroon star) reflectivities and corresponding fits (solid lines) for the multilayer S1 for H = 100 Oe, as a function of the wave-vector transfer $Q_{z,}$ at 125 and 5 K, respectively.

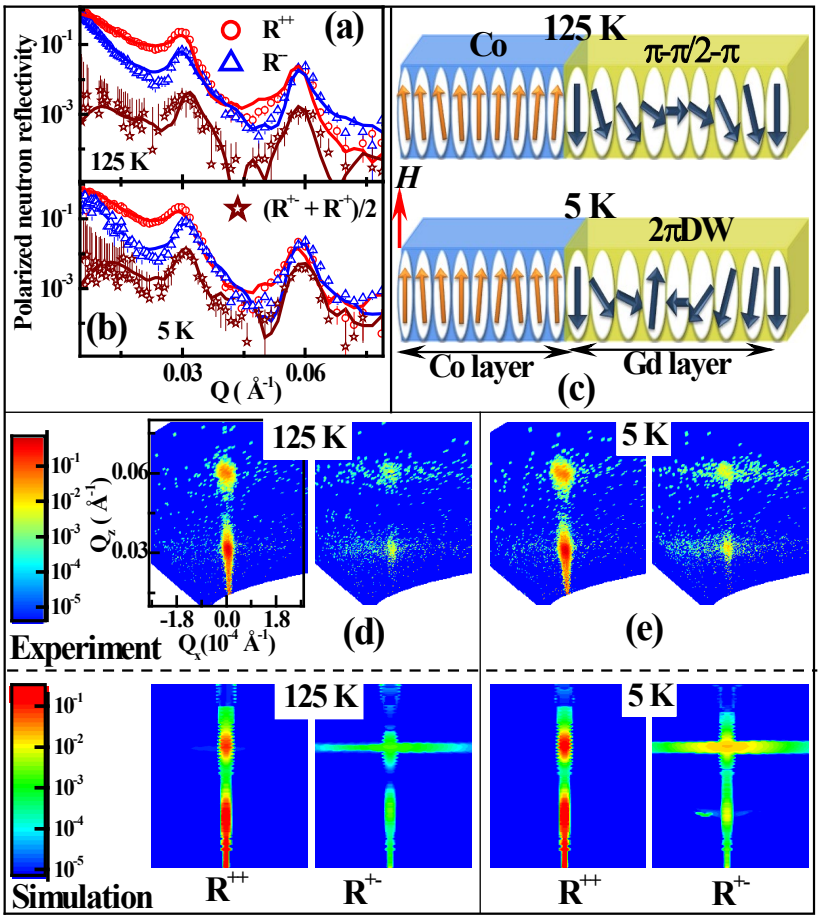

Fig. 4.12: Specular PNR data [NSF: R^{++} (red circles), R^{--} (blue triangles), and SF: (R^{+-} + R^{-+})/2.0 (maroon star)] and corresponding fits (solid lines) for the Gd/Co multilayer S1 in 100 Oe at 125 K (a) and 5 K (b). (c) Representation of magnetization in a bilayer of Gd/Co multilayer obtained from PNR data at 125 K and 5 K. Off-specular PNR data (Q_x-Q_z map) in NSF (R^{++}) and SF (R^{+-}) modes (upper panel) and simulated profiles (lower panel) for the Gd/Co multilayer S1 at 125 K (d) and 5 K (e) for an applied field of 100 Oe. The colour patterns corresponding to the reflected intensity for experimental (top) and simulated (bottom) profiles.

We observed strong specular SF [(R^{+-} + R^{-+})/2.0] reflectivities at these temperatures. Specular PNR data at 125 and 5 K [Fig. 4.12(a) and (b)] revealed a completely different

magnetic structure along the depth of multilayer and is shown in Fig. 4.12(c), which is different from the layer structure obtained for the multilayer at 500 Oe (Fig. 4.8 (b)]. The schematic of magnetic structure in Fig 4.12(c) is a representation for a bilayer of Gd/Co in the multilayer S1 at 125 and 5 K. We found that the magnetization of the Gd sub-layer follows a π-(π/2)-π rotation and the magnetization of the Co sub-layers is aligned along the direction of the applied field [upper panel of Fig. 4.12(c)] at T = 125 K. While PNR data at 5 K suggested a full 2π rotation of the magnetization for Gd sub-layers and magnetization of Co sub-layers are still aligned along the direction of an applied field with larger tilt angle from the applied field as shown in the lower panel of Fig. 4.12 (c). It is noted that at the interfaces, the Gd and Co have coupled antiferromagnetically at both 125 and 5 K, which is consistent with the earlier findings for the RE-TM system [66,67]. The field-dependent alignment of the magnetization of the Gd and Co layers at Gd/Co interfaces at low temperatures across T_{comp} is evident from the magnetic structure of Gd/Co bilayer at two fields 100 and 500 Oe. We found Gd moments are aligned antiparallel (parallel) to the applied field of 100 Oe (500 Oe), which is consistent with an earlier study of the Gd/Fe multilayer in the low field [146], where Fe (Gd) moments are aligned along (opposite) the applied field throughout the temperature range. However, the Gd and the Co are antiferromagnetically coupled at Gd/Co interfaces for both the applied fields at these temperatures.

Figure 4.12(d) and (e) show the off-specular NSF (R^{++}) and SF (R^{+-}) data (Q_x–Q_z intensity map) (top) and corresponding simulated intensity map (bottom) for the multilayer S1 in an applied field of H = 100 Oe at 125 and 5 K, respectively. Unlike at 500 Oe, we observed Bragg sheet (off-specular intensity along Q_x at Bragg positions with $Q_z \sim 0.06$ Å^{-1}), for off-specular SF mode at both 125 and 5 K, however, the multilayer S1 shows a stronger

off-specular SF signal at 5 K than that at 125 K at 100 Oe, indicating more magnetic inhomogeneities at 5 K.

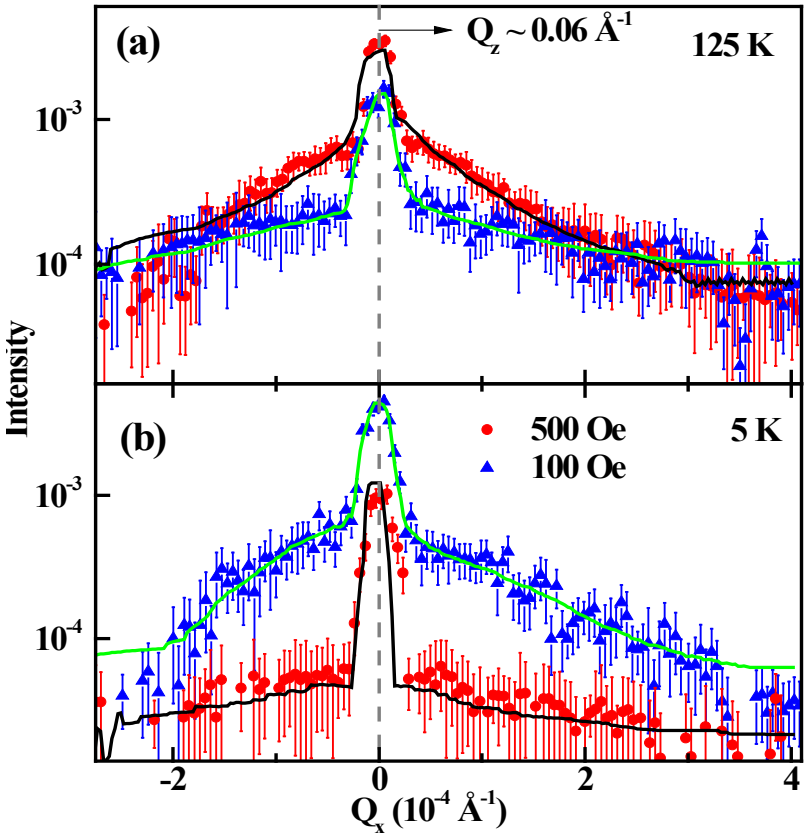

Fig. 4.13: Comparison of off-specular SF (R^{+-}) data (scattered) and corresponding fit (solid lines) as a function of Q_x at 2nd Bragg peak (Q_z ~ 0.06 Å^{-1}) for different fields at 125 K (a) and 5 K (b) for multilayer S1.

On fitting the off-specular PNR for the multilayer at 125 K, we obtained an in-plane correlation length (ξ ~ magnetic domains) of 0.11±0.02μmfor the central region (thickness ~20-25 Å with *rms* magnetic roughness, σ_m ~ 5±1 Å) of each Gd layer with the magnetization direction perpendicular to the applied field in the multilayer. However, the Bragg sheet in the off-specular SF intensity map at 5 K is well described by an in-plane correlation length (ξ) of 0.14±0.02 μm and σ_m ~ 6±2 Å for the central region (magnetization

perpendicular to the applied field) of each Gd layer in the multilayer. Moreover σ_m for these intermediate (25 Å thick central part of each Gd layer) Gd layers at 125 and 5 K are vertically correlated.

The field dependent comparison of one-dimensional off-specular SF PNR data (symbols) with simulated profiles (solid lines) as a function of Q_x near the 2nd Bragg peak at temperatures 125 and 5 K are presented in Fig. 4.13 (a) and (b), respectively. The one-dimensional off-specular intensity profile (Fig. 4.13) is a line cut along Q_x at $Q_z \sim 0.06$ Å^{-1}. At 125 K, we find higher off-specular SF intensity in an applied field of 500 Oe as compared to that at 100 Oe. While at 5 K the off-specular SF intensity for 100 Oe field is larger than that for 500 Oe. Analysis of off-specular PNR data suggests a distinctively different in-plane correlation length and roughness for the vertically correlated central part of each Gd layer in the two fields. We obtained a ξ (σ_m) of ~ 0.17±0.02μm (9±2 Å) and 0.09±0.02 μm (2±1 Å) at 125 and 5 K, respectively, on cooling the multilayer in a field of 500 Oe [19]. In contrast, at 100 Oe we obtained smaller values of the ξ and σ_m at 125 K as compared to that at 5 K.

4.4 Discussion

The depth dependence study using specular XRR (Fig. 4.1) and PNR (Fig. 4.7) measurements clearly suggested the dependence of the interface structure on the growth parameter (argon pressure) and we found that the Gd and Co layers grown at higher argon pressure show higher interface roughness. The increase in the interface roughness indicates significant intermixing/interdiffusion at the interfaces, hence, interfacial modifications can influence the exchange interaction between Gd-Co ($J_{Gd\text{-}Co}$) near interfaces. The additional exchange interaction ($J_{Gd\text{-}Gd}$ and $J_{Co\text{-}Co}$) at the interface due to intermixing may also be contributing towards the irreversibility of FC and ZFC data $\leq T_{comp}$ in the S2 and S3. For S1

negligible irreversibility in FC and ZFC data were observed which is grown with lower interface roughness. Specular PNR suggested the temperature dependent magnetic structure within the Gd and Co layers of the multilayers. The formation of 2π planar DWs in both Gd and Co layers at the T_{comp} was observed for S1 and S2. However, PNR data for S3 showed different magnetic structures for the top and bottom 4 BLs, which were grown at different Ar pressures. We believe that a higher intermixing at the Co/Gd interface in the top 4 BLs of S3modify the interactions at interfaces that might be contributing to the formation of helical magnetic structure in the Gd layer above (200 K) T_{comp}(140 K).

One of the interesting findings in this study was the observation of different *M*(H) behaviors for the multilayers across the $T_{comp.}$ The shift of the hysteresis curve along the opposite direction of the applied field (negative exchange bias) for S1 and S2 below their corresponding T_{comp} may be due to the formation of planar 2π DW at the interfaces with strong AFM coupling. While the vertical shift and asymmetric nature of the *M*(H) curve at low temperature for S2 may be due to the pinning of moments at the interface as a result of modified interface morphology. For S3 we observed DHLs above $T_{comp,}$ similar DHLs were earlier observed at a higher temperature (room temperature and below) in the CoNi/Gd/CoNi [155] and Py/Gd/Py [148] trilayer systems. The double loop behavior observed for Py/Gd/Py heterostructure [148] near the room and intermediate temperatures were attributed to the formation of antiparallel alignment of magnetization in Py and a DW behavior within Gd layer. While in the case of CoNi/Gd/CoNi heterostructures [155], the DHLs were only observed for trilayers having thicker (≥ 8 nm) Gd layer, which decoupled the two FM (CoNi) layers. The CoNi/Gd BL did not display any DHL behaviors. DHLs behavior in the trilayer was attributed to the interaction of the CoNi(top)/Gd hard ferromagnetic and CoNi (bottom) soft ferromagnetic subsystems, which are decoupled at higher temperatures. In the present study, the multilayers have Gd of thickness ~ 14 nm and are decoupled at 300 K. We also

observed higher intermixing at the interface for both the S2 and S3, which showed different temperature-dependent evolution of the magnetization loops. We believe the DHLs behavior observed for S3 at temperatures $>T_{comp}$ might be resulting due to the coexistence of two magnetic subsystems (top and bottom 4 BLs grown with different argon pressures), which are decoupled and show different magnetic structures within the Gd and Co layers. PNR clearly suggested a different magnetic structure for top and bottom BLs at temperatures $>T_{comp.}$ Whereas at low temperatures Gd moments increase, which results in a strong coupling across interfaces as well as the evolution of symmetric loops. However, the contribution of the interface cannot be neglected completely.

Another significant finding of the present study is the different MR behaviors of multilayers in the low field region near $T_{comp.}$ The MR data from all three multilayers, well above and below $T_{comp,}$ show similar behavior as shown by other RE-TM multilayers in the low field range [65,146,150,151]. Near T_{comp} for S1and S2, we observed an antisymmetric MR, where MR shows peaks in the opposite direction on sweeping the magnetization in the opposite direction. However, the antisymmetric MR behavior is not as prominent as compared to S1. Different mechanisms are proposed to understand the MR effects in magnetic materials, however, these effects share the common symmetry with respect to magnetization reversal, namely MR (H) = MR ($-H$). It is believed that the variation of multi-domain configuration during the magnetization reversal process with MR (H) = -MR ($-H$) anomaly contributes to antisymmetric MR [156-158]. However, there are mixed reports regarding the experimental conditions required for the observation of antisymmetric MR [156-158]. Specular and off-specular PNR data suggested the evolution of perpendicular (in-plane) magnetization in the central part of each Gd layer and the growth of magnetic roughness for these interfaces which are vertically correlated. These magnetic domains with higher magnetic roughness contribute to a Bragg sheet in SF off-specular PNR data. Thus the

mutual perpendicular direction of the domain wall, the current, and the magnetization for the intermediate Gd layer might be contributing to the possible antisymmetric nature of MR at T_{comp}. A similar geometry of these parameters was attributed to the observation of antisymmetric MR in Pt/Co multilayer [156]. However, the variation of helical magnetization as a function of temperature for all the multilayers may be contributing towards the additional irreversibility observed in MR across $T_{comp.}$ While the MR for S3 around T_{comp} shows larger irreversibility throughout the field scan, this may be due to a rotation of magnetization within the Gd and Co layer for two BLs which are decoupled and provide additional resistance in the system on changing the direction of the field.

4.5 Summary

We have studied the exchange coupling in Gd/Co multilayers with different interface morphology (deposited on different growth conditions) on field cooling the multilayers in an in-plane magnetic field of 500 Oe at different temperatures. The magnetic measurements revealed that multilayer S1 and S2, having lower intermixing at interfaces are strongly coupled and showed negative exchange bias $<T_{comp}$ (~ 125 K for S1, 140 K for S2), with a highest E_B of ~ -75Oe and -60 Oe at 5 K for S1 and S2, respectively. Whereas the multilayer S3 with different interface structure for the top and bottom 4 BLs are decoupled above T_{comp} (150 K) and showed DHLs with exchange bias for temperatures $>T_{comp.}$ Specular PNR provided a detailed depth-dependent magnetic structure of multilayers at different temperatures and suggested the formation of planar 2πDW, within both the Co and Gd layers of S1 and S2 at T_{comp}. In contrast, specular PNR for S3 revealed different magnetic configurations for two sets of 4 BLs with different interface morphology. Spin-dependent off-specular PNR measurements demonstrated the evolution of magnetic inhomogeneities in terms of magnetic roughness and evolution of the magnetic domain (in-plane correlation

length). A Bragg sheet in off-specular SF PNR data from multilayers S1 and S2 suggested the formation of the magnetic domain of size 0.17μm and 0.12 μm with magnetization direction perpendicular (but in the plane) to the applied field in the central part of each Gd layer at T_{comp}, which are highly correlated along the thickness and contributed to the antisymmetric MR observed in these multilayers at T_{comp}. Off-specular PNR for S3 at T_{comp} revealed a smaller domain (~0.08 μm) and magnetic roughness, which are not correlated vertically. While the magnetic roughness (inhomogeneities) increases at 5 K for both the multilayers, which are uncorrelated vertically. The field dependent PNR results from S1 revealed the AF coupling at the Gd/Co interfaces; however, the alignment of Gd (Co) moment along the applied field is highly dependent on the field. The study revealed the interface dependent magnetic structure in Gd/Co multilayers strongly contributes to different macroscopic magnetic and magnetotransport properties and thus it can have promising applications in device technology.

Chapter 5

Annealing driven structure and magnetic properties of Fe-Cu-Pt heterostructures

5.1 Introduction

Recently, ferromagnetic (FM)/heavy metal heterostructures have attracted much attention in the spin-based technological application through spin-orbit torques [159], spin Hall effect [134,160], spin pumping [161,162], Dzyaloshinskii-Moriya interactions [133, 163], etc., phenomena. In particular, Fe (FM)/Pt (heavy metal) systems have been studied due to its magnetic properties that can be used for possible ultrahigh density magnetic recording applications [164-166]. FePt alloy thin films with ordered face-centered tetragonal (*fct*) or $L1_0$ phase exhibit very high uniaxial magnetocrystalline anisotropy along the c direction of the crystal structure and shows perpendicular magnetic anisotropy, which is desirable for high-density magnetic recording storage devices. Nanoparticles of FePt ordered alloy have also shown promising electro-catalysis towards the oxygen reduction reaction in proton-exchange membrane fuel cells [167-169]. However, as-grown FePt alloy film shows a disordered face-centered cubic (*fcc*) phase (soft phase) and to obtain *fct* phase of FePt films a high temperature annealing of as-grown *fcc* FePt phase is necessary. In general, an annealing temperature of T_a> 600 °C is required to transform the disordered structure to an ordered one. Efforts have been made to reduce the ordering temperature of FePt films by introducing (a) buffer layer [170-172], (b) capping layer [173,174], and (c) addition of the third element into the FePt system to form a ternary alloy compound [77,175,176]. One of the effective ways to

reduce the ordering (*fcc* to *fct*) temperature of FePt film is by adding Cu into the FePt, which is very effective and studied extensively in the literature, and this results in the formation of $FePt_{(1-x)}Cu_x$ ternary alloy [76,177,178]. These ternary alloys show different magnetic properties [76,177,178].

For high-density magnetic storage application of FePt based alloy, superparamagnetic (SP) property is a limitation due to grain size-dependent exchange interaction between the grains of the alloy. However, excellent SP properties of nanoparticles of FePt based alloys have shown the potential system to be used in the next generation for biomedical applications [179]. Upon annealing the FePt/Cu multilayer system with a thicker Cu layer at 400 ^{o}C has resulted in the formation of *fct* ternary $(FePt)_{0.42}Cu_{0.58}$ alloy phase [77], which has shown a SP property.

The exchange bias effect at room temperature [180,181], without any field cooling procedure, in a FM coupled layers are very interesting systems that have been studied for the technological application. Conventionally, exchange bias is a consequence of the interfacial exchange interaction between an FM and antiferromagnetic (AFM) material [180,181] and is manifested by a shift of the FM hysteresis loop along the magnetic field axis after field cooling through the Neel temperature of the AFM. However, an induced exchange bias behaviour has also been observed in systems with two coupled FM materials such as a Pt/Co multilayer and a NiFe thin film [43,182], which is attributed to the interplay between out-of-plane and in-plane anisotropies of the Pt/Co multilayer and NiFe thin film, respectively. Similarly, bilayers of soft and hard ferromagnetic thin films also showed remarkable exchange bias [27,183,184]. Navas et al., [27] observed an exchange bias effect in a low applied magnetic field, consisting of a shift of the in-plane minor hysteresis loops along the field axis in $Co_{0.66}Cr_{0.22}Pt_{0.12}$/Ni (hard/soft) ferromagnetic bilayer, whereas there was no shift in hysteresis loop on applying the larger field. The composite films consisting of $L1_0$ FePt as

hard magnetic and soft magnetic (e.g. Fe, Co, etc.) phases also exhibit interface dependent complex magnetic properties, e.g. exchange spring phenomena [185, 186], exchange bias effect [42,187,188], magnetization reversal process [189, 190], etc. Both disordered and ordered FePt phases are expected to form on thermal annealing of Fe/Pt multilayer, which may give rise to these complex magnetic properties. However, to understand the mechanism and kinetics of the transformation of Fe-Cu-Pt heterostructures due to annealing a systematic interdiffusion and the depth-dependent structure-magnetic correlation in the nm length scale is highly desirable. Such a study is also important for understanding the phase transformation, evolution of new phases, and investigation of possible improvement in the properties desirable for the technological application of the system.

In this chapter, we systematically investigated, in detail, the evolution of structure and magnetic properties of the as-deposited and post-annealed Fe-Pt-Cu heterostructures grown on silicon substrates with Cu as an intermediate layer (Fe/Cu/Pt heterostructure) and a capping layer (Fe/Pt/Cu heterostructure). The structure-magnetic property correlation of Fe-Cu-Pt heterostructures, as a function of annealing temperature (300 to 600 ^{o}C) has been studied by combining various *ex-situ* techniques including, grazing incidence x-ray diffraction (GIXRD), secondary ion mass spectrometry (SIMS), x-ray reflectivity (XRR), polarized neutron reflectivity (PNR) and superconducting quantum interference device (SQUID) magnetometer. The systems, which in the as-grown state exhibit soft ferromagnetism with easy axis in the plane of the film, show many interesting magnetic properties on annealing at successively higher temperatures.

5.2 Experimental Details

Two Fe-Cu-Pt trilayer heterostructures with a nominal structure of Si(100)/[Fe(200Å)/Cu(50Å)/Pt(200Å)] and Si(100)/[Fe(200Å)/Pt(200Å)/Cu(50Å)], henceforth known as S1 and S2, respectively, were grown on Si(100) substrate using dc magnetron sputtering. Figure 5.1 shows the schematic representation of two heterostructures S1 and S2. A base pressure of 1×10^{-5} Pa was achieved before the deposition of trilayers. The deposition was carried out at room temperature and for achieving better uniformity we rotated substrate at 60 rpm on its own axis. The individual thickness of each layer was estimated using XRR measurements. The evolution of the structure and magnetic properties and alloy formation at the interfaces of the heterostructures were studied on successive annealing at 300, 400, 500, and 600 °C. Heterostructures were annealed at different temperatures under a vacuum (~10^{-5} Pa) for a time period of 30 minutes at each annealing stage.

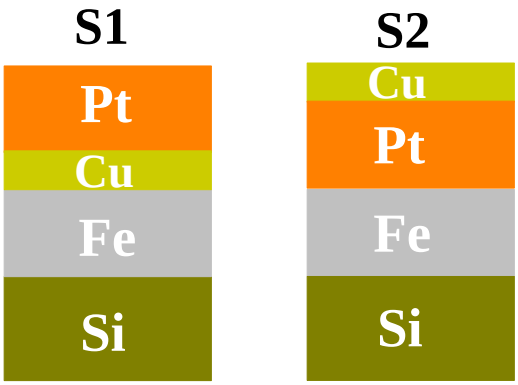

Fig. 5.1: Schematics of the structure of Fe-Pt-Cu heterostructures.

The crystalline structure of trilayers samples was investigated using GIXRD with Cu K_α radiations at a fixed grazing incidence of 1º. Elemental depth distribution analysis of Fe, Pt, and Cu present in the as-deposited and post annealed at 600 °C trilayer samples were carried out using Cameca IMS-7f SIMS instrument equipped with both oxygen duoplasmatron and

cesium thermal ion source. Macroscopic magnetization measurements were carried out using a SQUID magnetometer. All the magnetization measurements reported in this chapter were measured by applying the field along the plane of the film (along (001) Si substrate). The depth-dependent structural and magnetic properties of the trilayers were characterized using XRR and PNR techniques. PNR experiments were carried out using a PNR instrument (neutron wavelength ~ 2.9 Å) at DHRUVA, India [78]. An in-plane magnetic field of ~1.5 kOe was applied to the samples during PNR measurements. The details about the data analysis formalism used in this thesis are given in chapter 2.

5.3 Results

5.3.1 Structural characterization

GIXRD measurements

Figure 5.2(a) and (b) show the recorded GIXRD pattern for heterostructures S1 and S2, respectively, in the as-deposited and post-annealing at 300 ºC- 600 ºC conditions. For both the heterostructures in as-deposited cases, we observed polycrystalline face-centered cubic (*fcc*) and body-centered cubic (*bcc*) structures [191] for the Pt and the Fe layers, respectively. However, the Pt layer in S1 and S2 shows preferential growth along (111) and (200) direction, respectively. This can be seen in Fig.5.2(c) where we have plotted the intensity ratio ($I_{Pt(111)}/I_{Pt(200)}$) of the (111) and (200) peaks as a function of annealing temperature (0 ^{o}C corresponds to as-deposited heterostructures). We have not observed any change in the crystalline structure on annealing the heterostructures at 300 °C, except that there was a small change in the intensity ratio ($I_{Pt(111)}/I_{Pt(200)}$), which decreases (increases) on annealing the S1(S2) heterostructure at 300 °C. No significant difference in GIXRD data from the S1 annealed at 400 °C was observed and only a reduction in intensity ratio [Fig.5.2(c)] was

found. In contrast, on annealing S2 at 400 °C, we observed additional Bragg peaks corresponding to the ordered (*fct*) FePt alloy phase [191] (Inset of Fig.5.2 (b) shows the double peaks correspond to Pt(111) and FePt(111) near 2θ ~40 degrees, for S2 annealed at 400 °C).

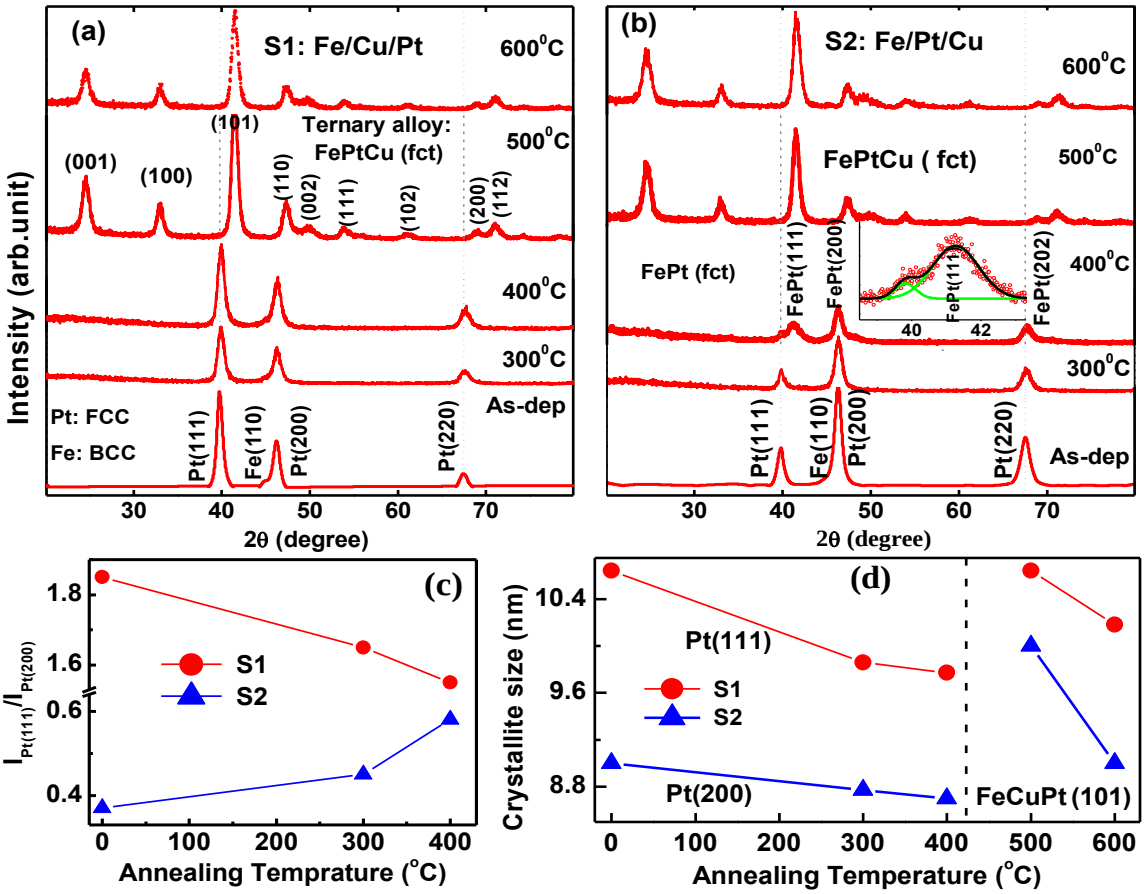

Fig. 5.2: GIXRD pattern from as-deposited and annealed heterostructures S1 (a) and S2 (b). Bragg reflections corresponding to different elements are indexed in (a) and (b). (c) Intensity ratio for (111) and (200) Pt reflection as a function of annealing. (d) Variation of crystallite size of Pt and FePtCu as a function of annealing temperatures.

Formation of a thinner *fct* alloy layer on annealing heterostructure S2 at 400 °C as compared to S1 clearly indicates low interdiffusion at interfaces (in nm length scales) at low temperatures ≤ 400 °C. For the S2, Pt is directly grown on Fe as compared to S1 where a thin

Cu layer separates the Fe and Pt layers, therefore FePt alloy formed in S2 is due to low interdiffusion of Fe and Pt at 400 °C. With further annealing of both the heterostructures at 500 and 600 °C, we observed the formation of a polycrystalline FePtCu ternary alloy. The emergence of the (001) and (100) Bragg peaks at low angles (Fig.5.2) and other Bragg peaks are indexed in Fig.5.2(a) for heterostructures annealed at 500 and 600 °C also confirms alloy formation. The GIXRD data for post-annealed heterostructures at temperature $\leq 500^{o}$C further suggests a preferential growth of ordered (*fct*) ternary alloy phase of FePtCu along (101) direction [191].

The evolution of structural properties with the annealing temperatures is further studied by estimating the grain (crystalline) size of different elements in both the heterostructures using the Scherrer formula as given in chapter 2. We have used the highest intensity Bragg peaks of Pt, i.e. (111) and (200) reflections in heterostructures S1 and S2, respectively, annealed up to 400 ^{o}C. For heterostructures annealed at T $\geq$ 500 ^{o}C, we used the highest intensity Bragg peak of FeCuPt (101) alloy. Figure 5.2 (d) shows the variation of grain size as a function of annealing temperatures. In the as-deposited condition, we obtained a grain size of~ 11 nm and ~ 9 nm for Pt in heterostructures S1 and S2, respectively. Upon annealing the heterostructures at 300 ^{o}C and 400 ^{o}C a small decrease in the grain sizes was observed. Ternary FePtCu alloy phase with a crystallite size of ~ 10 nm was observed on annealing both the heterostructures at 500 °C. A small reduction in the crystallite size of the ternary alloy is observed on further annealing of the heterostructures at 600 °C. Thus post-annealing of the heterostructures above 400 ^{o}C, fast, long-range interdiffusion was observed which accompanied the evolution of polycrystalline *fct* FePtCu alloy phase for both the heterostructures.

Depth dependence structure by XRR and SIMS

Figure 5.3(a) and (b) show the XRR data for heterostructures S1 and S2, respectively, in the as-deposited and post-annealed states. XRR data for different states are shifted vertically for better visualization. Solid lines in Fig. 5.3(a) and (b) represent the corresponding fits to XRR data from S1 and S2. Figure 5.3 (c) and (d) show the ESLD depth profiles of the heterostructures S1 and S2, respectively, for as-deposited and post-annealing at different temperatures.

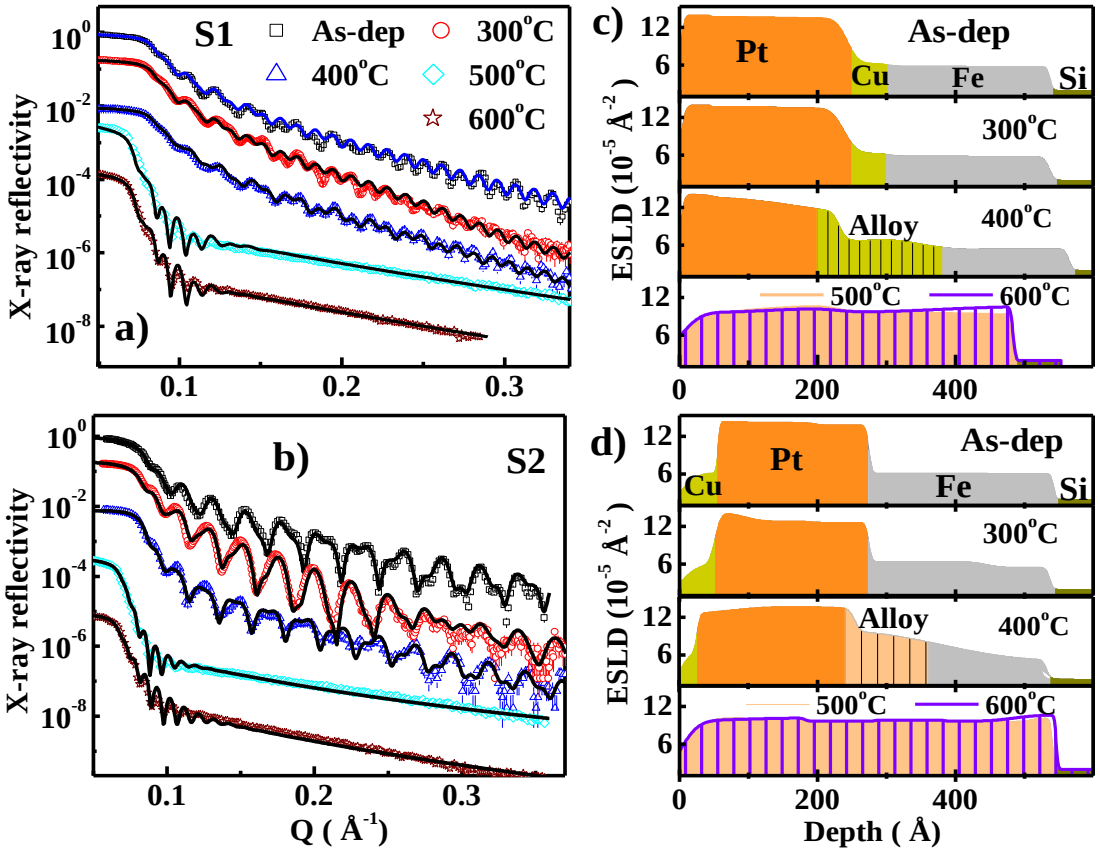

Fig. 5.3: X-ray reflectivity (XRR) data from heterostructures S1 (a) and S2 (b) for as-deposited and post-annealing at different temperatures. (c) and (d) The electron scattering length density (ESLD) depth profile of S1 and S2, which best fitted (solid lines) the XRR data in (a) and (b).

The parameters extracted from XRR measurements for as-deposited heterostructures S1 and S2 are given in Table 5.1. However, a small variation (within the error on parameters) in ESLD along the thickness of the Fe and the Pt layers (Fig.5.3 (c) and (d)) were considered to get the best fit for XRR data. On annealing the heterostructure S1 at 300 °C, we observed no significant change in the depth-dependent ESLD as compared to that of the as-deposited heterostructure. However on annealing S2 at 300 °C, a small variation of ESLD especially at interfaces was observed, suggesting interface dependent interdiffusion of elements (for S2, Fe and Pt diffuses fast as they are in direct contact with each other). On annealing the heterostructures at 400 ^{o}C we observed the formation of alloy phases at the interfaces. GIXRD data clearly suggested the formation of crystalline FePt alloy on annealing the heterostructure S2 at 400 ^{o}C and same can be observed as a change in the ESLD **(~** 10.4×10^{-5} $Å^{-2}$ for alloy layer) at the Fe/Pt (Pt on Fe interface) interface from XRR measurements (Fig.5.3 (d) highlighted area). There is also a change in ESLD at Pt/Cu interface, suggesting interdiffusion of Cu and Pt in the heterostructure.

Table 5.1: Parameters for Fe-Pt-Cu heterostructures S1 and S2 obtained from XRR in the as-deposited condition.

Parameters	S1: Si/Fe/Cu/Pt			S2: Si/Fe/Pt/Cu		
	Fe	Cu	Pt	Fe	Cu	Pt
Thickness(Å)	240±5	50±3	247±5	268±4	53±4	222±6
Roughness(Å)	7±2	9±2	5±1	4±1	11±2	4±1
SLD(10^{-6} $Å^{-2}$)	59.1±2.2	62.1±2.4	139.1±3.9	60.2±2.0	61.1±2.3	140.0±4.2

We also observed a variation in ESLD at the Cu/Pt and Fe/Cu interfaces in the heterostructure S1 on annealing at 400 ^{o}C. However, we have not observed any crystalline

phase for the alloy phases in S1 on annealing at 400 ^{o}C from GIXRD data. With further annealing of both the heterostructures at 500 and 600 ^{o}C, we observed a drastic change in the depth-dependent layer structure (XRR data) which precisely corroborates with the crystalline structure obtained from GIXRD measurements. We obtained a single alloy layer formation with an ESLD of ~$(9.6\pm0.5)\times10^{-5}$ Å^{-2} (corresponding to a ternary alloy FePtCu) for both the heterostructure on annealing at 500 and 600 ^{o}C, suggesting high interdiffusion of elements at interfaces (Fe/FePt, Pt/FePt, Cu/CuPt, etc., formed on annealing at 400 ^{o}C) on annealing at 500 ^{o}C. We have observed a small reduction in total thickness of heterostructure S1 and S2 on annealing at 500 and 600 ^{o}C.

SIMS Measurements

We also carried out SIMS measurements to confirm the depth dependence elemental distribution in both the heterostructures S1 and S2, for as-deposited and post-annealing of the heterostructures at 600 ^{o}C. Figure 5.4 (a) and (b) show the SIMS data for as-deposited heterostructures S1 and S2, respectively. SIMS data from heterostructures S1 and S2 annealed at 600 ^{o}C are shown in Fig. 5.4 (c) and (d), respectively. The time-axis represents the depth and the intensity-axis represents the concentration of the elements present in the heterostructures.

We observed the nearly constant intensity of Pt, Cu, and Fe for different regions along the depth (similar to their growth sequence) up to the Fe/Si interface, signifying the homogeneity of different layers in as-deposited (as-dep) heterostructures and consistent with XRR measurements. It is evident from Fig.5.4 (c) and (d) that Pt, Cu and Fe show nearly constant intensity for a whole range of the film up to the Fe/Si interface, indicating the formation of a homogeneous layer (alloy layer) on annealing of both the heterostructures S1

and S2 at 600 °C. Thus the SIMS data for as-deposited and post-annealed heterostructures at 600 °C corroborated the depth-dependent structure obtained from XRR measurements.

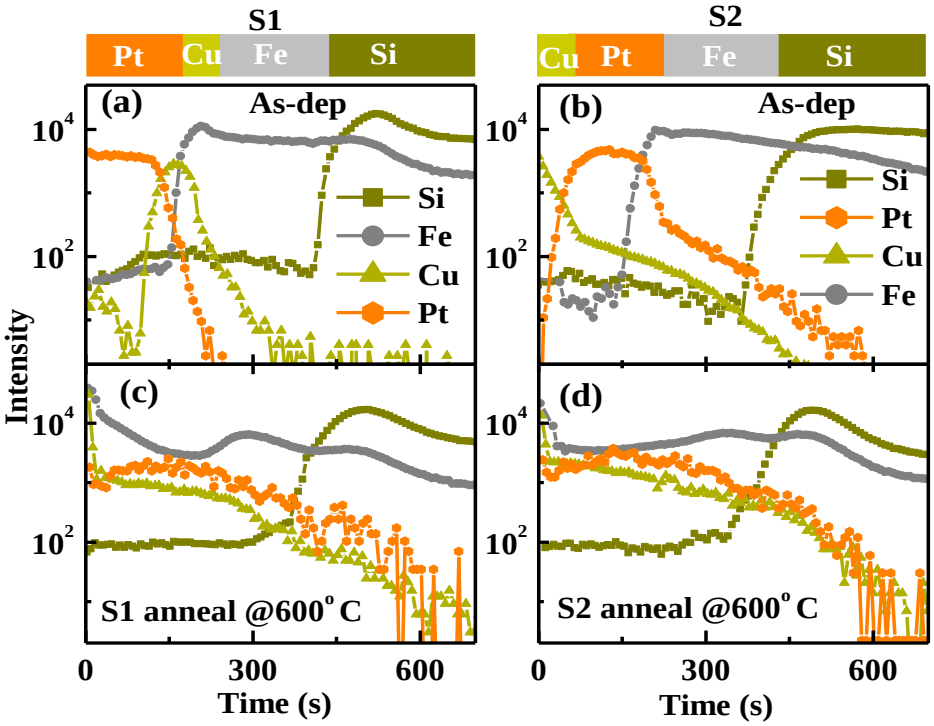

Fig. 5.4: Secondary ion mass spectrometry (SIMS) data from as-deposited S1 (a) and S2 (b). SIMS data from heterostructures S1 (c) and S2 (d) annealed at 600 °C.

5.3.2 Magnetic characterization

Macroscopic magnetic measurements (SQUID)

Figure 5.5(a) and (b) show the temperature-dependent macroscopic magnetization properties of the heterostructures S1 and S2, respectively, at different annealing temperatures. We carried out FC (closed) and ZFC (open) magnetization measurements as a function of temperature [$M(T)$] after cooling the heterostructures from 300 K to 5 K in an applied in-plane magnetic field of 500 Oe (for FC) and 0 Oe (for ZFC). These data were collected while warming the samples in an applied field of 500 Oe. For as-deposited and heterostructures

annealed at 300 ºC, we did not observe any changes in FC and ZFC data throughout the temperature range.

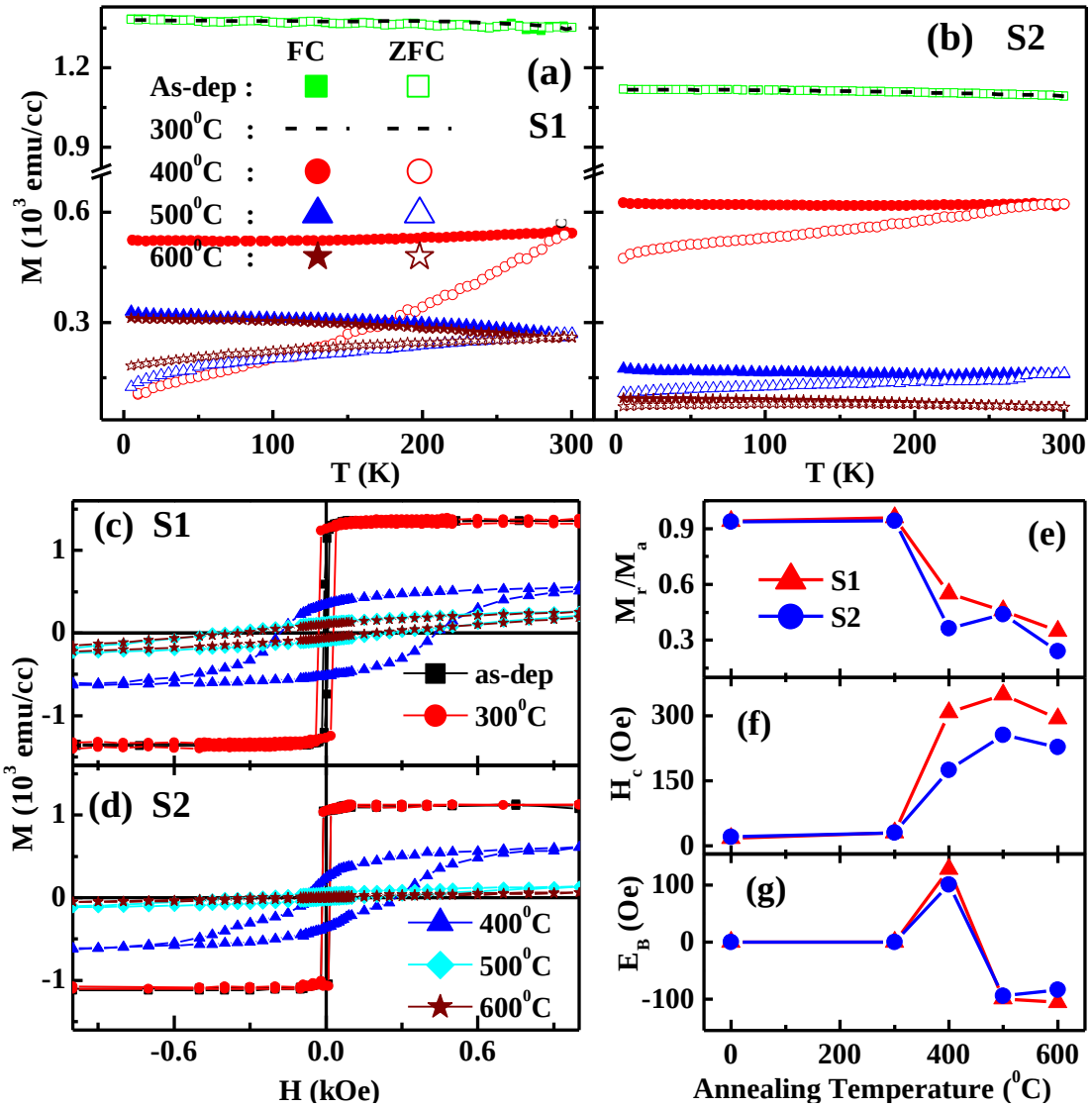

Fig. 5.5: Magnetization as a function temperature (M (T)) from as-deposited and post-annealing of heterostructures S1(a) and S2 (b) for FC and ZFC conditions. Room temperature hysteresis curves (M (H)) from as-deposited and post-annealing of heterostructures S1 (c) and S2 (d) at different annealing temperatures. Variation of the ratio of M_r/M_a (e), H_c (f), and Exchange bias (E_B) (g) as a function of annealing temperature for S1 and S2. Zero annealing temperature corresponds to an as-deposited condition.

It is noted that we have not observed any in-plane magnetic anisotropy (we obtained similar magnetization along two perpendicular in-plane, (001) and (010), the direction of the Si substrate) for both the heterostructures (as-deposited as well as post-annealed heterostructures at different temperatures). Figure 5.5 shows the SQUID data measured from the heterostructures under different conditions (as-deposited and post-annealed states) along (001) direction of Si substrate (in-plane direction), which is also the direction of applied field in PNR measurements. Upon annealing both the heterostructures at 400 ºC, an irreversible magnetic behavior of FC and ZFC (bifurcation) data for a whole range of temperature was observed. This clearly indicates the modifications in the magnetization in both the heterostructures S1 and S2 on annealing above 300 ºC. Further annealing, the heterostructures at higher temperatures (500 and 600 ^{o}C) the irreversibility of FC, and ZFC data slightly shift below room temperature (RT), 300 K. However, the decrease was predominant in the case of the S2 as compared to that of the S1.

Figure 5.5(c) and (d) show the RT (300 K) macroscopic magnetic hysteresis curves [$M(H)$] at different annealing temperatures for heterostructures S1 and S2, respectively. These hysteresis loops were measured in an applied field of ~ +2.5kOe after saturating the heterostructures at a higher field. S2 shows smaller averaged (saturation) magnetization (M_a) as compared to that of S1 for as-deposited heterostructures. We have not observed any significant change in macroscopic magnetization properties of both the heterostructures on annealing at 300 °C. Observation of a very small coercive field ($H_c \approx 30$ Oe) for both as-deposited as well as post-annealed heterostructures at 300 °C suggests soft ferromagnetic nature for both the heterostructures. Variation of the ratio of the remanent magnetization (M_r) with M_a (i. e. M_r/M_a) and H_c as a function of annealing temperature, have been shown in Fig. 5.5 (d) and (e), respectively. The M_a at different temperatures of annealing is average magnetization measured at an applied field of 1.7 kOe (the same field was applied during

PNR measurements). Annealing of the heterostructures at 400 °C shows a sharp increase in the coercivity with H_c ~ 310 Oe for S1 and 175 Oe for S2, which is ~ 6 to 10 times of the H_c for as-deposited heterostructures. Interestingly, we also observed a shift in the hysteresis curve towards positive field (equivalent to positive exchange bias (E_B)) axis with an $E_B \approx$ +120Oe for both the heterostructures. On annealing the heterostructures at 500 °C, we obtained a small increase in H_c, which decreases on further annealing of the heterostructures at 600 ^{o}C [Fig.5.5 (f)]. Remarkably we observed another shift in the hysteresis loop (M (H)) of the heterostructures on annealing at 500 and 600 °C, which is towards the negative field axis (equivalent to negative exchange bias (E_B)). We obtained an E_B of ~ -100 Oe on annealing of both the heterostructures, S1 and S2, at these higher temperatures, which is in contrast to the positive E_B (~ +120 Oe) obtained for heterostructures annealed at 400 °C. Figure 5.5 (g) shows the variation of the E_B field as a function of annealing temperature. The M_r/M_a ratio decreases from 0.95 (soft FM) to 0.20 (hard FM) on annealing the heterostructures from 300 to 600 °C, suggesting the modification in the magnetization of the whole system. The occurrence of the exchange bias phenomenon in these heterostructures on annealing above 300 °C indicates the presence of plausible hard and soft magnetic phases in the system, where Fe and alloy layer (e.g. FePt, FePtCu, FeCu, etc.) act as a soft and hard ferromagnetic layer, respectively. Previous reports also show observation of E_B in FePt/Fe systems [42,187,188]. We believe the macroscopic magnetization modulations of these systems are due to the formation of alloy phases at interfaces and hence depth-dependent structure-magnetic property investigation will help to understand these phenomena.

Depth dependence magnetization by PNR measurements

Figure 5.6(a) and (b) show the PNR data for as-deposited and post annealed heterostructures S1 and S2, respectively, at different temperatures. The open circles and

triangles in Fig. 5.6(a) and (b)represents the spin up (R^+) and spin down (R^-) PNR data and solid lines represent the corresponding fit to the PNR data. A clear modification in spin-dependent PNR data at different annealing temperatures is evident from Fig. 5.6. This modification suggests a different evolution process of magnetization on annealing of the heterostructures.

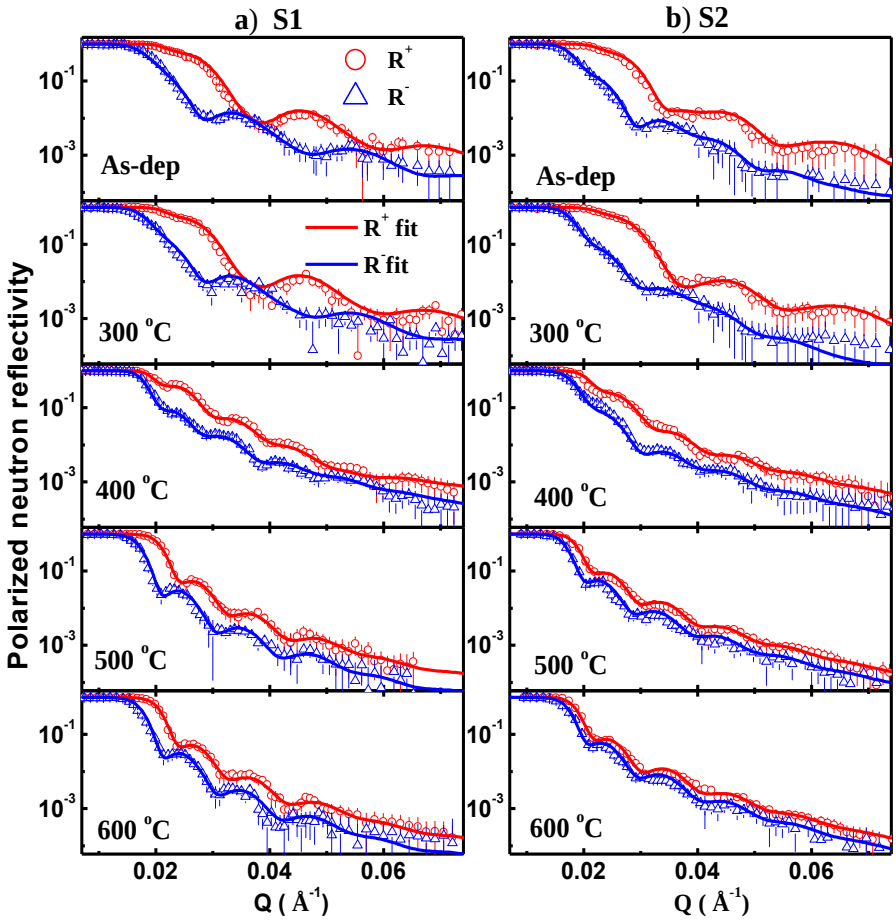

Fig. 5.6: Polarized neutron reflectivity data from as-deposited (as-dep) and annealed heterostructures S1 (a) and S2 (b) at different temperatures.

Figure 5.7 (a) and (b) show the nuclear scattering length density (NSLD) and the corresponding magnetic scattering length density (MSLD) (blue shaded regions) depth profiles across the interfaces of the heterostructures S1 and S2, respectively, obtained from

the PNR data at different annealing temperatures. The structural parameters for as-deposited heterostructures, obtained from PNR data are listed in Table 5.2, which are consistent with the parameters obtained from XRR (Table 5.1). We obtained an MSLD of ~ (4.40±0.35)×10^{-6} $Å^{-2}$ (average magnetic moment of ~1.80±0.12 μ_B/atom) for as-deposited heterostructures S1 and S2. Upon annealing, the heterostructures S1 and S2, at 300 °C, a small decrease in MSLD ~ (3.85±0.45)×10^{-6} $Å^{-2}$ (~1.62±0.12 μ_B/atom) was observed, which may be due to increasing in inhomogeneities of Fe layer due to interdiffusion at this temperature.

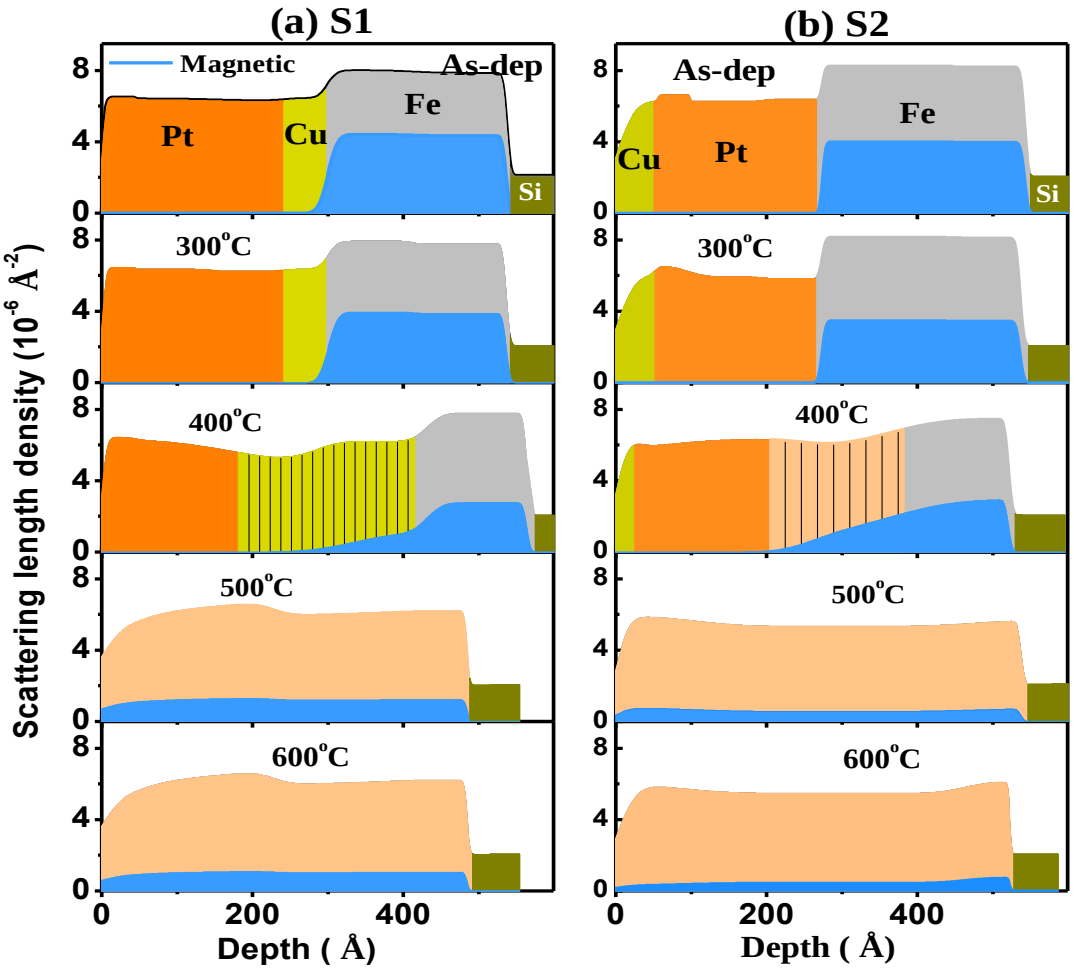

Fig. 5.7: Nuclear and magnetic (blue shaded region) scattering length density (NSLD and MSLD) depth profiles of heterostructures S1 (a) and S2 (b) for as-deposited and post-annealing at different temperatures.

Further decrease in magnetization is observed for both the heterostructures on annealing at 400 °C. A larger reduction in magnetization for heterostructure S1 on annealing at 400 ^{o}C was observed, suggesting the formation of possible alloy phase/mixing at Fe/Cu and Cu/Pt interfaces (highlighted by vertical lines in Fig. 5.7 (a)) with a small magnetic contribution. The different magnetic response of the alloy phase (maybe hard magnetic properties) and rest of Fe (soft phase) layer on annealing of S1 at 400 ^{0}C may also be contributing to the possible positive exchange bias in this heterostructure. While annealing of heterostructure S2 at 400 ^{0}C, we also observed the formation of the alloy at the Fe/Pt interface but it is FePt phase as seen in GIXRD pattern, thus the hard/soft (FePt/Fe) interface in this system contribute to positive exchange bias. In addition, S2 shows a small reduction in magnetization on annealing it from 300 ^{0}C to 400 ^{0}C as compared to that of S1, which further confirms the FM phase of the FePt alloy in S2. Further reduction/modification in the magnetization of the heterostructures post-annealing at 500 and 600 ^{0}C was observed. Post-annealing of the heterostructures at 500 and 600 ^{o}C, we obtained a ternary alloy formation.

Table 5.2: Parameters for Fe-Pt-Cu heterostructures S1 and S2 obtained from PNR for the as-deposited condition.

Parameters	S1: Si/Fe/Cu/Pt			S2: Si/Fe/Pt/Cu		
	Fe	Cu	Pt	Fe	Cu	Pt
Thickness(Å)	242±5	51±3	246±5	266±5	52±3	225±4
Roughness(Å)	6±2	8±2	6±2	5±1	9±2	5±2
SLD(10^{-6} Å^{-2})	7.89±0.25	6.30±0.16	6.35±0.19	7.88±0.27	6.28±0.20	6.36±0.23

A small variation in ESLD (from XRR) and NSLD (from PNR, Fig. 5.7 (a) and (b)) of S1 and S2 on annealing at 500 and 600 ^{o}C, indicates the coexistence of different phases (hard and soft magnetic) along the thickness of the film, which may result into low magnetization and negative exchange bias. The average magnetization at room temperature obtained by SQUID and thickness weighted magnetization obtained from PNR as a function of annealing temperature for heterostructures S1 and S2 are shown in Fig. 5.8 (a), suggesting macroscopic magnetization (SQUID) measurements are consistent with the PNR measurements.

5.4 Discussion

The composition of the alloy layer formed on annealing of a heterostructure as a result of interdiffusion at the interfaces and complete mixing can be theoretically calculated using their density and thickness [192]. For a binary alloy system with two elements (say A and B), the composition ratio (x : y) for alloy can be calculated using $x/y = n(A)d(A)/n(B)d(B)$, where n(A) and n(B) are the density of A and B, respectively and d(A) and d(B) are the thickness of these layers. Using the density of Fe, Pt and Cu elements, the particle density of these elements will be $n(Fe) = 8.47\times10^{22}$ cm^{-3}, $n(Pt) = 6.61\times10^{22}$ cm^{-3} and $n(Cu) = 8.49\times10^{22}$ cm^{-3}, respectively. Within the first approximation, using the layer thickness and number (particle) density of each element, we have calculated the expected composition of the ternary alloy phase, which is $(Fe_{0.56}Pt_{0.44})_{0.9}Cu_{0.1}$ and $(Fe_{0.61}Pt_{0.39})_{0.9}Cu_{0.1}$ for heterostructures S1 and S2, respectively. The theoretical ESLD and NSLD for these alloy phases in heterostructure S1 (S2) are 10.1×10^{-5} Å^{-2} (10.2×10^{-5} Å^{-2}) and 6.58×10^{-6} Å^{-2} (7.0×10^{-6} Å^{-2}), respectively. The ESLD and NSLD for the alloy phases in heterostructure S1 (S2) (on annealing at 500 and 600 ^{o} C) obtained from XRR and PNR were 9.6×10^{-5} Å^{-2} (9.5×10^{-5} Å^{-2}) and 6.2×10^{-6} Å^{-2} (5.7×10^{-6} Å^{-2}), which are in close agreement to the theoretically calculated values for these alloy phases and hence confirmed the ternary alloy phase formation on annealing the heterostructures at

500 and 600 ^{o} C. We also observed a reduction (from 600^{o}C to 500 ^{o}C) in the ordering temperature of ternary alloy by introducing 10% of Cu in Fe-Cu-Pt heterostructures.

The E_B in an FM/AFM system is attributed to a competition between the interfacial exchange interaction and the Zeeman energy [180,181]. E_B has also been reported in systems with ferrimagnetic/FM [193], ferrimagnetic/AFM [194], ferrimagnetic/ferrimagnetic [195, 196], and hard/soft FM/FM interfaces [42,187,188]. In general, E_B is a measure of the shift of hysteresis loop opposite to the (saturation) cooling field, i.e., negative E_B. In some systems, positive E_B was found where the shift is in the same direction as the cooling fields. The exchange bias field, E_B, is given by [193]: $E_B = {}^{\Delta\varepsilon}/_{2M_f t_f}$, where M_f is the saturation magnetization of the ferromagnetic layer and t_f is its thickness. $\Delta\varepsilon$ is the difference between the interface energies for a net magnetization of the ferromagnetic layer in parallel and antiparallel direction to the applied magnetic field. Depending on coupling at the interface, $\Delta\varepsilon$ will be positive (antiferromagnetic) or negative (ferromagnetic), which will determine the type of exchange bias [193]. The schematics of two types of coupling and related exchange bias phenomena are depicted in Fig.5.8 (b). The Positive and negative exchange bias for FM/AFM systems was successfully described earlier using the interface coupling depicted in Fig. 5.8 (b) [197, 198].

The evolution of structure and magnetic properties of the Fe-Cu-Pt heterostructures as a function of annealing temperature clearly suggested the formation of alloy phases above 400 ^{0}C, which also showed modification in the magnetization of the system. XRR and PNR result also suggested minor inhomogeneities in SLD depth profiles for alloy phase on annealing of both the heterostructures above 400 ^{0}C, which may suggest the coexistence of different phases (e.g. Fe, FePt, FePtCu, FePt (*fcc* and *fct*). However ordered *fct* phase of the alloy was in majority on annealing the heterostructures above 400 ^{0}C, which was also confirmed by GIXRD measurements. The coexistence of these phases provides a matrix of

soft/superparamagnetic (Fe / *fcc* alloy phases of FePt and FePtCu) and hard (*fct* alloy phases of FePt and FePtCu) ferromagnetic phases. Post-annealing of both the heterostructures at 400 ^{o}C exhibited a shift of hysteresis loop to positive field direction (positive exchange bias) at RT, where hard phases (FePt, FePtCu, etc.) are in minority.

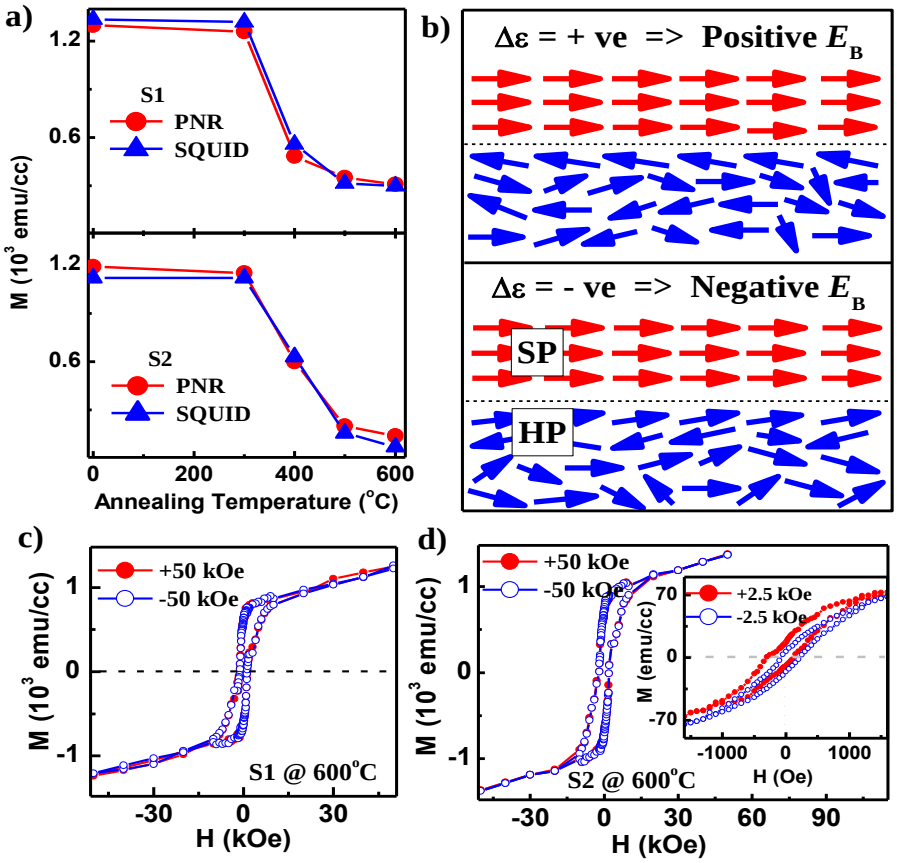

Fig. 5.8: (a) Comparison of magnetization of the heterostructures obtained from SQUID and PNR (thickness-weighted magnetization) measurements (in a field of 1.5 kOe) as a function of annealing temperature. (b) Representation of spin configuration at the interface assuming AFM/FM in the hard phase (HP)/soft phase (SP) magnetism. Magnetization (M) as a function field from post-annealed (600 ^{o}C) heterostructures S1 (c) and S2 (d) at room temperature after saturating the heterostructures in an in-plane magnetic field of ± 50 kOe. Inset of (d) shows the magnetization of the heterostructure S2 annealed at 600 ^{o}C at room temperature after applying an in-plane magnetic field of ± 2.5 kOe.

Coexistence of soft-hard magnetic phases on annealing of the heterostructures at temperatures ≥ 400 ^{o}C may also be contributing to magnetic disorder in these systems which results in the splitting of FC-ZFC magnetization data for these annealing temperatures. The coexistence of hard and soft magnetic phases along the thickness may create magnetic domains at the interface of these phases that differ from the rest of the film (the majority of phase) and hence may be contributing to exchange bias in this system. Reduction in average magnetization on annealing ≥ 400 ^{o}C for both the heterostructures also suggests different magnetic phases (antiferromagnetic/superparamagnetic etc.) at interfaces of the hard-soft magnetic phases.

The structural evolutions as a function of annealing clearly suggest the formation of the hard magnetic phase in minority (majority) on annealing of both heterostructures at 400 ^{0}C (above 400 ^{0}C). Since the majority of phase is the hard magnetic phase for both the heterostructures annealed above 400 ^{0}C, it is important to see the behaviour of the magnetization at the high magnetic field when the hard phase also contributes. Figure 5.8 (c) and (d) show the magnetization data at room temperature from post-annealed (at 600 ^{o}C) heterostructures S1 and S2, respectively, on saturating the heterostructures in an in-plane magnetic field of + 50 kOe (red closed circles) and -50 kOe (blue open circles). These $M(H)$ curves resemble a typical soft/hard magnetic system [36, 184], suggesting the presence of both soft and hard magnetic phases. We observed that the $M(H)$ curves measured after saturating both the samples in a field of ±50 kOe do not show any shift along the field axis. However, the $M(H)$ curves (inset of Fig. 5.8 (d)) measured for post-annealed (at 600 ^{o}C) heterostructures S2 on applying a small magnetic field of + 2.5 kOe (red closed circles) and -2.5 kOe (blue open circles) clearly suggest a shift of the curve along the field axis. These findings are consistent with earlier measurements on hard/soft ferromagnet bilayer systems

[27, 43]. The field-dependent shift of in-plane hysteresis loop in hard (Pt/Co)/soft (permalloy) system observed by Sort et al., [43] was attributed to the coupling between the permalloy layer and an uncompensated in-plane magnetic moment in the Pt/Co multilayer induced after saturating the ML with the initial large in-plane field. Whereas the shift in the in-plane hysteresis loop along field axis in hard ($Co_{0.66}Cr_{0.22}Pt_{0.12}$)/soft (Ni) bilayer at low magnetic field observed by Navas et al., [27] is attributed to ferromagnetic domain configurations at the interfaces in the system. Navas et al., [27] also observed the shift in hysteresis loop is highly dependent on the polarity of the applied magnetic field and there is no shift in the hysteresis loop along field axis in the higher applied field, same as we observed for the heterostructures annealed at 600 ^{o}C. Positive and negative exchange bias has already been observed in hard/soft magnetic core/shell nanoparticles [199], bulk manganite $NdMnO_3$ [200]. Aaset al.,[201], in their theoretical investigation, have observed a modification in the exchange interaction at the interfaces of Fe/FePt (soft/hard magnet) system and observed a small AFM coupling at the interfaces. We believe the exchange bias in the low magnetic field observed in the present system is also a consequence of the uncompensated magnetic domains in the hard phase near the hard/soft ferromagnet interfaces. However, the opposite shift of hysteresis loop for heterostructures annealed at 400 ^{o}C (hard phase is in minority) and >400 ^{o}C (hard phase is in the majority) might be due to the FM and AFM coupling, respectively, at the interfaces between soft magnetic domain and uncompensated (antiferromagnetic) domains of hard phases, as depicted in Fig. 5.8 (b). Thus the combination of these coupling at the soft/hard magnetic interfaces and the annealing-induced domination of these soft/hard magnetic phases might be contributing to the presence of both positive and negative exchange bias in these systems at different annealing temperatures.

These results also confirm the formation of $L1_0$ ordering of ternary alloy as well as inhomogeneities of soft/hard phases upon annealing, which modulates the magnetic

properties. However, earlier reports [202,203] also suggested diffusion of Fe in Si substrate at ~ 800 ^{o}C, which leads to the formation of iron silicide and a strong decrease of the magnetic moment value to 0.97 μB/atom at low temperatures. Our measurements are well below the above-mentioned annealing temperature, so such a contribution is negligible. However to investigate any such effect we have simulated PNR data by considering a thin (thickness ~ 6 nm) $FeSi_2$ layer at the Si/Fe interface (substrate/film interface) with a magnetic moment of 0.97 μB/atom. Figure 5.9 (a) shows the normalized spin asymmetry (NSA = $(R^+ - R^-)/(R^+ + R^-)$, where $R^{\pm}$ are spin-dependent PNR data), data for heterostructure S2 annealed at 600 ^{o}C and fits assuming: (a) a single alloy layer (Fig. 5.9 (b)) which best fitted the data and discussed earlier, (b) considering alloy layer and a $FeSi_2$ layer (thickness ~ 6 nm) at the Si/Fe interface (Fig. 5.9 (b)). The fit for NSA data assuming model (a) and (b) are shown as a solid line (blue) and a line with a star (black), respectively, in Fig. 5.9 (a). It is clear from Fig. 5.9 that considering a thin $FeSi_2$ layer with a magnetic moment of 0.97 μ_B/atom did not fit the NSA (PNR) data over the whole Q-range.

Further to see the behaviour of the exchange bias at low temperature we compared the *M*(*H*) curves (Fig. 5.9 (c) and (d)) at 300 and 5 K, for as-deposited and post-annealed heterostructures S1 and S2 at different temperatures. It is evident from Fig. 5.9(c) and (d) that we observed similar exchange bias phenomena at 300 and 5 K upon post-annealing of both the heterostructures above 300 ^{o}C. For as-deposited and annealed heterostructures S1 and S2 at 300 ^{o}C, we obtained an increase in H_C at 5 K, which is a well-known phenomenon for soft Fe film. The other features of hysteresis curve e.g. saturation magnetization (M_s) and M_r/M_s, remain the same at low temperature on annealing the heterostructures at different temperatures, suggesting a good temperature-dependent thermal stability for the observed magnetic properties of the systems on annealing at different temperatures. The strong thermal

stability and annealing dependent coupling in these heterostructures can be exploited for possible application in magnetic devices.

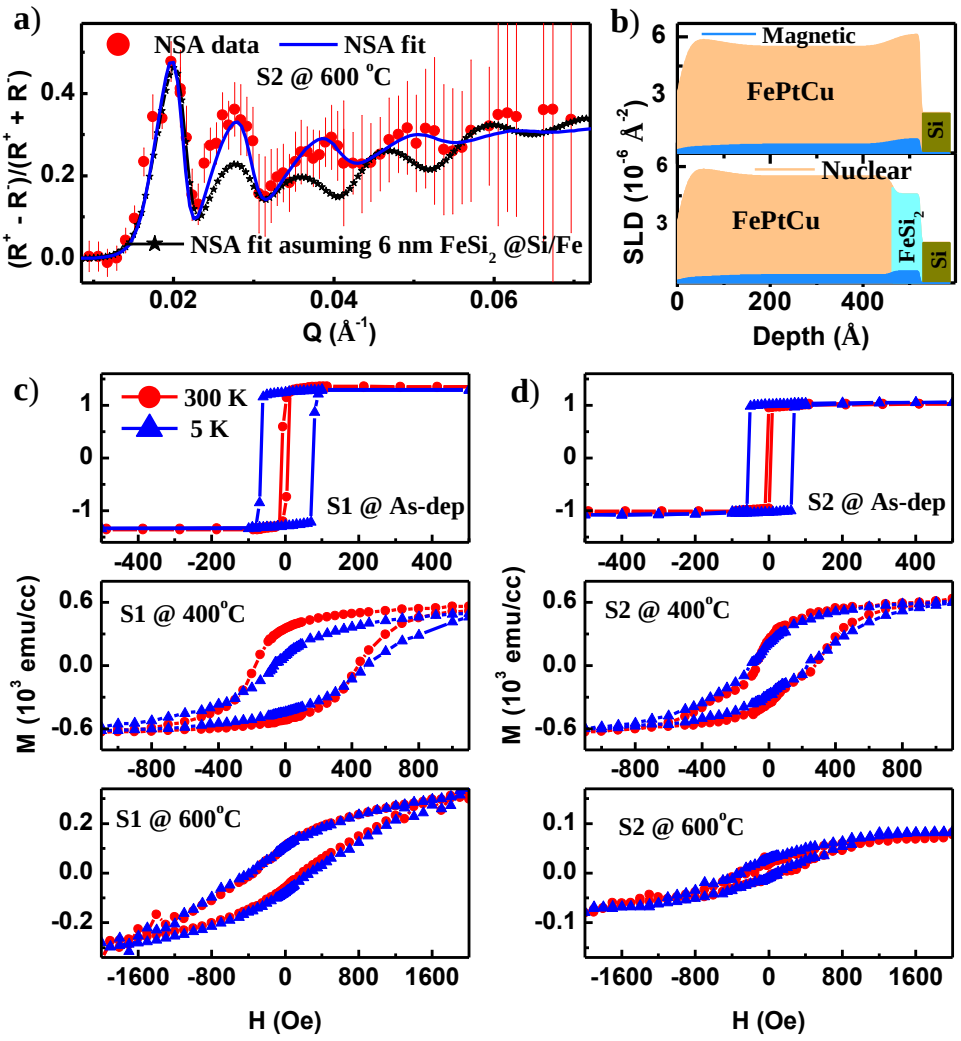

Fig. 5.9: (a) Normalized spin asymmetry (NSA = $(R^+ - R^-)/(R^+ + R^-)$) data from heterostructure S2 on annealing at 600 °C. (b) NSLD and MSLD depth profile of the layer structure assuming a single alloy phase and a $FeSi_2$ layer at the substrate film interface. Assuming a $FeSi_2$ layer at the substrate film interface did not fit NSA profile (line with a star, black) as shown in (a). Comparison of magnetization *M* (*H*) curves at 300 K and 5 K from heterostructures S1 (c) and S2 (d) for as-deposited and annealing at different temperatures conditions.

5.5 Summary

In summary, annealing induced structure and magnetic properties of Fe-Cu-Pt heterostructures with Cu as a capping and an intermediate layer have been studied. Very small and short-range interdiffusions of elements (Fe, Cu, and Pt) across the interfaces were observed in heterostructures upon annealing at temperature ≤ 400 ^{o}C. Whereas a rapid and long-range interdiffusion with alloy formation upon annealing of the heterostructures at temperature > 400 ^{o}C was observed. Both the heterostructures exhibited a positive exchange bias (~ +120 Oe) at room temperature and 5 K, upon annealing at 400 ^{o}C. However, annealing of the heterostructures at a temperature > 400 ^{o}C resulted into negative exchange bias (~ -100 Oe) at room temperature and 5 K. Depth-dependent structure and magnetic properties obtained from XRR and PNR suggested strong correlation between the transition in exchange bias for heterostructures on annealing at and above 400 ^{o}C with the coexistence of hard-soft magnetic phases along the thickness of the systems. The observation of annealing-induced exchange bias effect suggests a different sign of the interface magnetic exchange interaction and uncompensated magnetic (antiferromagnetic) domains in hard phase at low field, which is highly dependent on the majority of phase (hard/soft), present in the system and hence can prove useful in magnetic devices.

Chapter 6

Structure and magnetic properties of FePt/Cu multilayers on annealing

6.1 Introduction

The equiatomic ordered $L1_0$ or face-centred tetragonal (*fct*) $Fe_{50}Pt_{50}$ (FePt) films have attracted considerable attention due to properties such as high magnetocrystalline anisotropy (K_u) ~ 10^8 erg/cm^3, saturation magnetization, and high perpendicular magnetic anisotropy which has potential applications in the high-density recording media [165, 204-206]. Nanoparticles of $L1_0$ ordered FePt alloy have also shown promising electrocatalysis towards the oxygen reduction reaction in a proton-exchange membrane fuel cell [167-169,207]. A relatively high temperature (> 600 ^oC) annealing is necessary to transform as-deposited disordered face-cantered-cubic (*fcc*) phase (*A*1 phase) of FePt films into the ordered tetragonal $L1_0$ phase. Efforts have been made to reduce the ordering (annealing) temperature of this transformation by the addition of a third element to form a FePt-based ternary alloy compounds [77,170-172,174-176,208-211]. Reduction in ordering temperature for transforming *fcc* FePt alloy film grown on Si substrate to *fct* phase has also been achieved by introducing dynamic stress, where a chemical reaction between the substrate (Si) and Fe/Pt form silicides on annealing the as-deposited alloy for a longer time [202,203,212-217]. Formation of silicides induces dynamic stress by volume expansion at the substrate-film interface, which accelerates the ordering temperature much faster as well as makes a

diffusion barrier at the substrate-film interface for reducing the further diffusion of Fe/Pt into the Si substrate.

The addition of Cu in FePt film is suggested as one of the effective ways to reduce the kinetic ordering temperature, which has been explored by forming $(FePt)_{100-x}Cu_x$ ternary alloys [38,76,117,218-221]. It is believed that in the formation of a ternary alloy (FePtCu), Cu replaces the Fe lattice sites in FePt alloy [221] and thus deviates from the equiatomic ratio of the A (Fe or Cu): B(Pt) sites of the alloy responsible for obtaining high anisotropy applications. Gilbert *et al.*[177] achieved nearly equiatomic (001) orientated $L1_0$ $(Fe_{1-x}Cu_x)_{55}Pt_{45}$ thin films with magnetic anisotropy up to 3.6×10^7 erg/cm^3 on rapid annealing of $[Fe/Cu/Pt]_{x16}$ multilayers at 400 ^oC. However $(FePt)_{100-x}Cu_x$ ternary alloys with different Cu atomic % show drastically different magnetic properties [38,76,77,217-221]. Brombacher *et al.*,[76] reported the formation of ternary $[Fe51Pt49]_{100-x}Cu_x$ alloy phases with a Cu content of 0-21% [variation of Cu content is shown in Fig. 6.1] on rapid annealing of $Fe_{51}Pt_{49}$/Cu bilayers of different thicknesses and found modification in magnetic properties as a function of both annealing temperature (500 to 800 ^oC) and Cu content. The study suggested that the addition of Cu systematically reduced the perpendicular magnetic anisotropy and enhancement of both the $A1$-$L1_0$ phase transformation and the development of the (001) texture was also observed. Recently we found annealing dependent exchange bias effect for ternary alloy $[(FePt)_{90}Cu_{10}]$ at room temperature on annealing a Fe-Cu-Pt trilayer up to 600 ^oC [38]. Whereas a superparamagnetic phase for the ternary alloy $[(FePt)_{42}Cu_{58}]$ was observed on annealing the FePt/Cu multilayer at a temperature range of 400- 600 ^oC for 0.5 hr in an inert Ar environment at one atmosphere [77].

In this chapter we present the evolution of structure and magnetism of ternary alloys $[(FePt)_{65}Cu_{35}]$ and $[(FePt)_{50}Cu_{50}]$ [shown as open red square in Fig. 6.1] formed on annealing of multilayers [FePt (100 Å)/ Cu (d Å)]5 with $d \approx 50$ and 100 Å at different temperatures

(300 – 600 °C) for a fixed time ~ 0.5 hr (isochronal) and fixed temperature (600 °C) for different time (isothermal). Depth dependent characterization probes, x-ray reflectivity (XRR), and polarized neutron reflectivity (PNR), in combination with the macroscopic characterization techniques revealed diffusion induced nucleation of alloy within isochronal and isothermal annealing (in a vacuum) of FePt/Cu multilayers. Figure 6.1 indicates different study reported for FePt/Cu system where Cu content is varied and our study in this system fills a gap for the systematic study of the evolution of structure and magnetic properties of ternary alloy in the composition phase diagram of FePt/Cu multilayers with Cu content of 35 and 50 %.

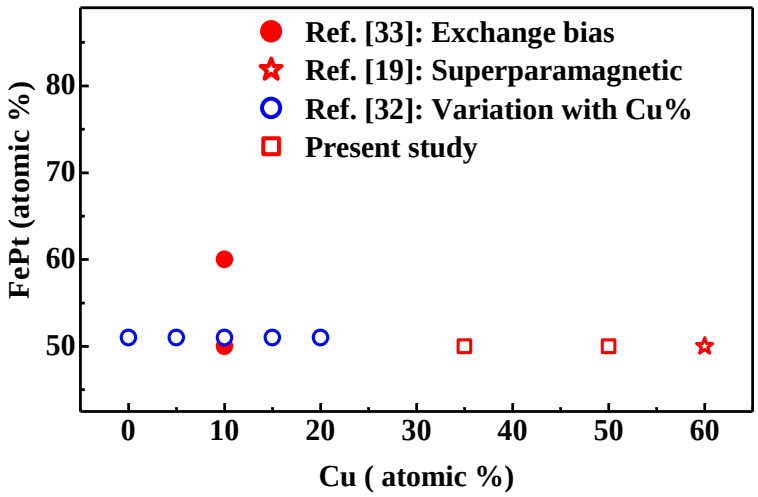

Fig. 6.1: $(Fe_{50}Pt_{50})_{1-x}Cu_x$ ternary alloy with variation in atomic % of Cu, which showed different magnetic properties.

6.2 Sample preparation and experimental details

Two multilayers of FePt and Cu with a nominal structure of Si(001)/[FePt(100 Å)/Cu(50 Å)]$_5$ and Si(001)/[FePt(100 Å)/Cu(100 Å)]$_5$, where 5 is the number of repeats of bilayers, henceforth known as S1 and S2, respectively, were grown on silicon substrates

using dc magnetron sputtering. Before deposition, a base pressure of 1×10^{-5} Pa was achieved. The substrate was kept at room temperature (RT) during the growth of these multilayers. By varying the thickness of the Cu layer, the stoichiometric ratio for the two ternary alloys $[(FePt)_{100-x}Cu_x]$ was achieved. The thickness of the Cu and the FePt layers are chosen such that the Cu content is achieved to 35 and 50 atomic % [Fig 6.1] with ternary alloys $[(FePt)_{65}Cu_{35}]$ and $[(FePt)_{50}Cu_{50}]$, on complete mixing of the layers upon annealing [77,192].

These multilayers were then annealed for 0.5 hr at different temperatures (isochronal annealing) of 300, 400, 500, and 600 ^{0}C under a vacuum of ~ 10^{-4} Pa. After each annealing, the multilayers were characterized for tracking the evolution of structure and magnetic properties. These multilayers were also annealed under the same vacuum at a fixed temperature of 600 ^{0}C (isothermal annealing) for different times (0.5 hr to 6.5 hr) and the evolution of different phases was studied.

Grazing incidence x-ray diffraction (GIXRD) and XRR with Cu K_α radiation (λ = 1.54 Å) was used to study phase formation (crystalline structure) and layer structure evolution of the multilayers at different annealing stages. Elemental depth distributions in the as-deposited and post annealed at 600 ^{o}C were carried out using Cameca IMS-7f secondary ion mass spectrometry (SIMS) instrument equipped with both oxygen duo plasmatron and cesium thermal ion source. Macroscopic magnetization measurements were carried out using a superconducting quantum interference device (SQUID). The depth dependent magnetic properties of the multilayers were characterized using PNR [36]. PNR experiments were carried out using the polarized neutron reflectometer instrument (neutron wavelength ~ 2.9 Å) at DHRUVA, India [78]. An in-plane magnetic field of 1.5 kG was applied to the sample during PNR measurements. Details about the non-destructive depth dependent characterization techniques (XRR and PNR) and data analysis formalism are given in chapter 2.

6.3 Results

6.3.1 Structure and magnetic properties under isochronal annealing

Figure 6.2(a) and (b) show the GIXRD profiles at a grazing angle of incidence of 1°, for the two multilayers S1 and S2, respectively, for different cases i.e., as-deposited (as-dep) and annealed at different temperatures (300 - 600 °C). GIXRD results reveal a polycrystalline *fcc* structure for both FePt and Cu layers in the as-deposited multilayers S1 and S2. We find a higher intensity for (111) reflection as compared to other planes, suggesting the growth of textured grains for both FePt and Cu layers. The Cu peaks are distinctly visible in the S2, while in the S1 they are inconspicuous but the broadening of FePt peaks indicates the presence of crystalline Cu layers, which may be due to higher thickness of the Cu layer in the S2.

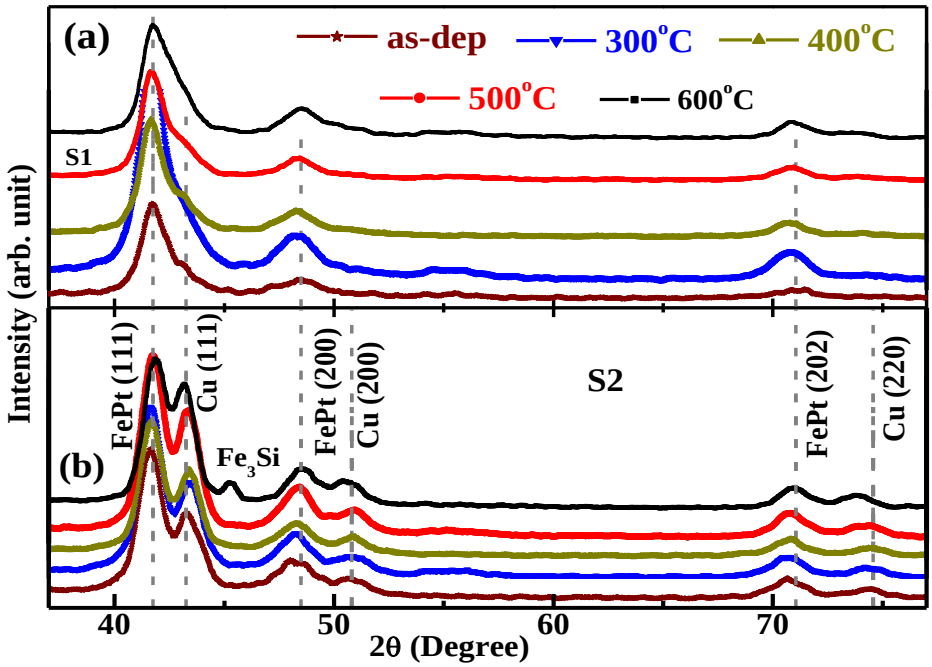

Fig. 6.2: GIXRD pattern from the as-deposited and annealed multilayers S1 (a) and S2 (b) at different temperatures (300-600 °C) for 0.5 hr.

GIXRD measurements for both the multilayers indicate no $A1$-$L1_0$ structural transformation (no additional Bragg peaks corresponding to the *fct* phase was observed) on annealing for 0.5 hr at different temperatures up to 600 °C. However, a small shift in position (angle) and width of diffraction peaks was observed on annealing the multilayers, suggesting a variation in crystallite sizes of different phases. We estimated the grain sizes of the FePt and Cu crystallites using (111) reflection of diffraction peaks from the S1 and S2 at different annealing temperatures. GIXRD data indicate a crystallite size of 8.0±0.1 (7±0.1) nm and 5.0±0.1 (8±0.1) nm for the FePt and Cu, respectively, in as-deposited S1 (S2). Upon annealing S1 at 600 °C, a small reduction (increase) in the crystallite size of the Cu (FePt) with 4.0±0.1 (10.0±0.1) nm was observed. No significant change in the crystallite size of FePt and Cu for the S2 was observed on annealing at 600 °C. The GIXRD pattern of the S2 annealed at 600 °C suggests the formation of crystalline iron silicide as indicated by the emergence of a new peak at $2\theta \approx 45.2°$.

Figure 6.3(a) and (b) show the XRR data from the S1 and S2, respectively, for as-deposited and post-annealing for 0.5 hr at different temperatures (300 -600 °C). XRR data for different annealing temperatures are shifted vertically for better visualization. Solid lines in Fig. 6.3(a) and (b) represent the corresponding fit to XRR data for different annealing temperatures. Fig. 6.3(c to e), and Fig. 6.3(f to h) show the ESLD depth profiles of S1 and S2, respectively, for as-deposited and post-annealing at 300 and 600 °C. The structural parameters extracted from the fits of XRR data for the as-deposited multilayers S1 and S2 are given in Table 6.1. Small variations (within the error on parameters) in the interface roughness of the FePt and Cu layers were considered to get the best fit to XRR data. The insets of Fig. 6.3 (a) and (b) show XRR data on the same scale for S1 and S2, respectively, which suggests clear variation in the reflectivity near Bragg peak on increasing the annealing

temperature. We observe a clear decrease in the Bragg peak intensity on annealing (300 to 600 °C) S1, suggesting an increase in interdiffusion/intermixing at interfaces and multilayers annealed at 600 °C show the maximum decrease in Bragg peak intensity [inset of Fig. 6.3(a)].

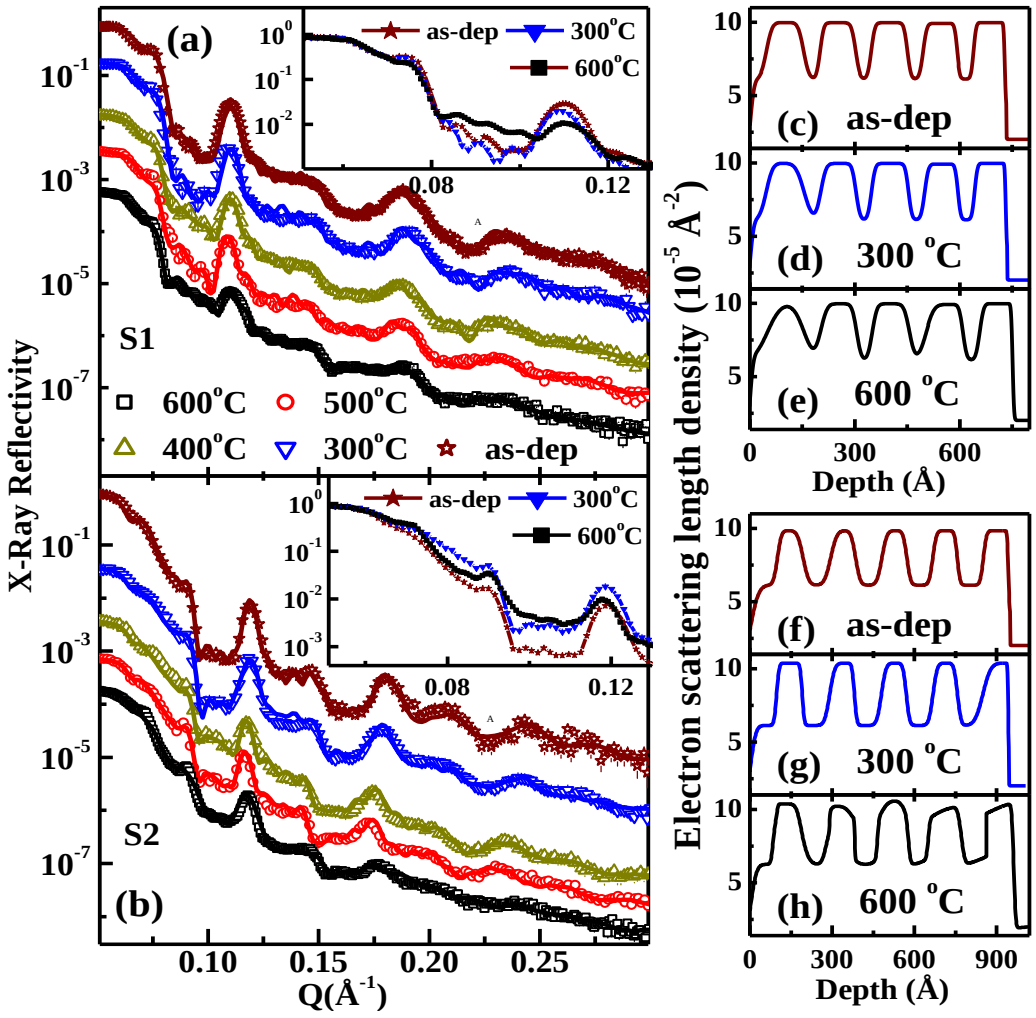

Fig. 6.3: X-ray reflectivity (XRR) profiles from multilayers S1 (a) and S2 (b) for as-deposited and post-annealing at different temperatures (300-600 ^{o}C). (c-h) The electron scattering length density depth profiles for the multilayers at different annealing conditions which best fitted (solid lines) the XRR data in (a) and (b).

The increase in interdiffusion at interfaces on annealing S1 were observed in terms of average interface roughness (averaged over 5 interfaces) with 8 Å (as-dep) to 13 Å (600 °C

annealed) for the FePt/Cu (Cu on FePt) interface and 9 Å (as-dep) to 14 Å (600 °C) for the Cu/FePt interface. XRR also revealed a larger interface roughness of 12 and 14 Å for the FePt/Cu and Cu/FePt interfaces, respectively, for as-deposited S2 as compared to that of S1. In contrast to S1, we observe an increase in Bragg peak intensity on annealing S2 at 300 ^{o}C [inset of Fig. 6.3(b)], suggesting a small decrease in the interface roughness. With further annealing of the S2 from 400 -600 °C, an increase in the average interface roughness was observed. XRR results for S2 annealed at 600 ^{o}C also suggest a small modification in ESLD at substrate/film interface, indicating the formation of a thin layer of iron silicide, which was also confirmed by GIXRD data.

Table 6.1: Structural parameters for as-deposited FePt/Cu multilayers S1 and S2, obtained from the XRR data.

Parameters	**S1: Si/[FePt(100 Å)/Cu(50 Å)]$_5$**		**S2: Si/[FePt(100 Å)/Cu(100 Å)]$_5$**	
	FePt	Cu	FePt	Cu
Thickness(Å)	99±5	46±3	99±4	92±4
Average Roughness(Å)	8±1	9±2	12±2	14±2
ESLD(10^{-5} Å^{-2})	9.95±0.42	6.14±0.35	9.87±0.44	6.14±0.33

SIMS data

The elemental distribution along the depth of the as-deposited multilayers and post annealed multilayers at 600 ^{o}C are carried out using SIMS measurements. SIMS data for as-deposited multilayers S1 and S2 are shown in Fig. 6.4(a) and (b), respectively. Figure 6.4(c) and (d) show the SIMS data for S1 and S2, respectively, on annealing at 600 ^{o}C. The time-axis indicates the depth and the normalized intensity axis represents the concentration. The FePt/Si interface (film-substrate interface) is indicated by vertical dashed lines in Fig. 6.4(a-

d). We find the nearly constant intensity of Pt, Cu and Fe for different regions along the depth (similar to their growth sequence) up to the Fe/Si interface signifying the multilayer structure in as-deposited multilayers [Fig. 6.4(a) and (b)]. It is evident from Fig. 6.4(c) and (d) that Pt, Cu and Fe show nearly similar profiles as obtained in the case of as-deposited S1 and S2 [Fig. 6.4(a) and (b)], indicating multilayer structures for both S1 and S2 on annealing at 600 ^{o}C. Therefore the SIMS data for as-deposited and post annealed heterostructures at 600 ^{o}C (for 0.5 hr) corroborated the depth dependent structure obtained from XRR measurements.

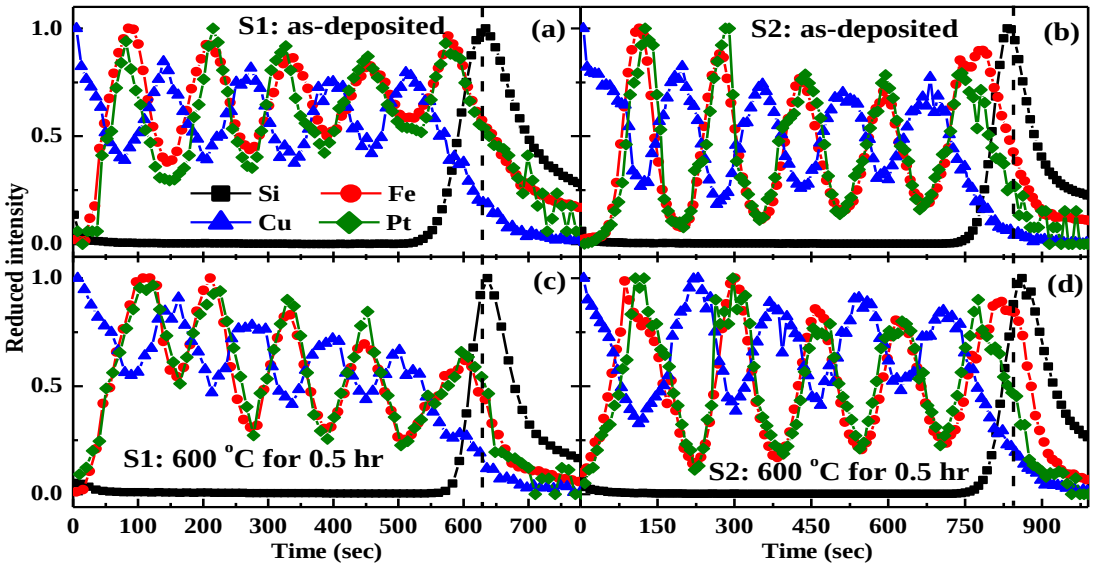

Fig. 6.4: Secondary ion mass spectrometry (SIMS) data for as-deposited multilayers S1 (a) and S2 (b). SIMS data for multilayers S1 (c) and S2 (d) on annealing at 600 ^{o}C for 0.5 hr.

Magnetization measurements

Figure 6.5(a) and (b) show the temperature dependent magnetization [M (T)] plots for S1 and S2, respectively, for both as-deposited and annealed (600 °C) cases. The (M (T)) data were recorded in both field cooled (FC) and zero field cooled (ZFC) mode in an in-plane applied magnetic field of 500 Oe. The [M (T)] data reveal a decrease in the net magnetization on annealing of both the multilayers over the entire temperature range (300 -5 K). Figure

6.5(c) and (d) show magnetic hysteresis curves [*M* (*H*)] for as-deposited S1 and S2, respectively, at 300 (room temperature, RT) and 5 K. Figure 6.5 (e) and (f) show *M* (*H*) curves for S1 and S2, respectively, on annealing at 600 ^{o}C for 0.5 hr. Magnetization data show a saturation magnetization (M_s) of ~1070 (~970) emu/cc for the as-deposited S1 (S2) at RT and the coercivity (H_c) of ~ 30 Oe for both the multilayers at RT.

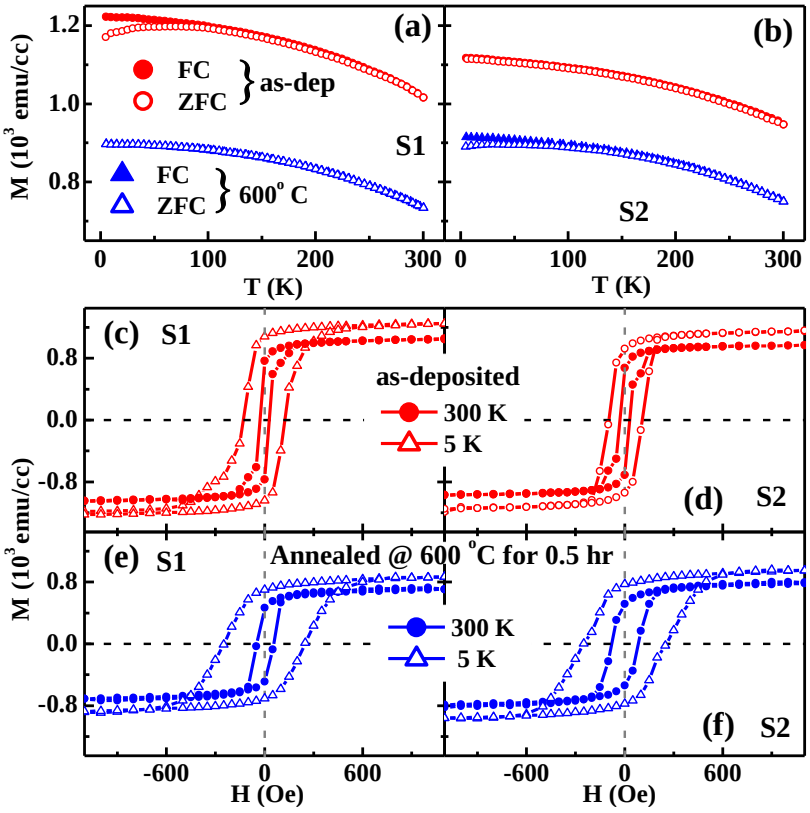

Fig. 6.5: Magnetization (M) as a function temperature from as-deposited (as-dep) and post-annealing (at 600 °C) of multilayers S1 (a) and S2 (b) for FC and ZFC condition. Hysteresis curves [*M* (*H*)] at 300 and 5 K for multilayers in conditions, as-deposited (c and d) and post-annealing at 600 °C (e and f).

Magnetization measurements (Fig. 6.5) for both the multilayers suggest a soft ferromagnetic nature, which is consistent with the soft ferromagnetic behavior for the as-deposited *fcc* phase of FePt alloy [76]. Upon annealing at 600 °C, we find a decrease in the

M_s to ~725 (~780) emu/cc for the S1 (S2), while H_c changes to ~55 Oe for S1 and ~80 Oe for S2. Like a metallic ferromagnet, both the multilayers show an increase in M_s and H_c at low temperature (5 K). An increase in H_c at RT for both the multilayers with an increase in the annealing temperature is believed to result from the decrease in the soft ferromagnet phase.

Figure 6.6(a) and (b) show the PNR measurements for S1 and S2, respectively, for as-deposited and post annealed (600 °C for 0.5 hr) conditions. Closed circles and triangles in Fig. 6.6 (a) and (b) depict the spin up (R^+) and spin down (R^-) PNR data, respectively, and the solid lines are the corresponding fits to the PNR data.

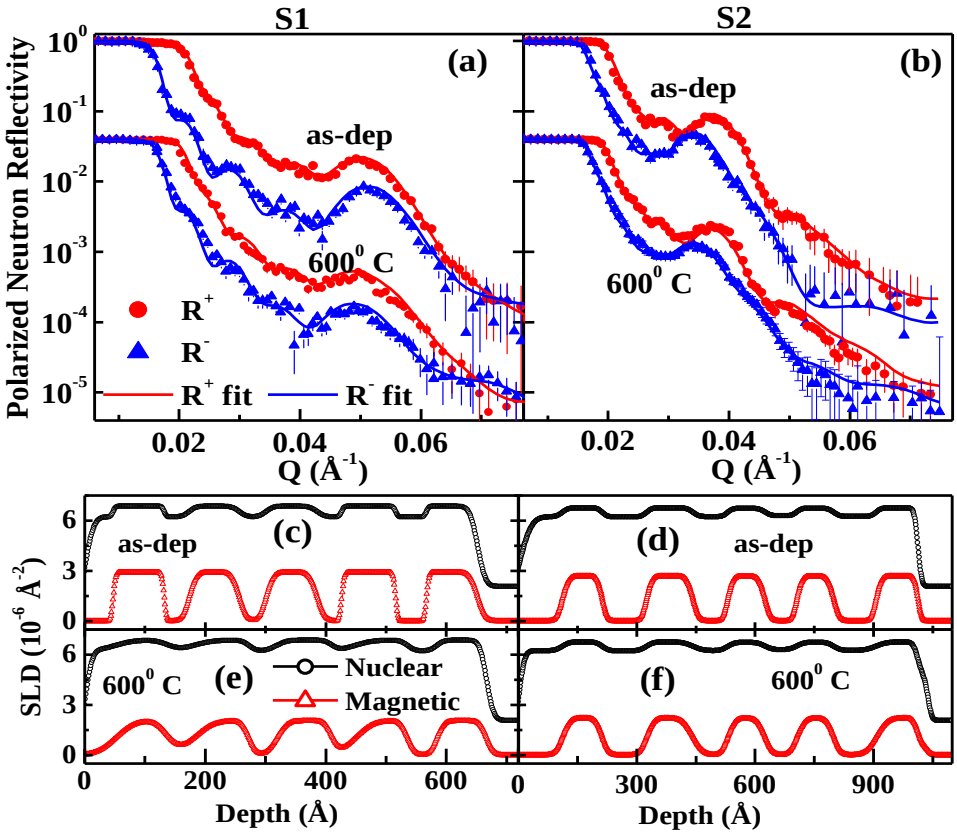

Fig. 6.6: Polarized neutron reflectivity (PNR) data from as-deposited (as-dep) and post-annealing (600 °C) of multilayers S1 (a) and S2 (b). The nuclear and magnetic scattering length density (NSLD and MSLD) depth profiles which best fitted the PNR data for S1 (c and e) and S2 (d and f) at different annealing conditions.

In general, the difference between spin dependent specular reflectivities (R^+ - R^-) provides the depth dependent magnetization profile in the multilayer. The NSLD and MSLD depth profiles for as-deposited and annealed (600 ^oC) multilayers are shown in Fig. 6.6(c to f). The structural parameters for as-deposited multilayers obtained from PNR data are listed in Table 6.2, and XRR results and PNR results are found (ESLD and NSLD) to be consistent with each other. PNR results show a MSLD of ~ (2.95±0.25)×10^{-6} $Å^{-2}$ (~ 1030±55 emu/cc) and ~ (2.75±0.30)×10^{-6} $Å^{-2}$ (~ 945±60 emu/cc) for as-deposited S1 and S2, respectively. PNR data also indicate a small decrease in MSLD with ~ (2.00±0.24)×10^{-6} $Å^{-2}$ (~ 690±50 emu/cc) and ~(2.25±0.25)×10^{-6} $Å^{-2}$ with (~ 750±50 emu/cc) for S1 and S2, respectively, on annealing the multilayers at 600 °C. This decrease may be attributed to an increase in inhomogeneities (roughness) of the FePt layer due to interdiffusion near the interfaces on annealing. Both the NSLD and MSLD profiles of S1 and S2 show that the interfaces are no longer sharp and both structural and magnetic roughness increase as the multilayers are annealed at 600 °C. Moreover, for S2 annealed at 600 °C, we consider an interface layer of thickness ~ 25 Å with an average magnetization of ~150±20 emu/cc at the substrate-film interface to get best fit to PNR data, suggesting iron silicide is ferromagnetic at RT.

Table 6.2: Structural parameters for as-deposited FePt/Cu multilayers S1 and S2, obtained from the PNR data.

Parameters	**S1: Si/[FePt(100 Å)/Cu(50 Å)]$_5$**		**S2: Si/[FePt(100 Å)/Cu(100 Å)]$_5$**	
	FePt	Cu	FePt	Cu
Thickness (Å)	92±4	45±3	99±5	91±5
Average Roughness (Å)	6±2	7±2	10±2	12±2
NSLD(10^{-6} $Å^{-2}$)	6.86±0.28	6.22±0.21	6.75±0.27	6.24±0.23

6.3.2 Structure and magnetic properties under isothermal annealing

Structural properties

Figure 6.7 (a) and (b) show the GIXRD patterns at a fixed grazing incidence of 1° for S1 and S2, respectively, on annealing isothermally (at a fixed temperature 600 °C) for different time intervals. The emergence of a new Bragg peak at $2\theta \approx 24.3°$ in the GIXRD patterns for both S1 and S2 indicates the formation of the polycrystalline *fct* phase of FePtCu ternary alloy on annealing the multilayers at 600 °C for 1.5 hr. Moreover, we find a small shift in Bragg peaks of different planes (101), (200) and (202) of FePt reflections to lower angle, which correspond to the ternary alloy (FePtCu) phase as indicated in Fig. 6.7. GIXRD data also indicate a mixed phase of *fct* and *fcc* structures for ternary alloy on annealing the multilayers S1 and S2 at 600 ^{0}C for a time $\geq$ 1.5 hr, as a result of interdiffusion of Cu, Fe and Pt across interfaces. However the growth of the *fct* phase in both the multilayers increases with the increase of the annealing time and can be seen in Fig. 6.7 (c) as an increase in the ratio of the intensity of the reflections of the planes (001) and (101) of *fct* and *fcc* phases [$I_{FePtCu\ (001)}/I_{FePtCu(101)}$] of ternary alloy, respectively, with annealing time.

Interestingly we observed the formation of the iron silicide phase (strong Bragg peak correspond to Fe_3Si (220) reflection at $2\theta \sim 45.2$ degrees) for both the multilayers on annealing at 600 ^{0}C for a time $\geq$ 1.5 hr, which evolves strongly on annealing the multilayers for longer times. The formation of iron silicides on annealing for longer duration is consistent with previous studies [202,203,212-217]. Fig. 6.7(d) shows the variation in the intensity ratio of (001) reflection of *fct* phase of ternary alloy and (220) reflection of Fe_3Si phase [$I_{FePtCu\ (001)}/I_{Fe3Si\ (220)}$] with annealing time and suggest the growth of both FePtCu and silicide phases on annealing, though it is more prominent for S2 as compared to S1. The growth of crystallite size on annealing for a longer duration, for both (001) *fct* ternary alloy and Fe_3Si phase for two multilayers are depicted in Fig. 6.7(e) and (f), respectively. An increase in grain size of

ternary alloy and silicide phases with an increase in annealing time confirms the evolution of these phases on longer annealing times. It is evident from Fig. 6.7 that we find more intense Bragg peaks corresponding to the *fct* phase for S2 as compared to the ones in S1, which confirms higher fraction and strong *fct* phase formation in S2 on annealing for longer times.

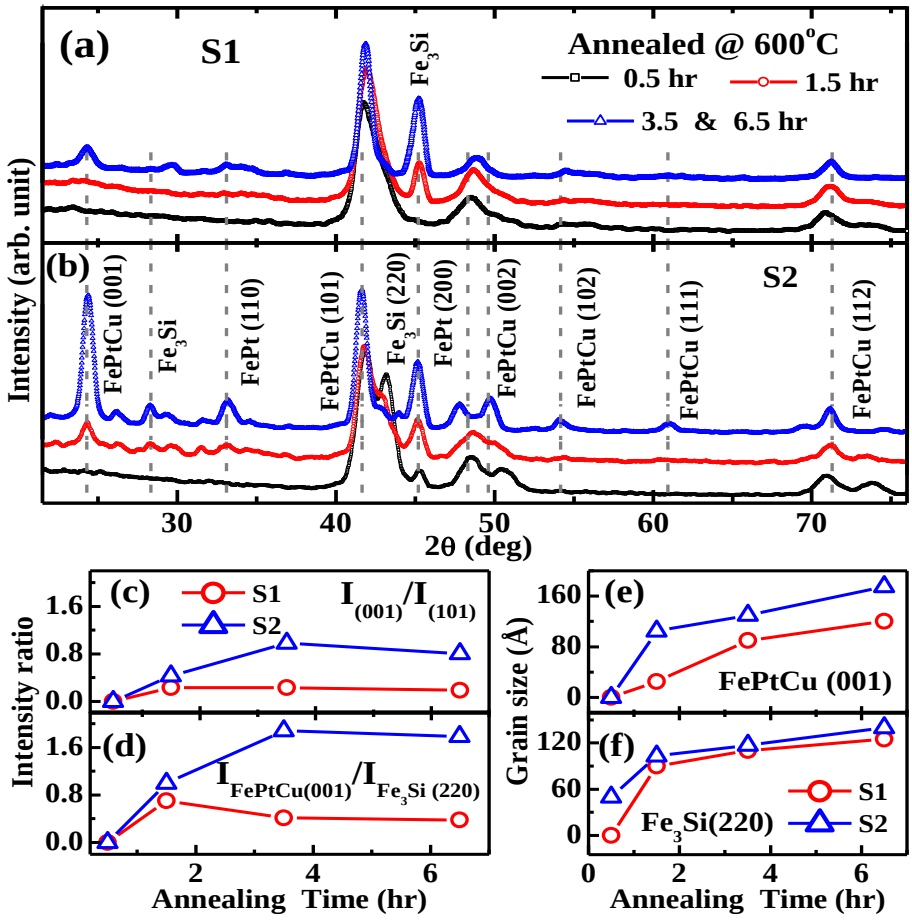

Fig. 6.7: GIXRD pattern from multilayers S1 (a) and S2 (b) annealed at 600 ^{o}C for different time periods. Variation of the intensity ratio of (001) and (101) reflection of FePtCu ternary alloy (c) and (001) and (220) reflections of FePtCu and Fe_3Si phases (d) with annealing time of the multilayers annealed at 600 ^{o}C. Evolution of crystallite size of ternary FePtCu alloy (e) and Fe_3Si (f) phases on annealing multilayers at 600 ^{o}C for different times.

Figure 6.8(a) and (b) show the XRR data (symbols) and corresponding fit (solid line) for multilayers S1 and S2, respectively, on annealing at 600 ^{o}C for different times (0.5 - 6.5 hr). XRR data for different annealing times are shifted vertically for better visualization. Fig. 6.8 (c to e) and (f to h) show the ESLD depth profile of multilayers S1 and S2, respectively, for different annealing times.

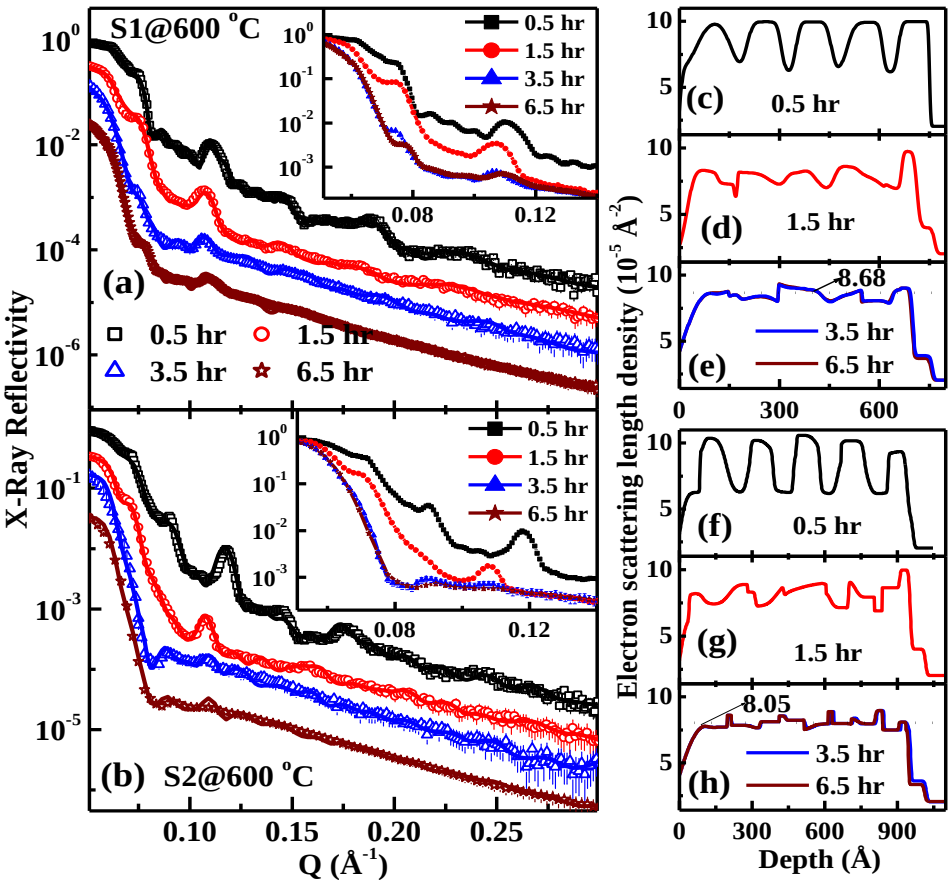

Fig. 6.8: X-ray reflectivity (XRR) data for multilayers S1 (a) and S2 (b) annealed at 600 ^{o}C for different times. XRR data for different annealing time are shifted vertically for better visualization. Inset of (a) and (b) show the comparison of experimental XRR data at different annealing times in the low *Q* range for S1 and S2, respectively. The electron scattering length density (ESLD) depth profile of multilayers S1(c-e) and S2 (f-h) annealed at 600 ^{o}C for different times, which best fitted (solid lines) the XRR data in (a) and (b).

The insets of Fig. 6.8 (a) and (b) show XRR data within lower *Q* range on the same scale for S1 and S2, respectively, which clearly show a variation in the Bragg peak intensities on annealing at 600 ^{o}C for different times. XRR results suggested a strong modification in layer structure on annealing the multilayers at 600 ^{o}C for longer times. Annealing multilayers for 1.5 hr indicate significant interdiffusion at interfaces, which is evident from the reduction of Bragg peak intensity accompanied by its shift to a lower Q position as well as modification in the ESLD profiles obtained from the XRR data. The ESLD profiles for both the multilayers annealed for 1.5 hr suggest a loss of repeated bilayer structure accompanied by the evolution of ternary alloy formation and Fe_3Si alloy layer at the substrate interface, as indicated by GIXRD results. Further annealing of the multilayers for longer times i.e. 3.5 and 6.5 hr, the layered structure is highly compromised and whole multilayer structure modifies to an equivalent single layer structure with average ESLD of $(8.68\pm0.20)\times10^{-5}$ and $(8.05\pm0.20)\times10^{-5}$ Å^{-2} [dashed horizontal lines in Fig. 6.8(e) and (h)] for S1 and S2, respectively, which gives clear evidence of the ternary alloy phase. However, we find small variation in ESLD along the thickness of the multilayers suggesting the coexistence of different phases on annealing for longer times. The XRR results also suggested an increase in the thickness (~ 50 Å) of the silicide layer at the substrate interface upon annealing of both the multilayers at 600 ^{o}C from 1.5 to 3.5 hr, although a further increase in the thickness of silicide layer was not observed on annealing multilayers for 6.5 hr.

Magnetic properties

Figure 6.9(a) and (b) show the temperature-dependent in-plane *M* (*T*) plots in an applied field of 500 Oe for S1 and S2, respectively, annealed at 600 ^{o}C for different times (0.5-6.5 hr) under FC (closed symbols) and ZFC (open symbols) conditions. Upon annealing S2 at 600 ^{o}C for 3.5 and 6.5 hr, we find similar *M*(*T*) data with very small magnetization in an

applied field of 500 Oe. *M* (*T*) data for both the multilayers for annealing time ≥ 1.5 hr show bifurcation between FC and ZFC data, suggesting the evolution of the magnetic disorder phase on annealing for longer times.

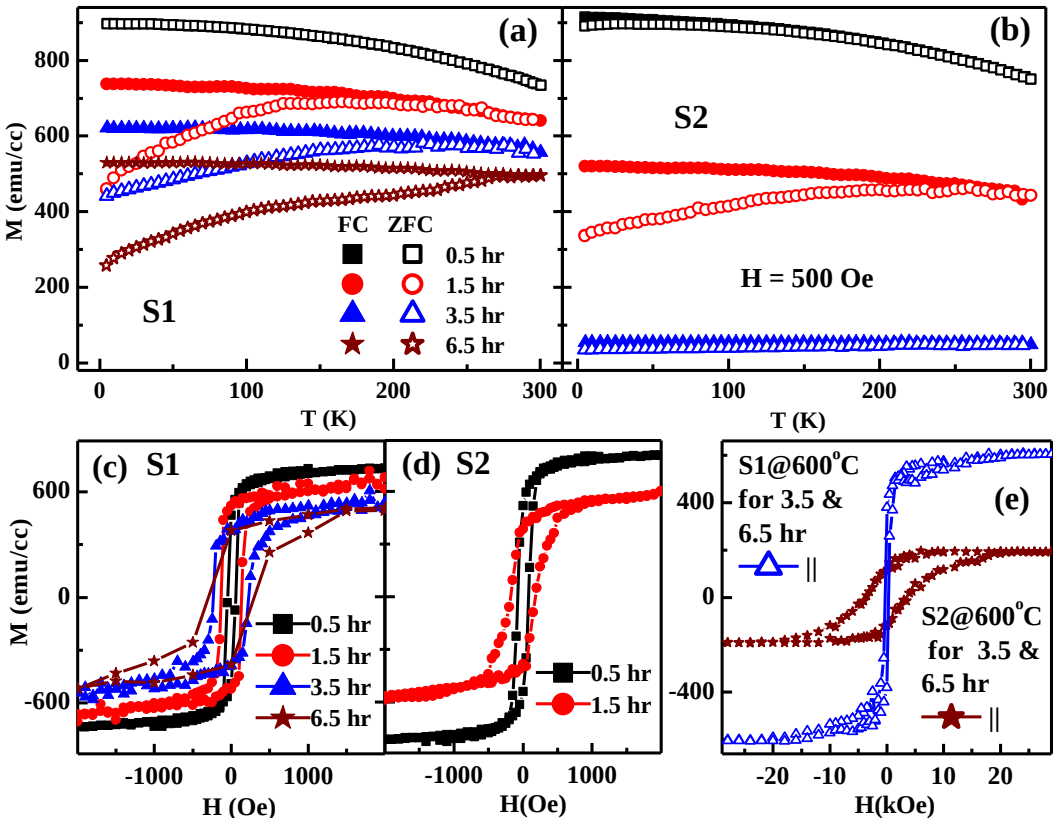

Fig. 6.9: Magnetization (*M*) as a function temperature for multilayers S1 (a) and S2 (b) annealed at 600 °C for different times (0.5 -6.5 hr) under FC and ZFC condition. Room temperature hysteresis curves [*M* (*H*)] for multilayers S1 (c) and S2 (d) annealed at 600 °C for different times (0.5 -6.5 hr). (e) *M* (*H*) curves for S1 and S2 in the in-plane (||) direction on annealing at 600 °C for 3.5 and 6.5 hr.

The results show an overall reduction in average magnetization over the entire temperature range for both the multilayers on increasing the annealing period, with a significantly larger decrease in magnetization for the S2. Figure 6.9(c) and (d) show the *M* (*H*) curves at RT for S1 and S2, respectively, measured in an in-plane applied field of ±2500

Oe after annealing at 600 ^{o}C for different times (0.5 to 6.5 hr). *M* (*H*) results from S1 (annealed at 600 ^{o}C) also suggested a well-defined hysteresis loop within an in-plane magnetic field of ±2500 Oe for whole annealing periods (0.5 – 6.5 hr) with a H_c of 55 and 300 Oe for annealing time of 0.5 and 6.5 hr, respectively. Whereas we obtained a H_c of 80 and 180 Oe for multilayer S2 annealed at 600 ^{o}C for 0.5 and 1.5 hr, respectively. *M* (*H*) data of S2 for an annealing time ≥ 3.5 hr show a very small signal and is not shown in Fig. 6.9 (d). We find a decrease in M_s and an increase in H_c for both the multilayers on annealing at 600 ^{o}C for longer times, however, the reduction in M_s for S2 was found to be larger.

It is noted that we find a soft ferromagnetic hysteresis behaviour, even at the low applied field (±2500 Oe), of the S1 on annealing at 600 ^{o}C for a longer time (~ 6.5 hr), which may be due to a phase coexistence of *fcc* and *fct* phase of ternary alloy with a larger fraction of *fcc* phase (soft ferromagnet). However for S2, which showed rapid growth of *fct* phase of ternary alloy on annealing S2 at 600 ^{o}C for a time ≥ 1.5 hr, we do not find any ferromagnetic hysteric nature at the low applied field. Thus, we carried out the *M*(*H*) measurements at a higher applied field of ±50 kOe along both in-plane and out-of-plane direction for the multilayers S1 and S2 annealed at 600 ^{o}C for longer times (3.5 and 6.5 hr) [Fig. 6.9(e)]. The hysteresis curve along in-plane direction for S1 annealed for a time of 3.5 and 6.5 hr show soft ferromagnetic nature with a small H_c of ~300 Oe, whereas the out-of-plane direction is still a hard axis (hysteresis curve is not shown) for the system. In contrast S2 on annealing at 600 ^{o}C for a longer time (3.5 and 6.5 hr) shows almost similar hysteresis curves [Fig. 6.9(e)] in both the directions (in-plane and out-of-plane) with a M_s of ~ 200 emu/cc and H_c as large as 6 kOe. The evolution of drastically different magnetization properties of the multilayers annealed for longer times at 600 ^{o}C is directly correlated to the structural properties of the multilayers.

Figure 6.10(a) and (b) show the PNR measurements for S1 and S2, respectively, annealed at 600 ^{o}C for different times from 0.5 hr to 6.5 hr. Closed circles and triangles in Fig. 6.10 (a) and (b) depict the spin up (R^{+}) and spin down (R^{-}) PNR data and solid lines are corresponding fit to PNR data. The NSLD and MSLD depth profiles obtained for S1 at different annealing times are shown in Fig. 6.10 (c to f) and (g to j), respectively. Similarly, the NSLD and MSLD depth profiles for S2 at different annealing times are shown in Fig. 6.10 (k to n) and (o to r), respectively.

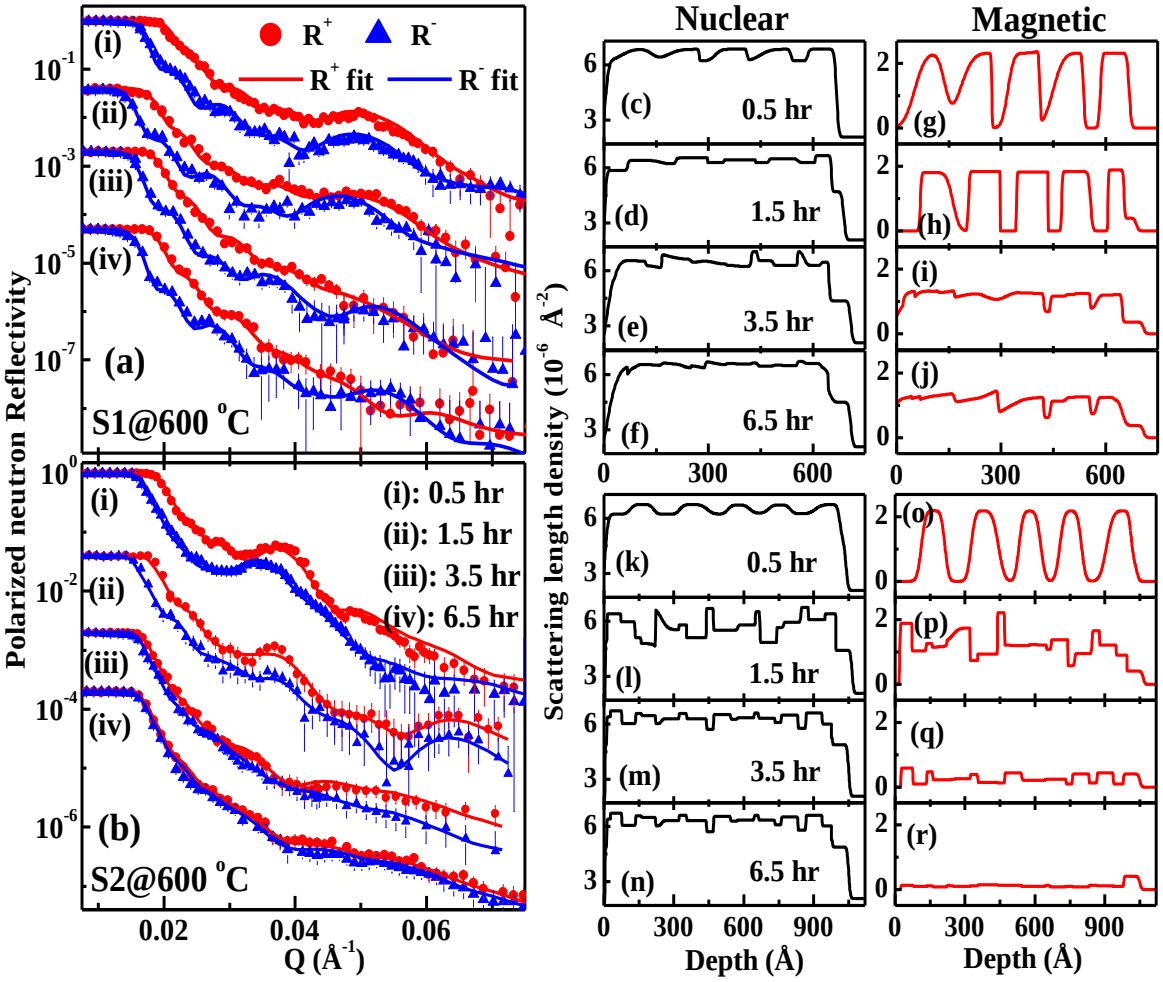

Fig. 6.10: Polarized neutron reflectivity (PNR) data for S1 (a) and S2 (b) annealed at 600 ^{o}C for different times. PNR data for different annealing time are shifted vertically for better visualization. The nuclear and magnetic scattering length density (NSLD and MSLD) for S1 (c-j) and S2 (k-r) at 600 ^{o}C for different times.

The spin dependent PNR data from the multilayers annealed at 600 ^{o}C for different times (0.5 -6.5 hr) show distinctly different variations. While both the multilayers show a reduction in the difference between two reflectivities (R^{+} - R^{-}), a measure of magnetization, on increasing the annealing time, we find a marginal difference between (R^{+} - R^{-}) on annealing S2 for 3.5 to 6.5 hr. We also observe the complete suppression of Bragg peak and appearance of new oscillations in PNR data for higher annealing times, suggesting modulation in-depth profiling of both structure and magnetization of the multilayers annealed for a longer period at 600 ^{o}C. The evolution of NSLD depth profiles for different annealing times for both the multilayers show similar variation as obtained from XRR measurements (ESLD depth profiles). Like XRR results we found a single alloy layer with NSLD of ~ $(6.60\pm0.10)\times10^{-6}$ Å^{-2} and ~$(6.50\pm0.15)\times10^{-6}$ Å^{-2} for S1 and S2, respectively, on annealing for ≥ 3.5 hr at 600 ^{o}C, Again, small variations in NSLD depth profiles suggest co-existence of different phases on annealing the multilayers for a longer time. The MSLD depth profile for S1 annealed for a time period ≥ 1.5 hr shows stronger magnetization as compared to that of S2. We found an average MSLD of ~ $(1.80\pm0.15)\times10^{-6}$ Å^{-2} (618±50 emu/cc) and $(1.40\pm0.16)\times10^{-6}$ Å^{-2} (480±30 emu/cc) for S1 and S2 on annealing at 600 ^{o}C for 1.5 hr, which is consistent with the SQUID measurements. However, annealing of multilayers S1 and S2 for a longer period (3.5 and 6.5 hr) at 600 ^{o}C showed a large reduction in the MSLD values with ~$(1.30\pm0.14)\times10^{-6}$ Å^{-2} (450±34 emu/cc) for S1 and ~$(0.20\pm0.05)\times10^{-6}$ Å^{-2} (70±15 emu/cc) for S2. It is noted that PNR measurements are carried out at room temperature in an applied in-plane field of ~ 1.5 kOe, therefore PNR results for the S2 annealed for 3.5 and 6.5 hr indicate the average magnetization at this field. PNR results also suggested the formation of alloy (silicide) layer of thickness ~60±15 Å at substrate interface,

which has been found to be magnetic at RT with a MSLD of ~$(0.40\pm0.06)\times10^{-6}$ $Å^{-2}$ (140±25 emu/cc).

6.4 Discussion

Evolution of structure and magnetic properties of FePt/Cu multilayers, S1 and S2, upon vacuum annealing for 0.5 hr at different temperatures (isochronal anneal) did not show any alloy formation at interfaces. However a small modification in the form of a change in grain size, interface roughness, saturation magnetization, and coercivity of multilayers annealed at different temperatures was observed. While GIXRD data revealed no significant change in the crystalline structure of both the multilayers on annealing, layer structure obtained from XRR data suggested an increase in interface roughness (reduction in Bragg peak) of S1 with increasing annealing temperature. In the case of multilayer S2, which showed higher interface roughness in as-deposited condition, we first find a reduction in interface roughness on annealing at 300 °C and then an increase in roughness was found on subsequent annealing to higher temperatures. GIXRD, XRR, and PNR result for multilayers on annealing at intermediate temperatures (400 and 500 ^{o}C) did not show significant change. Annealing of the S2 at 600 ^{o}C for 0.5 hr also indicates the formation of a very thin layer of the iron silicide at the film-substrate interface.

Upon annealing of both the multilayers at 600 °C for 1.5 hr, we observed large interdiffusion at the interfaces which were accompanied by a reduction in the intensity of Cu Bragg peaks and emergence of new Bragg peaks corresponding to ternary (FePtCu) alloy and silicide (at substrate interface) phases. Evolution of Bragg peak at $2\theta \sim 24.25$ deg also confirms the formation of ordered *fct* phase of ternary alloy [(001) reflection] in both the multilayers on annealing at 600 °C for 1.5 hr. On annealing the multilayers at 600 °C from 0.5 to 1.5 hr we also observed reduction (increase) in M_s (H_c) with multilayer S2 showing a

reduction of 40% in M_s as compared to that of S1 (15%). With further annealing of the multilayers at the same temperature for longer times (3.5 and 6.5 hr) the evolution of the *fct* alloy phase becomes stronger, though we also find the coexistence of phases (e.g. *fcc*). The isothermal annealing for a longer time also revealed one to one growth of the *fct* phase with the silicide phase near the substrate interface. Annealing of S2 for a period ≥ 3.5 hr at 600 ^{o}C exhibit drastically different magnetization properties with a large reduction in M_s, a large increase in H_c (~ 6 kOe) and similar hysteresis curves along both in-plane and out-of-plane direction of the multilayer. Whereas S1, for whole annealing (isothermal at 600 ^{o}C) period (≤ 0.5 hr), shows soft ferromagnetic behavior with almost a square hysteresis curve and a low H_c (~250 Oe) along the in-plane direction of the multilayer. It is evident from Fig. 6.6 that on annealing the multilayers at 600 ^{0}C for a time ≥1.5 hr, the *fct* phase (hard magnetic phase) grows faster than *fcc* phase (soft magnetic phase) of ternary alloy in S2 as compared to S1, which may be contributing for different magnetic properties of the multilayers annealed for longer times.

XRR and PNR suggested the formation of a single alloy layer on annealing the multilayers for a period ≥ 3.5 hr at 600 ^{o}C. Theoretically it is possible to calculate the composition of the alloy phase formed on complete mixing of elements using their density and thickness [77,78,192]. Using the particle density of n(FePt) = 7.25×10^{22} cm^{-3} and n(Cu) = 8.43×10^{22} cm^{-3} and thickness of FePt and Cu layer for two multilayers, the composition of homogeneous alloy for S1 and S2 would be $(FePt)_{65}Cu_{35}$and $(FePt)_{50}Cu_{50}$, respectively, on complete mixing [77,78,192]. Experimentally we can estimate the exact composition of the alloy using ESLD and NSLD values obtained for alloy phase using XRR and PNR measurements, respectively [77,78,192]. By fitting spin dependent neutron reflectivity data (R^+ and R^-) we obtain $\rho^{\pm}(z)$ for each layer and the NSLD for each layer can be extracted from $\rho_n = (\rho^+ - \rho^-)/2$. Thus on comparing ρ_n and ρ_x of the alloy layer (formed on annealing the

multilayers for a time ≥ 3.5 hr) obtained from PNR and XRR data, respectively, the stoichiometry of the alloy layer was estimated [77,78,192]. We find a composition of $(FePt)_{0.66}Cu_{0.34}$ and $(FePt)_{0.49}Cu_{0.51}$ for S1 and S2, respectively, which are close to the expected composition calculated assuming complete mixing of the atoms, as discussed above. Previous studies clearly indicate the existence of an ordered *fct* and disordered *fcc* phase of Cu rich ternary alloy on annealing at 600 ^{o}C [222]. Thus we believe that the different compositions with mixed-phase for two multilayers annealed at 600 ^{o}C for ≥ 3.5 hr and a different fraction of *fct* and *fcc* ternary alloy phase in two multilayers is responsible for drastically different magnetic properties.

The isothermal annealing of multilayers at 600 ^{o}C for a longer period ≥ 1.5 hr suggests that the evolution of the *fct* ternary phase is highly correlated to the growth of the iron silicide phase at the substrate interface. Thus it is important to understand the role of the silicide phase as well as annealing temperature for the growth kinetics of FePtCu ternary alloy. Formation of ternary alloy phase in S2 on annealing for a time ≥ 1.5 hr also suggested drastic change in magnetic properties. The reduction in magnetization and an increase in ordering temperature for the *fct* FePt alloy was also found earlier and attributed to the formation of Fe silicide at the substrate-film interface on annealing at high temperature [212]. In contrast, Lai *et al*.,[213] found a reduction in ordering temperature of FePt alloy due to the formation of Cu silicide on annealing a rather complex heterostructure of Si/Cu/CoFe/Pt/FePt. The study also suggested an increase in the in-plane H_c due to the formation of Cu silicide, which induced the stress in the system. The chemical reaction at the substrate-film interface with the formation of the silicide phase has indicated a mixed report for its dependence on ordering temperature and rapid growth of ordered domains [212-217]. However the interface reaction between film and substrate is strongly dependent on the interfacial structure, film thickness and diffusivity of the elements [223]. We believe the silicide phase, which grows with

annealing time, and the induced dynamical stress play an important role in the growth of *fct* ternary alloy.

In order to see the effect of lower annealing temperature and longer annealing time for the evolution of structure and magnetic properties of the ternary alloy phase and its correlation with the silicide phase, we have measured the GIXRD and XRR measurements for multilayer S2 on annealing at 400 ^{o}C for 6.5 hr. Figure 6.11 (a) and (b) show the comparison of GIXRD and XRR data, respectively, for S2 on annealing at 400 ^{o}C for 6.5 hr and 600 ^{o}C for 0.5 and 6.5 hr. It is evident from Fig. 6.11 that the GIXRD and XRR data for S2 annealed at 400 ^{o}C closely match with that for annealed at 600 ^{o}C for 0.5 hr.

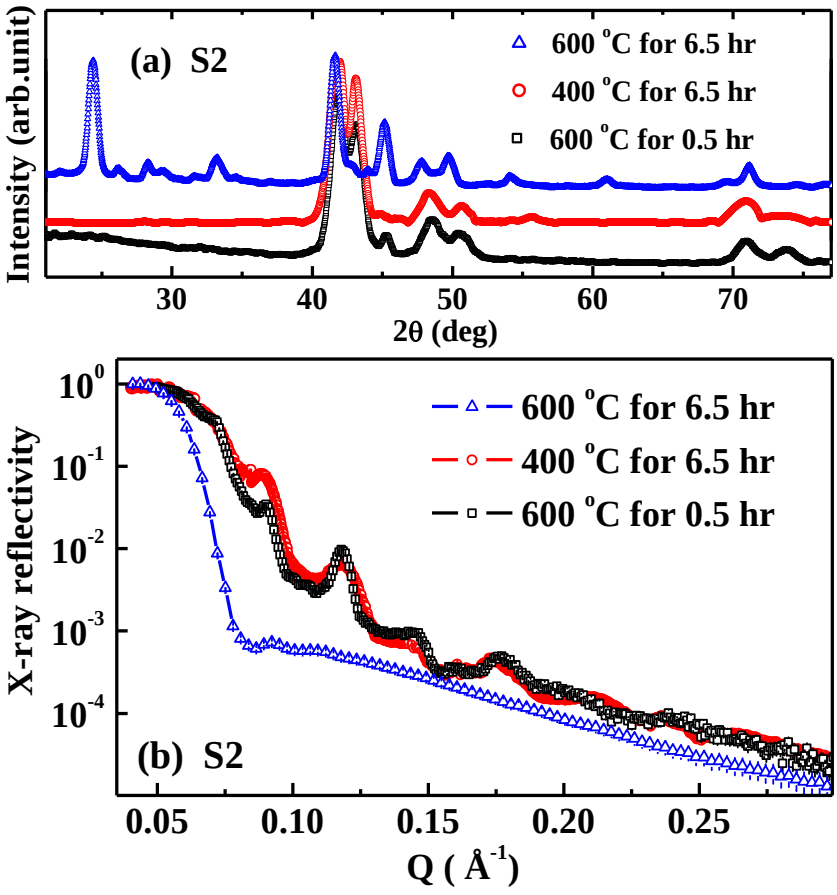

Fig. 6.11: Comparison of GIXRD (a) and XRR (b) data for S2 on annealing at 400 ^{o}C for 6.5 hr and 600 ^{o}C for 0.5 hr and 6.5 hr.

Absence of *fct* ternary alloy and silicide phases for S2 on annealing at 400 ^{o}C even for 6.5 hr clearly suggest that iron silicide phase formed at high annealing temperature and growth of *fct* ternary phase evolve along with the silicide phase, which is consistent with the earlier studies [212, 217]. A close match of XRR data for S2 annealed at 400 ^{o}C for 6.5 hr and 600 ^{o}C for 0.5 hr indicate that multilayer annealed for a longer time at a lower temperature cannot induce a silicide and ternary alloy phase formation. Thus the silicide phase formation at the substrate-film interface is important for nucleation of the ternary alloy phase with *fct* order on annealing of FePt/Cu multilayer with a Cu content of 35-50 atomic %.

6.5 Summary

We have carried out the systematic structural and magnetic characterization of FePt/Cu multilayers on annealing isochronally and isothermally in a vacuum. While isochronal annealing (at a temperature range 300-600 °C for a fixed time ~ 0.5 hr) of multilayers suggests a small interdiffusion of elements at FePt/Cu (Cu on FePt) and Cu/FePt interfaces, which resulted in a marginal suppression in magnetic properties. Upon isothermal annealing (at 600 °C) for longer times (1.5-6.5 hr), multilayers showed large interdiffusion at interfaces and formation of ternary alloy and iron silicide (at substrate-film interface) phases. Using reflectivity measurements, the stoichiometry of ternary alloy was found to be $(FePt)_{0.66}Cu_{0.34}$ and $(FePt)_{0.49}Cu_{0.51}$ for S1 and S2, respectively, which is close to the theoretical estimation of the compositions. We found that the high temperature annealing of multilayers for a longer period produces an iron silicide phase at the substrate-film interface that helps to evolve the FePtCu ternary phase. In the FePtCu ternary alloy film, the increased Cu content (S2) leads to phase coexistence with a larger fraction of the *fct* phase, which is responsible for its low saturation magnetization with a high coercivity of 6 kOe at room temperature. Isothermal annealing of multilayers also suggested a decrease in saturation magnetization with an

increase in Cu content. These results demonstrate a mechanism of producing a ternary alloy phase of designed compositions on annealing the multilayers of different thicknesses, which showed distinctly different magnetic properties. The tuning of magnetic properties of ternary alloy by adding different Cu content may be desirable for future magnetic devices.

Chapter 7

Summary and future scope

The focus of the research work presented in the thesis was the investigation of interface dependent structure and magnetic properties of ferromagnetic (magnetic/magnetic and magnetic/non-magnetic) multilayers using non-destructive techniques. The interface properties of the multilayers were controlled and varied by growing these multilayers under different deposition conditions and annealing at different temperatures. The interface dependent structure and magnetic properties have been studied using both macroscopic (XRD, SQUID) and depth dependent (SIMS, XRR, and PNR) characterization techniques. We have mainly studied two systems, 1) Gd/Co multilayers, and 2) Fe-Pt-Cu heterostructures and FePt/Cu multilayers, which have been grown by the sputter deposition technique. The Gd/Co system as a RE/TM multilayer has shown many interesting interface-driven magnetic properties, especially near compensation temperature and is being considered an important artificial ferrimagnet for all spin-based technological applications. Whereas the FePt alloy currently is one of the favorite materials for storage applications though requires a high-temperature treatment for the chemical ordering, which induces unfavorable properties for the application. We have studied the effect of the addition of Cu with different atomic % in FePt alloy by annealing of Fe-Cu-Pt heterostructures and FePt/Cu multilayers and observed interesting magnetic properties at different annealing temperatures.

Gd/Co multilayers grown on different substrates (glass and Si) with varying deposition conditions showed improved layer structures with different interface morphology (interface roughness, etc.). The Gd layers showed a polycrystalline growth with a face-centered cubic

(*fcc*) structure, as compared to previous studies where the Gd was grown either in the amorphous phase or in hexagonal-closed packed (*hcp*) phase, which may be the reason for obtaining high-quality multilayer structure without alloy formation. Gd/Co multilayers grown on glass substrates showed higher interface roughness as compared to that grown on Si substrate at identical deposition conditions. Gd/Co multilayers grown on glass substrates were also used to study the annealing dependent magnetic properties, whereas multilayers deposited on Si substrates were used to investigate the temperature and field dependent magnetic properties. We have shown that the compensation temperature (T_{comp}), which is a signature of the antiferromagnetic exchange interaction between Co and Gd at interfaces, is strongly correlated to the interface morphology and increases with an increase in interface roughness. Annealing of Gd/Co multilayers resulted in an increase in roughness as well as the formation of an alloy layer at interfaces, leading to modification in magnetic properties with additional magnetically complex phases at low temperatures.

We have further explored the interface-driven exchange coupling in Gd/Co multilayers as a function of temperature and field. The magnetic measurements revealed that multilayer having lower intermixing at interfaces are strongly coupled and showed negative exchange bias at temperatures < T_{comp}. Multilayers having lower interface roughness also showed a planar 2π domain wall (DW), within both the Co and Gd layers at $T_{comp.}$ In addition growth of the magnetic domain with magnetization perpendicular (in-plane) to the applied field in the central part of each Gd layer at T_{comp} was observed for the multilayer with lower interface roughness. These magnetic inhomogeneities in the central part of each Gd layer are highly correlated and contributed to the antisymmetric magnetoresistance (MR) observed in these multilayers at T_{comp}. The formation of magnetic helical structure around T_{comp} showed additional irreversibility in MR as a function of field. Like other studies on RE/TM multilayers, the Gd/Co multilayers also showed temperature-dependent magnetic phases with

AFM coupling at Gd/Co interfaces at all the temperatures. Field dependent measurement suggested an increase in the compensation temperature with an increase in the applied field and the alignment of the Gd (Co) moment along the applied field is highly dependent on the field.

Other systems with magnetic (FePt) and nonmagnetic (Cu) layer studied here deals with evolution of structure and magnetic properties of a FePtCu ternary alloy formed upon annealing of a Fe-Cu-Pt trilayers and FePt/Cu multilayers. The trilayers and multilayers showed drastically different magnetic properties on annealing isochronally (300 to 600 ^{o}C) for 0.5 hr under similar conditions, suggesting interface dependent interdiffusion kinetics in these systems. We observed a rapid and long-range interdiffusion of atoms at interfaces with the formation of an alloy layer on annealing the trilayer heterostructures at temperature > 400 ^{o}C. The trilayers exhibited different exchange bias at room temperature on annealing at different temperatures. It showed a positive exchange bias (~ +120 Oe) on annealing at 400 ^{o}C, which on further annealing at higher temperature ($\geq$ 500 ^{o}C) showed a negative exchange bias (~ -100 Oe). The study suggested the coexistence of hard-soft magnetic phases along the thickness of the systems on annealing above 400 ^{o}C, which contributes to the observed exchange bias. Whereas annealing of FePt/Cu multilayers under similar conditions up to a temperature of 600 ^{o}C suggest a small interdiffusion of atoms at different interfaces, which resulted in a marginal suppression in magnetic properties. Upon isothermal annealing (at 600 °C) for longer times (1.5-6.5 hr), multilayers showed large interdiffusion at interfaces and formation of ternary alloy and iron silicide (at substrate-film interface) phases. The study also suggested that evolution of ternary alloy is highly dependent of iron silicide phase formed in the multilayers system. Using reflectivity measurements, we also estimated the composition of ternary alloys formed in these systems, which is close to theoretical calculation of the compositions. In the FePtCu ternary alloy film, the increased Cu content (higher Cu content

sample) leads to phase coexistence with larger fraction of face-centered tetragonal (*fct*) phase, which is responsible for its low saturation magnetization with a high coercivity at room temperature. These results demonstrate a mechanism of producing a ternary alloy phase of designed compositions on annealing the multilayers of different thickness, which showed distinctly different magnetic properties. The tuning of magnetic properties of ternary alloy by adding different Cu content may be desirable for future magnetic devices.

The results have shown a strong influence of the film growth and thereby interface structure and morphology on the magnetic properties. As a future prospectus the correlation of interface driven magnetic properties in RE/TM system can be strengthened by the macromagnetic simulations, which will further help in designing the system for technological application. Annealing of the RE/TM multilayer also suggested modification in magnetic properties at low temperatures therefore a study of temperature and field dependent magnetic structure in RE/TM multilayer annealed at different temperature will be interesting for both application and fundamental research point of view. In addition, finding a RE/TM multilayer system with a compensation temperature near room temperature will be very promising system for technological application, especially for helicity dependent magnetic properties. In the case of FePt based system we observed interesting low temperature magnetic behaviour in SQUID measurements therefore it will be interesting to see detail depth dependent magnetic temperature at low temperatures using PNR. In addition, the study can be pursued by search for more suitable nonmagnetic material, e.g. Ag or Au, which is miscible with FePt alloy and provides improved magnetic properties of the alloy for technological application.

Homi Bhabha National Institute

Recommendations of the Viva Voce Committee

As members of the Viva Voce Committee, we certify that we have read the dissertation prepared by Mr. Mulla Ahmad Basha entitled "Evolution of depth dependent structure and magnetic properties of multilayers on annealing" and recommend that it may be accepted as fulfilling the thesis requirement for the award of Degree of Doctor of Philosophy.

Chairman – Dr. S. L. Chaplot	S. L. Chaplot 15-09-2020.
Guide / Convener – Dr. Surendra Singh	Surendra Singh
Examiner - Prof. B. N. Dev	
Member 1- Prof. M. Senthil Kumar	
Member 2- Dr. V. K. Aswal	
Member 3- Dr. D. Bhattachryya	

Final approval and acceptance of this thesis is contingent upon the candidate's submission of the final copies of the thesis to HBNI.

I hereby certify that I have read this thesis prepared under my direction and recommend that it may be accepted as fulfilling the thesis requirement.

Date: 15-09-2020

Place: Mumbai

Surendra Singh

Signature

Guide

STATEMENT BY AUTHOR

This dissertation has been submitted in partial fulfillment of requirements for an advanced degree at Homi Bhabha National Institute (HBNI) and is deposited in the library to be made available to borrowers under rules of the HBNI

Brief quotations from this dissertation are allowable without special permission, provided that accurate acknowledgement of source is made. Requests for permission for extended quotation from or reproduction of this manuscript in whole or in part may be granted by the Competent Authority of HBNI when in his or her judgment the proposed use of the material is in the interests of scholarship. In all other instances, however permission must be obtained from the author.

M. Ahmad Basha

(Mulla Ahmad Basha)

Declaration

I, hereby declare that the investigation presented in the thesis have been carried out by me. The work is original and has not been submitted earlier as a whole or in part for a degree / diploma at this or any other institution /university.

(Mulla Ahmad Basha)

Declaration

I, hereby declare that the queries raised by the examiners of the thesis as well as the corrections suggested by examiners have been incorporated.

Surendra Singh

Surendra Singh

(Guide)

List of Publications arising from the thesis

Journals

1. "Interface induced magnetic properties of Gd/Co heterostructures", **M.A. Basha**, C.L. Prajapat, M. Gupta, H. Bhatt, Y. Kumar, S.K. Ghosh, V. Karki, S. Basu, S. Singh, *Physical Chemistry Chemical Physics* **2018,** *20 (33),* 21580-21589**.**

2. "Antisymmetric magnetoresistance and helical magnetic structure in a compensated Gd/Co multilayer", S. Singh, **M.A. Basha**, C.L. Prajapat, H. Bhatt, Y. Kumar, M. Gupta, C.J. Kinane, J. Cooper, M.R. Gonal, S. Langridge, S. Basu, *Phys. Rev. B* **2019,** *100 (14),* 140405(R).

3. "Annealing driven positive and negative exchange bias in Fe-Cu-Pt heterostructures at room temperature", **M.A. Basha**, H. Bhatt, Y. Kumar, C.L. Prajapat, M. Gupta, V. Karki, S. Basu, S. Singh, *Journal of Alloys and Compounds* **2020,** *815*, 152640**.**

4. "Evolution of structural and magnetic properties of FePtCu alloy films on annealing of FePt/Cu multilayers", **M.A. Basha**, H. Bhatt, Y. Kumar, C.L. Prajapat, M. Gupta, V. Karki, S.K. Ghosh, S. Basu and S. Singh, *Physical Chemistry Chemical Physics***,** **2020,** *22*, 16107 – 16116.

5. "Field dependent helical magnetic structure in a compensated Gd/Co multilayer", **M.A. Basha**, C. L. Prajapat, H. Bhatt, Y. Kumar, M. Gupta, C. J. Kinane, J.F. K. Cooper, S. Langridge, S. Basu and S. Singh, *Journal of Magnetism and Magnetic Materials*, **2020,** 516, 167331**.**

6. "Helical magnetic structure and exchange bias across the compensation temperature of Gd/Co multilayers", **M.A.** Basha, C.L. Prajapat, H. Bhatt, Y. Kumar, M. Gupta, C.J. Kinane, J.F.K. Cooper, A. Caruana, M. R. Gonal, S. Langridge, S. Basu, and S. Singh, *Journal of Applied Physics*, **2020,** 128, 103901**.**

7. "Formation of an intermetallic $GdCo_2$ alloy on controlled annealing of a Gd/Co multilayer", **M.A. Basha**, H. Bhatt, Y. Kumar, C.L. Prajapat, M. Gupta, S. Basu, and S. Singh, **2020** (*under review*).

Conference proceedings

8. "Optimization and characterization of cobalt & gadolinium films using X-ray scattering", **M.A. Basha**, C.L. Prajapat, S. Singh, S. Basu, *AIP Conference Proceedings,* **2017***,* 1832 (1), 080051**.**

9. "Optimization of co-sputtered FePt films using x-ray scattering techniques", **M.A. Basha**, M. Gupta, C.L. Prajapat, S. Basu, S. Singh, *AIP Conference Proceedings,* **2018**, 1942 (1), 080015.

10. Interface dependent diffusivity in Gd/Co multilayer, **M.A. Basha**, C.L. Prajapat, H. Bhatt, Y. Kumar, M. Gupta, S. Basu, S. Singh, *AIP Conference Proceedings,* **2019,** 2115 (1), 030310.

11. Annealing driven interface diffusivity in FePt/Cu multilayer, **M.A. Basha**, H. Bhatt, Y. Kumar, C.L. Prajapat, M. Gupta, S. Basu, S. Singh, *AIP Conference Proceedings,* **2020,** *in press.*

Poster presentation

1. "Depth dependent structure and magnetic characterization of thin films using X-ray and polarized neutron reflectivity", **M.A. Basha**, S. Basu and S. Singh, 16th Asia Oceania Neutron Scattering Association (AONSA) School, 15-19 November, 2016, BARC, Mumbai, Maharashtra.

2. “Structural study of Gd/Co multilayer on annealing”, **M.A. Basha,** S. Basu and S. Singh, International conference on thin films (ICTF), 13-17 November, 2017, CSIR-National Physical Laboratory, New Delhi.
3. “Interface study of Gd/Co multilayer film for magneto-optical storage devices”, **M.A. Basha**, and S. Singh, Materials & Technologies for Energy Conversion and Storage (M-TECS), 26-29 September, 2018, BARC, Mumbai, Maharashtra.
4. “Interface dependent structure and magnetic properties of Gd/Co multilayer on annealing”, **M.A. Basha**, and S. Singh, International conference on magnetic materials and applications (ICMAGMA), 9-13 December, 2018, NISER, Bhubaneswar, Jatni, Odisha, India.

M. Ahmad Basha

(Mulla Ahmad Basha)

Dedicated to

My Mother: Noorjahan

&

My best friend: Komal Tiwari

LIST OF FIGURES

(c) (d) $M(H)$ curves for S1, S2, and S3 at $T_{comp.}$ The variation of H_c (e) and E_B (f) with temperature.

4.6 MR (%) data in an applied in-plane magnetic field (longitudinal direction: Current and field are applied in the same direction) at different temperatures for the multilayers S1 (left panel), S2(middle panel) and S3 (right panel).

4.7 Spin dependent specular PNR data [NSF: R^{++} (red open circles) and R^{--}(blue open triangles); SF: $(R^{+-} + R^{-+})/2.0$ (maroon star)] along with fit (solid lines) at different temperatures for the multilayers S1 (left panel), S2 (middle panel) and S3 (right panel). NSLD and MSLD depth profiles obtained from specular PNR data at 300 K for multilayers S1, S2, and S3 are shown in the corresponding lower panel.

4.8 (a) schematic of the magnetic helical structure. Representation of magnetic structures along the depth of a bilayer of Gd/Co in multilayers S1 (b), S2(c) and S3 (d) at different temperatures. For S3 the magnetic structures below 300 K in (d) represents for top 4 BLs.

4.9 (a-d) Specular PNR data [NSF: R^{++} (red open circles) and R^{--} (blue open triangles); SF: $(R^{+-} + R^{-+})/2.0$ (maroon star)] of S2 at 140 K. Solid lines are fits to data considering different magnetic models shown in (e).

4.10 Experimental PNR data (Q_x-Q_z map) (upper part) from the Gd/Co multilayers S1 (a), S2(b), and S3 (c), at different temperatures in NSF (R^{++}) and SF (R^{+-}) modes under an applied in-plane field (H) of 500 Oe. Simulated profiles at different temperatures are shown in a row below the experimental data. (d) Comparison of SF (R^{+-}) intensity (scattered) and fit (continuous line) around the $Q_z \sim 0.06$ Å^{-1} for three multilayers at their corresponding T_{comp}. (e) Schematic of spin alignment of the central Gd sub-layer in a bilayer, contributing to the Bragg sheet in R^{+-} intensity at 125 K and 140 K for S1 and S2, respectively.

LIST OF TABLES

LIST OF ABBREVIATIONS

2D	Two dimensional
EB	Exchange Bias
SQUID	Superconducting Quantum Interference Device
RE	Rare Earth
TM	Transition Metal
FM	Ferromagnetic
AFM	Anti Ferro Magnetic
SP	Super-Paramagnetic
DWs	Domain Walls
FC	Field Cool
ZFC	Zero Field Cool
XRR	X-ray Reflectivity
PNR	Polarized Neutron Reflectivity
ESLD	Electron Scattering length Density
NSLD	Nuclear Scattering Length Density
MSLD	Magnetic Scattering Length Density
DHL	Double Hysteresis Loop
FWHM	Full width at Half Maximum
MR	Magneto Resistance
DWBA	Distorted Wave Born Approximation
PSD	Position Sensitive Detector
NSF	Non Spin Flip
SF	Spin Flip
GIXRD	Grazing incidence X-ray Diffraction
SIMS	Secondary Ion Mass Spectrometry
XRD	X-ray Diffraction

Thesis Highlight

Name of the Student: MULLA AHMAD BASHA

Name of the CI/OCC: BARC, Mumbai **Enrolment No.:** PHYS01201604027

Thesis Title: Evolution of depth dependent structure and magnetism of multilayers on annealing

Discipline: Physical Sciences **Sub-Area of Discipline:** Thin film magnetism

Date of viva voce: 12/09/2020

Antiferromagnetically (AFM) coupled Rare earth (RE)–Transition metal (TM) heterostructures are known to exhibit a number of magnetic structures at different temperatures and magnetic fields, which are highly effected by interface morphology. RE-TM heterostructures also behave as a artificial ferrimagnet due to AFM coupling at interfaces, hence, these systems are potential candidate materials for realizing devices with higher speed and density. We have studied the evolution of depth-dependent structure and magnetism across compensation temperature (T_{comp} = temperature at which the resultant magnetization of the system tends to zero) for Gd/Co multilayers grown under different growth conditions. We found a negative exchange bias in the Gd/Co multilayer below T_{comp} and antisymmetric magnetoresistance (MR) at T_{comp} using macroscopic magnetization and magneto-transport measurements. Specular polarized neutron reflectivity (PNR) with spin polarization analysis results showed the formation of a helical magnetic structure with planner 2π domain walls in the Gd/Co multilayer at a temperature ≤ T_{comp}, which is responsible for the observed negative exchange bias in this system. Annealing of these multilayers resulted in the modification of interface structure (increase in roughness and formation of alloying), which drastically changes the magnetic properties of the multilayers. We successfully correlated the interface induced macroscopic properties with the depth dependence structure and magnetic properties of these systems.

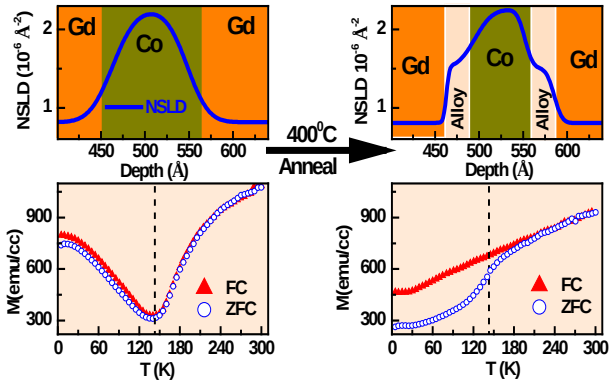

Figure 1. Nuclear scattering length density (NSLD) and corresponding temperature dependent magnetization curves of as-deposited and annealed Gd/Co multilayer

Besides Gd/Co multilayer systems, Fe (FM)/Pt (heavy metal) systems have attracted considerable attention in recent years because of its magnetic properties, which are deployable in ultrahigh-density information storage devices. We have studied the evolution of alloy formation at interfaces of Fe-Pt-Cu systems, assuming different interfaces e.g. Fe-Cu-Pt heterostructures (Fe/Cu/Pt and Fe/Pt/Cu trilayers grown on Si substrates) and FePt/Cu multilayers. Using depth dependent non-destructive characterization techniques (x-ray reflectivity and PNR) and macroscopic magnetic measurements (SQUID), we have shown annealing driven drastically different structure and magnetism for two systems (Fe-Cu-Pt trilayers and FePt/Cu multilayers). For trilayer heterostructures, we observed long-range interdiffusion and evolution and ternary phase alloy, showing exchange bias effect on annealing above 400 °C. For multilayer systems we observed silicide phase at the substrate interface which helps to grow the FCT phase of ternary alloy. Large variations in magnetic properties of the FePt/Cu multilayer on annealing for longer time (> 2 hr) at 600 °C were observed for the multilayer with thicker Cu layer.